SINGLE-PHASE LAMINAR FLOW HEAT TRANSFER FROM CONFINED ELECTRON BEAM ENHANCED SURFACES

This thesis is submitted for the degree of Engineering Doctorate

by

Arben FERHATI

School of Engineering and Design

Brunel University

July 2014

ABSTRACT

The continuing requirement for computational processing power, multi-functional devices and component miniaturization have emphasised the need for thermal management systems able to maintain the temperature at safe operating condition. The thermal management industry is constantly seeking for new cutting edge, efficient, cost effective heat transfer enhancement technologies. The aim of this study is to utilize the electron beam treatment for the improvement of the heat transfer area in liquid cooled plates and experimentally evaluate the performance. Considering the complexity of the technology, this thesis focuses on the design and production of electron beam enhanced test samples, construction of the test facility, testing procedure and evaluation of thermal and hydraulic characteristics. In particular, the current research presented in this thesis contains a number of challenging and cutting edge technological developments that include: (1) an overview of the semiconductor industry, cooling requirements, the market of thermal management systems, (2) an integral literature review of pin-fin enhancement technology, (3) design and fabrication of the electron beam enhanced test samples, (4) upgrade and construction of the experimental test rig and the development of the test procedure, (5) reduction of the experimental data and analysis to evaluate thermal and hydraulic performance. The experimental results show that the capability of the electron beam treatment to improve the thermal efficiency of current untreated liquid cooled plates is approximately three times. The highest heat transfer rate was observed for the sample S3; this is attributed to the irregularities of the enhanced structure, which improves the heat transfer area, mixing, and disturbs the thermal and velocity boundary layers. Enhancement of heat transfer for all three samples was characterised by an increase of pressure drop. The electron beam enhancement technique is a rapid process with zero material waste and cost effective. It allows thermal management systems to be produced smaller and faster, reduce material usage, without compromising safety, labour cost or the environment.

DECLARATION

The research presented in this thesis is an original work of the author, except where otherwise specified, or where acknowledgements are made by references. This project was collaboration between Thermacore Europe, TWI and Brunel University and was headed by the School of Engineering and Design, Brunel University, under the supervision of Prof. T. G. Krayiannis.

Arben Ferhati

ACKNOWLEDGEMENTS

I would like to take this opportunity to express my highest gratitude to Prof. Tassos Karayiannis, Prof. David Reay, Dr. John Lewis, and Dr. Ryan McGlenn for continuous supervision, guidance, encouragement, and constant assistance throughout this work.

I would like to acknowledge EPSRC, Brunel University, Thermacore Europe and The Welding Institute for providing technical and financial support for the project.

I would like to thank colleagues at Thermacore Europe, especially Kevin Lynn, David Mullen, Dr. Andreas Engelhard for their help and support at the various stages of this project.

Words fail to express my gratitude, for the endless love, care and support to my family.

Finally, I would like to express my gratitude to all friends and colleagues at both Brunel University and at Thermacore Europe for their support.

CONTENTS

1 Introduction.. 1

1.1 Aims and objectives 9

1.2 Structure of thesis 12

1.3 Contribution to knowledge 13

1.3.1 List of publications 15

2 Electronic modules and energy performance 16

2.1 Overview 16

2.2 History of semiconductor industry 17

2.3 Current e future developments 19

2.3.1 Market of semiconductor components 24

2.4 Packing and thermal behaviour 26

2.4.1 Semiconductor material 26

2.4.2 Microprocessor manufacturing process 27

2.4.3 Information technology sector and energy requirements 28

2.4.4 Reliability and safety 30

2.4.5 Electronic component packaging levels 30

2.4.6 Market of thermal management systems for electronics industry 32

2.4.7 Summary 34

3 Literature review 36

3.1 Enhancement technologies 36

3.1.1 Passive techniques 37

3.1.2 Active techniques 38

3.1.3 Compound techniques 39

3.1.4 Published literature 39
3.2 General consideration 40
3.2.1 Forced convection internal flows 41
3.2.2 Pressure drop in the smooth and fined ducts 43
3.2.3 Nusselt number 45
3.3 Pin-fin heat transfer enhancement 49
3.3.1 Pin-fin and end-wall heat transfer rates 55
3.3.2 Heat transfer variation in the heat sink 57
3.3.3 Arrangement effects 61
3.3.4 Pin-fin aspect ratio effect 68
3.3.5 Pin-fin shape effect 70
3.3.6 Clearance effect 76
3.3.7 Reynolds number effect 80
3.4 Emerging enhancement technologies for liquid cooling application 80
3.5 Summary 84
4 Electron beam treatment and preparation of the test module 88
4.1 Overview 88
4.2 Surfi-Sculpt process 89
4.3 Electron beam technology 90
4.3.1 Electron beam 91
4.3.2 Electron beam control 92
4.3.3 Electron beam for industrial applications 93
4.4 Electron beam system 93
4.4.1 Electron beam gun 94
4.4.2 Vacuum chamber 97
4.5 Surfi-Sculpt working principle 97

4.5.1 Potential benefits of surface treatment for heat transfer applications 102
4.6 Current electron beam treatment 103
4.6.1 Description of the process 104
4.6.2 Conceptual design 105
4.6.3 Summary 116
5 FD study for the smooth sample 119
5.1 Geometry 120
5.2 Model 123
5.2.1 Boundary conditions 123
5.3 Mesh dependency 124
5.4 Simulation process 126
5.5 Post processing and results 126
5.5.1 Analysis for mass flow rate 0.01 kg/s 126
5.5.2 Analysis for mass flow rate 0.02 kg/s 131
5.5.3 Analysis for mass flow rate 0.03 kg/s 133
5.5.4 Analysis for mass flow rate 0.04 kg/s 136
5.6 Results 139
5.6.1 Heat transfer 139
5.6.2 Pressure drop 139
5.7 Summary 140
6 Experimental facility and methodology 142
6.1 Test rig design 142
6.1.1 Test module 144
6.1.2 Measurement system 150
6.1.3 Test procedure 156
6.1.4 Operating condition 157

6.2 Data reduction 157
6.2.1 First method 158
6.2.2 Second method 164
6.3 Uncertainty Analysis 168
6.3.1 Geometrical parameters 171
6.3.2 Heat transfer 172
6.3.3 Friction factor 174
6.3.4 Summary 175
6.4 Validation of the test rig 175
6.4.1 Experimental and CFD data for the heat transfer coefficient .. 176
6.4.2 Experimental and CFD data for the pressure drop 177
6.4.3 Summary 178
7 Experimental Results 180
7.1 Estimation of heat loss 180
7.2 Fist method 185
7.2.1 Friction factor 185
7.2.2 Heat transfer 188
7.2.3 Summary 192
7.3 Second method 194
7.3.1 Flow characteristics 194
7.3.2 Comparison of the fin friction factor with other researchers ... 196
7.3.3 Heat transfer characteristics 199
7.3.4 Comparison of experimental Nusselt number with other researchers 200
7.4 Summary 204
7.4.1 Pressure drop 204
7.4.2 Heat transfer 206

8 Conclusion and recommendations 208
8.1 Future work 213
9 Appendix 216
9.1 Experimental data 216
10 References 220

LIST OF FIGURES

Figure 1.1: Transistor size through years (Intel, 2013)................................. 2
Figure 1.2: Thermal resistance of given working fluid, (Bejan & Kraus, 2003). 7
Figure 2.1: Thermal management market 2013, (Electronics.Ca, 2014)...... 33
Figure 2.2: Electronic cooling system components market 2011, (Thermacore, 2012). 33
Figure 2.3: Thermal management product sale for three main sectors, (Electronics.Ca, 2014). 34
Figure 3.1: Published enhanced heat transfer technology, (ScienceDirect, 2014).. 40
Figure 3.2: Steady-state heat conduction in fin. 47
Figure 3.3: Pin fin heat sinks, (Alsic, 2013). 49
Figure 3.4: Pin-fin heat sink parameters. 51
Figure 3.5: Nusselt numbers versus Reynolds number for circular shape fins, generated by computing in “MS Excel” respective correlations.................... 52
Figure 3.6: Friction factor versus Reynolds number for circular shape fin, generated by computing in “MS Excel” respective correlations.................... 53
Figure 3.7: Variation of heat transfer in pin-fin heat sink against the row number, (Metzeger, et al., 1982) 59
Figure 3.8: The average Nusselt number as function of Reynolds number. (Kosar & Peles, 2006). 60
Figure 3.9: Comparison between measured and predicted values of Nusselt number. 61
Figure 3.10: Staggered arrangement, Nusselt number versus Reynolds number, (Metzeger & Haley, 1982). 62
Figure 3.11: Nusselt number versus Reynolds number for different stream-wise spacing for Pr=7... 63
Figure 3.12: Nusselt number versus stream-wise aspect ratio, (Bilen, et al., 2001).. 64
Figure 3.13: The average Nusselt number as a function of dimensional pumping power, (Jeng, 2006). 65

Figure 3.14: Non-dimensional pressure drop as a function of Reynolds number for in-line arrangement of square pin-fin, (Jeng & Tzeng, 2007)..... 66
Figure 3.15: Thermal performance of all geometries tested, (Lawson, et al., 2011).......... 68
Figure 3.16: Design of the test sample, (Peles, et al., 2005). 69
Figure 3.17: Thermo-hydraulic performance, (Soodphakdee & Copeland, 2001).......... 71
Figure 3.18: Tested geometries, (Ricci & Montelpare, 2006).......... 71
Figure 3.19: Thermal performance of four fin geometries, (Ricci & Montelpare, 2006).......... 72
Figure 3.20: SLM technology heat sinks, (Wong, et al., 2009).......... 73
Figure 3.21: Experimental Nusselt number compared to the available equations, (Liu, et al., 2011). 74
Figure 3.22: Friction factor for fin structures, (Liu, et al., 2011).......... 74
Figure 3.23: Nusselt number versus Reynolds number, (Tullius, et al., 2012). 75
Figure 3.24: Pressure drop versus maximum axial-velocity, (Tullius, et al., 2012).......... 75
Figure 3.25: Side and top view of the heat sink, (Dogrouz M.B. et al., 2005). 77
Figure 3.26: Staggered circular pin fins with and without tip clearance, (Moores, et al., 2009).......... 78
Figure 3.27: Variation of Nusselt number over Reynolds number for different clearance ratios, (Mei, et al., 2014).......... 79
Figure 3.28: Variation of friction factor over Reynolds number for different clearance ratios, (Mei, et al., 2014).......... 80
Figure 3.29: Micro Deformation Technology (MTD) structure, (Wolverine, 2013).......... 81
Figure 3.30: Laser Surface Treatment, (TWI, 2013). 82
Figure 3.31: Metal Injection Moulding Technology fin height 2.5 mm, (Amulare, 2013) 82
Figure 3.32: Electron Beam Treated Surface, produced by optical microscope x 10, (TWI, 2009).......... 83

Figure 4.1: Electron beam enhanced area, picture taken by optical microscope.. 90
Figure 4.2: Electron beam treatment system courtesy of TWI. 94
Figure 4.3: Electron beam gun view, (TWI).. 95
Figure 4.4: Simple diagram of electron beam machine................................ 96
Figure 4.5: Electron beam process in metals, (TWI, 2002). 98
Figure 4.6: Electron beam treatment, left single and right multi fin, microscope image. 99
Figure 4.7. Electron beam treatments holes with size 500μm, microscopy image. 102
Figure 4.8: Electron beam treatment process control diagram. 105
Figure 4.9: 3D model of Sample S1 generated with Solid-Works software.106
Figure 4.10: Drawing of Sample S1 from the 3D-model, generated by Solid-Works software. 107
Figure 4.11: 3D model of Sample S2 generated with Solid-Works software. 107
Figure 4.12: Drawing of Sample S2 from the 3D-model, generated by Solid-Works software. 108
Figure 4.13: 3D model of Sample S3 generated with Solid-Works software. 108
Figure 4.14: Drawing of Sample S3 from the 3D-model, generated by Solid-Works software. 109
Figure 4.15: Diagram of electron beam movement required to build spikes and holes. 110
Figure 4.16: Electron beam treatment process path for sample S1. 110
Figure 4.17: Electron beam treatment process, sample S2. 111
Figure 4.18: Electron beam treatment process, sample S3. 111
Figure 4.19: Electron beam swipe path for sample S1.............................. 112
Figure 4.20: Electron beam swipe path for sample S2.............................. 112
Figure 4.21: Electron beam swipe path for sample S3.............................. 112
Figure 4.22: Sample 1 (left), Sample 2 (centre) and Sample 3 (right), each (35 mm x 55 mm)... 113
Figure 4.23: View of the treatment pattern (4.3 x 4.1) mm^2, for Sample S1114
Figure 4.24: Close pictures of Sample 1 114

Figure 4.25: Sample 2 protrusion. 115
Figure 4.26: Sample 2, upper view of the treatment. 115
Figure 4.27: Sample 3 upper view. 116
Figure 4.28: Sample 3, close view of protrusions. 116
Figure 5.1: View of the test module. 121
Figure 5.2: Axonometric transparent view of heated test module. 122
Figure 5.3: Frontal cut and side cut views of the test module 122
Figure 5.4: View of the grid on the test module. 125
Figure 5.5: View of the mesh of the fluid domain. 125
Figure 5.6: H. at distribution through the test module for m=0.01 kg/s. 127
Figure 5.7: Temperature profile in the centre plane perpendicular to the flow, for m=0.01 kg/s. 127
Figure 5.8: Temperature profile of the flow for m=0.01 kg/s. 128
Figure 5.9: The fluid temperature increase in the channel for m=0.01 kg/s. 128
Figure 5.10: Velocity vectors coloured by temperature for m= 0.01 kg/s. .. 129
Figure 5.11: Centre plane velocity profile, m=0.01 kg/s. 130
Figure 5.12: Pressure distribution of the flow for m=0.01kg/s. 130
Figure 5.13: Pressure drop through the smooth channel, m=0.01 kg/s. 131
Figure 5.14: Fluid temperature rise in the channel for 0.02 kg/s fluid flow. 131
Figure 5.15: Heated surface temperature for mass flow rate 0.02 kg/s. 132
Figure 5.16: Pressure drop in the channel, for mass flow rate 0.02 kg/s. .. 133
Figure 5.17: Heat distribution through the test module for mass flow rate 0.03 kg/s. 134
Figure 5.18: Temperature profile through the fluid for mass flow rate 0.03 kg/s. 134
Figure 5.19: Fluid temperature from inlet to outlet, mass flow rate 0.03 kg/s. 135
Figure 5.20: Temperature distribution over the smooth surface for 0.03 kg/s mass flow rates. 135
Figure 5.21: Pressure drop in the channel mass flow rate 0.03 kg/s. 136
Figure 5.22: Temperature profile of the fluid flow for mass flow rate 0.04 kg/s 137

Figure 5.23: Fluid temperature from inlet to outlet, mass flow rate 0.04 kg/s. 137
Figure 5.24: Surface temperature for mass flow rate 0.04 kg/s.................. 138
Figure 5.25: Pressure drop in the channel mass flow rate 0.04 kg/s.......... 138
Figure 5.26: The Nusselt number versus Reynolds number for mass flow rates 0.01 kg/s to 0.04 kg/s and heat input 600 W. 139
Figure 5.27: The pressure drop versus Reynolds number for mass flow rates 0.01 kg/s to 0.04 kg/s and heat input 600 W. 140
Figure 6.1: Schematic of the test flow loop. 143
Figure 6.2: Picture of the test rig. 144
Figure 6.3: Schematic view of the test module. 145
Figure 6.4: Picture of the Test Module. 146
Figure 6.5: Interior view of test sample. 147
Figure 6.6: Three enhanced test samples. 147
Figure 6.7: Schematic view of test module. 149
Figure 6.8: Picture of the test module insulation. 150
Figure 6.9: Thermocouple calibration process using (Isotech 2140) device. 152
Figure 6.10: Schematics of liquid circulation and cooling system. 154
Figure 6.11: Frontal view perpendicular to the flow of the fin. 159
Figure 6.12: Protrusion dimensions. 165
Figure 6.13: The uncertainty of the temperature measurements. 170
Figure 6.14: Uncertainty versus heat transfer coefficient. 172
Figure 6.15: Uncertainty of heat transfer coefficient versus heat transfer rate. 173
Figure 6.16: Uncertainty of the Nusselt number versus Nusselt number. .. 174
Figure 6.17: Uncertainty of the friction factor coefficient versus friction factor coefficient. 175
Figure 6.18: Nusselt number results for the CFD study, experimental work and Stephan (1959) Equation (7.2) versus Reynolds number. 177
Figure 6.19: Comparison between experimental, CFD and prediction from Equation (6.10) of pressure drop for smooth sample. 178
Figure 7.1: Heat transfer rate to water versus electrical power input, for sample S1. 182

Figure 7.2: Heat transfer rate to water versus electrical power, for sample S2. 183
Figure 7.3: Heat transfer rate to fluid versus electrical power input, for sample S3. 184
Figure 7.4: Heat transfer rate to fluid versus Electrical Power, for the smooth sample. 185
Figure 7.5: Friction factor versus Reynolds number for all four samples. .. 186
Figure 7.6: Thermal resistance = 1/hA (K/W) for each sample. 188
Figure 7.7: Heat flux versus surface temperature for constant mass flow rate of 0.045 kg/s, (Re ~ 1850) and inlet fluid temperature ≈19 °C. 189
Figure 7.8: Nusselt number versus Reynolds number for all four samples. 190
Figure 7.9: Efficiency index versus Reynolds number for three enhanced samples. 192
Figure 7.10: Pressure drop versus Reynolds number for three enhanced samples. 195
Figure 7.11: Friction factor versus Reynolds number for Sample S1. 196
Figure 7.12: Friction factor versus Reynolds number for sample S2.......... 197
Figure 7.13: Friction factor versus Reynolds Number for sample S3 198
Figure 7.14: Heat transfer versus Pressure drop for three enhanced samples 199
Figure 7.15: Heat transfer coefficient of equivalent pin-fin structure versus Reynolds number for three enhanced samples. 200
Figure 7.16: Nusselt number versus Reynolds number for sample S1. 201
Figure 7.17: Nusselt number versus Reynolds number for sample S2. 202
Figure 7.18: Nusselt number versus Reynolds number for sample S3. 203
Figure 7.19: Friction factor for the test samples compared with those in literature versus Reynolds number. 205
Figure 7.20: Comparison of the Nusselt number for the experimental work with those available in the literature versus Reynolds number. 207

LIST OF TABLES

Table 1.1. Intel processors transistor density (Intel, 2013). 2
Table 2.1: Operating parameters for a range of semiconductor modules, (ITRS, 2013). 21
Table 2.2: Global semiconductors market for the year 2012 and 2013, (SIA, 2014). 26
Table 2.3: Comparison of heat fluxes between microprocessor and light bulb. 29
Table 2.4: Cooling technologies for each packing level, (Bejan & Kraus, 2003) 32
Table 3.1: Classification of various Enhancement Techniques, (Webb & Kim, 2005). 37
Table 3.2: Nusselt number correlations for cross flow through circular fins. 54
Table 3.3: Some of the friction factor correlations in literature. 55
Table 4.1: Factors that affect the electron beam product quality.Error! Not a valid link. 101
Table 4.2 Electron beam treatment parameters for sample S1, S2 and S3 in copper Cu 101 and aluminium Al 7075. 118
Table 5.1: Mesh information from the CFD. 124
Table 6.1: List of the test loop elements. 144
Table 6.2: Protrusions and channel dimensions. 148
Table 6.3: Geometrical parameters of protrusions. 167
Table 7.1: Friction factor data correlations, Reynolds number applicability and mean absolute error. 187
Table 7.2: The heat transfer data correlations, Reynolds number applicability and mean absolute error. 191
Table 7.3: Friction factor data correlations, Reynolds number applicability and mean absolute error. 198
Table 7.4: Nusselt number data correlations, Reynolds number applicability and mean absolute error for the current experimental data 203
Table 9.1: Experimental data for the Sample S1....................................... 216
Table 9.2: Experimental data for the Sample S2....................................... 217

Table 9.3: Experimental data for the Sample S3.. 218
Table 9.4: Experimental data for the Smooth sample. 219

1 INTRODUCTION

As the economy shifts from paper-based to electronic information management, requirements for higher storage capacities, faster processing, communication and networking is essential to the functioning of private and government sectors. Data and computer centres are found in nearly every sector of the economy: financial, public services, media, telecommunication, universities, military, government institutions, and many others operate computers and data centres to facilitate everyday processes, information management, and communications functions of their organizations.

The electronics sector has become an integral part of economic and social development around the world. In recent years the energy consumption from the IT sector and as a consequence, the environmental impact, has become a “hot issue” for both operators and policy makers, (EPA, 2013). Data centres and communication sectors are identified to be the fastest growing sectors, (Frontier, 2011), therefore, energy requirements are anticipated to increase and reach 144 GW by 2020 (Electronics.Ca, 2012), (EPA, 2013). Furthermore, energy prices are continually rising, impacting heavily operational costs for such businesses and prices for their services. Requirements for powerful and multifunctional computers are increasing rapidly leading to miniaturization and high component densities in small space envelopes. However, the energy efficiency of electronic equipment and servers has not risen at the same rate. This has resulted in real high heat fluxes, which require aggressive cooling technologies.

Requirements, to remove higher heat fluxes from small volumes are now present in modern technology. Gordon E. Moore, one of the co-founders of Intel, in 1965 predicted that the processing power of a microchip would double every 18-24 months (Moore, 1965). The microprocessor industry has followed this trend for over 40 years, Table 1.1.

According to Table 1.1 in 2013 transistor density in processor, increased by a factor 106 compared to 1972, while the transistor size has decreased to 22 nm and is expected to decrease at 14 nm by 2016, this will further increase the heat dissipation.

Table 1.1. Intel processors transistor density (Intel, 2013).

Year	Intel Processor	Transistors
1972	404	2.30E+03
1974	8080	6.00E+03
1978	8086	2.90E+04
1982	80286	1.34E+05
1986	Intel 386 DX	2.75E+05
1992	Intel 486 DX	1.20E+06
1994	Intel DX4	1.60E+06
1999	Intel mobile Pentium 2	2.70E+06
2002	Intel Celeron Ultra low voltage	1.40E+08
2005	Intel Pentium 4 (660-630)	1.69E+08
2007	Quad Core Intel Xenon	8.20E+08
2008	Intel Xenon MP E7450	1.90E+09
2012	Intel Extreme	2.20E+09
2013	Intel® Core™ i7-3970X Processor	2.27E+09

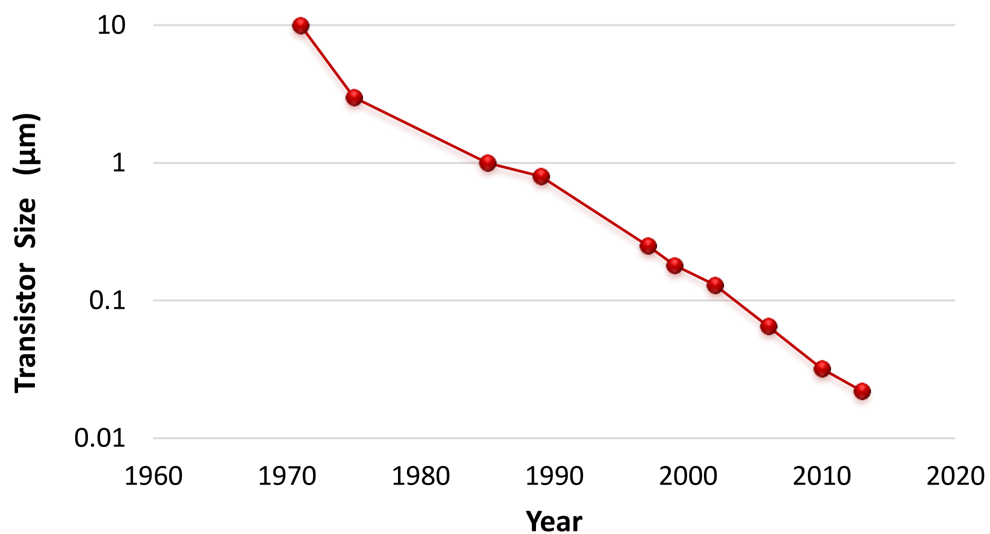

Figure 1.1: Transistor size through years (Intel, 2013)

Aiming to improve the performance and maintain heat dissipation at current levels, single processor architecture is being replaced by multi-core processor architecture. This allows an increase in processing performance by utilizing particular cores for specific functions without generating excessive or unmanageable heat fluxes. Moreover, the properties of the semiconductors have been technologically customized to enable processors to deliver higher performance and withstand elevated temperatures. However, the increase in transistor density has increased further heat dissipation at levels that require active cooling techniques

The conventional, natural and forced convection air cooling methods are still used in many applications to maintain the component operating temperature. This technique can only provide moderate thermal performance. The continually increasing demand for higher processing power and smaller devices has made air cooling techniques inadequate in ensuring the required operating conditions such as junction temperature and new, high-performance cooling devices are required.

Nowadays the local heat fluxes from the hotspots in electronic components have reached values of 500 W/cm2 to 1500 W/cm2 as reported by (Yang, et al., 2007) and (Wei, 2008) respectively. The hotspot heat fluxes are up to 20 times higher compared to those in other parts of the microprocessor. Furthermore, heat fluxes are expected to increase since the transistor size is continuously decreasing, i.e. current lithography capability has reached 22nm that is around 30% lower compared to that of the previous transistor 32nm in 2012-2013, (Intel, 2014). The required operating temperature at the junction for Intel microprocessor is set below 100 ^{o}C, (Intel, 2014), for every 10 ^{o}C rise in operating temperature over the specified maximum junction temperature, the time to failure is halved (Nnanna, et al., 2009), and the processor speed will decrease 10% to 15%, (Yang, et al., 2007). Therefore, there is a concern for the reliability of electronic equipment. Current natural and, forced air cooling heat sink technology, has reached its thermal limits, that are approximately 150 W/cm2, (Zhao & Bi, 2001). In order to overcome

the air cooling issues1 some systems use thermoelectric cooling technique. This technique is based on the cold junction theory, however, such systems have low cooling capacity and a very low efficiency, (Yang, et al., 2007). Another cooling technique that has been used previously in the early electronic modules is jet impingement direct liquid cooling method. This technique has the capability to dissipate approximately 250 W/cm2 when water is used as a working fluid, (Natarjan & Bezama, 2007). Currently the majority of cooling systems for electronic modules are composed of heat pipe assemblies that utilise passive two-phase heat transfer regime to transport heat from the heat source to a region that is remotely located from the electronics that can accommodate large heat sinks or fin stacks. Such systems provide a relatively low heat removal capacity around 50 W/cm2 and increase to 250 W/cm2 when the pulsating heat pipe is used, (Zimbeck, et al., 2008) and (Zou, et al., 2000).

In order to improve the heat removal capacity single phase liquid cooling in micro-channels have been investigated by a number of researchers (Kang, et al., 2007) and (Xie, et al., 2009). Tuckerman and Pease in 1981 studied the water flow over silicon micro-channels and claimed to have been able to remove heat fluxes equal to 790 W/cm2, (Tuckerman & Pease, 1981). However, later research from (Zhang, et al., 2005), (Xie, et al., 2009), and (Kang, et al., 2007) have shown lower heat dissipation rates, respectively 130 W/cm2, 256 W/cm2, and 500 W/cm2. Other techniques as nucleate and flow boiling have been as well investigated. In the nucleate boiling cooling technique, the electronic module is immersed in a dielectric fluid. These fluids have very poor conductive properties compared to water, therefore, can initiate thermal stresses due to active boiling and temperature variation2 on the surface, (Mudawar, 2001). The heat dissipation achieved with dielectric fluids is approximately 20 W/cm2, (Geisler, et al., 2004), however, can increase up to 100 W/cm2 with surface enhancement such as pin-fin, (Mudawar, 2001). The research demonstrates that, heat dissipation rates

[1] Large heat sinks and air blowers required to dissipate additional power to thermoelectric cooler.

[2] Dielectric fluids have a small contact angle with a surface (quantifies the surface wettability). Therefore large surface temperatures will be required to initiate boiling

from dielectric fluids are low compared to single phase water flow cooling technique. The two-phase flow boiling technique is very efficient because lower volume flow rates are required compared to single phase flow, for the same heat duty and as a result, lower pumping power is required. The compared heat dissipation for the two phase flow regime is higher in comparison to other techniques. Heat fluxes of 350 W/cm2 and 840 W/cm2 have been recorded respectively by (Agostini, et al., 2008) and (Lee & Mudawar, 2009) with refrigerant R236 as the working fluid.

Utilization of liquid cooling for electronic components is not a new technology; it has been used during the 1980s in bipolar chip technology, (Incroprera, 1999). However, to improve thermal efficiency and produce compact systems, recently heat transfer enhancement technologies are being incorporated into liquid cooling devices.

Heat transfer enhancement techniques have been successfully used to improve thermal efficiency and reduce equipment size in many sectors including energy generation, domestic (cooling and heating), chemical, automotive, turbo-machinery and lately electronics cooling. A variety of heat transfer enhancement techniques have been developed that can be classified into three main groups: (a) passive techniques, (b) active techniques, which require additional external power, and (c) compound techniques, involving a combination of (a) and (b) techniques to achieve a greater enhancement than a single technique alone, (Reay, 1991), (Bergles & Webb, 1985), and (Siddique, et al., 2010).

The most common enhancement techniques are passive because they do not require additional energy input. Active and combined techniques are less attractive due to their operational and maintenance costs. Enhancement techniques offer improvement by providing a higher hA (Watt / Kelvin) per unit base area. This can be used to complete one of three objectives:

i. Compact and small units, i.e. if the heat duty remains constant, the overall size of heat exchanger can be reduced.
ii. Increased hA, that can have two purposes:

a. Reduce operating temperature, if the heat duty and size are held constant. This provides higher thermal efficiency.
b. Increase heat duty, if the size is held constant.

iii. Reduce pumping power for fixed heat duty. This will require a large frontal area which may not be desired, (Webb & Kim, 2005).

Enhancement techniques can be used to achieve the above objectives depending on the design requirements, i.e. objective (i) will reduce material costs. It also can reduce the working fluid required that will provide considerable savings in case of costly working fluids such as refrigerants. Whereas objectives (ii) and (iii) can improve the “life cycle” and operational costs, by reducing operating temperature, pumping power, or increasing the heat transfer capacity.

Consequently, research concerning application of enhanced techniques to improve performance in electronics cooling has been intensive, (Sparrow, et al., 1982), (Chomdee & Kiatsiriroat, 2006), (Kim, 2007), (Luviano-Ortiz, et al., 2008), and (Zhang, et al., 2010). In this area micro-channels, offset strip fins and vortex generators have been studied with interest by (Rosa, et al., 2009), (Weilin & Mudawar, 2003), (Salamon, et al., 2010) and (Aris, et al., 2011). However, lately, attention has moved towards micro-pin-fin structures, (Kosar & Peles, 2007), (Kosar, 2008), (Qu & Siu-Ho, 2009), (Yuan, et al., 2009) and (Moores, et al., 2009) etc. The effect of enhancement techniques as circular, rectangular, elliptical and triangular pin-fins in the single phase flow regime and the heat transfer characteristics has been studied by, (Webb & Eckert, 1972), (Kandikar & Grande, 2004), (Rao, et al., 2011), (Dong, et al., 2007), (G.P. Celata et al, 2006), (Owhaib & Palm, 2004), (Young & Kandlikar, 2008). Literature shows that for both single and two-phase flow applications, enhancement technologies can improve the heat transfer considerably. A comparison between cooling methods and working fluids in relation to thermal resistance is presented in Figure 1.2. Single phase convective cooling techniques guarantee the transfer of high heat fluxes in rather small areas. However, for very high heat dissipation two phase boiling processes are seen as an efficient method for cooling. According to Figure 1.2, of the fluids compared, water is the best working fluid for both forced

convection and boiling regimes. This is an attribute of both physical parameters: the heat capacity (ρc_p) and the thermal conductivity that are higher compared to other fluids.

In the two-phase boiling regime enhancement techniques as surface irregularities and cavities are used to increase the critical heat flux and maintain nucleate boiling, which can transfer high heat flux as a result of phase change and also avoid the development of film boiling on smooth surfaces that under very high heat fluxes rapidly increases the temperature, resulting in premature failure of electronic equipment.

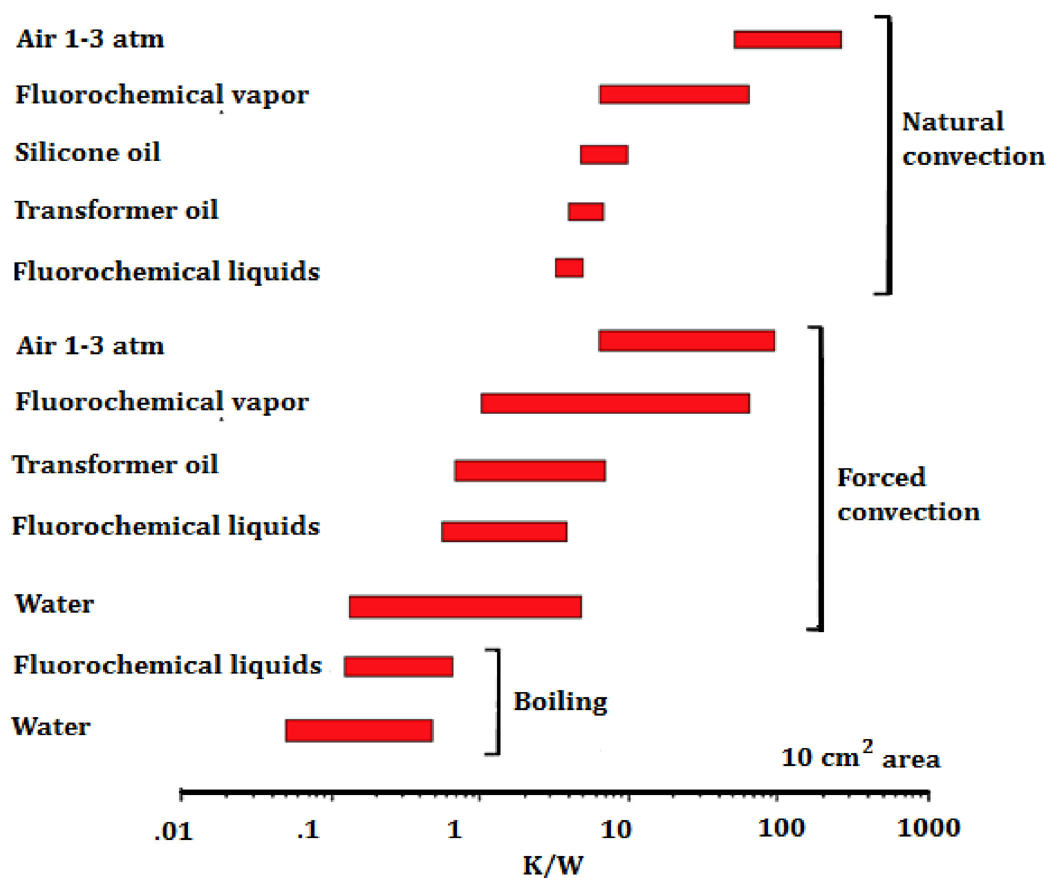

Figure 1.2: Thermal resistance of given working fluid, (Bejan & Kraus, 2003).

Thermacore Europe and TWI[1] have collaborated on the 'Advanced Surface Tailoring for Innovative Applications' (ASTIA) project to create surface treatments that enhance heat transfer characteristics. Various different complex 3D surface geometries were manufactured using an electron beam surface treatment technology known as Surfi-Sculpt™. This new surface modification technique developed at TWI is able to rapidly produce at low cost, unconventional tailored surfaces. Those are shown in this thesis to improve heat transfer in single-phase flow and also have been shown to enhance pool boiling applications (Ahmad, et al., 2014). In addition, the surface treatments can potentially be tailored to enhance flow boiling heat transfer.

In the Surfi-Sculpt process, the electron beam is manipulated using specialist hardware (custom electron beam gun) and complex beam guidance software. The electron beam is deflected rapidly at specific locations over a metallic surface to create particularly tailored features. As the beam is moved across the surface, it melts and begins to vaporize the substrate material, which under the combined effects of the vapour pressure and surface tension, is displaced in the direction opposite to the beam travel, to a cooler region of the surface where the material re-solidifies. Repeated beam passes over the same overlapping locations results in cumulative growth of protrusions above the original surface level, accompanied by associating cavities in the substrate. An entire array of protrusions can be rapidly created simultaneously across the surface of a work-piece. By accurate control of the EB process, a wide variety of well-defined patterns is possible; see (Dance & Buxton, 2007) and (Buxton, et al., 2009). The process can be used on a range of metals, polymers and ceramics and takes only a few seconds to treat a square centimetre of surface, depending on the treatment complexity.

The electron beam treatment is able to generate a large range of surface treatments that are not possible to manufacture with current conventional

[1] The Welding Institute, UK.

technologies. Therefore, it has the potential to produce treatments that can improve thermal efficiency, be cost effective and have low material usage1.

Understanding of thermo-hydraulic performance of the electron beam treatment is important to form the basis for the design of enhanced liquid cooling systems. As a result, the work in this study focused on two aspects; the first, in the optimization of EB treatments suitable for single-phase liquid cooling applications, production of test samples and the second on the experimental setup and evaluation of thermal and hydraulic characteristics of the enhanced surfaces.

1.1 AIMS AND OBJECTIVES

The current study initiates the application of the electron beam treatment for the improvement of heat transfer in liquid cooling applications and investigates thermal and fluid flow characteristics. The aims of the investigation are to evaluate the heat transfer enhancement and the flow characteristics by an experimental investigation. In addition generate the heat transfer and friction factor correlations that facilitate the design and manufacturing of efficient liquid cooling devices for thermal management systems.

In order to achieve the aims, the following objectives were set:

- Conduct a review of the cooling requirements of the electronics sector.

Requirements for efficient thermal management technologies in the electronics industry have increased rapidly. For that reason, understanding the present and future developments is essential in order to develop efficient and cost effective thermal management systems.

[1] Zero material waste.

- TWI to develop and optimize the EB system to create unique heat exchange surfaces[1].

Electron beam treatment is a very advanced technological process that requires an iterative adjustment of physical variables[2] to achieve the desired settings for each new surface treatment. Trials were performed to set the optimal electron beam parameters for each treatment. The process was performed using a machine designed for electron beam welding, thus a custom electron beam gun was developed by TWI to achieve a controllable[3] and focused beam[4].

- Identify current enhancement techniques used in thermal management products for the electronics industry. Optimise the electron beam pattern and treatment to achieve the best heat transfer behaviour.

A literature review was performed for the heat transfer enhancement technology aiming to specify the thermo-hydraulic behaviour of a range of enhancement structures. This information was used to generate treatments that can improve the thermal performance. Based on the capability of the electron beam machine three enhanced structures with different protrusion height, density and configuration were generated for thermo-hydraulic evaluation by TWI.

- Experimental investigation of thermo-hydraulic performance in single phase flow regime of three enhanced surfaces

The electron beam treatment technology use concentrated beam to melt and move the material at desired locations, therefore during the solidification processes due to the effect of the surface tensions irregularities are formed on the surface of the material, therefore it is essential to evaluate thermo-hydraulic behaviour experimentally and compare against other regular enhancement techniques.

[1] Electron beam treated surfaces.
[2] Beam power, frequency, focus and deflection.
[3] Deflection coils.
[4] Concentration coils.

- Construction of the test rig

A test rig was refurbished to deploy a custom designed thermal test section for the analyses of the enhanced structure that is integrated in a liquid cooled plate. Upgrade includes an accurate mass flow rate control system, temperature and pressure instrumentation, together with an electrical power supply. The instrumentation was calibrated and incorporated into the test sample and measurements were logged and recorded for post processing

- Test sample design and manufacturing

The test sample was designed as a representation of a liquid cooled plate that is used for microprocessor cooling. The electron beam treatment applied at the centre allows for a smooth inlet and outlet section. The flow inlet and outlet connectors are mounted in a polycarbonate transparent cover that covers the liquid cooled plate. All three samples were identical, allowing them to be tested in similar conditions.

- Obtain fluid flow rate

The working fluid is measured with a Coriolis flow meter and the flow rate data is recorded every second via Pico-logger technology into a personal computer.

- Obtain heat transfer data

With the purpose to evaluate the thermal performance, temperature is measured at the inlet and the outlet of the test sample. Measurements of the temperature are also taken in four vertical positions in the heater block and in two other points, at the inlet and at the outlet. Thermocouples are calibrated and all measurements recorded for every second via Pico-logger technology into a personal computer.

- Obtain pressure drop data

Pressure between the inlet and outlet of the enhanced area is measured via a differential pressure transducer. Data are logged and recorded for every second via a Pico-logger technology into a personal computer.

- Provide heat transfer and flow characteristics.

The experimental data is processed to provide the heat transfer rate and the fluid flow characteristics in terms of the friction factor. Results are compared to other research papers for the pin-fin enhancement structures to give an overview to the enhanced capability.

- Correlate the experimental data.

Experimental data for the heat transfer rate has been expressed in terms of Nusselt number. Whilst, the pressure drop data has been expressed in terms of friction factor. Results are correlated to allow performance evaluation of such structures.

1.2 STRUCTURE OF THESIS

The current thesis is divided into eight chapters and begins with the current chapter “Introduction”.

The second chapter presents a literature review of current cooling requirements in the electronics sector and predicted future developments.

Chapter three presents a review of the literature for single-phase flow heat transfer enhancement technologies, and in particular the pin-fin technology. The literature examines the effect of pin-fin geometry and arrangement on thermo-hydraulic performance. It also highlights the technical and financial benefits.

The fourth chapter is dedicated to the electron beam enhancement technology. The chapter gives an overview of the development of the technology, describes the working principle and introduces the construction of test samples.

The fifth chapter introduces CFD analysis of a smooth (untreated) test sample. The CFD data are compared to the experimental data for the smooth sample and also with available correlations. The experimental data for the smooth sample is used to provide the base comparative data with the experimental data for the enhanced samples. .

The sixth chapter explains the experimental work, experimental facility, test piece manufacture, measurement process and calibration of instruments, test methodology, data reduction for the heat transfer and pressure drop. In this chapter the uncertainty of the experimental results is also analysed.

The seventh chapter presents the fluid flow and thermal performance of three experimentally tested electron beam enhanced samples. The experimental data is compared to other conventional pin-fin enhanced structures and with the smooth test sample.

The eighth chapter presents the conclusions of this work and future analysis that is required to improve understanding of the electron beam technique for the heat transfer enhancement.

The temperature and pressure drop measured experimental data are presented in the Appendix.

1.3 CONTRIBUTION TO KNOWLEDGE

The improvement of the heat transfer efficiency has large financial and environmental benefits. This research has contributed to the development and the evaluation of a new electron beam enhancement technique for the heat transfer processes. The technology is unique and it has the capability to generate treatments that are not possible with conventional manufacturing techniques. In this study are reviewed the latest developments in the electronics industry, requirements for thermal management systems, and the market value. In the particular this study is focused in the experimental

evaluation of thermal and hydraulic performance. This includes design and manufacture of three electron beam treated test sample. An upgrade and construction of a test rig, selection and calibration of the measurement system, preparation of the experimental procedure, and the data reduction process. The experimental data has been correlated and can be utilized in the design processes to evaluate the performance of the current electron beam enhanced structures.

1.3.1 List of publications

Buxton, A. L.; Ferhati, A.; Glen, R. J. M.; Dance, B. G. I.; Mullen, D.; Karayiannis, T.: EB Surface Engineering for High Performance Heat Exchangers. Proceedings of the First International Electron Beam Welding Conference, Chicago, IL, USA 2009.

Ferhati, A., Karayiannis, T. G., Lewis, J. S., McGlenn, R. J., Reay, D. A., "Single-Phase laminar flow heat transfer from confined electron beam enhanced surfaces", 13th UK Heat Transfer Conference, 2013.

Ferhati, A., Karayiannis, T. G., Lewis, J. S., McGlenn, R. J., Reay, D. A., "Single-Phase laminar flow heat transfer from confined electron beam enhanced surfaces", Heat Transfer Engineering. 2014.

2 ELECTRONIC MODULES AND ENERGY PERFORMANCE

2.1 OVERVIEW

An important development in the second part of the 20th century has been the utilization of semiconductor materials for production of electronic components and the development of integrated circuits for power control, information processing and the optimization of such components for operation in extreme conditions. Despite the latest technological developments in multi-core processor functionality and significant reduction in the transistor switching energy, the requirements for cooling capacities still remain high and have the tendency to grow. Currently, high performance commercially available processors contain more than two billion transistors and dissipate 150 W/cm^2 (Intel, 2013). Furthermore, heat dissipation is expected to increase as the need for processing power and speed remains high. Therefore, to maintain this growth thermal management systems capable of delivering high heat fluxes are required.

Thermal management is a term that describes the design and construction of heat transfer systems that extract heat from the electronic modules or other heat generating equipment to protect them from overheating. It has lately attracted a lot of attention from the industry because it is critical for the reliability of electronic modules. Electronic modules are composed of many different components and materials which due to their properties perform a range of functions, e.g. microprocessor. Joining of components and the moulding process for the production of the electronic modules is critical to the forming of effective pathways for heat dissipation. The heat dissipated by a single component has to pass through several junctions, interface and conductive materials, that increases the complexity in modelling efficient thermal management systems. However, in cases when space is available the large mass heat sinks have proven efficient, while in small volumes this

is not possible and alternative methods are required to provide adequate cooling. The increase of heat fluxes inevitably increases the temperature drop in the heat sink at such values that affect the thermal performance for both natural and forced air cooling regimes. Also, due to low heat capacity of air, large amount of flow rate is needed; this requires powerful blowers that are costly and noisy to run. Therefore, liquid cooling systems, that are compact, efficient and cost effective, are required. In order to meet such requirements, enhancement heat transfer technologies are used. Improvement of the surface area by utilizing electron beam treatment Surfi-Sculpt™ is one of the methods that can be effective for the production of efficient heat sinks.

2.2 HISTORY OF SEMICONDUCTOR INDUSTRY

Currently, the majority of electronic components are made of semiconductor materials. The early development of this sector started with the invention of the vacuum tube diode in 1883 by Thomas Edison, (Bakish, 1962 a). The technology was developed and utilized to produce a range of electronic components such as the vacuum tube triode, tetrode, pentode etc., that were used widely in radio, radar, and TV communication until the 1950s. Vacuum tubes were utilized to build the world's first digital computer in 1946, which required a significant amount of energy and suffered from a continuous failure of vacuum tubes (Hoeflinger, 2012). The invention of the transistor in 1948 was a revolutionary idea. New components were made of semiconductor material, firstly from germanium that offered stability and reliability at high operating temperatures above 100 ^{o}C. Later on with the development of the technology, lower grade semiconductor materials such as silicon were utilized to produce a large number of electronic components. Today silicon is the conventional base material and is used widely in electronics manufacturing.

Semiconductor materials with conductive properties are positioned between insulators and conductors. On the other hand, semiconductor properties can be manipulated to achieve desired properties and produce electronic components such as transistors, diodes, thermistors, integrated circuits, etc. The best conductive properties of semiconductors are found in germanium and silicon materials (Colinge, J. P; Colinge, C. A, 2002). Germanium is a rare material and is usually combined with other components as, lead, silver or copper; therefore it is costly, while silicon is less expensive to obtain. Other semiconductor materials are cadmium sulphide, lead sulphide, and gallium arsenide that are used mainly to make variable resistors (Shimura, 1989).

The invention of the integrated circuit (IC)[1] in 1959 was the beginning of a new area in the electronics industry and this is due to three names, Robert Noyce, Andy Grove and Gordon Moore, that together created Intel Corporation[2], (Hoeflinger, 2012). In the 1970s, Intel Corporation developed the first microprocessor "Intel 404" and continues to be the leading manufacturer by doubling the transistor density every 18-24 months following Moore's[3] law, (Moore, 1975).

Microprocessor functionality, processing power and, as a result, heat dissipation has been increasing steadily during the recent years and this has been mainly due to the increase in transistor density and miniaturization. Although thermo-physical parameters of semiconductor allow operation at elevated temperatures of 110 ^{o}C to 125 ^{o}C at the junction, to ensure safe operating conditions the junction temperature for commercial electronic packages in the 1980s was set to be 85 ^{o}C, (Bejan & Kraus, 2003). Over the years a steady increase in processing power has reduced the temperature difference between the processor and surrounding enclosure, and continuously has challenged the industry for better thermal management systems. The main frame computers during the 1980s used bipolar-chip technology and due to high heat generation were water cooled, (Incroprera,

[1] Integration of transistors, diodes, capacitors and resistors together in a single module or chip is called IC.
[2] This was the first organisation to produce the ICs.
[3] One of the Intel Corporation cofounders.

1999). The other semiconductor technologies such as metal oxide on silicon and very large scale integration chips that offered lower power dissipation became widely applicable during the 1990s. Thus, cooling mechanisms such as, conduction (spreader), natural or forced convection, combined with heat sinks, were efficient methods to maintain operating conditions.

Currently, due to the market pressures for powerful, multifunctional and compact computers, requirements for advanced and efficient thermal management technologies have seen a rapid growth. Cutting-edge and powerful computer systems in military, medical, aerospace and communication sectors are anticipated quickly to develop further. Literature shows that chip power dissipation in 2016 for the high performance category will increase by 40% compared to 2012,

In order to manage such increases considerable improvement is required in chip architecture, software operation, semiconductor composition, manufacturing technology, and thermal management systems to ensure the junction temperature is below 85 ^{o}C, (SIA, 2014).

2.3 CURRENT E FUTURE DEVELOPMENTS

The chip performance evaluation for a long period has been related to the operating frequency[1] (processor clock speed) given in MHz or GHz, however, this has changed and today the performance evaluation is based on accomplishment of a given application.

Currently, there is a wide application of electronic components in power control, frequency generators and high-temperature environments which are of great importance for many industrial processes. Components such as

[1] This a measure of the rate at which a processing cycle is completed by the processor. I.e. 1GHz is equivalent to 10^9 cycles per second.

IGBT[1], MOSFET[2], CMOS[3], SiC[4] etc., operate at a high power input, therefore, are very sensitive to temperature change and are still required to operate close to their temperature operating limits, in applications that require reliability. At the same time commercial pressure for small, cheap and powerful components that are made of materials which have a low environmental impact[5] have increased the requirement for efficient thermal management systems.

At present, microprocessors are prepared from a semiconductor material that is thermally stable. Optimization of the processor micro-architecture, the operation procedure, and perfection of software codes jointly with the efficient use of the memory has increased further their efficiency, functionality and the reliability; however, due to requirements for processing power heat dissipation continues to increase. The transistor density in a microprocessor has risen from three million in 1993 to 2.2 billion currently, (Intel, 2013). If the technology follows this trend soon the processor will generate large heat fluxes that will be unmanageable with the current air cooling technology. This will require advanced liquid cooling systems that do not just need to ensure heat removal and respond to continuous size and noise reduction, but also to allow an increase in the performance and speed.

In order to understand the future requirements for thermal management systems it is important to study latest developing technologies. For this purpose, the information gathered from the International Technology Roadmap for Semiconductor (ITRS) is summarized in Table 2.1.

[1] Integrated Bipolar Gate Transistor
[2] Metal-Oxide-Semiconductor Field Effect transistor.
[3] Complementary Metal Oxide Semiconductor.
[4] Silicon carbide transistor.
[5] Short life time and in some cases poor reliability.

Table 2.1: Operating parameters for a range of semiconductor modules, (ITRS, 2013).

Technology	**Year of Commercialization**				
	2012	**2013**	**2014**	**2015**	**2016**
Commodity (Domestic)					
Power dissipation, (W)	0.5	0.5	0.5	0.5	0.5
Chip size, (mm^2)	40	40	40	40	40
Heat flux, (W/cm^2)	1.25	1.25	1.25	1.25	1.25
On-chip frequency, (GHz)	50	50	50	50	50
Junction temperature, (^oC)	125	125	125	125	125
Ambient temperature, (^oC)	85	85	85	85	85
Pin count	100	100	100	100	100
Handheld (M/Phone, Tablets)					
Power dissipation, (W)	1.2	1	1	1	1
Chip size, (mm^2)	100	100	100	100	100
Heat flux, (W/cm^2)	1.2	1	1	1	1
On-chip frequency, (GHz)	1.3	1.3	1.3	1.3	1.3
Junction temperature, (^oC)	105	105	105	105	105
Ambient temperature, (^oC)	45	45	45	45	45
Pin count	188-1000	198-1050	207-1100	218-1150	218-1151
Memory (DRAM)					
Power dissipation, (W)	1.5	1.5	1.5	1.5	1.5
Chip size, (mm^2)	24	24	24	24	24
Heat flux, (W/cm^2)	6.25	6.25	6.25	6.25	6.25
On-chip frequency, (GHz)	n/a				
Junction temperature, (^oC)	85	85	85	85	85
Ambient temperature, (^oC)	45	45	45	45	45
Pin count	84-240	84-240	84-240	84-240	84-241
Cost performance					
Power dissipation, (W)	105	112	119	126	133
Chip size, (mm^2)	140	140	140	140	140
Heat flux, (W/cm^2)	75	80	85	90	95
On-chip frequency, (GHz)	6.82	7.34	7.91	8.52	9.18
Junction temperature, (^oC)	90	90	90	90	90
Ambient temperature, (^oC)	45	45	45	45	45
Pin count	720-3367	800-3704	800-4075	880-4482	880-4930
High performance					
Power dissipation, (W)	375	400	450	487	525
Chip size, (mm^2)	750	750	750	750	750
Heat flux, (W/cm^2)	50	55	60	65	70
On-chip frequency, (GHz)	6.82	7.34	7.91	8.52	9.18
Junction temperature, (^oC)	85	80	80	80	75
Ambient temperature, (^oC)	45	45	45	45	45
Pin count	5358	5616	5896	6191	6501
Automotive					
Power dissipation, (W)	24	25	25	26	27
Chip size, (mm^2)	100	100	100	100	100
Heat flux, (W/cm^2)	24	25	25	26	27
On-chip frequency, (MHz)	171	188	207	227	250
Junction temperature, (^oC)	175	175	175	175	175
Ambient temperature, (^oC)	-40 to 200	-40 to 201	-40 to 202	-40 to 203	-40 to 204
Pin count	492	517	543	570	599

Table 2.1 shows operating parameters of microprocessors, the information has been classified by applicability in a range of electronic systems and is given for the years 2012 to 2016. The information is divided into groups based on functionality and the processing power of the component. The information is gathered from the (ITRS, 2013) and Semiconductor Industry Association (SIA, 2014). The data, that is presented, provides main parameters that can describe the cooling needs, for example, processing power, processor speed, junction temperature and size.

The first category, named “Commodity (Domestic)”[1], utilizes natural convective cooling combined with air recirculation or passive techniques as heat spreaders or heat sinks to ensure operating conditions. Devices in this category operate at low processing power and at an elevated junction temperature of 125 ^{o}C. Lately, due to miniaturisation and compactness it is anticipated that the internal temperature (inside enclosure temperature) can increase up to 85 ^{o}C, this will limit the heat removal capability, (ITRS, 2013).

In the second category are handheld devices such as mobile and smart phones, PDA, GPS navigators, game players, tablets, which are mobile and operate with battery, cooling power face similar constraints. In these systems, cooling is provided by heat spreaders that distribute the heat to external parts and maintain junction temperature below 105 ^{o}C, (SEMI, 2013), (ITRS, 2013). Since the processing power in handheld devices is a function of the power availability, anticipated increases of the battery power in the future will increase cooling requirements.

The multi-functional electronic packages are grouped into the third category. This includes integrated graphic cards and large memory capabilities. Such devices generate a small amount of heat as a single unit, however, when packed together heat dissipation increases considerably and forced convective cooling methods are required to maintain the junction operating temperature below a required value of 85 ^{o}C. Requirements for memory

[1] This category includes devices with low power dissipation as: TV processors, CD or DVD players, drivers, microcontrollers, personal displays, Wi-Fi connectors, digital receivers, etc.

capacity are anticipated to increase in order to support processor multi functionalities; therefore the cooling needs are expected to rise.

The “cost performance” equipment such as portable devices, high-performance notebooks, desktop computers, etc., were grouped in the fourth category. The cooling systems in this category deploy forced air cooling systems combined with heat sinks[1] and heat pipes to guarantee the operating temperature. Then again, requirements for higher processing power gradually have increased the need for high performance cooling designs. According to Table 2.1 heat fluxes for this category will increase approximately 20%, reaching 95 W/cm^2 by 2016. The new emerging portable devices[2], which are battery powered, are faced with limited cooling possibilities. Currently operating conditions are maintained by passive cooling techniques such as low fin heat sinks, air-circulation, conductive cases[3] combined with heat spreaders and heat pipes. Advances in this category will pose great challenges for the thermal management sector.

The high-performance category is continuously growing and is faced regularly with high requirements for cooling power. During the last two decades, there has been a rapid growth in this sector and aggressive air and liquid cooling techniques, passive enhancement technologies combined with heat pipe and thermo-electric cooling are used to maintain operating conditions. Currently power dissipation is approximately 400 W/chip with processor heat fluxes at the spreader level in a range of 55 W/cm^2; however, research suggests that power dissipation will increase up to 525 W/chip while operating frequency will reach 9 GHz from 2016. Although the power is anticipated to increase, the volume will remain the same, and heat fluxes of 70 W/cm^2 are expected to be reached by 2016. Therefore, the combined application of liquid cooling and enhancement heat transfer techniques will be required to provide adequate cooling power.

Due to the operating environment, electronic packages for the automotive industry operate at elevated junction temperature over 175 ^{o}C and are

[1] Increase heat transfer area.
[2] Thin or slim line notebooks dedicated portable systems and professional tablets.
[3] Improve heat dissipation to the ambient.

predicted to reach 220 ^{o}C in 2016, Table 2.1. The processor size of 1 cm^2 is expected to remain constant while power dissipation is predicted to increase from 25 W to 27 W in 2016, Table 2.1.

Heat fluxes in this category are comparable with those of high-performance equipment. In terms of cooling requirements, the automotive industry presents a challenge because of the low temperature difference between junction and ambient. Forced convective cooling technologies combined with heat spreaders, heat sinks, heat pipes and thermo-electric cooling are currently used, while for extreme applications[1] such as Integrated Gate Bipolar Transistors (IGBT-s) single-phase liquid cooling is implemented, (Thermacore, 2013).

Considering the continuous miniaturization of the electronic components and limitations on photo-lithography technology[2] the further size decrease of silicon components will soon face limits. Moreover, nanotechnology itself faces other issues, such as hotspots at the drain[3] zone, (Pop, et al., 2006). The effect of novel semiconductor materials and unconventional transistor geometries[4] poses problems for the heat conduction and are likely to instigate hotspots. From the study of the literature, it is clear that the requirements for effective cooling systems are continuously increasing. Therefore, it will be a challenge for the thermal management sector to provide required heat removal capacities.

2.3.1 Market of semiconductor components

Production of the semiconductor industry can be divided into four main semiconductor categories: microprocessor, memory, IC[5], and system on

[1] Limited volumes
[2] Wave length
[3] Emitter of the transistor
[4] Ultra-thin body part, encase gate, extreme thin wires.
[5] Integrated Circuit.

chip[1]. The microprocessor market remains the most profitable category due to the very advanced manufacturing technology. The semiconductor market in 2010 increased by 7% compared to 2009, while the investment in the research for 2009 and 2010 reached $100 billion, (SEMI, 2013). The largest increase was recorded in the communication sector that counted in total 6 billion mobile devices in the last decade with 4 billion active devices in 2010, (SIA, 2014). This has been one of the fastest growing branches in the electronics sector in recent years that has pushed developments of the nano-electronics industry. Despite the hit from the financial recession, the semiconductor industry increased by $100 billion from 2010 to 2011 and is predicted to reach $450 billion by 2020. However, if in the coming years the economy will follow pre-recession economic growth the value may reach $600 billion, (SIA, 2014).

Globally, the semiconductor industry during the third quarter of 2013 reached sales of a value of $80.92 billion, 8.4% higher than the previous quarter and just for the month of September sales were $26.97 billion, 8.7% higher compared to the same period in the previous year. The semiconductor market in the year 2013 was in a stronger position with sales increasing for memory, analogue and logic products. The global semiconductor sale figures reached $305 in 2013, 4.8% higher than the previous year, Table 2.2, and (WSTS, 2014). The information and communications industry is expected to reach $7 trillion by 2020 and is anticipated to support the global economy with an increase by 2.5%, (SEMI, 2013).

[1] Integrated circuit that combines both the chip and auxiliary system in a single unit to perform a given process.

Table 2.2: Global semiconductors market for the year 2012 and 2013, (SIA, 2014).

Semiconductor Market			
Market $ Billions	2012	2013	Change %
America	54.36	61.5	13.1
Europe	33.16	34.88	5.2
Japan	41.06	34.8	-15.2
Asia	162.98	174.41	7.0
Total	291.56	305.59	4.8

2.4 PACKING AND THERMAL BEHAVIOUR

The processor or (chip) contains billions of components, which are connected (wired) together to create an integrated circuit that is used to modify analogue signals, process and save digital data. Through microscopic wires, billions of transistors operate together as switches to create different logic circuits that perform logical or mathematical operations by following instructions from software or other forms of input process.

2.4.1 Semiconductor material

Solid materials can be divided into three groups based on their electrical properties: conductors, semiconductors and insulators. The electrical properties depend on their atomic structure and particularly on the free electrons and particularly on those in the outer orbits of atoms that can be easily freed.

Conductors such as gold, silver, copper or aluminium have free electrons (due to their weak atomic bond between electrons in the outer orbit to the nucleus). Therefore, it is easy that under an electrical potential difference or electrical field to energize electrons and create an electric current.

Insulators have a good bond between the nuclei and electrons; therefore, there are no free electrons in the structure to create currents. Semiconductors are between conductors and insulators. At low temperature, they behave like insulators, while with increase of the temperature a small number of electrons become free and transfer low values of current. However, semiconductors have some useful characteristics compared to both insulators and conductors. Their ability to transfer electricity can be manipulated by introducing impurities into their structure to create new carriers (electrons) or positive (holes) charged carriers.

2.4.2 Microprocessor manufacturing process

The manufacturing of a microprocessor is divided into four main steps: preparation of material, crystal growth, wafer fabrication, assembly and testing. The processor manufacturing begins with the design process that aims to fulfil required functionality and technical specifications. The first step of the manufacturing starts with processing and purification of raw materials. The second step is the growth of silicon crystal of purified silicon that results in a perfect silicon lattice structure. The third step is the fabrication of thin wafer discs by photo-lithographic technique which transfers the structure. Before the photo-lithography treatment, the silicon disc is coated with a photo-resistant layer in a spin process. Ultraviolet (UV) light transfers the prepared printed design from the mask into the thin semiconductor. The exposed parts of the wafer to UV light are dissolvable and removed with liquids. The final structures are tiny transistors. The process, that follows, is the implantation, which establishes the properties of the components. During this process, small amounts of impurities (doping atoms) are shot into the silicon structure to regulate the conductivity and create the positive (p) and negative (n) charged parts known as p and n type junctions.

Pure copper is used to interlink components after an insulating layer is applied at desired locations to avoid short circuits[1]. The process is controlled by a powerful microscope. The following process is packing, where small

[1] Wires touching each other

silver contacts are integrated into the wafer to connect the chip to the frame. The wafer is cut by fine cutters in parts and bonded to the frames that are sealed with a cover, creating the processor.

2.4.3 Information technology sector and energy requirements

In 2010, the global electronic communication system[1] was composed of 36 million servers and used around 10% (~36 GW) of the total electrical power installed in Europe (IEA, 2014). Furthermore, 20% of the global installed electric power[2] in 2010 was used by information and communication technology sector, (EPA, 2013). Energy requirements from the electronics sector are expected to continue to escalate as chip processing power, memory, communication density and speed increases.

The energy demand from data centres or so called 'Server Farms' is increasing fast. These systems use a considerable amount for operation and cooling capacity[3] that is used to maintain operating conditions. Although a large number of such systems have been moved to cold climates, to reduce the cooling energy required, their density is increasing and the demand for energy remains high, (IEA, 2013).

By the year 2020, if the technology will follow the previous trend, data centres will require four times more energy reaching 144 GW, this equals to 40 % of the current installed electrical power in Europe, (EPA, 2013).

2.4.3.1 Processor heat dissipation

Increase of power dissipation from electronic components is mainly a result of processor speed and transistor density (miniaturization). Over the years, transistor size has decreased rapidly while speed has increased. Currently, commercially available processors dissipate 150 W (Intel, 2013). In order to understand the power levels and their impact on the electronic component

[1] Back-bone of the Internet
[2] (2 TW = 2×10^{12} W)
[3] Powerful chillers or air-conditioning units.

and surrounding, a comparison between a light bulb with 7 cm diameter to an Intel processor "Intel Core i7 – 980X Extreme editions" (Intel, 2013), can be seen in Table 2.3.

Table 2.3: Comparison of heat fluxes between microprocessor and light bulb.

	Intel Processor i7-980X	Light Bulb
Power Dissipation (W)	130	130
Surface Area (cm^2)	2.39	153.86
Heat Flux (W/cm^2)	54.39	0.84

According to Table 2.3 heat flux of the Intel Processor i7-980X is 64 times higher than that of a light bulb 130 W. Furthermore a light bulb can dissipate heat to the environment while the processor is in a small volume enclosed by other heat generating components PCB boards. Thus, the importance and the challenge of thermal management technology to allow further increase in the processing power and functionality are understandable. Irrespective of the functionality, heat dissipation in electronic devices depends on three other components:

i. Switching current that creates a capacity load respectively at transistor gate and interconnections.
ii. Short circuit current that flow through the p-n junction when the signal is in transition mode at the gate.
iii. Current leakage that is a function of the potential difference (voltage) and operating temperature of the transistor.

The anticipated increase in transistor density will increase above values (i, ii & iii) resulting in higher heat fluxes, therefore, thermal engineers are always in search of new and efficient cooling techniques.

2.4.4 Reliability and safety

At present, safe operation of powerful electronic packages depends on the thermal management systems. The failure of such systems can reduce the performance of the electronic component and damage package integrity. The temperature increase in an electronic component, instigates thermal expansion of the component, and as a result increases of thermal and mechanical stresses, which may lead to an internal damage (i.e. attachment of die to silicon or connection between silicon and wires). Moreover, elevated temperatures of the package over the design specification can initiate melting and combustion of components. At the same time variation of the temperature over the design conditions can affect: semiconductor conductivity behaviour, switching frequency (operation), carrier density (electrons and holes) and the sub-atomic behaviour, as well as can create a structural damage. This affects the performance and may create hazardous conditions. Therefore, thermal management techniques are vital to maintaining electronics component at the specified operating temperature.

The semiconductor components are safe to operate, however, when billions of them are packed in a small package it is a challenge to maintain their operating conditions. Electronic components operate well at lower temperatures, i.e. below 85°C, however, in practice the operating temperatures depend also on other external factors (i.e. ambient temperature, humidity, airflow speed, etc.). The operating performance and costs are driven by market requirements. Therefore, to ensure the life of the product, the thermal management system needs to be carefully designed to compensate for any malfunction of components and be financially cost effective.

2.4.5 Electronic component packaging levels

Evaluation of heat transfer rates through electronic components, and in particular packaging levels, are essential for the design of cooling systems. For example, if the thermal resistance through packaging levels is high, it will require a very efficient (powerful) cooling system to maintain the anticipated

heat removal rate. Hence, it is very important that the thermal resistance is reduced at the lowest possible levels to allow a better heat flow. Conventionally the module, that houses the microprocessor, is the first level of packaging. The circuit board, that connects the microprocessor with other electronic components, is the second level. While connection between boards and other accommodating parts (module, rack) is level three, (Bejan & Kraus, 2003).

A summary of cooling methods for each packaging level is presented in Table 2.4. In the first level heat is transferred by conduction from the chip to the package. The most effective way, to reduce the operating temperature, is to reduce thermal resistance between the silicon and the package. For this reason, parts are attached together by using conductive paste.

The heat at level two is transferred by conduction to the board and convection to surrounding; therefore good conductive properties are required to improve spreading. Integration of heat pipes, heat spreaders and heat sinks to the board to improve cooling are a common practice. In other equipment where convective cooling is not possible boards serve as heat transfer conductors, and heat sinks are attached on the opposite side of the board to improve heat transfer area. In other applications where convective cooling is not permitted heat is conducted from the board to the edges of the device (or case) where cooling can be supplied.

Most of the today's electronic components are packed on level one and two. Heat sinks, protrusions, heat pipes, thermo-electric, parallel, rectangular, elliptical, hexagonal and circular fins are usually attached to the components at level two to improve heat transfer to the environment. While at the level three cooling involves the use of active systems, i.e. cooled air handling units, liquid cooling and direct refrigeration cooling systems.

Table 2.4: Cooling technologies for each packing level, (Bejan & Kraus, 2003).

Packing Level	Active Cooling Methods	Passive Cooling Methods
First Level (chip package)	Forced air cooling	Natural air convective cooling
	Air spurt Impingement	Heat spreader (Cooper, Aluminium)
	Thermoelectric cooling	High conductive plates (Encapsulated Graphite)
	Liquid cold plate cooling	Phase change materials
	Dielectric liquid	Heat sink
		Heat pipe combined with a spreader, heat sink or fin stack
		Dielectric immersion cooling
		High conductivity thermal compounds
Second level (PCB)	Forced air cooling directed)	Conductive material heat spreader
	Liquid cold plates	Natural air convective cooling
		Heat pipes
		Heat sinks
Third level (module)	Forced air cooling (directed)	Natural air convective cooling
	Air handling cooling systems	Heat pipe combined with a spreader, heat sink or fin stack
	Refrigeration air cooling systems	
	Liquid cold plate	

2.4.6 Market of thermal management systems for electronics industry

The global thermal management sector in 2011 is valued to be at around $8 billion, (Electronics.Ca, 2012). In 2013 the market, was divided 80% of thermal management hardware (heat sinks, air-fans and other equipment), Figure 2.2, and other remaining 20% on (software, interface and substrate materials) and other auxiliaries. Heat exchange, heat sinks, and heat sink integrated with heat pipe technology make up more than 85% of component sale for thermal management, Figure 2.2. In 2013 global market was $10.1

billion and is expected to reach $10.6 billion by 2014, (Electronics.Ca, 2014) .

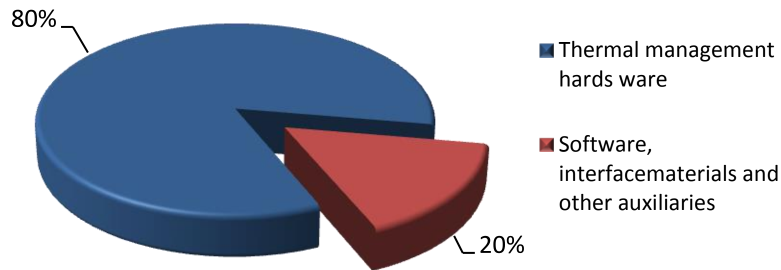

Figure 2.1: Thermal management market 2013, (Electronics.Ca, 2014).

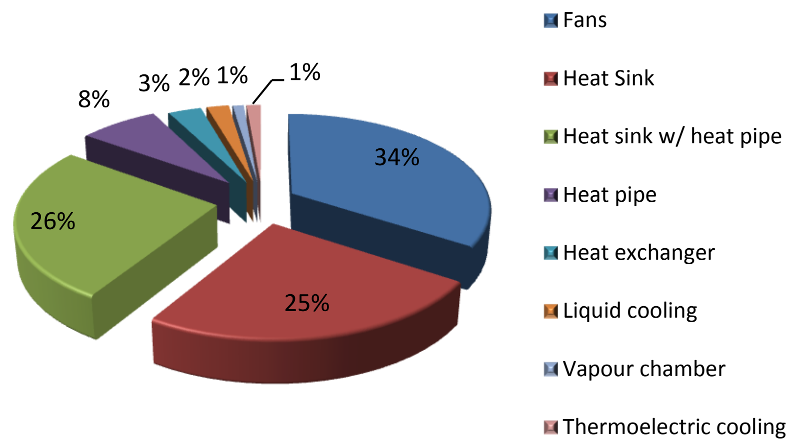

Figure 2.2: Electronic cooling system components market 2011, (Thermacore, 2012).

Presently, computer industry remains the main user of thermal management products with 50.8% of total revenue, followed by telecommunication and medical/office equipment that respectively are 16.8% and 11.5%, Figure 2.3. According to Figure 2.3 the future of the thermal management industry for the computer sector is expected to grow and reach 57.1% by 2015, product for telecommunication sector is predicted to decrease to 13.6%, while the

medical/office equipment remains the same at 11.5%, (Researchandmarkets, 2014) and (Electronics.Ca, 2014).

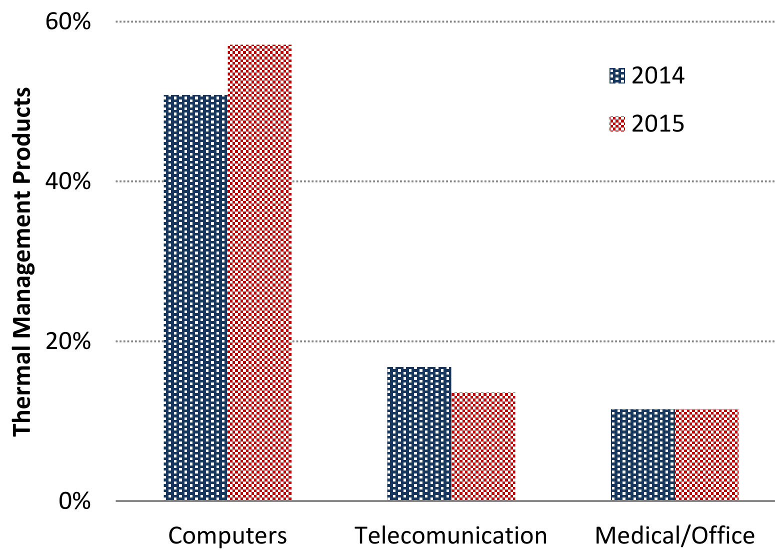

Figure 2.3: Thermal management product sale for three main sectors, (Electronics.Ca, 2014).

2.4.7 Summary

The social and technological development is inevitably related to information and communication technology, therefore, computational processing power and functionality is expected to increase continuously. The optimal operation of the electronic system is an important factor for a reliable and constant performance. Increases in processing power and speed require large transistor densities to be installed in small volumes and as a consequence large amount of heat is generated. Even though important steps have been taken in reducing transistor switching energy and optimization of the processor operation (software), requirements for energy are still increasing.

Thermal management technology has improved considerably to maintain a steady development of the electronics sector. However, due to the small volume of electronic modules the conventional air cooling techniques are reaching their limits; therefore, attention is focused on the liquid cooling

technologies. Requirements for efficient cooling techniques from cost and high-performance category, including and the automotive industry have initiated a growth in utilization of the heat transfer enhancement technologies. Currently a number of enhancement technologies such as pin-fins, micro-channels, folded parallel and wavy plate fins, offset strip fins, etc., are integrated in liquid cooled plates to improve the efficiency and reduce the size. The computer manufacturing industry remains the main user of thermal management systems, followed by telecommunication and medical/office industry. Thus, the development of heat transfer enhancement technology remains an area of great importance to improve reliability of electronic equipment during the operation and reduce energy usage for cooling.

The following chapter presents a review of the passive heat transfer enhancement technology, and particularly the pin-fin enhancement technology, that has attracted the attention for electronic cooling applications due to the high thermal performance and moderate pressure drop.

3 LITERATURE REVIEW

3.1 ENHANCEMENT TECHNOLOGIES

The economic cost is a prime consideration in design processes. Therefore, there is a continuous trend for compact engineering systems that reduce the material and space required. Conversely, size reduction in thermal design increases heat fluxes, hence, advanced enhancement heat transfer technologies are required to maintain the heat transfer duty in the reduced volume. Enhanced heat transfer techniques are divided into two groups: passive and active, (Reay, 1991), (Webb & Kim, 2005), (Stone, 1996), (Zimparov, 2002), (Siddique, et al., 2010); see Table 3.1.

Passive techniques in comparison with active techniques do not require external energy input. These techniques are conventional surface modifications, such as offset strip, louver and wavy fins, or micro-roughness that is integrated or attached to the surface. Extended surfaces provide heat transfer enhancement by increasing the contact area, and other passive techniques change fluid flow behaviour by increasing turbulence, disturbing temperature, velocity and concentration of boundary layers. However, such techniques increase the friction coefficient and as a result, the pressure drop and pumping power is increased.

Active techniques use the external power to manipulate the flow and increase heat transfer. Those techniques involve mechanical means of stirring, high intensity electrostatic fields, surface rotation or surface and fluid vibration, and vapour suction, shown in Table 3.1.

A combination of passive and active technique to achieve a higher heat transfer compared to a single technique is classified as a compound technique. Application of these methods in relation to the mode of heat transfer determines their efficiency.

Table 3.1: Classification of various Enhancement Techniques, (Webb & Kim, 2005).

Enhancement techniques	
Passive	**Active**
Treated surfaces	Mechanical aids
Rough surfaces	Surface vibration
Extended surfaces	Fluid vibration
Displaced enhancement devices	Electrostatic fields
Swirl flow devices	Suction or Injection
Coiled tubes	Jet impingement
Surface tension devices	Surface rotation
Additives for liquids	
Additives for gases	

3.1.1 Passive techniques

Passive techniques are mainly technological treatments made on the surface of materials to increase the interaction of the surface with the fluid. Below is a short description of the techniques and thermo-hydraulic effects.

Treated surfaces are fine metallic or non-metallic surface coatings, or micro-structures on the heat transfer surface. Such surfaces can be integral or made by adding roughness or micro-structures on the surface.

Rough surfaces usually are integral (machined) with the surface or made by attaching roughness elements to the surface. In the single-phase flow regime, the enhancement provides disturbances to the boundary layer formation. While in two phase regimes and especially in nucleate boiling, increase of roughness elements provide artificial nucleation sites and increases thermal performance compared to the smooth surfaces.

Extended surfaces in heat exchangers particularly increase the heat transfer area on the air-side. However, well-designed fins have combined influences on enlargement of the heat transfer area and the fluid flow mixing.

Displaced flow insert devices placed inside the flow channel improve turbulence, disturb boundary layers, and create bulk mixing. Both single and two-phase flows use this technique.

Swirl flow devices include a number of geometrical arrangements, which could improve mixing by introducing secondary flows. These devices include full-length twisted tape inserts, vortex generators, different inserts such as screw-type windings, etc.

Coiled tubes used in heat exchangers provide mixing of the flow and increase heat transfer area for a given volume. The small diameter coil tubes (≤19 mm) have proven to be efficient while the enhancement effect for higher diameter tubes is negligible, (Webb & Kim, 2005).

Surface tension devices consist of wicking or grooved surfaces. They promote the flow of fluid over the heated surface to improve boiling. On the other hand, hydrophobic surfaces aid drop-wise condensation by weakening surface tension forces, (Webb & Kim, 2005).

Additives for liquids are solid particles, which change the thermal properties of the fluid[1]. Solid particles increase liquid conductivity and increase mixing. Lately, there is an increasing interest in nano-particle technology for the improvement of the thermal performance, (Webb & Kim, 2005).

3.1.2 Active techniques

Active techniques require an external energy to operate. Some of those include the application of alternating (AC) or direct current (DC) of high intensity, mechanical aids, surface or fluid vibration and vapour suction, Table 3.1.

Mechanical aids involve internal mechanical liquid mixing or rotation of the equipment by mechanical means, (Steinke & Kandlikar, 2004).

Surface vibrations include application of different frequencies to single-phase flow to increase mixing, i.e. piezoelectric devices that use electricity to generate vibration, (Cheng, et al., 2009).

[1] Nano-fluids

Fluid vibration involves a range of frequencies, from 1 Hz to 1 MHz and is applied in single-phase flow application, (Nesis, et al., 1994).

Electrostatic fields are practical to increase bulk mixing of the fluid close to the surface. This is known as the Electro-hydrodynamic (EHD) enhancement technique, (Karayiannis, 1998).

The injection technique involves supply of fluid or gas in a single-phase flow through porous surfaces to improve mixing, (Webb & Kim, 2005).

Suction involves, vapour removal through a porous media to disrupt boundary layers in heated surface and to avoid the film boiling formation in the nucleate boiling process, (Siddique, et al., 2010).

Jet impingement involves a forced fluid flow normal to the surface, which can be effective for single-phase flow and boiling applications. This technique has proven efficient in electronics cooling applications, (Incropera, 1999).

3.1.3 Compound techniques

Compound techniques aim to achieve higher enhancement than a single technique by using two or more (active or passive) techniques. The majority of enhancement techniques used are passive (due to cost consideration and simplicity). However, current developments in the EHD technique have increased the interest in combining passive and the EHD technique to achieve a better performance, (Ahmad, et al., 2014).

3.1.4 Published literature

Manglik and Bergles in 2004 presented a full review of the literature and other published sources from enhanced heat transfer field up to 2001, (Maglik & Bergles, 2004). According to this review from the 1950's there, has been a significant increase in research and publications in the field of enhanced heat transfer. In 2013, 'Science Direct', lists 75,819 published research papers on enhanced heat transfer technology. Figure 3.1 shows the trend for the last four years. Another resource of heat transfer enhancement

technology is patent literature. Today, patent offices have a register of 69933 patented enhancement techniques recorded (Scirus, 2013). Manufacturing information remains a practical source of data. However, most product information, especially if the enhancement is not visible in the product, is not available.

Figure 3.1: Published enhanced heat transfer technology, (ScienceDirect, 2014).

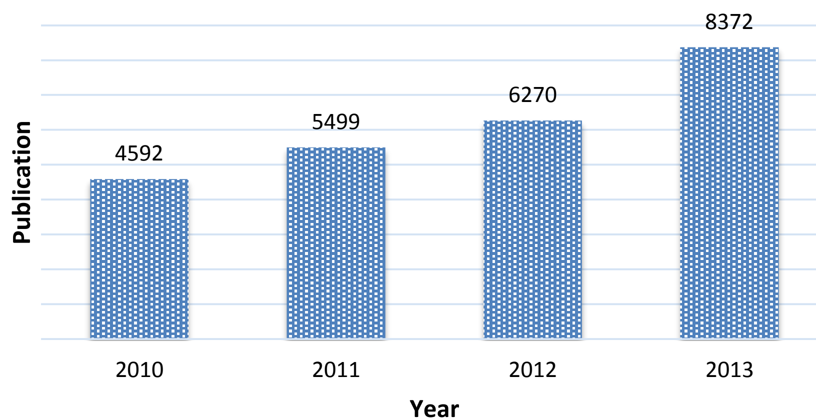

3.2 GENERAL CONSIDERATION

Performance evaluation of enhancement techniques is complex due to flow and heat transfer rate distribution. However, during the selection the financial costs, design, production, operation, maintenance, reliability and safety factors also need to be considered. The focus of this study is given on the thermal and hydraulic aspects of the pin fin enhancement technology, because of the similarity with current EB treatments that are experimentally evaluated in this study.

The improvement of heat transfer through enhanced technology is accompanied by negative effects on the pumping power. The efficiency evaluation in the literature is shown as a comparison between the thermal and hydraulic performance of enhancement and the smooth (plain) surface.

Enhancement technology provides a higher heat transfer coefficient (*h)* per unit surface area. Nevertheless, the efficiency of the enhancement technique depends also on the objective and operating conditions:

i. The enhancement objectives, i.e. increase the heat duty, reduce the size, or reduce operating temperature.
ii. The operating environment (fluid entry conditions, mass flow rate and temperature).
iii. The operating constrains as the cross flow area, velocity and acceptable pressure drop.

In the literature, performance evaluation is expressed in terms of the Colburn *j*-factor and the friction *f*-factor over increasing Reynolds number, (Webb & Kim, 2005). In practice, it is very useful to have a relationship between friction and Nusselt number. According to the Reynolds analogy at Pr~1; thermal and molecular diffusivity from a heated surface to the fluid are equal, (Cengel, 2006). This analogy relates velocity, thermal, and concentration boundary layers assuming the Prandtl number is close to unity[1]. Therefore, it enables the calculation of one of the parameters, when the other is known. This analogy is found to be valid for Pr~1.

3.2.1 Forced convection internal flows

Fluid flows in closed ducts are classified as internal flows. In the general flow sections are circular, because they can operate at larger pressures compared to other configurations. Whereas, noncircular ducts are mainly used in the built environment, electronics cooling systems and other low pressure applications, (Incropera, 1999). In relation to the heat transfer, for a fixed cross sectional area the circular pipes have the largest heat rate

[1] Thermal and velocity boundary layers develop simultaneously

dissipation and the lowest pressure drop, (Cengel, 2006). For that reason, circular pipes are popular in heat transfer equipment. Rectangular shaped channels are commonly used in the electronics cooling applications, i.e. machined heat sinks or other liquid cooling plates.

Though the conceptual theory of internal fluid flow is well studied, thermo-hydraulic models exist just for laminar or turbulent flow in circular pipes, while for other flow configurations that operate in the developing or transient regimes the main sources of data are empirical studies.

3.2.1.1 Dimensionless geometrical parameters

The thermo-hydraulic evaluation of the internal flow depends on the flow regime, which is defined by the Reynolds number, (Incropera, 1999):

$$\mathrm{Re}_{D_h} = \frac{\rho V_{avg} D_h}{\mu} = \frac{V_{avg} D_h}{\upsilon} \tag{3.1}$$

Where $D_h=4A_c/P$ is the hydraulic diameter of a rectangular shaped duct, V_{avg} represents the average flow velocity, P is the wetted perimeter and $\upsilon = \mu/\rho$ is the kinetic viscosity of the working fluid. However, for the finned ducts the majority of studies uses the hydraulic diameter that is based on the pin-fin diameter (d) and is given as, (Webb & Kim, 2005):

$$\mathrm{Re}_{d} = \frac{\rho V_{avg} d}{\mu} = \frac{V_{avg} d}{\upsilon} \tag{3.2}$$

Reynolds number <2300 are characteristic of laminar flow regimes, while for Re>4000 the flow is turbulent, and transitional in between. Fully turbulent regimes in some cases are reached at much higher Reynolds numbers, (Cengel, 2006).

Hydrodynamic boundary layers develop in the pipe, due to friction between fluid and pipe. The hydrodynamic entry length is the distance from the inlet to where the velocity reaches 99% of the fully developed value, (Shah &

London, 1978). In the laminar regime, the hydrodynamic entry length is given approximately for flow in circular ducts as:

$$L_{h_laminar} = 0.055\,\mathrm{Re}\,D_h \qquad (3.3)$$

While for parallel plates, the coefficient is 0.011, (Incropera, 1999). Hydraulic conditions have an effect on the thermal boundary layer that is given approximately as, (Kays & Crawford, 1993):

$$L_{th_laminar} \approx 0.05\,\mathrm{Re}\,\mathrm{Pr}\,D_h \qquad (3.4)$$

In the turbulent regime, the boundary layer develops quickly; therefore, fully developed thermal and hydrodynamic conditions are approximately at $10D_h$, (Incropera, 1999).

$$L_{h_turbulent} = L_{th_turbulent} = 10D_h \qquad (3.5)$$

3.2.2 Pressure drop in the smooth and fined ducts

The pressure drop determines the pumping power required to maintain the fluid flow. This for a smooth duct is expressed using the Darcy-Weisbach equation given as, (Cengel, 2006):

$$\Delta P = 4 f_{fd} \frac{L}{D_h} \frac{\rho V^2}{2} \qquad (3.6)$$

Here ($\rho V^2/2$) is the dynamic pressure, and *f* is the Fanning friction factor. For laminar fully developed flows, the friction factor is inversely proportional to the Reynolds number and is given as, $f_{FD}=C/Re_{Dh}$. Here the constant C depends on the duct cross section geometry and values are available in most heat transfer books for both boundary conditions: of constant heat flux and constant surface temperature as functions of the duct aspect ratio, i.e. (Incropera, 1999), (Incropera, et al., 2006), (Cengel, 2006). Approximately, the friction factor can be evaluated for a fully turbulent flow inside the channels from the correlation presented below, (Incropera, 1999):

$$f_{fd} = 0.079\,\mathrm{Re}_{D_h}^{-1/4} \qquad \mathrm{Re}_{D_h} < 2*10^4 \tag{3.7}$$

$$f_{fd} = 0.046\,\mathrm{Re}_{D_h}^{-1/5} \qquad \mathrm{Re}_{D_h} > 2*10^4 \tag{3.8}$$

(Shah & London, 1978), recommended the following equation for developing laminar flows:

$$f_{app}\mathrm{Re}_{D_h} = \frac{3.44}{(x_*)^{1/2}} + \frac{C_1 + C_2/(4*x_*) - 3.44/(x_*)^{1/2}}{1 + C_3(x_*)^{-2}} \tag{3.9}$$

where (*C_1=16, C_2=1.25, C_3=0.00021)* are the values of the coefficients relating to the circular ducts, while for the parallel plate channels values are (*C_1=24, C_2=0.674, C_3=0.000029)*. The dimensionless longitudinal position is given as, $x_* = \frac{L/D_h}{\mathrm{Re}_{D_h}\,\mathrm{Pr}}$ where (*L)* is the length in the direction of the flow. The product of Reynolds number and the apparent fanning friction factor *(f_{app} Re_{Dh})* approaches *($f_{fd}Re_{Dh}$)* fully turbulent conditions with increasing of dimensionless longitudinal position x_*. For smooth rectangular channels (Phillips, 1988), developed the following correlation, see (Incropera, 1999):

$$f_{app} = A\,\mathrm{Re}_{D_h}^{B} \tag{3.10}$$

Here A and B are given as:

$$A = 0.0929 + \frac{1.0161}{L_{th}/D_h} \tag{3.11}$$

$$B = -0.2680 - \frac{0.3193}{L_{th}/D_h} \tag{3.12}$$

The pressure drop through pin fin structures is proportional to number of rows (N_L), friction factor, correction factor (ҳ) and dynamic pressure ($\rho V^2/2$) (Incropera, et al., 2006) and is given as:

$$\Delta P = N_L f \chi \frac{\rho V^2}{2} \quad (3.13)$$

3.2.3 Nusselt number

In the case when there is a constant heat flux, the heat transfer coefficient varies in the flow direction and the heat transfer rate is expected to be higher at the inlet due to low inlet fluid temperature. In literature the convection heat transfer coefficient is given in terms of Nusselt number, which is a dimensionless quantity that expresses the ratio of the convective heat transfer coefficient and conductive heat transfer coefficient. Nusselt number for circular ducts with constant heat flux is $Nu=hD_h/k=4.36$. While for constant surface temperature condition is $Nu=3.66$. For rectangular duct geometries, the heat transfer correlation is given by (Shah & London, 1978) as:

$$Nu_{D_h} = 8.235\left(1 - \frac{2.0421}{\alpha} + \frac{3.0853}{\alpha^2} - \frac{2.4765}{\alpha^3} + \frac{1.0578}{\alpha^4} - \frac{0.181}{\alpha^5}\right) \quad (3.14)$$

where, α is the channel aspect ratio (W_{ch}/H_{ch}).

For constant surface temperature, the correlation is given as:

$$Nu_{D_h} = 7.541\left(1 - \frac{2.610}{\alpha} + \frac{4.970}{\alpha^2} - \frac{5.119}{\alpha^3} + \frac{2.702}{\alpha^4} - \frac{0.548}{\alpha^5}\right) \quad (3.15)$$

3.2.3.1 Fin temperature spreading and heat transfer rate

The fined surfaces are widely used to enhance the heat transfer performance of thermal management systems. These are available as a variety of geometrical shape fins. However, most common are regular geometries such as, rectangular, circular, epileptic, plate fins, etc. In order to simplify thermal and hydraulic analysis of pin fin enhancement structures a number of assumptions are required to be made and those are listed below:

i. The process is considered to be steady state with no heat generation in the fin.
ii. The thermal conductivity of the material is constant.
iii. The convection heat transfer coefficient is constant over the fin surface.
iv. The temperature distribution at the fin base is uniform.
v. The heat transfer from the fin top is negligible compared to that of the side surface.
vi. The fin diameter is rather small compared to the length and the temperature gradient normal to the surface is not considered.

The temperature distribution along the fin is a key step in the evaluation of the performance. Under steady state condition, the energy balance in the elementary volume of the fin, Figure 3.2, can be expressed as, (Incropera, 1999):

$$\frac{d^2T}{dx^2} = m^2(T - T_f) \tag{3.16}$$

In the equation (3.16, T is the fin temperature, x is the longitudinal length in the direction of the heat flow, T_f is the fluid temperature and $m = \left(\frac{hP}{kA_c}\right)^{0.5}$ is a fin parameter that describes the fin, where h is convection heat transfer coefficient, k is the fin material thermal conductivity, P is the fin perimeter, and Ac is the cross-section area of the fin. The general solution of the second-order differential equation (3.16 has the following form, (Incropera, 1999):

$$T - T_f = C_1 e^{mx} + C_2 e^{(-mx)} \tag{3.17}$$

where C_1 and C_2 are arbitrary constants that can be determined from the boundary conditions at the base and at the tip of fin: at $x=0$ (base), $T=T_f$, and $x=H_{fin}$ (tip), $dT/dx=0$. The application of the boundary conditions in the general solution (equation (3.17) for the fin with constant cross-section is given as:

Adiabatic fin tip: $$\frac{T - T_f}{T_b - T_f} = \frac{\cosh[m(H_{fin} - x)]}{\cosh(mH_{fin})} \tag{3.18}$$

where H_{fin} is the fin height, T_b temperature at the base.

The heat transfer rate in the fin is given at, (Cengel, 2006) as follow:

Adiabatic fin tip: $$Q_{fin} = kA_c \left.\frac{dT}{dx}\right|_{x=0} = (hPkA_c)^{0.5}(T_b - T_f)\tanh mH_{fin} \tag{3.19}$$

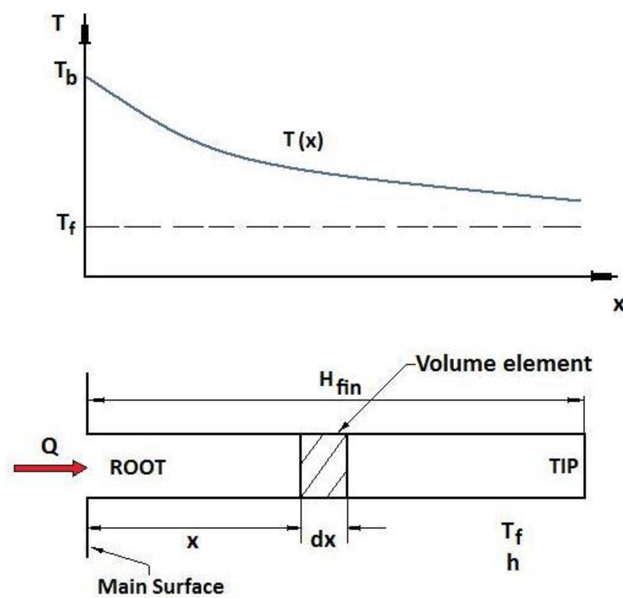

Figure 3.2: Steady-state heat conduction in fin.

3.2.3.1.1 Performance parameters

The evaluation of the fin performance can be expressed as the ratio of heat transferred by the fin, to that transferred from the primary surface that was covered by the fin base. This is effectiveness, ε_{fin}, and is given as, (Cengel, 2006):

$$\varepsilon_{fin} = \frac{Q_{fin}}{Q_{no_fin}} = \frac{Q_{fin}}{hA_{b\,fin}(T_b - T_f)} \tag{3.20}$$

Another parameter, to evaluate the fin performance, is the fin efficiency, η, which has been widely used in fin heat transfer studies. Fin efficiency is the ratio of the actual heat transfer rate from the fin to the ideal heat transfer rate from the fin in case when the fin is at base temperature.

Adiabatic fin tip: $$\eta_{fin} = \frac{Q_{fin}}{Q_{fin,\max}} = \frac{\tanh mH_f}{mH_f} \quad (3.21)$$

Furthermore overall surface efficiency η_o that characterize the efficiency of the base surface and the fin surface together, (Incropera, et al., 2006) is given as:

$$\eta_o = 1 - \frac{NA_f}{A_t}(1-\eta_f) \quad (3.22)$$

where A_t is the total heat transfer area associated with both fin and the free base area, A_f is the area of the fin surface and N is the number of fins. In cases when surface efficiency is known, the total heat transfer rate from the enhanced surface is given as:

$$Q_t = \eta_o h A_t (T_b - T_f) \quad (3.23)$$

The heat transfer performance of the pin-fin structures in general is studied experimentally due to the complexity that it presents to be analysed analytically. The pin-fin (staggered and in-line) arrangements are widely used in heat transfer enhancement therefore both are studied with interest by many researchers. The heat transfer characteristics depend on the fin configuration and number of the pin-fin rows in both transverse and in the flow direction. The study of heat transfer from tube bundles in fluid flow, Eq (3.24, (Zukauskas, 1972) is bases for the evaluation of the thermal performance of the pin-fin structures and is given below:

$$Nu_d = C\,\mathrm{Re}_d^m\,\mathrm{Pr}^{0.36}\left(\frac{\mathrm{Pr}}{\mathrm{Pr}_s}\right)^{1/4} \quad (3.24)$$

$N_L \geq 20$

$0.7 \leq Pr \leq 500$

$1000 \leq Re_D \leq 2x10^6$

where, (C) and the exponent (m) are constants related to the fin geometry and arrangements. These constants are given in tables in heat transfer literature, i.e. (Incropera, et al., 2006). While N_L is the number of pin-fin rows in a heat sink.

3.3 PIN-FIN HEAT TRANSFER ENHANCEMENT

The pin fin is one of the most efficient heat transfer enhancement techniques. The enhancement technique can be easily adapted to fit into different size electronic cooling systems. Because of the large heat transfer area, pin fin technology has an advantage in comparison with other current plate or segmented fin enhancement techniques. The most widespread pin fin geometries are circular, oval, square and diamond shape. Pin-fin heat sinks in general are made of high conductive materials such as copper and aluminium. The fin density is a function of heat transfer duty and available air or water flows (depending on the application).

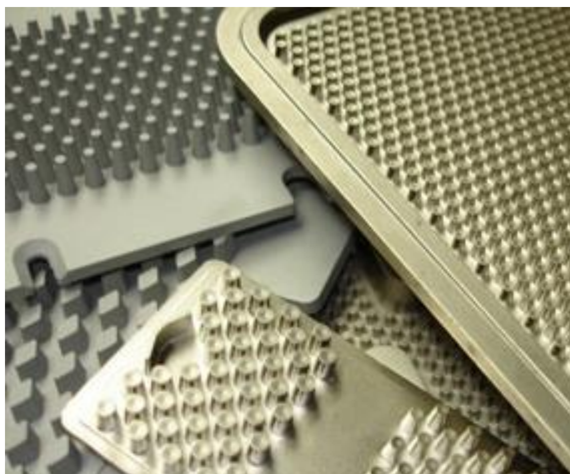

Figure 3.3: Pin fin heat sinks, (Alsic, 2013).

The good performance of pin-fin structures has made this technique attractive in liquid cooling applications. The common arrangements found in literature are in-line and staggered. In literature also, thermal performance or

the heat transfer rate from the fin surfaces is compared with the smooth uncovered base area (end-wall) of the heat sink or liquid cooled plate, (Webb & Kim, 2005). This chapter aims to explore the effects that the main geometry variables of the pin fin structures have on the heat transfer and pressure drop characteristics.

The following part discusses the thermal behaviour of the pin fin heat sink arrangement, and in particular the heat transfer rates from the fin structure and the end-wall. Furthermore explores, the effect on the heat transfer and on the pressure drop, of both the span-wise (S_T) and the stream-wise (S_L) spacing. This is followed by the examination of the effects that the fin shape and the aspect ratio (H/d) has on both heat transfer and pressure drop characteristics, and finally the effect of the Reynolds number is discussed.

The arrangement of the enhancement in the flow path affects the performance. For example the effect of the first row of fins towards the fluid flow for both staggered and in-line arrangements is similar; however, the difference is made by the following fin rows. In the in-line configuration, flow is directed to move between rows and the vortex flow effect created by fins diminishes while in the staggered configuration, flow is obstructed and vortex effects are higher. Positive effects of enhancement depend as well on the flow regime (laminar, transient or turbulent) and the geometry of the fin structure. In general, the geometry is characterized by three aspect ratios given as:

i. Transverse fin space (S_T) to fin diameter (d) ratio, (S_T/d),
ii. Stream wise fin space (S_L) to fin diameter ratio, (S_L/d),
iii. Fin length (H) to fin diameter ratio, (H/d).

A visual view of arrangement parameters used in the study is presented in Figure 3.4.

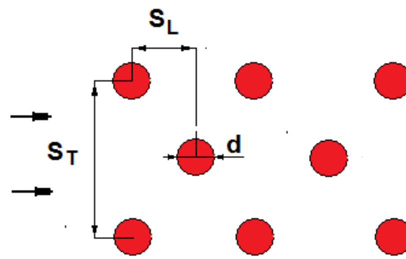

Figure 3.4: Pin-fin heat sink parameters.

The main manufacturing technique for production of pin-fin structures is the cold forging technology, since it maintains the consistency of the material, avoiding any structural irregularities or impurities that may affect thermal resistance. However, new technologies such as selective laser melting, skiving, electron and laser beam treatment, laser welding of mini-pin-fins in surface of material and metal injection mouldings are used lately as an alternative.

The design or selection of the pin-fin heat sink is based on three factors: available air or fluid flow, geometry and the material. The performance of the heat sink depends on both, the fluid flow rate and the fin density. Selection of the heat sink material varies on the application. For example, copper heat sinks have better thermal performance than aluminium, due to copper's low thermal resistance (high thermal conductivity). Still, the weight of copper is around three times that of aluminium. Thus, copper heat sinks are used mainly for high performance cooling system designs where weight is not an issue. The irregular pin fin heat sinks with fins positioned at different angle exhibit higher heat transfer due to improvement of fluid penetration and better interaction between pin-fins and the fluid. Flow characteristics and pressure drop within pin-fin structures are governed by boundary layer separation and vortex effects that in addition influence the heat transfer coefficient.

A number of the available correlations for the evaluation of the heat transfer on pin-fin structures are presented in Table 3.2. Overall, the heat transfer rates are observed to increase with Reynolds number, see Figure 3.5. The contributions of the pin-fin and the end-wall heat transfer rates and the effect

of the fin spacing and the fin ratio in the heat transfer and pressure drop performance are discussed in the following sections.

The pressure drop from the enhanced structures is significantly larger than that of the smooth surface. The staggered configuration has the largest pressure drop compared to the in-line configuration. Some of the predictions from the available correlations for the pressure drop evaluation of different geometries are presented in Table 3.3.

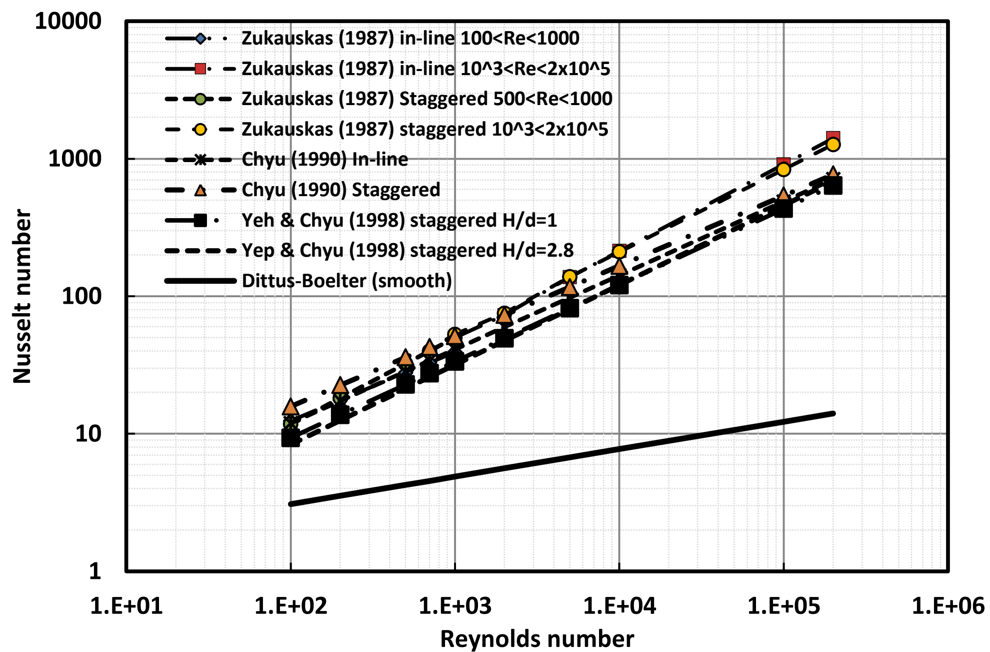

Figure 3.5: Nusselt numbers versus Reynolds number for circular shape fins, generated by computing in “MS Excel” respective correlations.

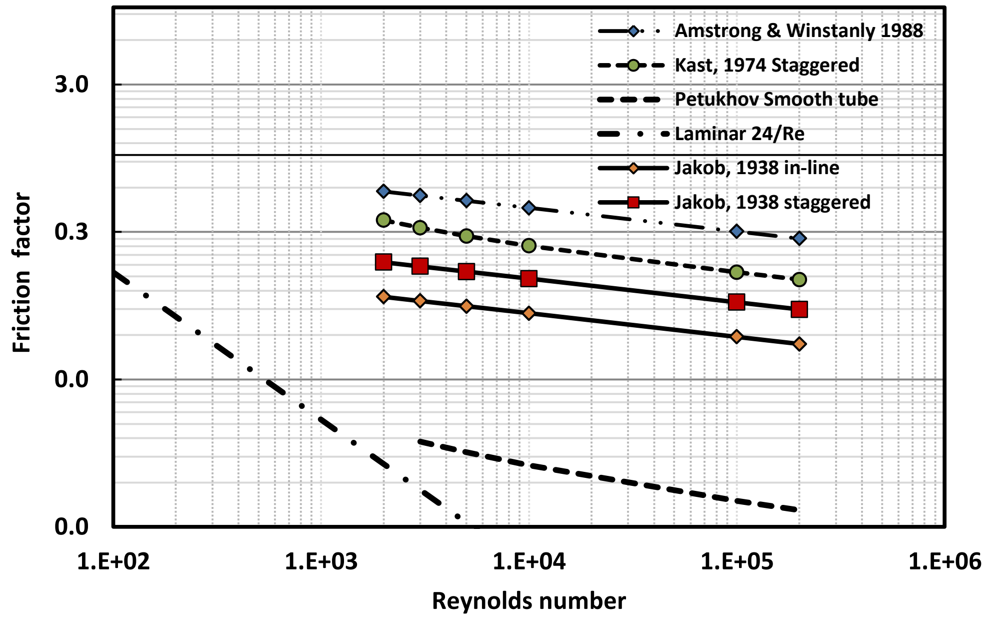

Figure 3.6: Friction factor versus Reynolds number for circular shape fin, generated by computing in “MS Excel” respective correlations.

Table 3.2: Nusselt number correlations for cross flow through circular fins.

Author	Arrangement	Re_d	Pin-fin	End-wall	Overall
(Zukauskas, 1987)	In-line Long tubes	100 <Re< 1000	$Nu_{av}=0.52Re^{0.5}Pr^{0.36}(Pr/Pr_s)^{0.25}$		
		10^3 <Re< $2x10^5$	$Nu_{av}=0.27Re^{0.63}Pr^{0.36}(Pr/Pr_s)^{0.25}$		
	Staggered	500<Re< 1000	$Nu_{av}=0.71Re^{0.5}Pr^{0.36}(Pr/Pr_s)^{0.25}$		
	Long tubes	1000<Re< $2x10^5$	$Nu_{av}=0.35(S_T/S_L)^{0.2}Re^{0.6}Pr^{0.36}(Pr/Pr_s)^{0.25}$		
(Chyu, 1990)	In-line $S_T/d=S_L/d=2.5$ $H/d=1$		$Nu_{av}=0.436Re^{0.537}Pr^{0.4}$		
	Staggered $S_T/d=S_L/d=2.5$ $H/d=1$		$Nu_{av}=0.69Re^{0.511}Pr^{0.4}$		
(Chyu, 1998)	In-line Similar to above		$Nu_{av}=0.155Re^{0.658}Pr^{0.4}$	$Nu_{av}=0.052Re^{0.759}Pr^{0.4}$	$Nu_{av}=0.068Re^{0.733}Pr^{0.4}$
	Staggered Similar to above		$Nu_{av}=0.337Re^{0.585}Pr^{0.4}$	$Nu_{av}=0.315Re^{0.582}Pr^{0.4}$	$Nu_{av}=0.320Re^{0.583}Pr^{0.4}$
(Metzger, 1982 a)	Staggered, $S_T/d=2.5$, $S_L/d=1.5$, $H/d=1$	10^3<Re<10^6			$Nu_{av}=0.092Re^{0.707}Pr^{0.4}$
	Staggered, $S_T/d=2.5$, $S_L/d=2.5$, $H/d=1$	10^3<Re<10^6			$Nu_{av}=0.069Re^{0.728}Pr^{0.4}$
(Qu and Siu-Ho, 2008)	Staggered	50<Re<180			$Nu_{av}=0.0241Re^{0.953}Pr^{0.36}(Pr/Pr_s)^{0.25}$
(Short, et al., 2002)	Staggered, , $2< S_T/d<6.41$, $1.83<S_L/d<3.21$, $1.9<H/d<7.5$	100< Re<1000			$Nu_{av}=0.419Re^{0.45}Pr^{1/3}(S_T/d)^{0.2}(S_L/d)^{0.77}(H/d)^{-0.3}$
(Short, et al., 2002, a)					$Nu_{av}=0.76Re^{0.33}Pr^{1/3}(S_T/d)^{0.2}(S_L/d)^{0.16}(H/d)^{-0.11}$
(Liu, et al., 2011)	Staggered,	0<Re<800			$Nu_{av}=0.1245Re^{0.6106}Pr^{0.36}(Pr/Pr_s)^{0.25}$

Table 3.3: Some of the friction factor correlations in literature.

Author	Pin-fin	Geometry
(Amstrong & Winstanly, 1988)	$f = 2.06(S_T/d)^{-0.11} Re_d^{-0.16}$	Circular
(Metzeger, et al., 1982)	$f = 1.268 Re_d^{0.132}$	Circular
(Moores & Joshi, 2003)	$f = 19.04(H_f/d_e)^{-0.742} Re^{-0.502}$	Circular
(Jakob, 1938), in-line	$f = (0.25+(0.118/((S_T-d)/d)^{1.08}) Re_d^{-0.16}$	Circular tube
staggered	$f = (0.04+(0.08/((S_T-d)/d)^{0.43+1.13d/S_L}) Re_d^{-0.15}$	Circular tube
(Kast, 1974)	$f = (128/Re_d)+(4/Re_d^{0.16})$	Circular
(Short, et al., 2002a)	$f = 140.4(S_L/d)^{-1/3}(S_T/d)^{-0.78}(H/d)^{-0.55} Re_d^{-0.65}$	Circular
(Konishi, et al., 2010)	$f = (55.631/Re_d)+(2.1114/Re_d^{0.096})$	Square
(Qu & Siu-Ho, 2008)	$f = 20.09 Re_d^{-0.55}$	Square
(Kosar, et al., 2005)	$f = 2.45(S_L/d)^{0.2}(S_T/d)^{0.2}(H/d)^{0.18}(1+D_h/d)^{0.2} Re_d^{-0.435}$	Triangle
	$f = 3.44(S_L/d)^{0.2}(S_T/d)^{0.2}(H/d)^{0.18}(1+D_h/d)^{0.2} Re_d^{-0.435}$	Ellipse
	$f = 4.43(S_L/d)^{0.2}(S_T/d)^{0.2}(H/d)^{0.18}(1+D_h/d)^{0.2} Re_d^{-0.435}$	Hexagonal

3.3.1 Pin-fin and end-wall heat transfer rates

In the literature, the pin-fin heat transfer coefficient is often compared to that of the end-wall. All studies agree on the fact that Nusselt number increases in the entrance region of the fin structure and decreases slightly in the flow direction after the fifth row, see Figure 3.7. The effect of the end-wall heat transfer rate in the overall performance has also been acknowledged and it is presented in literature. The earliest attempt to evaluate the thermo-hydraulic performance of pin fin structures was made in the year 1942 by Norris & Spofford, cited in (Sparrow & Liu, 1979). The objective of their work was to investigate the forced convection regime and assess thermal performance in relation to pin-fin geometrical parameters. Later on, the work of (Sparrow & Liu, 1979) established the effect on the thermo-hydraulic performance of the fin arrangement, i.e. continuous, in-line and staggered configuration of segmented fins showed different heat transfer rates. Tests were conducted for equal heat transfer area and pumping power. Results revealed that, segmented fins in the in-line configuration had a better heat transfer rate compared to the parallel fins when tested under fixed mass flow rate and for similar heat transfer area. The pressure drop in segmented fins arranged in-line was higher than parallel fins. Whilst, staggered configurations showed

better heat transfer rates, compared to the in-line configuration. However, the improvement of the heat transfer performance was associated with a higher-pressure drop in the staggered configuration. The enhancement technique was regarded as competitive in reducing volume and weight, despite the high-pressure drop for staggered configurations.

The research of Zukauskas on the flow and heat transfer characteristics across tube bundles has provided the bases for analytical evaluation of thermo-hydraulic performance of pin-fin enhancement structures, (Zukauskas, 1972). Zukauskas, evaluated the performance of 49 arrangements of tube banks and generated correlations to predict the performance in relation to the flow regime, arrangement and tube spacing. Table 3.2 presents a number of available correlations from Zukauskas and other researchers for the in-line and staggered arrangements. In addition, results are also compared and presented graphically in Figure 3.5, and show that staggered arrangement has higher heat transfer rates compared to the in-line arrangement.

VanFossen studied a staggered configuration of fins with $S_T/d=S_L/d=3.46$, fin aspect ratio H/d of 0.5 and 2.0 (VanFossen, 1981). Each configuration was composed of four rows. The results show that the heat transfer coefficient from the end wall was 35% lower compared to that of the fin structure. Under similar conditions Metzeger evaluated the heat transfer coefficient and friction factor for the staggered configuration and multiple row arrays, (Metzeger, et al., 1982). Both the end-wall and the fin heat transfer were observed for the short circular fins with $S_T/d=S_L/d=2.5$ and H/d=1. The conclusions reached by both studies were in agreement about the fact that the heat transfer rates from the fins were higher than that of the end-wall.

Metzger and Haley compared the performance from the pin-fin with that from the end-wall by using high conductive copper and wooden[1] fins attached to a copper base. The test samples explored had a fin aspect ratio H/d=1 and transverse and longitudinal aspect ratios as given: $S_T/d=2.5$, $S_L/d=1.5$, and $S_T/d=S_L/d=2.5$. Both heat transfer coefficients were compared in order to

[1] Wood fins were assumed isothermal and effect of the fin on the heat transfer is negligible.

evaluate end-wall heat transfer rate. Results show that the heat transfer rate for copper pin-fin structure increased with the increase of Reynolds number. The heat transfer rates from the pin-fins were 1.8 to 2 times higher than that of the end-wall, (Metzger & Haley, 1982). In comparison to previous results from (VanFossen, 1981) the heat transfer rates from the pin-fin were higher.

Investigation of the thermo-hydraulic performance of the pin-fin structure arranged in-line with equalized spacing: $S_T/d=S_L/d=2.5$ and fin aspect ratio H/d=1 was carried out by (Chyu, et al., 1998). Results showed that the heat transfer rate from the pin-fin was 10% to 20% higher than that of the end-wall heat transfer rate. These results were lower compared to those of (VanFossen, 1981) and (Metzeger, et al., 1982a). However, in general all agree that the heat transfer rates from the pin-fin structures were higher than those from the end-wall. As a further development, (Chyu, et al., 2009), studied the effect on the heat transfer rate from pin-fins in a staggered configuration with arrangement aspect ratios $S_T/d=S_L/d=2.5$, and the fin aspect ratio H/d varying from 2 to 4. Results showed the fin heat transfer coefficient to be 30% to 60% higher than that of the end-wall. Results are comparable to those of (VanFossen, 1981) and (Metzeger, et al., 1982). The dependency of the heat transfer coefficient on the Reynolds number was higher compared to the dependency on the fin aspect ratio.

3.3.2 Heat transfer variation in the heat sink

From the experimental evaluation of the heat transfer characteristics in the flow over tube banks, (Zukauskas, 1972) observed that there is an increase of the heat transfer coefficient in tube banks downstream the flow compared to those in the front row. The maximum value was recorded in the third row, while for the following rows the heat transfer coefficient remained constant. The increase of the thermal performance in the third row is an effect of the front row that acts as a turbulence initiator that as a result improves mixing for the following rows. In spite of this, the effect is observed to stabilize after the fourth row, (Incropera, et al., 2006).

(Metzeger, et al., 1982), studied in details the heat transfer rates from the pin-fin and the end-wall, for staggered arrangement with $S_T/d=S_L/d=2.5$ and H/d=1. Results showed a variation of heat transfer rates over the pin-fin structure. The highest heat transfer rate was observed between the third and fifth row. The experimental data are in line with findings of (Zukauskas, 1987), nevertheless they differ from those of the ongoing flow, since the heat transfer rates, decreased in the flow direction after the fifth raw.

(Chyu, 1990), performed the experimental investigation of the heat transfer rates and pressure drop of the short pin fins heat sinks. The in-line and staggered arrangements with a fin aspect ratio H/d=1 and equal transverse and stream-wise spacing $S_T/d=S_L/d= 2.5$ were tested. Results showed the superiority of the staggered arrangement in the thermal performance; yet this effected the pressure drop that increased compared to the in-line arrangement. The increase in the heat transfer performance was observed to be generated by the fluid flow separation. Together frontal and the upstream fins initiate the turbulence and the acceleration of the flow between fins for the following part and as consequence improve heat transfer performance. The maximum Nusselt number was recorded in the second row for the in-line and third row for the staggered arrangement. The similar findings were presented by (Zukauskas, 1987), (Metzger & Haley, 1982) and (Metzeger, et al., 1982) as shown in Figure 3.7.

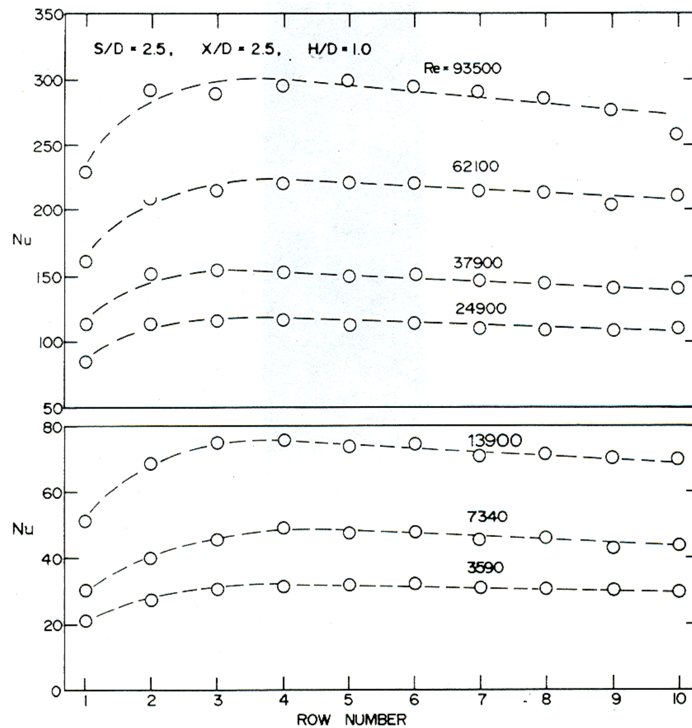

Figure 3.7: Variation of heat transfer in pin-fin heat sink against the row number, (Metzeger, et al., 1982)

(Donahoo, et al., 1999), developed a numerical 2D model for a staggered configuration of a pin-fin heat sink to examine the heat transfer and flow characteristics. Results showed the maximum heat transfer rate is achieved between the third and the fifth row of fins. These findings supported the results of (Metzeger, et al., 1982). Then again, the fact that the 2D model could not evaluate the effect of fin height leads to inconclusive results. Furthermore, (Ames, et al., 2005) evaluated numerically the thermal behaviour of the fin for a staggered configuration. The highest heat transfer rate was observed between second and third rows, which were similarly reported by previous studies (Metzeger, et al., 1982), (Donahoo, et al., 1999), (Chyu, 1990).

Additionally, the effects of the micro pin-fins structure made from n-type silicon on the heat transfer performance for a low range of Reynolds numbers (14 to 112), were studied by (Kosar & Peles, 2006). The experimental data showed that the positive effects of the enhancement are obvious. However, the experimental results underestimate those of the other

researchers (Zukauskas, 1972 a), (Whitaker, 1972), (Hwang & Yao, 1986) and (Short, et al., 2002), which can be seen in Figure 3.8.

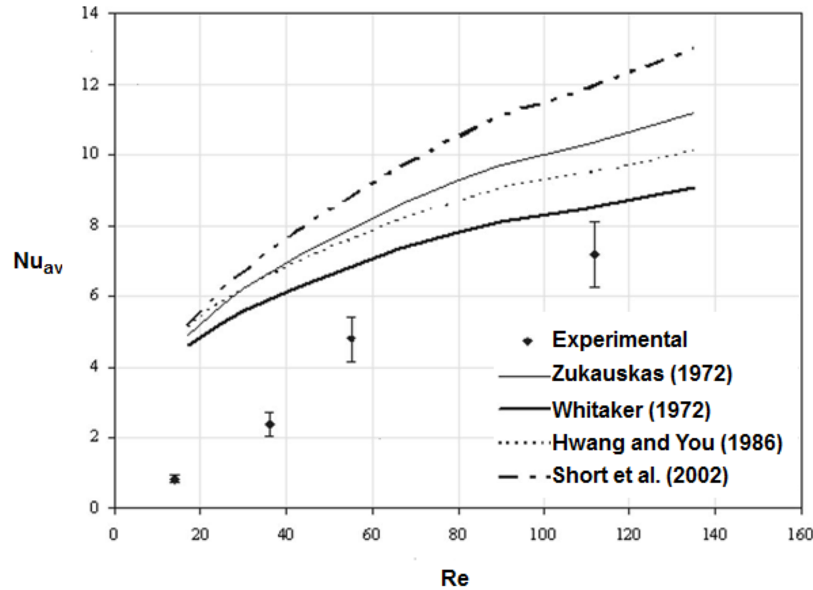

Figure 3.8: The average Nusselt number as function of Reynolds number. (Kosar & Peles, 2006).

(Siu-Ho, et al., 2006), conducted a thermo-hydraulic testing for a single-phase flow of water in a copper micro pin-fin heat sink. The heat sink test sample was composed of 1,950 square micro pin-fins arranged in a staggered configuration with a cross section of 200x200 μm^2 and height of 670 µm. Results show that friction decreases with the increase of the Reynolds number. The heat transfer coefficient achieved the highest value at the inlet, after that decreases gradually along the flow direction. The heat transfer results expressed as a function of the local Nusselt numbers are considerably higher than those presented by (Chyu, et al., 1999) in Figure 3.9.

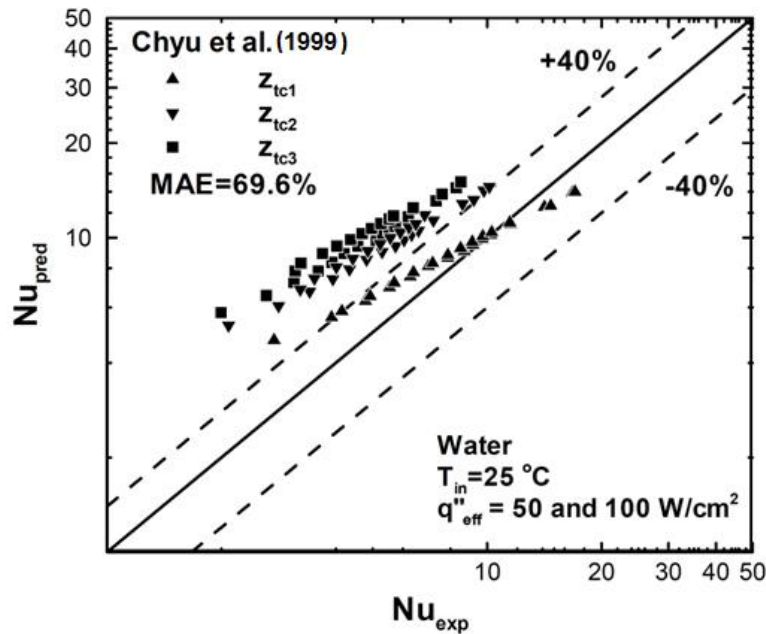

Figure 3.9: Comparison between measured and predicted values of Nusselt number.

(Lyall, et al., 2011), conducted a combined experimental and numerical study for the heat transfer and pressure drop in a single row of circular fins with aspect ratio H/d=1. A range of transverse spacing were investigated for 5000<Re<30000. Results show that the end-wall heat transfer coefficient was affected greatly by the transverse fin spacing. The maximum heat transfer was observed at four fin diameters downstream from the fin at Re<13000. The pin-fin heat transfer coefficient from the fin structure is higher than that of the end-wall. Pressure drop was observed to increase with reduction of the transverse fin spacing. The pressure drop results showed an increase by of 80% for the transverse aspect ratio S_T/d=2, and 25% for S_T/d=8 as compared to a smooth duct.

3.3.3 Arrangement effects

A considerable number of researchers have studied the effect of the fin spacing or the arrangement on the heat transfer performance. A large part has used air as a working fluid for the experimental investigations, and enhanced structures such as, pin-fins with aspect ratios close to H/d=1. For example, the effect of the stream-wise spacing was evaluated by (Metzger &

Heley, 1982). Experiments were carried out for a variety of spacing ratios in the flow direction that ranged from $S_L/d=1.05$ to 5.0. According to Figure 3.10, the average Nusselt number decreased when the fin distance increased in the flow direction. A similar effect in a small scale was observed from (Metzeger, et al., 1982); Figure 3.11. However, the positive effect of small stream-wise spacing between fins was observed to decrease with the increase of the Reynolds number, see Figure 3.11.

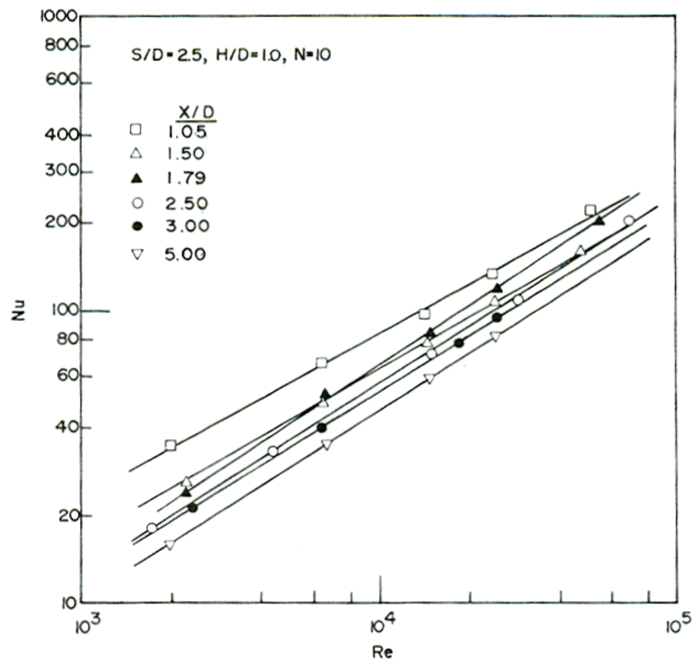

Figure 3.10: Staggered arrangement, Nusselt number versus Reynolds number, (Metzeger & Haley, 1982).

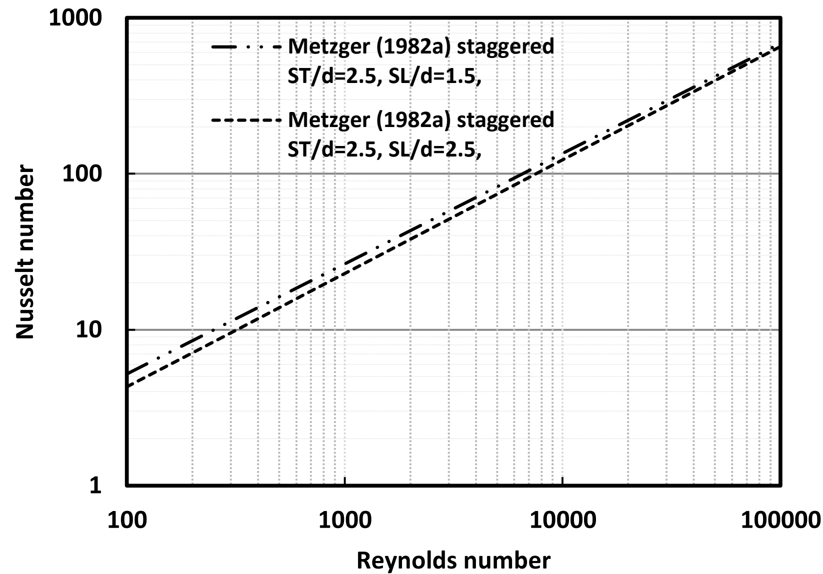

Figure 3.11: Nusselt number versus Reynolds number for different stream-wise spacing for Pr=7.

(Tahat, et al., 1994), experimentally investigated the thermo-hydraulic characteristics of airflow through varying fin configuration. Results showed that for the in-line and staggered configuration, the $S_T/d=1.3$ and $S_L/d=2.2$ achieved the best heat transfer coefficient. They also observed an increase of heat transfer coefficient in the second and third rows. Furthermore, the decrease of the stream-wise spacing was observed to improve heat transfer rates.

(Babus'Haq, et al., 1995), studied the effect of the thermal conductivity of the heat sink in the heat transfer performance by using various pin-fin materials, such as light aluminium, mild steel and poly-tetra-fluoro-ethylene (PTFE) with *k=1.7 W/m K*. The authors concluded that, for the best performance, in the span-wise direction the spacing to diameter ratio S_T/d for all pin fins should be 1.04, while in the stream-wise direction this ratio will depend on the material used and fin configuration,. These findings complement previous research results presented by (Metzger & Heley, 1982).

(Bilen, et al., 2001), tested under constant temperature a cylindrical pin-fin (H/d=5.8) structure for Reynolds number that ranged from 3700 to 30000. The cylindrical shaped fins attached on the surface were arranged in-line and

in a staggered configuration. Distance between fins in the flow direction was varied to observe the effect on the heat transfer rate. The test data showed that heat transfer rates increase with the increase of Reynolds number. The staggered fin arrangement performed better than the in line configuration. However, this was associated with a higher pressure drop. The stream-wise distance affected the Nusselt number and the best performance was noticed for S_T/d=2. 2 and S_L/d=2. 94, see Figure 3.12.

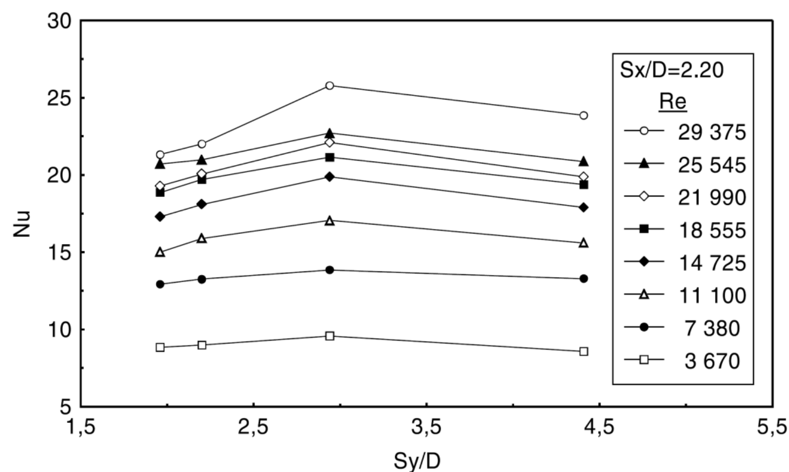

Figure 3.12: Nusselt number versus stream-wise aspect ratio, (Bilen, et al., 2001).

(Jeng, 2006), experimentally studied the thermo-hydraulic performance of an in-line diamond-shaped fin structure. The span-wise and stream-wise spacing was varied to achieve the optimal arrangement. The pressure drop increased with a decrease of span-wise spacing due to increase of the velocity between adjacent fins. The highest heat transfer coefficient under equal pumping power was observed for the S_T=1.41 and S_L=1.06 Figure 3.13.

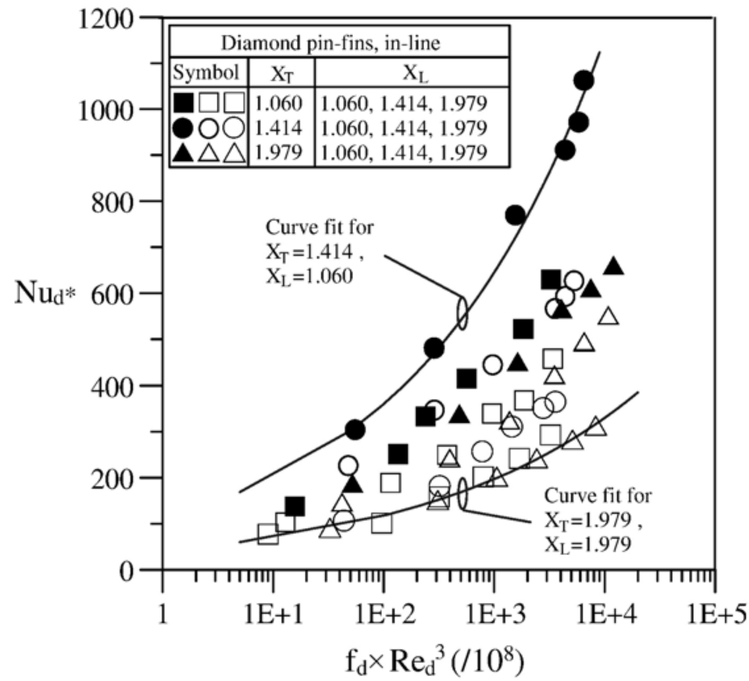

Figure 3.13: The average Nusselt number as a function of dimensional pumping power, (Jeng, 2006).

(Yakut, et al., 2006), tested experimentally the effect of hexagonal fins on the heat transfer performance. The effect of fin height and width was examined by changing span-wise and stream-wise distances between fins. Results show that, the geometry of the fin and mass flow rates affect the heat transfer performance. Based on the experimental results the optimum configuration was obtained at 150 mm fin height and 14 mm width. The span-wise and stream-wise space was set at 20mm. If the hexagonal fin is assumed cylindrical with diameter 14 mm, the corresponding span-wise and stream-wise ratios will be $S_T/d=S_L/d=1.43$, and fin aspect ratio H/d=10.71. The stream-wise aspect ratios are comparable with those presented by, (Metzeger, et al., 1982).

(Jeng & Tzeng, 2007), studied the pressure drop and the heat transfer of square aluminium pin-fins arranged in the in-line and staggered configuration. The pin-fin structures with height 75.5 mm and cross section (9.6x9.6) mm^2 were examined by varying span-wise and stream-wise fin spaces. The performance of squared pin-fins was compared to that of circular fins. The optimal geometrical configuration was selected based on

the highest value of the Nusselt number given from the tested pin-fin structures under identical pumping power. Results show that the Nusselt number for the in-line configuration was observed to be higher for aspect ratios $S_T/d=2$ and $S_L/d=1.5$, while for the staggered configuration the best performance was achieved for aspect ratios $S_T/d=1.5$ and $S_L/d=1.5$ respectively. This result agrees with those presented from (Yakut, et al., 2006). Friction factor increased with a decrease of the span-wise spacing see Figure 3.14.

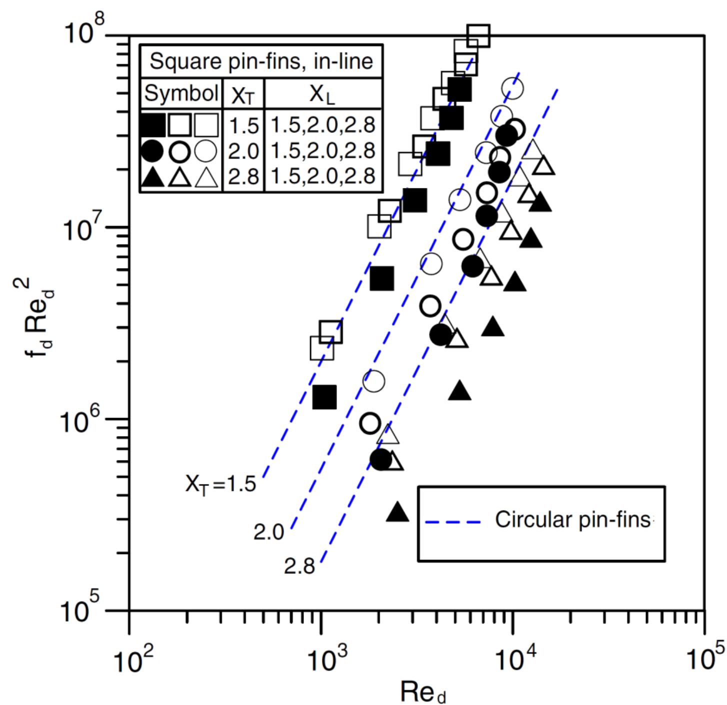

Figure 3.14: Non-dimensional pressure drop as a function of Reynolds number for in-line arrangement of square pin-fin, (Jeng & Tzeng, 2007).

A combined experimental and numerical assessment of heat transfer coefficient and pressure drop in a heat sink with pin-fins and dimples under turbulent flow regime using air as working fluid was conducted by (Rao, et al., 2011). The pin fin diameter was equal to the dimple diameter of 10 mm that has a depth of 2 mm. The structure was made of stainless steel; the span wise spacing to diameter ratio (S_t/d) and the stream wise spacing to diameter ratio (S_L/d) were equal to 2.5 while the pin fin height to diameter ratio (H/d) was equal to a unity. The results show that the surface composed

of pin-fin and dimples increases overall thermal performance and the best enhancement is observed for high Reynolds numbers in the range of $36700<Re<49500$. Results show the improvement that surface disruptions can have on the heat transfer. Changes in the flow surface introduce turbulence in the fluid flow; therefore, higher heat transfer coefficients are expected.

(Lyall, et al., 2011), also evaluated the effect of the three sets of span wise spacing 2, 4, and 8 on the heat transfer rates for fins with aspect ratio $H/d=1$. Results show that the heat transfer varies with the Reynolds number when stream-wise spacing to fin diameter ratios S_L/d range from 4 to 8. Results show that, decrease of the fin spacing in both span-wise and stream-wise direction increases the heat transfer rate. In spite of this, the strongest effect was observed to be from the stream-wise spacing. Similar results are presented by other researchers as discussed above; therefore maintaining low space between fins in the flow direction will help to improve the heat transfer coefficient.

(Lawson, et al., 2011), experimentally evaluated the effect of both span-wise and stream-wise spacing on the heat transfer and the pressure drop for multiple fin rows. The aspect ratios tested ranged from $S_T/d=2$ to 4 and $S_L/d=1.73$ to 3.46, while fin aspect ratio $H/d=1$ remained constant. Results show that the reduction of the transverse and stream-wise distances affected positively the heat transfer coefficient; observation showed that stream-wise spacing had the strongest effect on the heat transfer rate. According to Figure 3.15 the best performance was recorded for $S_T/d=2$ and $S_L/d=1.73$. In relation to the pressure drop, the span-wise spacing had the largest effect compared to stream-wise spacing. The above studies present similar results, therefore, thermal performance can be improved by decreasing stream-wise spacing and pressure drop can be improved by increasing the span-wise spacing.

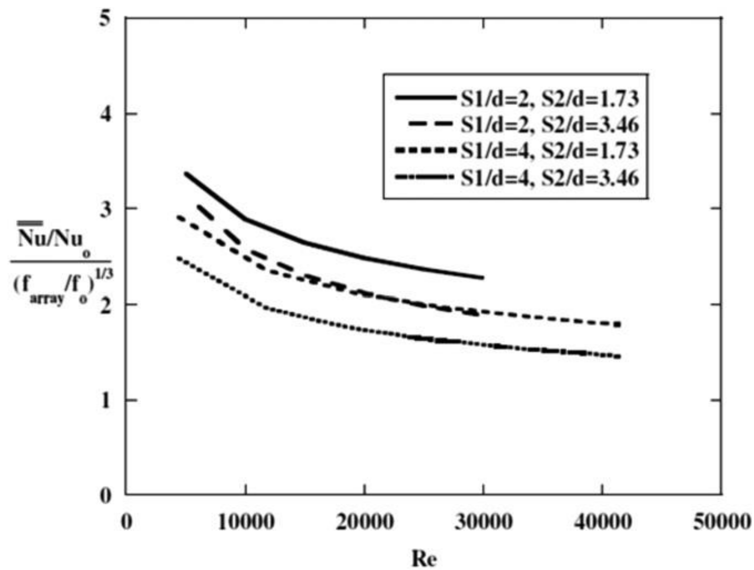

Figure 3.15: Thermal performance of all geometries tested, (Lawson, et al., 2011).

(Tullius, et al., 2012), examined the effect of fin spacing on the heat transfer rate and pressure drop. Decrease of the fin spacing increases the heat transfer rate; however the increase of the pressure drop is significant. The best thermal performance was recorded for fin spacing equal to the fin diameter or the fin width (for a square geometry). The optimal fin spacing from the experimental results in this study seems to be lower than previously observed from (Lyall, et al., 2011) and (Lawson, et al., 2011).

3.3.4 Pin-fin aspect ratio effect

(Metzger & Heley, 1982), compared the experimental data for short pin fins with Zukauskas equations for long tube banks and observed a discrepancy of 5%. The same procedure was followed by (Chyu, et al., 1999) and that recorded a discrepancy of 20%.

(Ames, et al., 2005), evaluated the frontal heat transfer rate from a pin-fin array with span-wise and stream wise to diameter ratios, $S_T/d= S_L/d=2.5$ and fin aspect ratio H/d=2. The experimental data extracted for $3000<Re<30000$ were in line with those from published by (Zukauskas, 1972), with the largest discrepancy of 11% recorded at Re~10000. Above studies indicate the effect of the fin aspect ratio on the heat transfer performance.

The experimental investigation of silicon micro pin-fin heat sinks Figure 3.16 was presented by, (Peles, et al., 2005). Experimental work was performed for a range of Reynolds numbers $10<Re<1000$ using water as the working fluid. Fins were arranged in a staggered configuration over a silicon plate (10x10) mm^2. Results showed that an increase of the fin diameter increased thermal resistance. For a given Reynolds number, heat transfer is inversely proportional to the pin diameter. At low wall temperatures large heat fluxes could be dissipated, therefore, to decrease convective resistance for high Reynolds numbers, dense fin configurations are preferable, while for low Reynolds number thin fins are advisable. The pressure drop increases with the mass flow rate and is inversely proportional to fin diameter, due to decrease of the flow path and increase of the velocity.

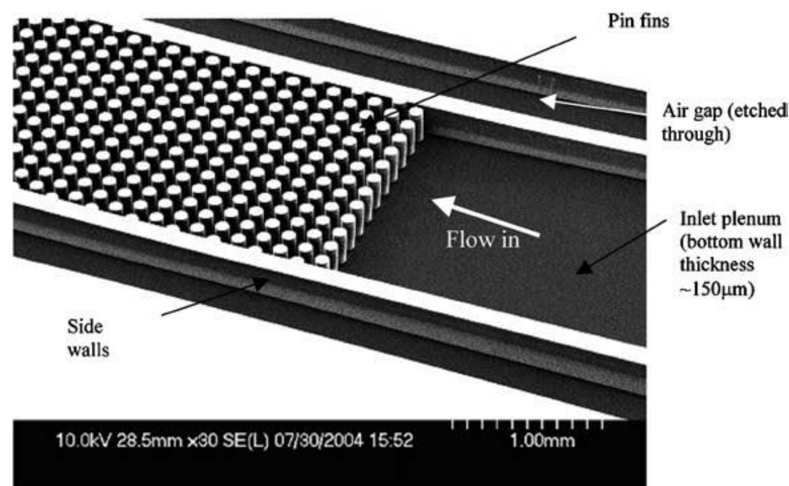

Figure 3.16: Design of the test sample, (Peles, et al., 2005).

(Chyu, et al., 2009), conducted an experimental evaluation of the effect that fin aspect ratio has on the heat transfer coefficient. Three fin aspect ratios H/d from 2 to 4 in a staggered arrangement with $S_T/d=S_L/d=2.5$ were tested. The Reynolds number ranged from 10^5 to 30^5. The overall heat transfer coefficient increases with the increase of the fin aspect ratio or height. The fin heat transfer rate was higher than that of the end-wall for $H/d>2$. The increase of the aspect ratio increased the pressure drop. The best thermal performance was achieved for $H/d=2$.

(Tullius, et al., 2012), evaluated the effect of the fin aspect ratio H/d on the heat transfer rate and pressure drop for a range of fin shapes. Results show the increase of the fin aspect ratio increases the Nusselt number; however, this is accompanied by an increase in the pressure drop. A similar effect was reported by (Chyu, et al., 2009).

3.3.5 Pin-fin shape effect

The pin fin shape effects the interaction between the fluid and the heated surface and as a consequence the overall performance. Thermo-hydraulic performance of short elliptical pin fins in rectangular ducts was tested experimentally for $700<Re<8000$ by (Li, et al., 1998). Results show the advantage of an elliptical pin fin over circular pin fins. The best performance was given by elliptical structures with span-wise and stream-wise to fin diameter ratios respectively $S_T/d = S_L/d = 2.50$.

(Soodphakdee & Copeland, 2001), numerically studied the effect of different fin geometries, such as; plate, cylindrical, elliptical, and square on the heat transfer and pressure drop performance. Fins were analysed in both arrangements, in-line and in staggered. According to Figure 3.17 staggered configuration has better heat transfer performance than in-line configuration. In addition, the elliptical fins offered overall better thermo-hydraulic performance. However, at high-pressure drop the performance of the circular fin in staggered configuration was higher. Pressure drop for the staggered configuration compared to the in-line configuration for all fin geometries was higher, Figure 3.17. Similar findings were reported by (Li, et al., 1998).

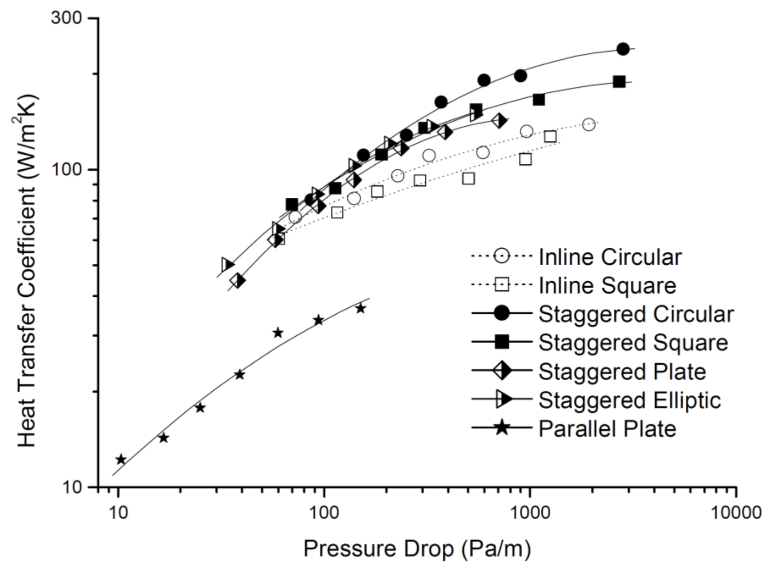

Figure 3.17: Thermo-hydraulic performance, (Soodphakdee & Copeland, 2001).

Ricci and Montelpare (2006), experimentally examined pin fin heat sinks with different fin geometries such as circular, square, triangular, and rhomboidal arranged in-line, Figure 3.18. Results revealed that the triangle and rhomboidal fin geometry have the best performance see Figure 3.19.

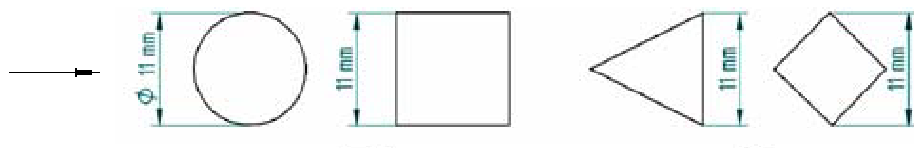

Figure 3.18: Tested geometries, (Ricci & Montelpare, 2006).

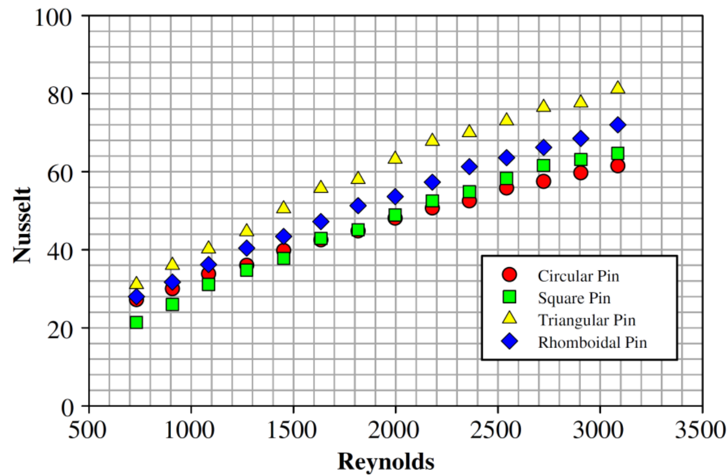

Figure 3.19: Thermal performance of four fin geometries, (Ricci & Montelpare, 2006).

Wong, et al in year 2009 experimentally tested six heat sinks that were fabricated by rapid melting technique known as Selective Laser Melting (SLM). (Wong, et al., 2009). The technology is already being used commercially in the dental implants sector and metal press tools. SLM is a laser-operated technology that produces up to 100% dense metal parts direct from modelling software (CAD data). The process performs well in low melting alloys, zinc, bronze, stainless steel, tool steel, titanium, silicon carbide, aluminium oxide and cobalt chrome. Parts do not require any post processing. The main research in the development of SLM products has been directed to the manufacture of micro-heat exchangers, ultra-light components for aerospace applications and implantable medical devices. In relation to heat transfer, Wong tested six heat sinks, which consisted of different fin geometries: circular, rectangular, rectangular with rounded corners, ellipse and lattice, Figure 3.20. Experimental results showed an increased heat surface area of lattice structure does not improve significantly the heat transfer performance. The lattice structure increases the hydraulic resistance to the flow considerably. Round corners improved airflow in rectangular fins, while elliptic fins offered the highest heat transfer per unit pressure drop compared to other tested samples. The results agree with those of (Jeng, 2006). Pressure drop for in-line and staggered segmented fin configuration were in the range ±20% compared to (Manglik & Bergles,

1995) correlation. The SLM method does present a good capability in surface structuring.

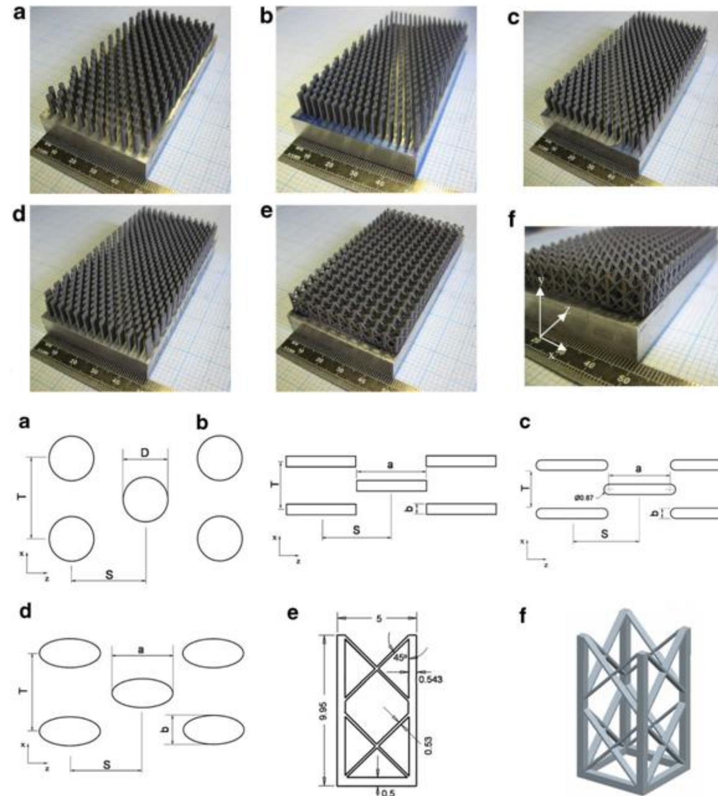

Figure 3.20: SLM technology heat sinks, (Wong, et al., 2009)

(Liu, et al., 2011), experimentally investigated pressure drop and heat transfer in micro square pin-fin heat sinks. Two heat sinks were fabricated from copper with a total heat transfer area of 20 x 20 mm^2, arranged in a staggered arrangement with the first (type 1) having square pin fins 559 x 559 μm^2, and (type 2) 445 x 445 μm^2. Tests were performed with water for $60<Re<800$. Results show high heat transfer rates for both pin-fin configurations. The type 2, for pressure drop under 1.1 kPa exhibits better thermal performance than type 1. Then again, with an increase of the pressure drops, type 1 heat sink exhibits the lowest thermal resistance. For both fin heat sinks, type 1 and type 2 heat transfer rate correlations were developed and were compared to that of (Qu & Siu-Ho, 2008) in Figure 3.21.

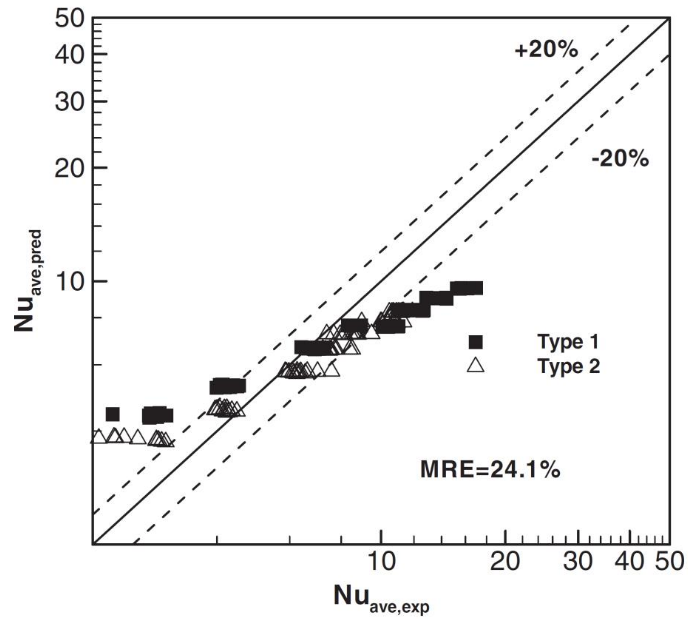

Figure 3.21: Experimental Nusselt number compared to the available equations, (Liu, et al., 2011).

While friction data for both heat sinks (Type 1 and 2), for Re_c<300 and 300<Re_c<550 are presented in the Figure 3.22**.**

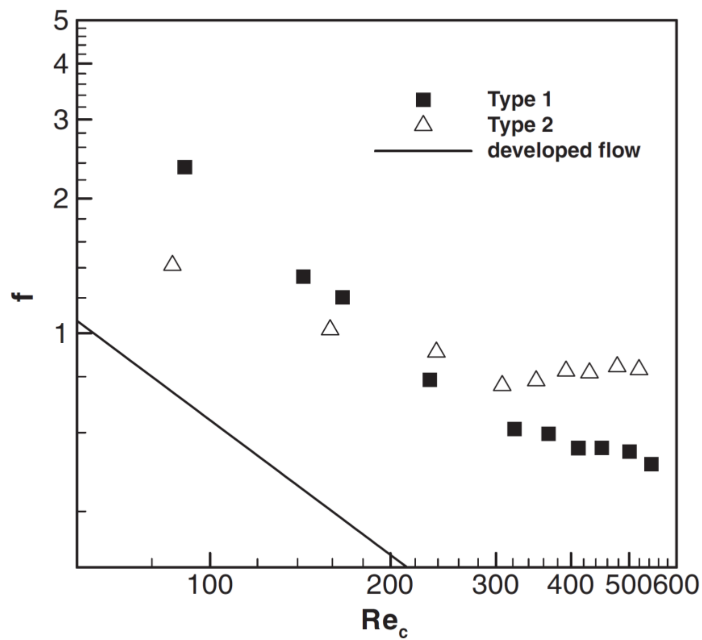

Figure 3.22: Friction factor for fin structures, (Liu, et al., 2011).

(Tullius, et al., 2012), numerically evaluated the effect of fin geometry on the heat transfer and pressure drop. Six pin-fin geometries: circle, ellipse, diamond, square, triangle, and hexagon arranged in a staggered configuration were analysed. The fin spacing was varied to evaluate the effect on the heat transfer rate and pressure drop. The highest heat transfer was observed for triangular fin with base 1 mm and equal span-wise and stream-wise spacing 2 mm. The lowest heat transfer was recorded for circular and elliptical fins, however the pressure drop for both was much lower, Figure 3.23 and Figure 3.24. Similar finding were reported by (Ricci & Montelpare, 2006). Nusselt number and pressure drop increased with an increase of fin height.

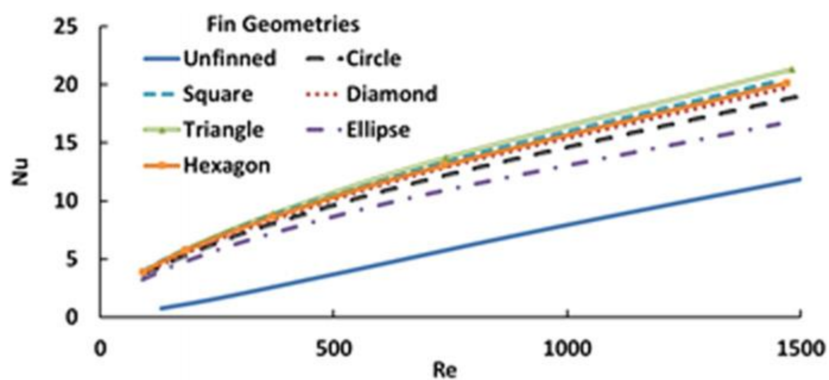

Figure 3.23: Nusselt number versus Reynolds number, (Tullius, et al., 2012).

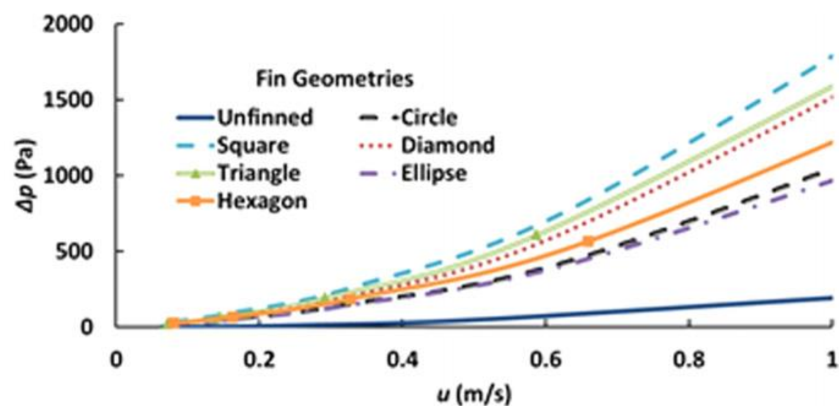

Figure 3.24: Pressure drop versus maximum axial-velocity, (Tullius, et al., 2012).

Hasan (2014) investigated numerically, square, triangular and circular fin geometries under constant wall temperature for $100<Re<900$, (Hasan, 2014). Results show that the circular fins have the best overall performance. Similar findings were reported by (Soodphakdee & Copeland, 2001).

3.3.6 Clearance effect

Hydraulic resistance and heat transfer of in-line, square pin fins, with different clearance ratios (clearance gap between fin top and upper wall) were experimentally tested and numerically analysed by (Dogrouz, et al., 2005), Figure 3.25. The heat sink was made of aluminium and had base dimensions 25x25x2.5 mm^3. Fins were rectangular in shape with a cross section, 1.5x1.5 mm^2, 2.0x2.0 mm^2 and 2.5x2.5 mm^2, see Figure 3.25. For in-line configuration, fin height ranged from 12.5 to 22.5 mm. Pressure data were collected for different clearance ratios (height of channel / clearance) ranging from 0 to 3.0. Results show that pressure drop increases with the decrease of the clearance ratio and thermal resistance increases with an increase of the clearance ratio. For low velocities, numerical predictions were very close to experimental results, while for high velocities numerical predictions were poor. This is an effect of the increase in velocity in the channel that becomes much more noticeable between the fins, and close to the by-pass zone. Therefore, the CFD model will require a very fine mesh to respond and to evaluate velocity changes.

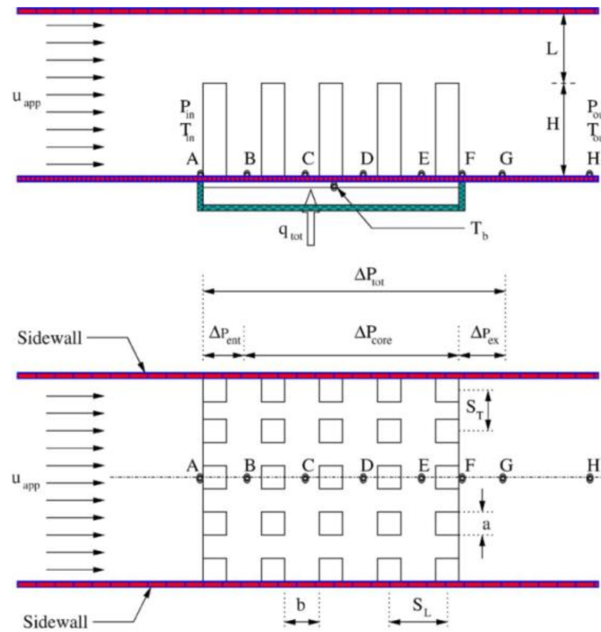

Figure 3.25: Side and top view of the heat sink, (Dogrouz M.B. et al., 2005).

The study of heat transfer using water flow in pin-fin arrays with and without tip clearance was completed by (Moores, et al., 2009), (Figure 3.26). Heat sinks with tip clearance up to 25% of fin height were investigated under a range 200 <Re< 20000. Three heat sinks with a height to diameter ratio H/d of 0.5 to 1.0 were studied to evaluate the effect of tip clearance. Results show that decrease of tip clearance increases the pressure drop. Similar effects were observed by (Dogrouz, et al., 2005). Higher heat transfer per unit pressure drop was observed for a dimensionless clearance ratio (clearance gap over pin diameter) = 0.2 compared to the case without clearance.

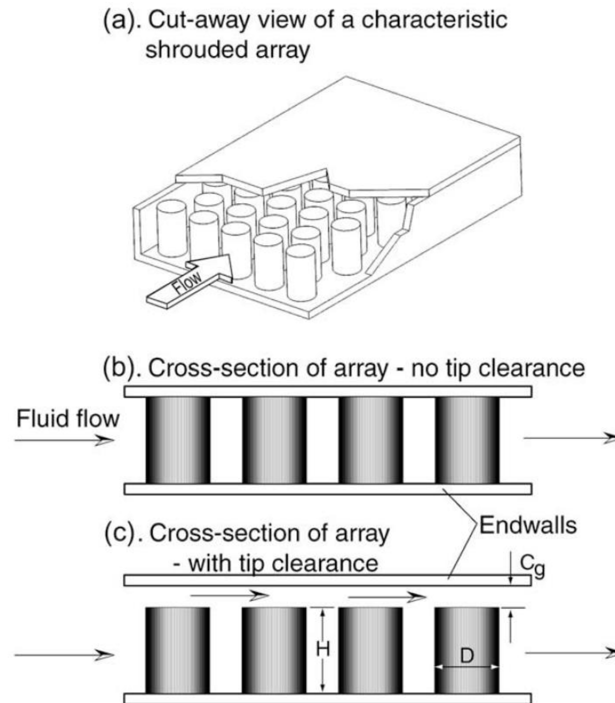

Figure 3.26: Staggered circular pin fins with and without tip clearance, (Moores, et al., 2009).

(Zhigang, et al., 2013), examined in-line and staggered arrangements of cylindrical fins with fin aspect ratio H/d=1, where H=d=0.5 mm, and varying tip clearance. The experimental data recorded for 8<Re<400 shows that the tip clearance has little effect on the thermo-hydraulic characteristics for low Reynolds number; however, the influence increases for high Reynolds number. The tip fin clearance decreases the pressure drop and affects the heat transfer coefficient. The heat transfer increase from the fin top is relatively small compared to the overall heat transfer rate, therefore, the effect is low. The clearance improves the overall performance, because it causes a decrease in the pressure drop.

(Mei, et al., 2014), studied experimentally and numerically the effect of tip clearance on the heat transfer rates and the pressure drop at low Reynolds numbers 30 to 350. Three tip clearance ratios[1] H_{ch}/H_f =1.2, 1.5 and 2 were experimentally tested. Results show an initial increase in the heat transfer rate at a low level of clearance ratio. This is the effect of the exposure of the fin top to the cooling fluid that provides additional heat transfer area.

[1] The tip clearance ratio in this study is the ratio of channel height (H_{ch}) to fin height (H_f).

Additionally, the top of the fin surface contributes to the enhancement by regenerating thermal boundary layer at clearance level. The same effects were observed by (Moores, et al., 2009). However a further increase in the clearance ratio over 1.2 decreases both heat transfer rate and pressure drop Figure 3.27. Friction factor decreases with the increase of the clearance ratio Figure 3.28. The experimental data shows a strong dependency of the heat transfer coefficient and friction factor on the tip clearance ratio.

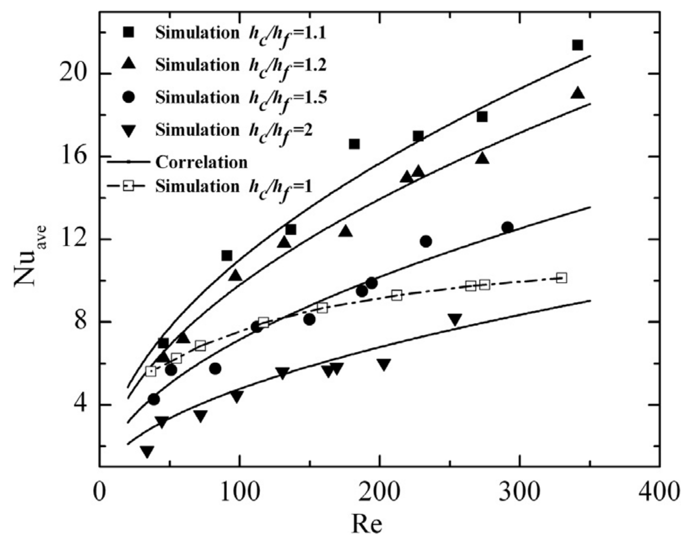

Figure 3.27: Variation of Nusselt number over Reynolds number for different clearance ratios, (Mei, et al., 2014).

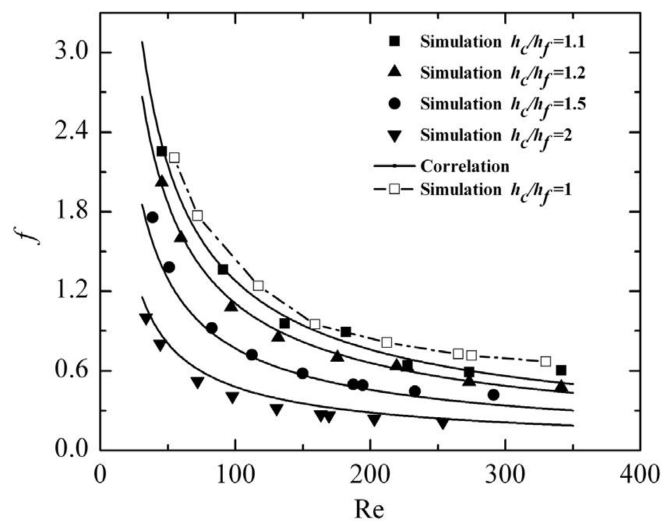

Figure 3.28: Variation of friction factor over Reynolds number for different clearance ratios, (Mei, et al., 2014).

Review on the clearance effects on the thermo-hydraulic performance shows that most of the research was performed with the air as a working fluid. With the exception of (Moores, et al., 2009) another research is performed for high fin aspect ratios. The positive effect of low aspect ratio on heat transfer performance requires further investigation. However, further research is required to understand flow characteristics and heat transfer behaviour in cases when the tip clearance is varied.

3.3.7 Reynolds number effect

The Reynolds number effect on the heat transfer varies between researchers. However, the effect of fin structure on the thermal performance is evident when it is compared to that of a smooth duct. The Reynolds number exponent from the Colburn Equation for the smooth ducts is given as 0.8 while for a flow in tube banks at (Zukauskas, 1972 a) it is given as 0.4 to 0.8 (exponent increases with Reynolds number), see (Zukauskas, 1987). The heat transfer correlations developed by (Metzeger, et al., 1982) and (VanFossen, 1981) contain a Reynolds number exponent of 0.7. Furthermore (Chyu, et al., 1999), related specific exponents to each fin arrangement; for the in-line configuration an exponent of 0.7 and for the staggered configuration an exponent of 0.6. The above research shows the dependency of both, the thermal and the pressure drop performance on the Reynolds number.

3.4 EMERGING ENHANCEMENT TECHNOLOGIES FOR LIQUID COOLING APPLICATION

The researches into low cost and high efficiency heat sinks for thermal management are intensive. A number of manufacturing techniques are developed to improve the geometrical range of pin-fins. Currently, Wolverine has developed the Micro Deformation Technology (MDT) to manufacture efficient fin structures, (Wolverine, 2013). The MDT is a machining process that uses the skiving technique to form a range of fin structures. The technology is promising because it has the capability to generate very high-density[1] fin structures that can offer large heat removal capacity. Wolverine has examined the performance of the product in the automotive sector with liquid flow; however limited data is available in the public domain. The technique has the capability to create a series of fins and regular geometries as shown in Figure 3.29. The process is rapid, does not require a tool change and is cost effective since it does not produce material waste.

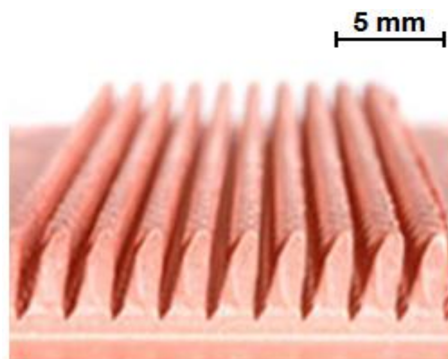

Figure 3.29: Micro Deformation Technology (MTD) structure, (Wolverine, 2013).

Laser surface treatment is cutting-edge technology for surface processing. It can tailor different configurations rapidly with precision. This technique generates a small amount of heat (limiting distortion of material) during the process, (TWI, 2013). The laser beam is automatically controlled, therefore, can produce different treatments very easy. Figure 3.30 shows the laser treatment on a rod of 10 mm diameter. The ability to generate complex structures for heat exchange processes makes the technology very competitive.

[1] Large heat transfer area.

Figure 3.30: Laser Surface Treatment, (TWI, 2013).

Metal Injection Moulding (MIM) is seen as an interesting manufacturing process by the thermal management industry. This technique uses fine metallic powder combined with bonding agent that is injection moulded under high temperature (the process is similar to plastic injection mouldings) (Amulare, 2013). After the moulding process heat sinks are placed inside an oven where the bounding agent evaporates and the final part is a homogeneous part with a density close to 100%. The MIM technique is very efficient in producing dense pin fin structures, Figure 3.31. In spite of this, it requires specially making moulds for a given configuration which can increase initial costs.

Figure 3.31: Metal Injection Moulding Technology fin height 2.5 mm, (Amulare, 2013)

Figure 3.32 shows a unique innovative Electron Beam (EB) treatment in a copper plate C101. This technique uses a powerful electron beam that is

manipulated by 3D modelling software. The precise control and power make the electron beam a very desirable tool for generating fine tailored treatments. The process takes place in a vacuum, therefore, is very clean[1]. However, during the trials as a consequence of the heat input into the workpiece during the treatment was observed that the substrate deformation and treatment nonconformity issues. Such problems are apparent on treatments with a fin height larger than 2.5 mm. Optimization of the EB treatment parameters that affect the power input into workpiece during the treatment such as beam frequency, deflection, accuracy and guidance, combined with a fluidised cooling bed (fluid cooling of the bed in contact with the workpiece during the treatment) can reduce the overheating effect and allow higher protrusions to be attained. Therefore, further work is required in the EB gun design to improve beam quality, control and optimize the process for a range of treatments.

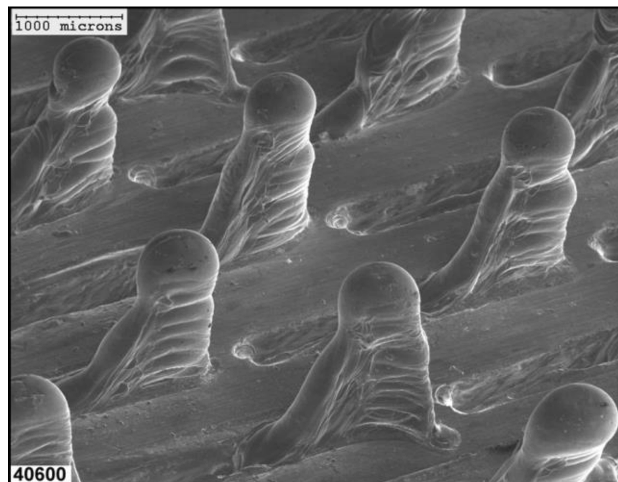

Figure 3.32: Electron Beam Treated Surface, produced by optical microscope x 10, (TWI, 2009).

The need for effective cooling systems have created a high demand for enhancement techniques that are able to transfer large amounts of heat fluxes in relatively small volumes. In this regard, new enhancement technologies can offer considerable thermal performance improvement. New

[1] The process complies with regulations required for the treatment of the medical implants or in the semiconductor industry.

technologies have the ability to create surface treatments that are impossible with conventional technologies. Furthermore, computerized control via 3D software increases flexibility for the design utilization. The treatments also can be applied at a desired density that can change over the heat transfer area to provide necessary heat transfer rates that avoid hot spots and maintain the pressure drop at desired values.

The following section describes in detail the EB technology, presents the development in this area, working principle and surface treatment technology. In this study, attempts are made to evaluate experimentally the thermo-hydraulic performance of three EB treatments. This technique has been seen with a particular interest because it offers various ranges of treatments and works well in all conductive materials. The EB surface treatment process changes the topology of the base surface, which inevitably interrupts the formation of boundary layers adjacent to the base and improves mixing during the fluid flow. The process is applied in vacuum therefore it is very clean and fulfils the requirements of medical, aerospace and electronics industry.

3.5 SUMMARY

The literature review of the pin-fin enhancement technologies for the single-phase flow regime in this study covers a range of pin-fin enhancement structures and their thermal and fluid flow characteristics. This passive method for heat transfer enhancement is desirable and is widely used due to the low initial, operation and maintenance costs. While active and combined techniques are mainly utilized for specific applications where the performance is a prime concern.

The interest in the heat transfer enhancement technologies has been intense due to economic considerations. This is well observed in the growing research and literature publication in this field. The performance evaluation

of the enhancement in the literature is given in relation to the smooth surface performance; i.e. the majority of papers has performed a comparison of single-phase flows on smooth ducts and pin-fin enhanced structures.

From the literature, there is substantial evidence that the pin-fin enhancement technology increases heat transfer coefficients considerably. This is accompanied by an increase in the pressure drop. Thermo-hydraulic performance of pin fin heat sinks depends upon a number of factors such as mass flow rate of working fluid, pin-fin geometry, arrangement, thermal conductivity of the material used, and temperature distribution through the heat sink. The effects of the fin geometry, arrangement, and clearance ratios on the heat transfer and pressure drop were also investigated. A number of correlations to predict thermohydraulic performance are available in the literature. Correlations evaluate laminar, transient and turbulent regimes. However, limited data exist for developing flows and entrance effects on the pin-fin heat sinks. Literature suggests that performance is related to Reynolds and Prandtl number. Thus, heat transfer characteristics in a variety of studies have been expressed as a function of the Nusselt and Prandtl number in the form $Nu=CRe^{m}Pr^{n}$ where C, m, n are constants. Heat sink performance in some studies is expressed in terms of thermal resistance for practicality. Most of the studies use the flow over tube bank's methodology to evaluate the performance. Since the methodology was developed for fluid flow through long tube banks, application for very short pin fins creates a slight discrepancy between experimental results and available correlations for tube banks. Staggered configuration offered the best thermal performance; however, it was accompanied by the large pressure drop.

Literature shows that, the heat transfer rates from the pin-fin structures were higher than those from the end-wall. The highest heat transfer coefficient was recorded between the second and fifth row. In addition, the fin height was observed to have an effect on the heat transfer coefficient and the friction factor for the turbulent regime. The fin spacing impacted heat transfer and hydraulic performance. Research shows a reduction of stream-wise fin spacing improved the heat transfer performance; however the effect is negligible for high Reynolds number. The similar effect was observed for the

span-wise spacing, but here span-wise space reduction increased the pressure drop. The majority of research evaluates the performance using the air as a working fluid; therefore more research would be beneficial with liquids. The effect of the pin fin aspect ratio of the heat transfer coefficient is not significant for values (H/d<2), however the effect increases with increasing aspect ratio H/d≥4. The cylindrical fins have higher efficiency than rectangular fins; however, the elliptical shape fins had the best performance. The fin orientation toward the flow with 30° (for rectangular shaped fins) also had a positive effect on the heat transfer. The effect of the clearance between the fin tip and the top cover in the heat transfer performance is negative however it reduces the pressure drop. Pressure drop was higher for the staggered arrangement compared to the in-line. The low span-wise spacing compared to the stream-wise spacing had a larger effect on the increase of the pressure drop.

From the study of the literature, it is shown that the pin-fin enhancement has beneficial thermal performance. The demand for effective techniques to increase heat transfers in the engineering sector and in particular the electronic industry is high. Engineers and researchers have been focused on the development of rapid and cost effective enhancement techniques to respond to the needs of the liquid cooling technology, which will allow further developments in the field of electronics. New technologies such as skiving, metal injection moulding, selective laser melting, laser treatment and electron beam treatment are being developed rapidly to respond to such demands.

This study has examined the application of electron beam to treat heat exchange surfaces for electronics liquid cooling systems. The technology is advanced and can be manipulated to generate treatments that are not achievable with conventional methodologies. Based on the literature review such structures will have a positive impact on the improvement of thermal efficiency. Chapter four gives a brief history of the development of electron beam technology and as well as describing the working principle and the treatments tailored for this particular study. In addition, the work follows with the experimental examination and evaluation of the thermo-hydraulic results.

4 ELECTRON BEAM TREATMENT AND PREPARATION OF THE TEST MODULE

The objective of this chapter is to develop three electron beam treatments in copper C101 material for thermo-hydraulic performance examination. In the following part, is given a short history of the electron beam development and the current technology level. The electron beam working principle and pattern generation process are also explained in details. The development of the test samples is described step by step from the array arrangement, motif, to the treatment procedure. Finally, treatment parameters for copper C101 and aluminium 7075 have been optimized.

4.1 OVERVIEW

"Advance Surface Tailoring for Innovative Application" (ASTIA) is a unique development project intending to offer a variety of electron beam tailored surface structures with different engineering functionalities that are applicable in the thermal management, aerospace and automotive industries. This collaborative project has been a partnership between a number of organizations headed by The Welding Institute (TWI) and financed by the Technology Strategy Board (TSB). The project intends to develop the Surfi-Sculpt™ technology for a range of applications in material joining, surface modification of medical metallic implants and heat exchange processes for heat transfer enhancement.

Thermacore Europe as a leading organization in the thermal management sector has participated in this project aiming to develop and utilise the electron beam technology for the treatment of heat exchange surfaces for

the improvement of heat transfer in liquid cooling applications. The Surfi-Sculpt technology is an innovative technique that enables tailoring of structures in a range of conductive materials. During this process, the material is treated by an intense electron beam melting process that displaces the material in a controlled manner to form desired protrusions. This technology has been developed in laboratory conditions since 1920s, but converted into industrial scale applications after the Second World War. Electron beam processing is used in a range of industrial manufacturing applications, such as aerospace (Russell, 1981), automotive sector (Schulze & Powers, 1998), marine (Galsworthy & Bird, 1998), nuclear waste containers (Nightinggale, et al., 1998), lithography, surface treatments (Buxton, et al., 2009) and material joining.

This chapter presents an overview of electron beam treatment technology starting with a short description of the historical development, explanation of the process and the working principle. This is followed by electron beam system and surface treatment technology for Surfi-Sculpt™ process, and it leads to an explanation of the treatment and structures developed for the heat transfer enhancement.

4.2 SURFI-SCULPT PROCESS

The Surfi-Sculpt process utilises electron beam technology to generate 3D designed features on a surface of the metal. In this process, a controlled electron beam is impinged rapidly over a substrate surface to melt and transfer the material in a controlled manner. The treatment creates protrusions above the surface, which are accompanied by related cavities[1] in the substrate. Treatment takes approximately 20 sec/cm^2 and can produce a range of geometries that are not achievable with conventional techniques (Buxton, et al., 2009). The electron beam processes can be adapted to

[1] Cavities are created as a result of material displacement.

produce a variety of desired configurations that can be specific to a given application.

The electron beam technology is a result of accumulated experience and knowledge in the field of engineering, manufacturing and electro-technical physics for more than three centuries. Although the physics of the electron ray (beam) has been well established in the late 18th century, the first industrial scale application of the technology took place around the 1950s, (Bakish, 1962 c).

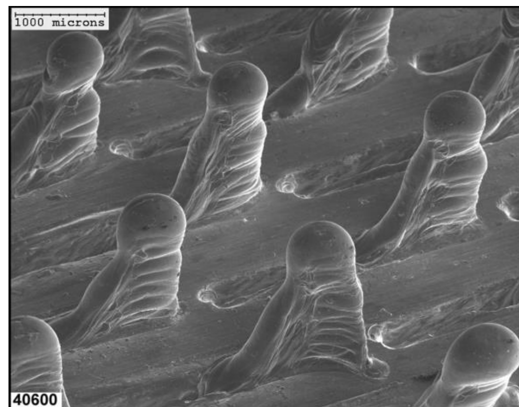

Figure 4.1: Electron beam enhanced area, picture taken by optical microscope.

4.3 ELECTRON BEAM TECHNOLOGY

The theoretical and practical developments in the field of electromagnetic physics have preceded the electron beam technology development. The theory emerged in the early 18th century with Faraday's postulation: "*An elastic medium filled the space between two charged bodies, and that, consequently, the force between reacting bodies was merely a state of strain in this medium*", (Bakish, 1962 b). However, Hans Ch. Oersted (1820) was the first to observe the existence of the magnetic field, (Blundell, 2012), while

Faraday experimentally established the foundations of electromagnetic effects and possibilities for the electricity generation. The mathematical explanation of the electromagnetic theory was presented by Maxwell in 1865 (Darrigol, 2000).

At the end of the 18th century and the beginning of the 19th century, the main research of physicists was focused to understand the electricity conduction through gases. The electricity discharge effect in a vacuum was firstly observed experimentally by John W. Hittorf in 1869, (Bakish, 1962 c). Thompson (1897) was the first to explain the formation of an electron beam, which he called a cathode ray[1]. Later work of Robert A. Millikan (1905-1917) aided one to determine accurately the electron charge[2], which made it possible to evaluate the beam power, (Bakish, 1962 c). Furthermore, the study of the wavy characteristics and corpuscular behaviour of electrons was published by Louis de Broglie in 1924 in Paris and proven independently by Davisson & Germer in 1927 and G.P. Thompson in 1928 (Bakish, 1962 c).

4.3.1 Electron beam

Electrons are negatively charged particles that respond to an electrical field by moving towards the positive pole (anode). These are extracted from a heated emitter (cathode) and accelerated by applying a high potential difference between the cathode and the anode.

The conventional cathode is made of tungsten that can be heated (directly or indirectly) to increase the internal energy, and as a consequence energises the electrons to overcome bonds of the molecular structure and become free. The electron beam treatment at TWI currently utilises the indirect heating method to protect the cathode, simplifying cabling and power requirements. A detailed description and technical performance data of the electron beam guns are given in (Sanderson & Ribton, 1998).

---

[1] The electron beam was emitted by the cathode therefore was called cathode ray.
[2] Electron charge is 1.6 x 10^{-19} coulomb.

Historically, Thomas A. Edison in 1881 was one of the first researchers that experimentally observed the thermionic emission[1] in a vacuum tube, (Darrigol, 2000) while in 1905, John A. Fleming used this effect to develop the first vacuum tube diode. His invention was followed by Lee de Forest who in 1907 improved the technology further by inserting another element in the vacuum tube diode that control the flow of electrons from the cathode to the anode and called it the triode. These developments set the foundations for the later developments in the electronics industry (Bakish, 1962 c). John J. Thomson 1899 experimentally studied electrical discharge in gases at reduced pressures and observed that BaO (barium oxide) and CaO (calcium oxide) cathode can produce an electrical discharge in cold conditions using a much lower potential difference (electrical field) compared to other materials (Zitzewitz, 2011). In addition, Wehnelt in 1904, proved that alkali-earth metal oxides can emit electrons at much lower temperatures compared to metals, (Bakish, 1962 c). These discoveries laid the foundations for the future research and basis to identify the compatible metals for the cathode construction.

4.3.2 Electron beam control

Electrons interact with magnetic and electrical fields and this behaviour is utilised to control their motion. The effect of the magnetic field on the electron ray is documented in studies made by Mac Gregor-Morris and Clinton in 1896, see (Bakish, 1962 c). In the first experimental setup, an electromagnet was placed between the cathode and the target around the beam, and by changing the current into an electromagnet; they proved to be able to control the electron beam size. Later on, Weichert in 1899 developed the technique further, by using concentrating coils (a magnetic field) to improve the beam quality and this research led to the development of the theory behind electro-magnetic controlling and opened a new field of electro-physics that of electron lenses. The later work of Rogowski and Fleger 1927 on electron

[1] Emission of electron from a heated surface.

lenses proved successful and made possible a generation of very sharp and focused electron beam see (Bakish, 1962 c).

4.3.3 Electron beam for industrial applications

Sir William Crookes 1879 was the first scientist to demonstrate the use of the electron beam technology for melting processes (Schultz, 1993).Nevertheless, the research of Marcello Von Pirani 1907 lead to a practical utilization of the electron beam technology to produce titanium homogeneous metals (Schultz, 1993). During the first part of the twentieth century a number of electron beam treatment facilities were built for research activities, while the first industrial scale electron beam melting system was launched in the USA from “Temescal Metallurgical Corporation” in 1957 (Bakish, 1962 c). In addition, the first electron beam welding process was achieved by “Carl Zeiss” (1950). The electron beam processes, that led to Surfi-Sculpt technology, had been patented by Von Bories in 1942 and practically considered by Steigerwald in 1953 (Schultz, 1993). A research laboratory in Baldock UK in 1956 was the site of the design of the first electron beam treatment zone refining process for the semiconductor industry (Bakish, 1962 c). The electron beam process has also been used for sintering of metal powders, testing of materials in 1953, and recording of information in 1961, (Bakish, 1962 c). Currently, electron beam processes are used widely for melting processes, small and large scale welding, sintering, surface treatments and other special technological processes.

4.4 ELECTRON BEAM SYSTEM

The electron beam process for surface texturing “Surfi-Sculpt” uses a powerful beam to melt and displace the material. The process is performed in a vacuum to avoid scattering of the electron beam and protect the

cathode. The electron beam system shown in Figure 4.2 is made of two main parts:

i. Electron beam gun
ii. Vacuum chamber

4.4.1 Electron beam gun

The electron beam gun is an electromagnetic device that generates, accelerates and controls the electron beam, Figure 4.3. The system is composed of two main parts, Figure 4.4.

i. Cathode - Electron generating part
ii. Focusing and deflection system

Electron beam guns are usually designed for a given process. However, the general designs range from low power for micro-machining to high power guns for melting materials. In between are a range of other guns that generate a variety of powers from 20 kV to 200 kV[1] and 1 mA to 1 A of current. The electron beam can be focused into diameters smaller than 0.2 mm.

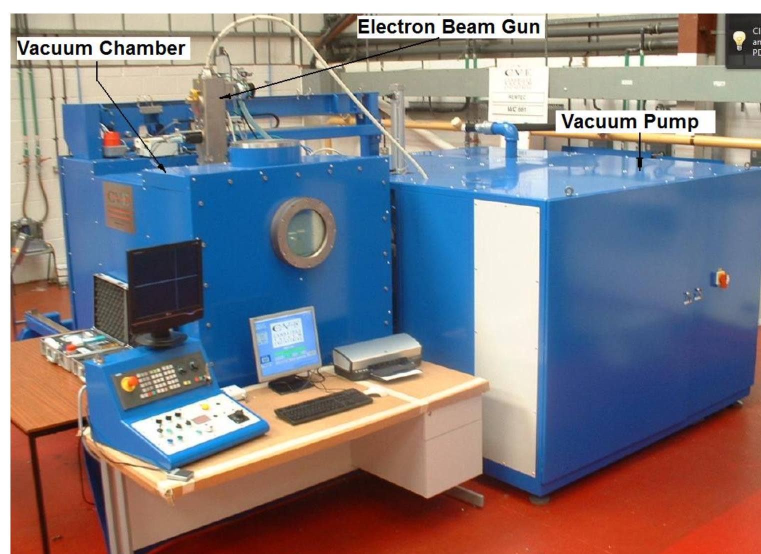

Figure 4.2: Electron beam treatment system courtesy of TWI.

[1] This depends on the process or available power.

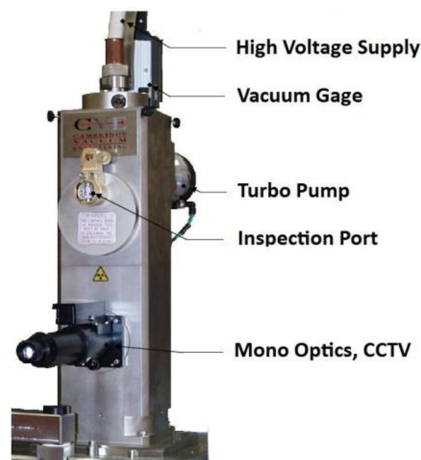

Figure 4.3: Electron beam gun view, (TWI).

An electron beam is generated at the cathode, accelerated by the electrical field and controlled by an electromagnetic field under vacuum conditions, Figure 4.4. In this way, it is possible to create an electron beam that can generate high levels of kinetic energy and transfer this energy in the impact with the workpiece. The cathode is the source of electrons and is usually made from tungsten or titanium. However the construction depends on the functionality and is, hence, divided into two groups: a) directly[1] heated, and b) indirectly[2] heated. The thermo-electro-magnetic mechanism is utilized to generate the electron beam. At zero Kelvin the energy level of the cathode structure is zero and molecular bonds are well defined. As the temperature of the material increases, electrons gain energy, start vibrating and move to the upper energy levels away from the atomic nucleus, thus decreasing the bonding forces. However, electrons cannot become free unless their kinetic energy can overcome the bonding forces. These forces are a function of molecular structure and composition of the cathode. For that reason, the cathode is selected to have high electron density and emissivity at low temperature. The cathode material choice also depends on the process. It must be mechanically stable and chemically resistant towards gasses that are released during the electron beam process.

[1] In this case a low voltage is applied at two ends of the cathode to increase the temperature.
[2] In this case a low voltage is applied at two ends of the heating element placed close to the cathode to increase the temperature.

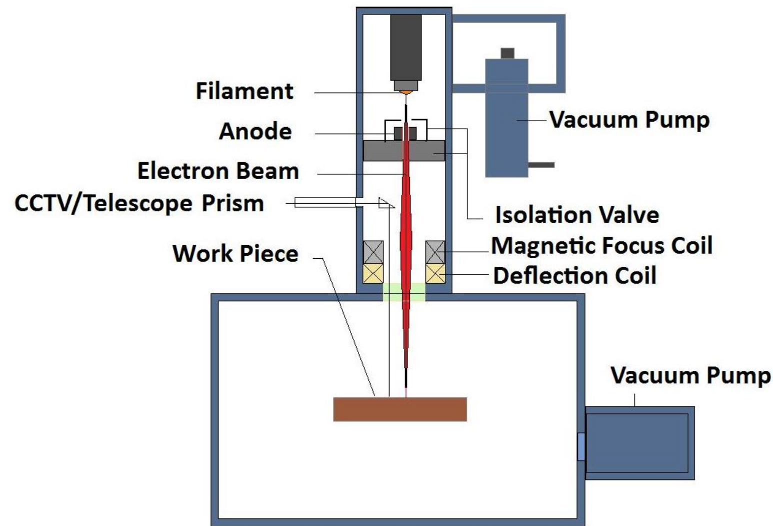

Figure 4.4: Simple diagram of electron beam machine.

The power and quality of the electron beam is a function of the electrical potential difference that is applied between anode and cathode (electrical field) and the magnetic focusing field. The electron beam leaving the cathode tends to spread; therefore magnetic focussing lenses concentrate the electron beam. In order to ensure a precise control of the movement of the focused beam, deflection coils are used, Figure 4.4. The electron beam gun operates in a pulsating mode, which is controlled by an isolating valve (or bias cathode). The bias cathode is negatively charged with the pulsating power at the same level as that of the cathode to control the electron beam flow, Figure 4.4. The majority of electron beam guns operate in a space-charge-limited condition and their current is proportional to the accelerating voltage and function of gun geometry (Gerken, 2007) given by a coefficient K expressed as follows:

$$I = JU^{3/2} \qquad (4.1)$$

where, I is the beams current in (mA), J is dimensionless constant that is related to the gun geometry, U is the beam voltage in (kV).

When the electron beam impinges on the solid, electrons penetrate into the surface and release the energy. Penetration is proportional to the kinetic energy and is inversely proportional to the material's density. During the

process, the temperature of the solid material increases rapidly depending on the physical properties of the solid.

The electron beam power is a function of the electrical field; therefore it is limited by the power availability. However, a higher voltage simplifies the gun design because it reduces the cathode current required (electron emission). In addition, high voltage guns over 100 kV are insulated by dielectric or viscous fluids to reduce the risk of discharge to the ambient. The electron beam guns over 50 kV are surrounded by a protective encapsulation made from heavy metals such as lead.

4.4.2 Vacuum chamber

The vacuum chamber is an enclosure evacuated of the air and gases. Inside the chamber is placed a static or a Computer Numerical Control (CNC) bed that, in combination with the beam deflection system, improves the degree of the treatment applicability and also facilitates batch production. In order to control the temperature distribution at the workpiece, in late models contemporary beds are water cooled internally. The vacuum at the gun compartment is maintained at a high value in the range of 10^{-5} mBar to prevent the oxidation of the cathode; this also avoids collision of electrons with air molecules that consequently maintains the beam power density and eliminates electrical discharge. The vacuum chamber pressure can vary; this depends on the process requirements and running costs.

4.5 SURFI-SCULPT WORKING PRINCIPLE

Electrons under an electrical field gain large kinetic energy and the force that the electrons exert is a sum of the electric and magnetic field forces (Bueche, 1985), and is given as:

$$F = eE + eV \times B \qquad (4.2)$$

Where, *e (1.6 x 10^{-19}* Columbus) is the electron charge, E is the electrical field (Volt/m), V is the velocity of the electron (m/s), and B is the magnetic field (Wb/m^2). In practice, the rate of energy input during the treatment is a function of the beam current, accelerating voltage, focal beam spot size and treatment speed. The beam transfers the kinetic energy when it comes in contact with the workpiece, depth of the penetration into workpiece is a function of accelerating voltage, and the material density. Beam power accumulates under the substrate surface and melts the material, Figure 4.5. When the beam translates sideways it creates a strip of molten material that under the effect of the vapour pressure and the surface tension moves in the opposite direction of the beam. By repeating this process at the same location, it is possible to excavate the material and layer by layer to build up a protrusion. The process is automatically controlled and parameters can be adjusted. A variation of the beam accelerating voltage, current, focusing point, deflection and frequency, can create a variety of designs Figure 4.6.

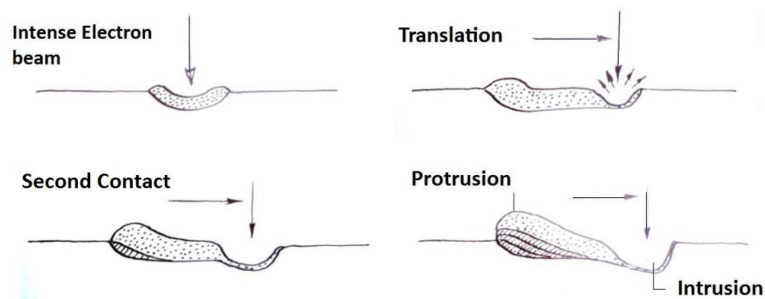

Figure 4.5: Electron beam process in metals, (TWI, 2002).

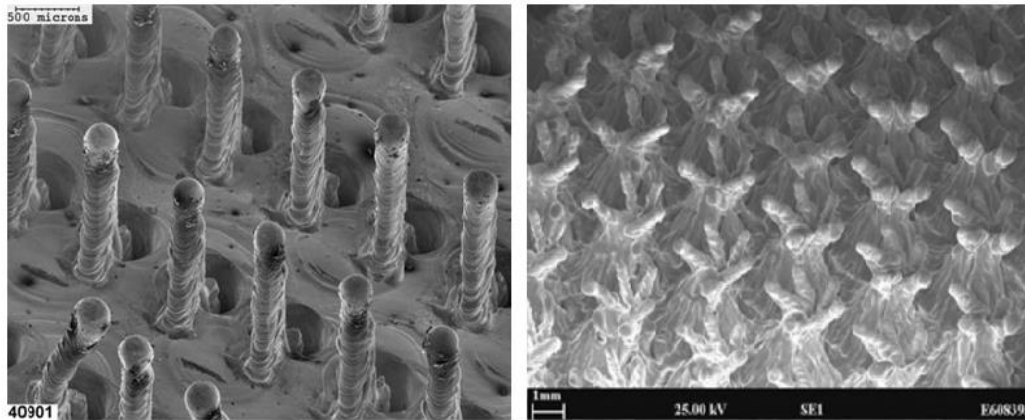

Figure 4.6: Electron beam treatment, left single and right multi fin, microscope image.

The characteristics of electron beam treatments depend on the material quality, geometry and surface conditions. However, the main factors are the treatment procedure and treatment parameters. Table 4.1 shows the main parameters that affect the electron beam process. Electron beam interacts with the material and as a consequence material quality inevitably affects the treatment. The material grade is an important parameter, because it indicates the composition of the material and this influences the behaviour during the treatment. Irregularities in the microstructure and residual flaws affect the process because can create uneven physical conditions in the material during the process. In addition, other physical parameters as; tensile strength, hardness, toughness, etc., affect the process since they are related to the material structure.

Material dimensions play an important role in the electron beam treatment because they affect the heat distribution into the workpiece. Surface finish and geometry variations also affect the process because the electron beam cannot be focused evenly throughout the surface. Poor surface conditions affect the interaction between the beam and the material; therefore surfaces are required to be free from corrosion and machined with the required roughness.

.

The treatment procedure is very important, the cathode condition and vacuum quality also need to be carefully assessed. During the treatment, gases are released and this may affect the beam. Electron beam machines have particular individual characteristics that are related to the electron beam gun setup or behaviour; therefore it is advisable that important technological electron beam processes are developed and completed from the same or a similar machine, Table 4.1.

In order to achieve the desired structure, it is important that treatment parameters as beam power, voltage, focus, speed and distance from the workpiece are set and maintained throughout the process. Oscillations of such parameters can affect the process and need to be avoided.

Table 4.1: Factors that affect the electron beam product quality.

Factors affecting electron beam treatment product quality				
Material Quality	**Material dimensions**	**Surface conditions**	**Treatment procedure**	**Treatment parameters**
Grade	Thickness variation	Surface contamination	Gun/cathode conditions	Beam power
Microstructure regularity	Eccentricity	Surface corrosion	Vacuum quality	Accelerating voltage
Residual material flaws	Surface finish	Surface finish	Background gas	Focus
Tensile strength	Geometric variations		Machine selection	Workpiece distance
Fatigue			Human element	Speed
Hardness				Oscillations
Corrosion				
Impact toughness				
Fracture toughness				

4.5.1 Potential benefits of surface treatment for heat transfer applications

The electron beam process is rapid and covers 10 cm^2 in approximately 20 to 30 seconds. The computer numerically controlled bed allows process control and batch production. In this study, the electron beam process uses a single beam gun; however multi-beam processes are currently available to increase the production efficiency and complexity of the treatment.

The Surfi-Sculpt™ treatment significantly improves the heat transfer surface area. The process is automatically controlled and can be manipulated to generate a range of treatments that are not possible with any other technique. The base surface and the surface around the protrusions are irregular due to the material displacement. This creates perfect conditions for heat transfer improvement since it interrupts the boundary layer formation and reduces thermal resistance. Moreover, by manipulating the design; it is possible to control the fluid flow characteristics over the surface. Figure 4.6 shows the capability of the process, i.e. fin-like features which may be used to separate the flow, improve the turbulence, disturb the boundary layer formation and promote turbulence.

The electron beam process can be used to drill cavities in the surface of the material, Figure 4.7. Cavities in the surface have shown to passively provide effective heat transfer enhancement (Thome, 1990) and (Webb, 1993).

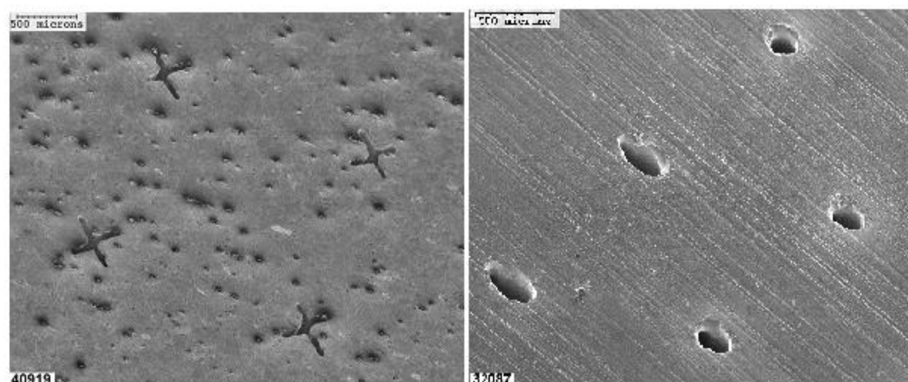

Figure 4.7. Electron beam treatments holes with size 500µm, microscopy image.

The technology has proven to work well in a range of conductive materials (Buxton, et al., 2009). Enhancements for heat sink applications on both aluminium and copper have proven successful. The surface treatments, that can be manufactured, are vast and can be tailored for individual applications. It is possible to customise treatments, i.e. the structure, height or thickness, and spacing between protrusions can be altered to achieve desired densities, leading to preferential cooling.

However, the electron beam process has its limitations that are related to the initial costs of the equipment, operation and maintenance. A desired surface treatment requires development and optimization before it is ready for an application. These activities require specialised work force and can increase development costs. The electron beam technique is applicable to a range of materials and can be used for a range of surface treatments and is particularly precise joining[1] processes. Though capital costs are high the process is rapid and if it is automated can increase production and become extremely competitive. The main considerations are the initial cost, whether the technology is viable for a given process and overhead costs.

4.6 CURRENT ELECTRON BEAM TREATMENT

The enhancement of heat transfer from pin fin structures is a widely used technique in engineering applications, see Chapter 3. The technique is applied in liquid cooling applications to enhance the heat transfer characteristics of the liquid cooled plates. The current available enhancement structures in the market are mainly regular shapes such as cylindrical, rectangular, diamond and elliptical. The electron beam treatment is effective in generating irregular protrusions that can’t be manufactured with current conventional techniques. The irregularity in the base surface and over the treatment creates conditions for better heat transfer performance.

[1] Welding

The pin-fin like electron beam treatments was firstly developed by TWI for material joining processes. However, in 1990s the development group of electron beam section at TWI pursued the application for heat transfer enhancement. The initial surface treatments were developed by using an adapted electron beam welding machine. Today the electron beam surface treatment systems are fitted with developed magnetic focus coils and a wider deflection capability, Figure 4.8. Improvements are also made to the beam visualisation, monitoring equipment, and various other adjustments. Figure 4.8 shows the electron beam surface treatment system used to generate current test samples for heat transfer enhancement.

4.6.1 Description of the process

The electron beam is guided by an advanced electronic system. This provides the required voltage on both, focusing and deflection coils to accurately control the beam movement. The electron beam treatment is developed by following a number of steps that are described below.

According to Figure 4.8 the first step is the conceptual design process. 3D-CAD software is used to generate the model. The second step transfers the conceptual 3D-model into the pattern generator software, where it is translated into an electrical signal. In the third step, the signal is fed into an arbitrary function generator that produces required voltage for each deflection coil. Finally, the voltage from the arbitrary function generator is amplified and transferred to the appropriate coil.

TWI’s 130 kW ‘HS2’ EB welding machine integrated with the beam deflection system was used for the development of patterns for this study. The electron beam welding machine operates at a maximum operating voltage of 60 kV. The beam power required for current treatments was of the order of 800W. The beam deflection equipment and pattern development software are of TWI’s own design. The deflection system allows for up to four axes of movement of the beam on two discrete Cartesian coordinate systems;

1. The X and Y high inductance coils, Figure 4.8.

2. The U and V low inductance coils, Figure 4.8.

The high inductance coils enable the beam to be moved slowly over large distances to create an array, and the low inductance coils allow the beam to be moved quickly over small distances to create the motif, Figure 4.8.

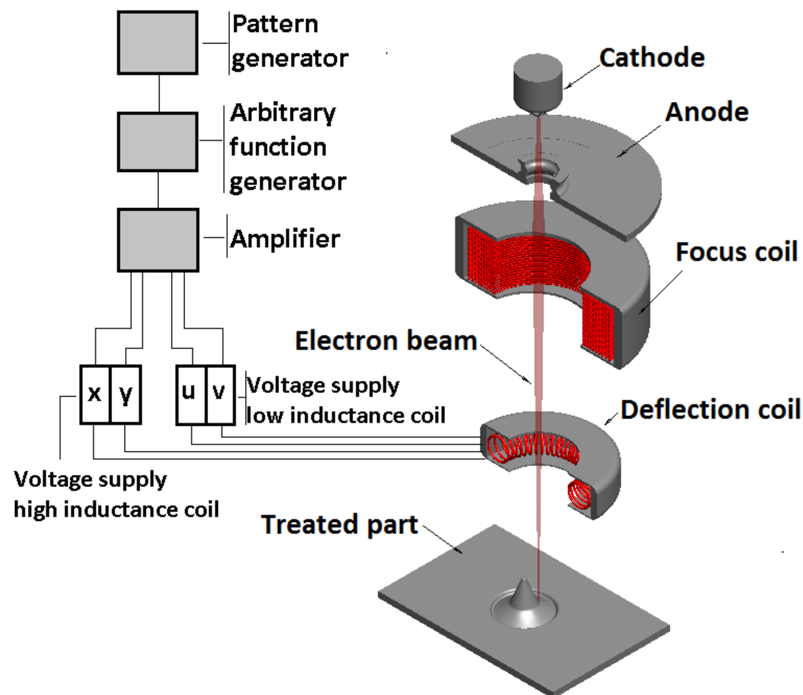

Figure 4.8: Electron beam treatment process control diagram.

4.6.2 Conceptual design

The conceptual design of the electron beam treatment is a complex problem, because it requires careful consideration of the material displacement. From the literature review, has been identified that the pin-fin in a staggered configuration provides higher heat transfer rates compared to the in-line configuration. Therefore, attempts have been made to design patterns (arrays) that are similar to the staggered configuration. The treatment density and the height are related to the design of the protrusion and pattern. For example, dense patterns will allow low protrusion heights because the material displaced is consumed largely to generate protrusions. While low-

density treatments can provide higher (longer) protrusions since more material will be available. The following part will describe the process used for each surface treatment from the model, pattern generator to the finished component.

4.6.2.1 Model for Sample S1

Figure 4.9 shows a 3D model of sample S1. In this case, the electron beam displaces the material from a given location to create a protrusion. Each protrusion is accompanied by its own cavity. The pattern is designed in such way that creates a staggered configuration. According to Figure 4.10 cavities, are set in the in-line configuration, but the displacement of material changes from one side to the other from one cavity to the next one. This way creates a staggered fin configuration Figure 4.9. The protrusion density is 13 per cm^2.

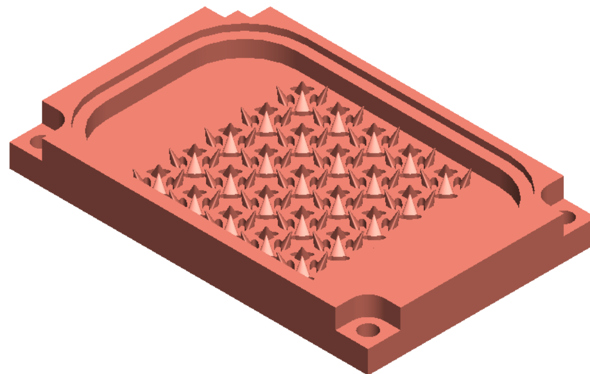

Figure 4.9: 3D model of Sample S1 generated with Solid-Works software.

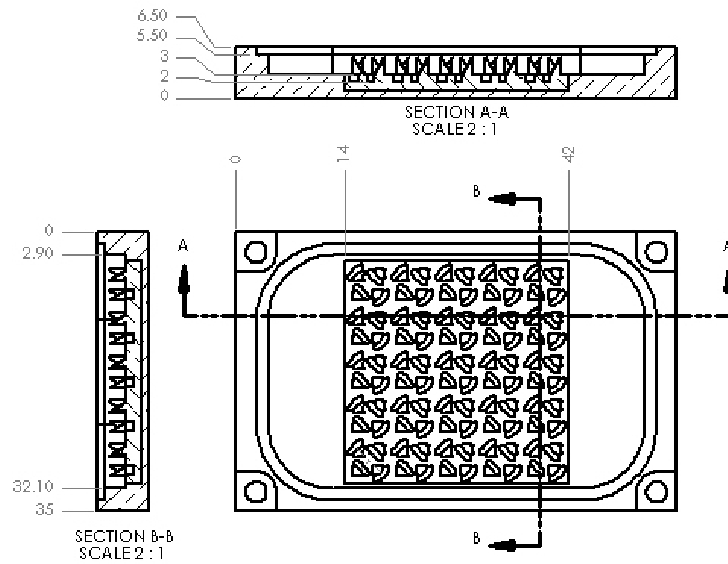

Figure 4.10: Drawing of Sample S1 from the 3D-model, generated by Solid-Works software.

4.6.2.2 Model for Sample S2

The model for sample S2 is shown in Figure 4.11. The pattern is designed in a staggered configuration, Figure 4.12. Material is moved from the surrounding area to create a protrusion. The protrusion density is 11 per cm^2.

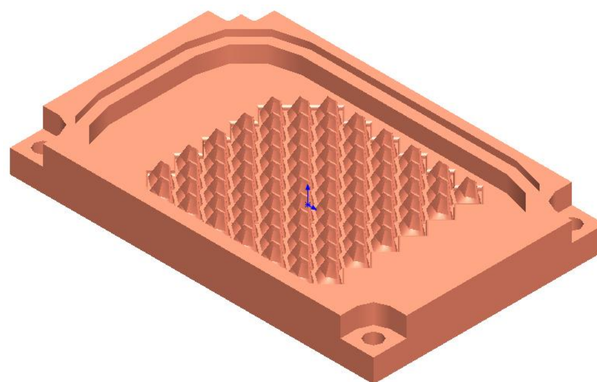

Figure 4.11: 3D model of Sample S2 generated with Solid-Works software.

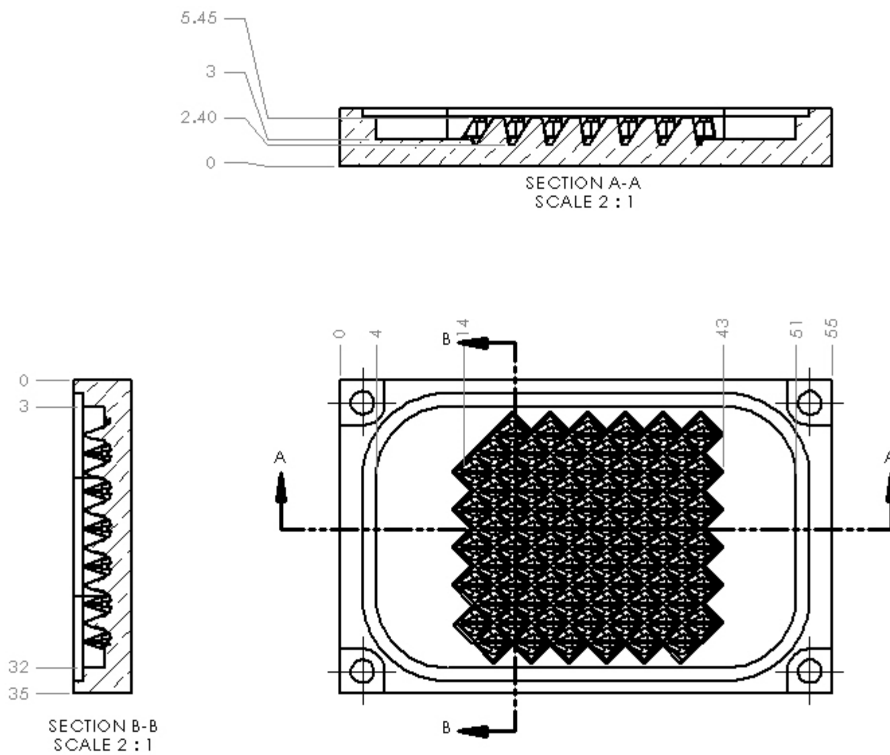

Figure 4.12: Drawing of Sample S2 from the 3D-model, generated by Solid-Works software.

4.6.2.3 Model for Sample S3

Figure 4.13 shows the model for sample S3. The pattern is designed in a staggered configuration. The material for the construction is dragged from two opposite directions to create a protrusion, Figure 4.14.

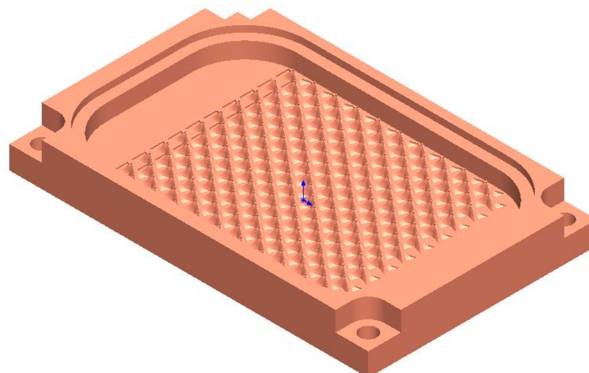

Figure 4.13: 3D model of Sample S3 generated with Solid-Works software.

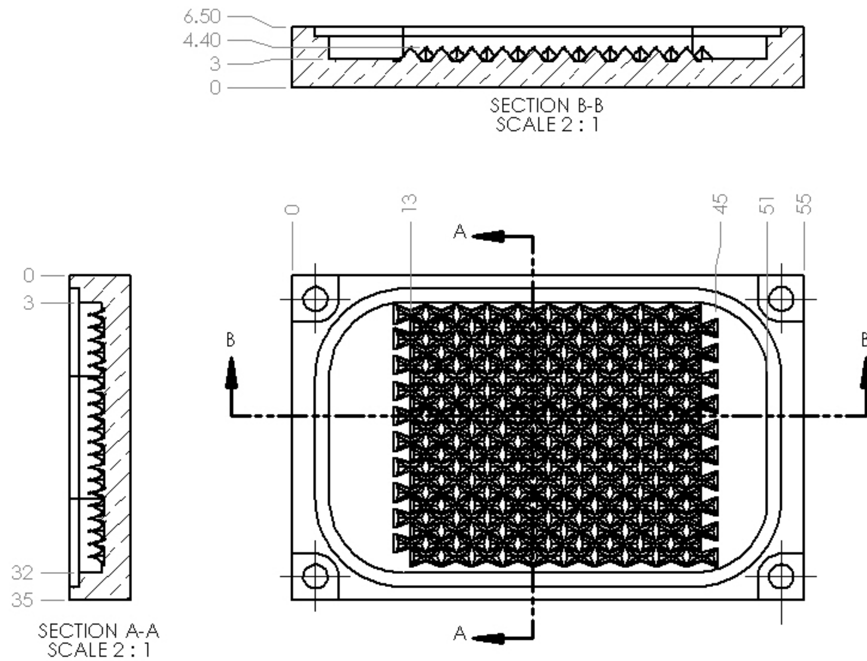

Figure 4.14: Drawing of Sample S3 from the 3D-model, generated by Solid-Works software.

4.6.2.4 Process strategy

The fundamental working principle is to displace material in the liquid phase to build up protrusions from the base material. The power required to liquefy the material and the displacement activities are generated by a defined electron beam.

The process is made possible by moving the electron beam at high speed in a complex route of 'swipes' over the work-piece surface. This is accomplished via a programmable pattern generator that excites the beam deflection system. In this study, the treatment was carried out in discrete 'patches'. Each 'patch' takes approximately 20 seconds to be complete and involves multiple steps, (Buxton, et al., 2009).

The process repeats a simple 'motif' of n_2 elements at several positions defined in an 'array' of n_1 elements, while f is the frequency or number of repeats. Figure 4.16, Figure 4.17 and Figure 4.18 shows the array and motif concept design for sample S1, S2 and S3 respectively.

The exact cycle and path of electron beam activity has a profound effect on the treatment process outcome as shown below. The use of separate X-Y and U-V deflection allows increased pattern complexity as well as the best control and optimisation of the process strategy.

Figure 4.15 shows the basic concept of electron beam treatment. The same principle is used to construct each pattern, though the beam path has been composed to achieve the desired outcome (protrusion). The material is displaced in the opposite direction of the beam movement. For that reason, the same pattern in reverse will either build spikes or make holes.

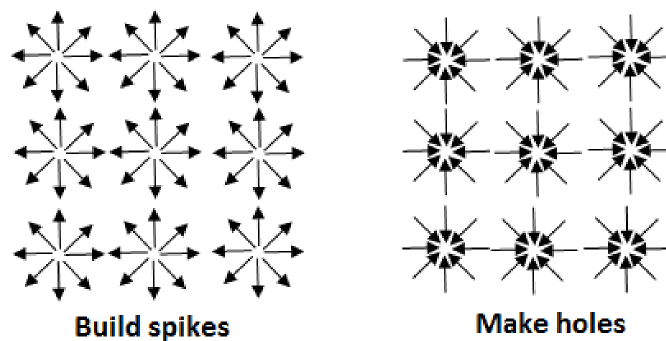

Figure 4.15: Diagram of electron beam movement required to build spikes and holes.

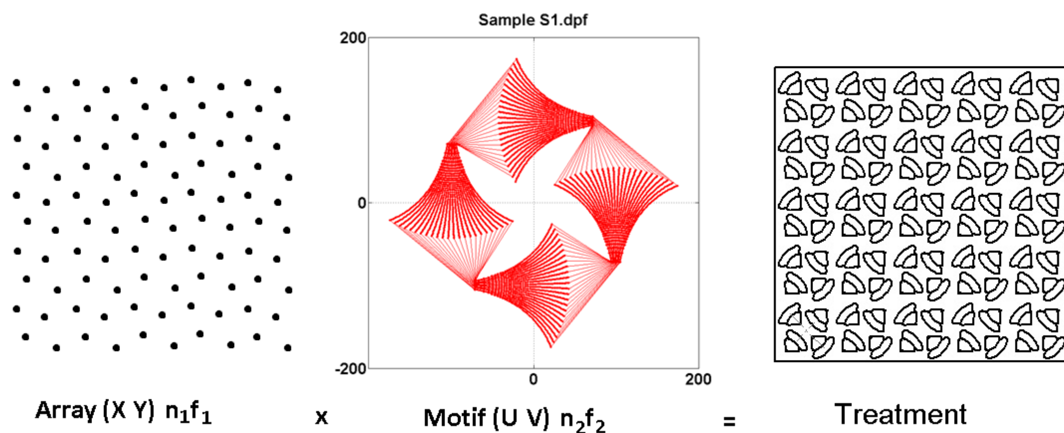

Figure 4.16: Electron beam treatment process path for sample S1.

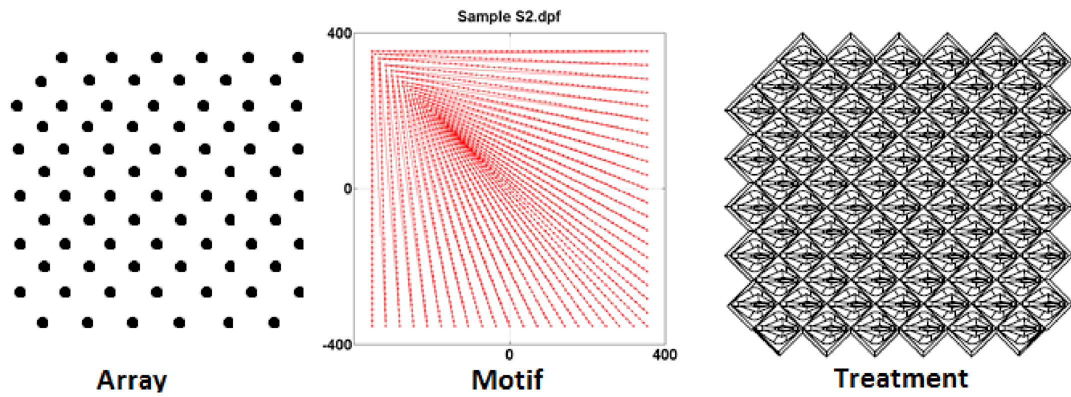

Figure 4.17: Electron beam treatment process, sample S2.

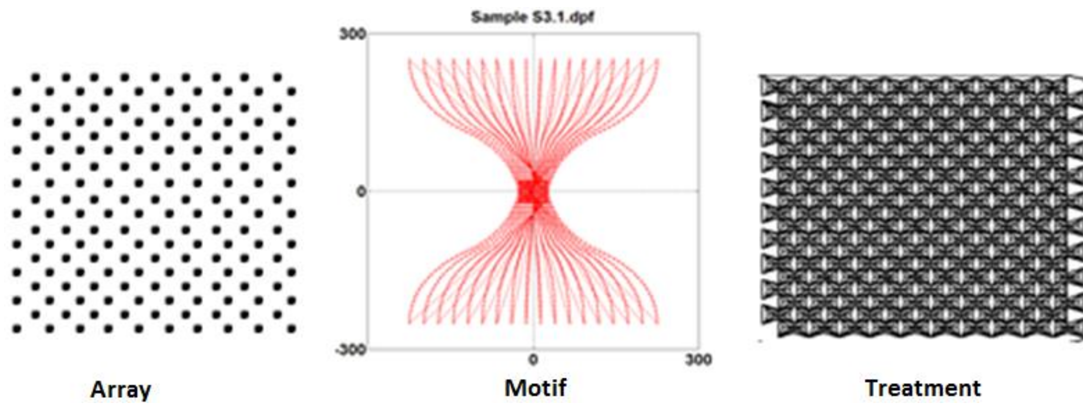

Figure 4.18: Electron beam treatment process, sample S3.

4.6.2.5 Pattern diagram and electron beam swipe path

The electron beam movement direction and path determine the protrusion's geometry. Figure 4.19, Figure 4.20 and Figure 4.21 shows the motif for each relevant pattern. Electron beam sequences change from one protrusion to the other to maintain even heat distribution over the surface.

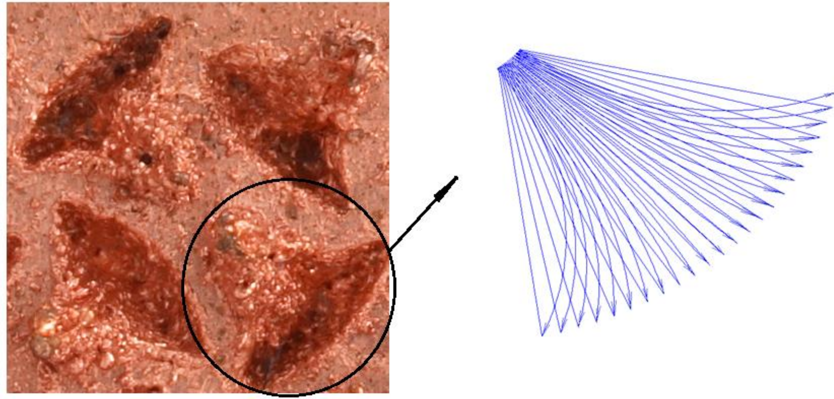

Figure 4.19: Electron beam swipe path for sample S1.

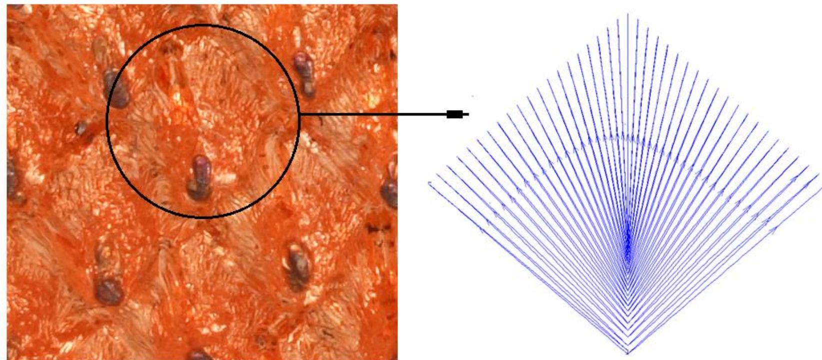

Figure 4.20: Electron beam swipe path for sample S2.

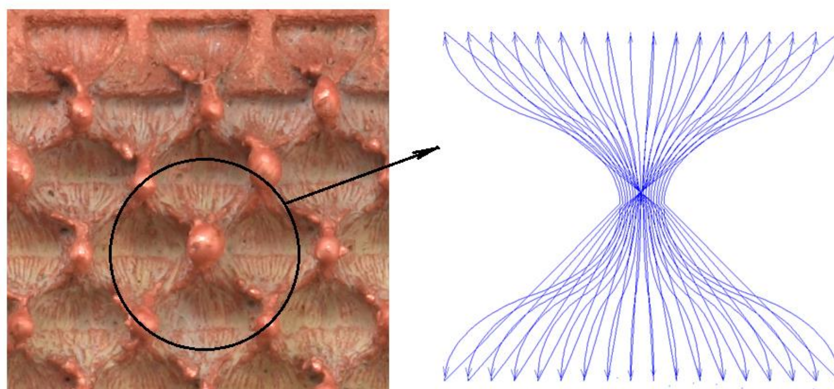

Figure 4.21: Electron beam swipe path for sample S3.

4.6.2.6 Manufacture of the test samples

Three conceptual treatments have been designed to improve the single phase heat transfer. The treatment is applied to a liquid cooled plate made of copper plates (55 mm x 35 mm), while treated area is approximately (32 mm x 28 mm), Figure 4.22. The treatment parameters have been developed for copper Cu 101 and aluminium Al 7075. Copper samples given in Figure 4.22 will be used for thermo-hydraulic experimental investigation.

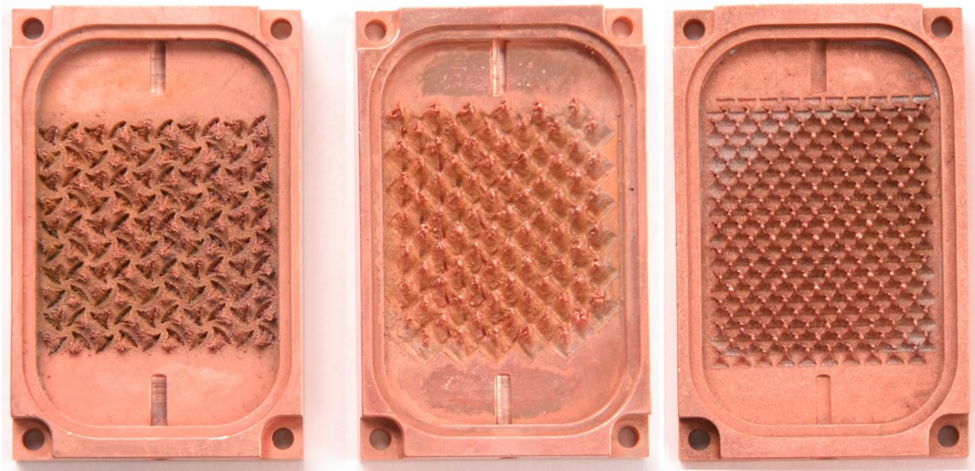

Figure 4.22: Sample 1 (left), Sample 2 (centre) and Sample 3 (right), each (35 mm x 55 mm).

4.6.2.7 Sample S1

The first sample has been designed as flower pattern, see Figure 4.23. The protrusion is constructed as a three faces pyramidal structure and is made by drawing material from nearby, see Figure 4.23. At first sight protrusions are constructed by many micro-layers (effect of beam swiping) that rise together to build the body of the protrusion, they all join in the culminating point of the pyramid. Near each fin is a small cavity, from which the material is drawn to build the fin. The internal cavity surface is irregular and made of many irregular micro-channels (the effect of the electron beam material drawing). From a very close look swipes create smooth rounded surfaces on each swipe path (effect of surface tension during solidification of melted material).

Protrusions also have an irregular disordered surface. Overall the outside surface of the structure is rough and there are many levels and micro-cavities through the micro-structure, see Figure 4.24.

Figure 4.23: View of the treatment pattern (4.3 x 4.1) mm^2, for Sample S1

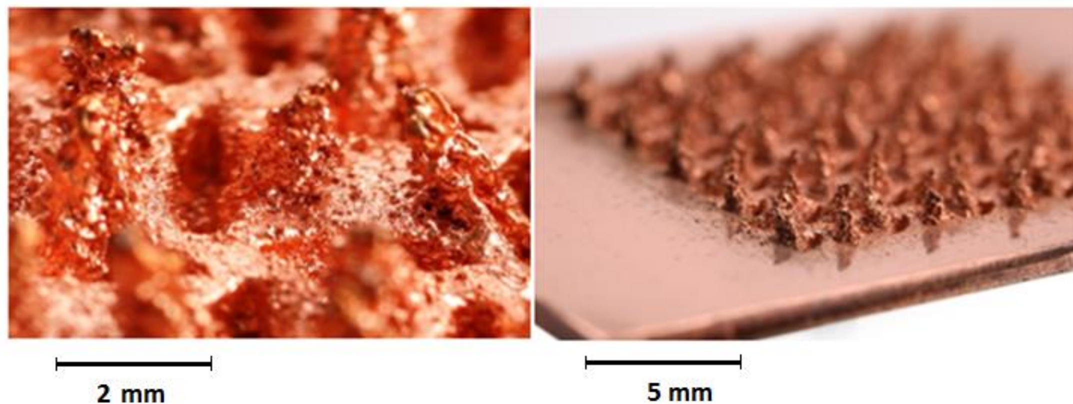

Figure 4.24: Close pictures of Sample 1

4.6.2.8 Sample S2

The surface of sample 2 consists of an array of sloping protrusions as shown in Figure 4.25. Each feature is grown from a rhombus base, with the material drawn from the surrounding area. The upper view is shown in Figure 4.26. Since the material is drawn from a wider area in comparison to the other treatments, the size of the protrusions is wider and higher. The protrusion is grown in a pyramidal shape, with an irregular surface around. The base area due to the effect of material draw, is also irregular. The protrusions are set in a staggered configuration.

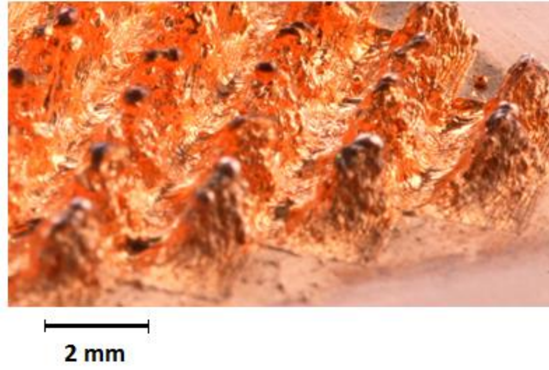

Figure 4.25: Sample 2 protrusion.

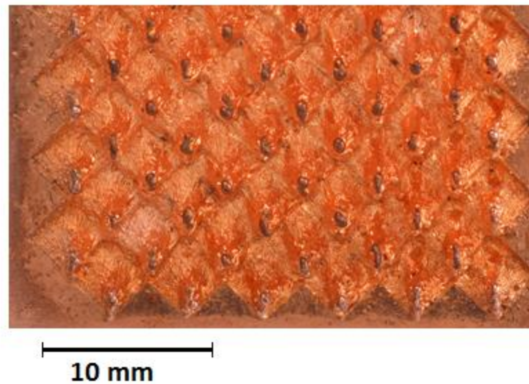

Figure 4.26: Sample 2, upper view of the treatment.

4.6.2.9 Sample S3

Sample 3 is designed with a fin density higher than the two above constructions. The structure is designed as an hourglass pattern, see Figure 4.27. The base surface has a variable grooved relief as a result of material taken to build the fin structure. The material is drawn from two opposite directions to build a single fin. The fins have an irregular all-around surface, see Figure 4.28. From a thermal prospect, the treatment is very dense, thus can increase the heat transfer area considerably. Enhancement also can improve fluid mixing and disruption of boundary layers.

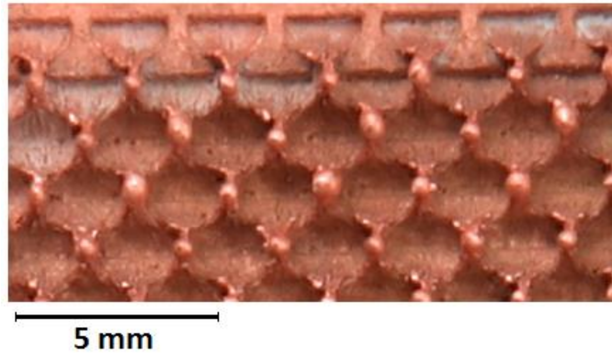

Figure 4.27: Sample 3 upper view.

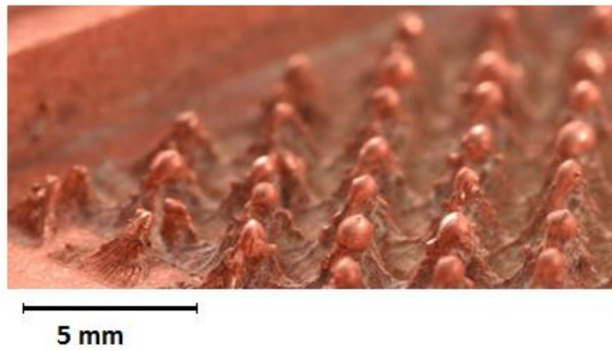

Figure 4.28: Sample 3, close view of protrusions.

4.6.3 Summary

The electron beam treatment is an advanced technological process, which can be used for a range of engineering applications. This study presents the development of the electron beam treatments for heat transfer enhancement applications. The electron beam process transfers great quantities of energy when in contact with the work-piece, therefore, requires rapid deflection and accurate control over the beam. The design process starts with a conceptual model that is carefully created based on the treatment pattern and protrusion geometry. Pattern generator software is used to model a motif that can reproduce the protrusion by moving the electron beam in a controlled manner. Data is fed to the deflection coils through an arbitrary function generator that controls x-y and u-v beam movement. By utilizing this methodology, three treatments with variable density and protrusion height

have been developed. The treatment parameters have been optimized and presented in Table 4.2.

.

Table 4.2 Electron beam treatment parameters for sample S1, S2 and S3 in copper Cu 101 and aluminium Al 7075.

Electron Beam Treatment for 60kV Machine.														
Treatment record sheet														
	Main Electron Beam Settings						**Beam deflection**						**Material**	
Sample	**Potential difference**	**Current**	**Filament**	**Time duration**	**Focus**	**Work distance**	**Amplitude**	**Amplitude**	**Frequency**	**Amplitude**	**Amplitude**	**Frequency**	**Pattern**	**Mat. No**	**Thickness**
	kV	mA	V	sec	mA	mm	x	y	xy	u	v	uv			mm
Sample S1	60	14	7.2	20	385.5	300	14	14	2	27	27	3.13	S1	Cu 101	3
Sample S2	60	14	6.9	20	380.5	300	18	18	2	12.5	11.5	20.24	S2	Cu 101	3
Sample S3	60	12	6.9	20	384.5	300	23	23	0.1	25	9	18	S3	Cu 101	3
Sample S1	60	5	6.8	20	380.5	300	14	14	2	27	27	3.13	S1	Al 7075	3
Sample S2	60	5	6.8	20	380.5	300	15	16	2	9.5	9.5	20.24	S2	Al 7075	3
Sample S3	60	5	6.8	20	380.5	300	23	23	0.1	25	9	18	S3	Al 7075	3

5 CFD STUDY FOR THE SMOOTH SAMPLE

The aim of this chapter is to provide the base data for the performance evaluation of the smooth sample and to compare those to the experimental work and available correlations. Computational Fluid Dynamics (CFD) is an analytical software for fluid flow and heat transfer engineering systems. The software uses numerical methods to solve and examine fluid flow and thermal problems. Initially CFD was used by the aerospace industry, but today CFD analysis cut across all disciplines where there is a need for fluid flow and heat transfer analysis. The CFD is a powerful tool to examine and understand the complexity of hydraulic and thermal processes. The outcome of the technique varies with the computer processing power, input data, simplifications and assumptions made. Accurate predictions are dependent on the input data and solving equations. In this chapter, an AutoDesk CFD 2013 software has been used to evaluate temperature distribution, pressure loss, and flow velocity throughout the test section. The model is geometrically similar to the original test sample. Boundary conditions approximate the operating conditions. The default automatic meshing was used to achieve a fine continuous mesh transfer from solid to the fluid parts. Results are presented visually and graphically and are discussed for each mass flow rate.

The aim of this chapter is to investigate temperature distribution and the pressure drop on a smooth sample, and discuss the flow field from inlet to outlet. The CFD data will be compared to the experimental results and the available data from the correlations, to confirm the experimental procedure.

Objectives:

i. To observe fluid flow pattern over a smooth surface sample
ii. To observe the temperature distribution in the solid and in the flow

iii. To observe the velocity and pressure distribution through the flow path

5.1 GEOMETRY

The test module is composed of five parts: a) copper heater block, b) copper test part and c) polycarbonate insulation cover, d) silver interface with thickness 0.08 mm and conductivity 371 W/mK between the test part and the heater block, and e) four cartridge heaters. In order to avoid the gap and reduce thermal resistance, between cartridge heaters, is placed an interface material with conductivity 5 W/mK. The size of the heater block is (WxLxH) (28x32x100) mm^3 Figure 5.1. Four cartridge heaters with dimensions 10 mm diameter and 60 mm long are accommodated at the bottom part of the heater block, Figure 5.2. Cartridges are placed in equalized distances from each-other and the walls. The input heat from cartridge heaters is conducted into the heater block, where a 40 mm distance from the top of the cartridges equalizes the temperature distribution through the heater block to the test sample, Figure 5.2. The test sample (WxL) (35x55) mm^2 is brazed in the upper side of the heater block where the flow of deionized water passes through. The flow path is enclosed by a transparent polycarbonate cover. Inlet and outlet holes with 6 mm diameter are drilled on both sides as shown in the Figure 5.3. From the inlet, fluid enters to a premixing chamber that equalizes the flow entering the channel, Figure 5.3. Flow passing through the channel at the outlet is collected in a chamber where it leaves the outlet pipe. A full transparent view of the test module under operating conditions is shown in Figure 5.2.

The temperature and pressure measurements are examined at the inlet and outlet of the heated area (32x28) mm^2 that is equal to that of the heater block attached to it. In the heat transfer calculations, the side walls with height 2.5

mm are also included in the heat transfer area. Figure 5.3 shows frontal and side cut views of the test sample.

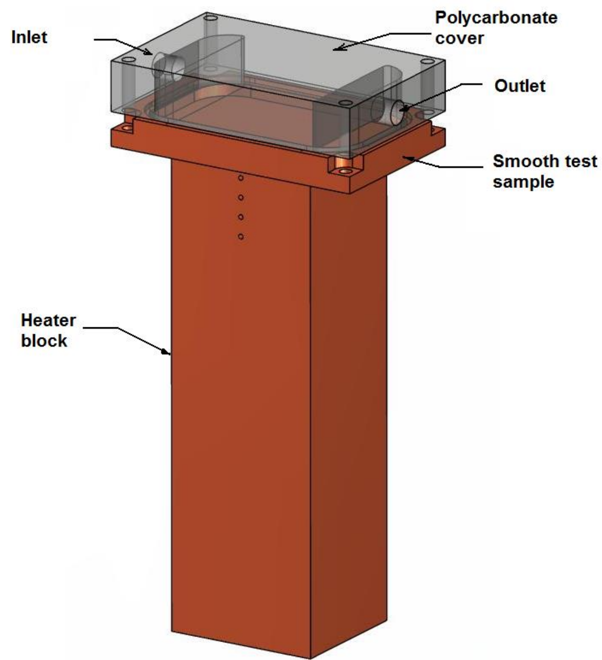

Figure 5.1: View of the test module.

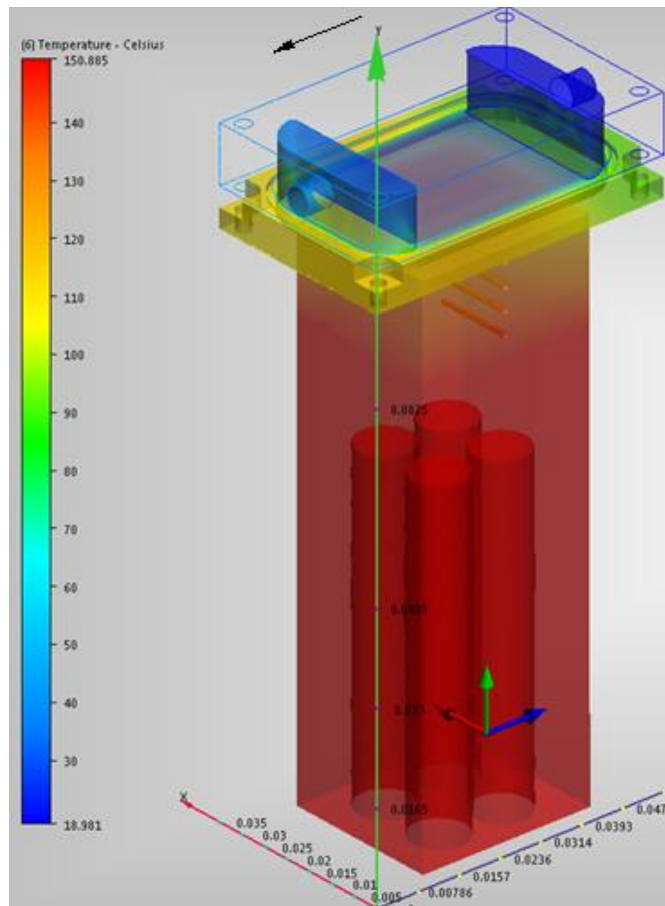

Figure 5.2: Axonometric transparent view of heated test module.

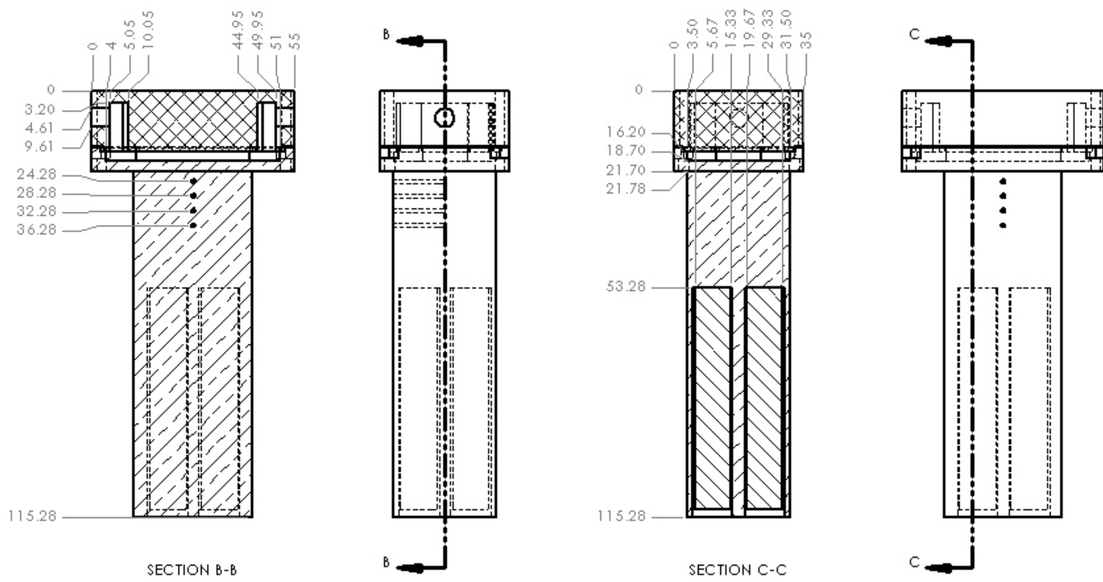

Figure 5.3: Frontal cut and side cut views of the test module

5.2 MODEL

The governing equations automatically define the method of solving. The default flow and temperature based solver, implicit formulation, steady state conditions and mass flow rate formulation were used. The physical model, energy equation and material specifications were set active. The operating condition flow rate, inlet temperature, power input, and boundary conditions, ambient temperature, and pressure at outlet were also defined.

5.2.1 Boundary conditions

The fluid flow is internal since it is surrounded by a surface and the fluid is in-viscid (viscous forces are very small in relation to the pressure drop). Fluid is also incompressible (variation of density in the flow path is neglected). The flow regime is evaluated from the CFD, in accordance with the flow geometry, velocity, and fluid properties, via the Reynolds number $Re=\rho VD_h/\mu$, where the hydraulic diameter is $D_h=4A_c/P$. Flow is steady (there is no change with the time) and analyses are performed for water flows in four steps, starting from 0.01 kg/s to 0.04 kg/s. The inlet temperature is set at 19 ^oC. The heat input 600 W remained constant for all mass flow rates. The outlet pressure equals atmospheric pressure. Since the sample has been well insulated to simplify the model the radiation to the ambient was neglected. Ambient temperature was controlled and set at 20 ^oC.

5.2.1.1 Heat transfer coefficient

The heat transfer coefficient h and Nusselt number Nu were calculated from the CFD data as:

$$h = \frac{mc_p(T_e - T_i)}{A_s \Delta T_{f-s}} \tag{5.1}$$

$$Nu = \frac{hD_h}{k_f} \tag{5.2}$$

where, Ti is the temperature at the inlet, Te is the temperature at the exit, Tf-s is the difference between the average bulk temperature of the fluid and the average temperature of the surface, As is the heat transfer area between including side walls, and kf is the fluid conductivity.

5.3 MESH DEPENDENCY

The default automatic mesh generation function is set active to simplify the process and ensures a smooth mesh transition between parts (simplifying the mathematical model during the transition from solid to fluid zones). Automatic mesh on the model generates a denser mesh in the areas where the gradient is higher, Figure 5.4. The mesh data are presented in Table 5.1.

Table 5.1: Mesh information from the CFD.

	Nodes	Elements
Solid	116803	729899
Fluid	233216	859445
Total	350019	1589344

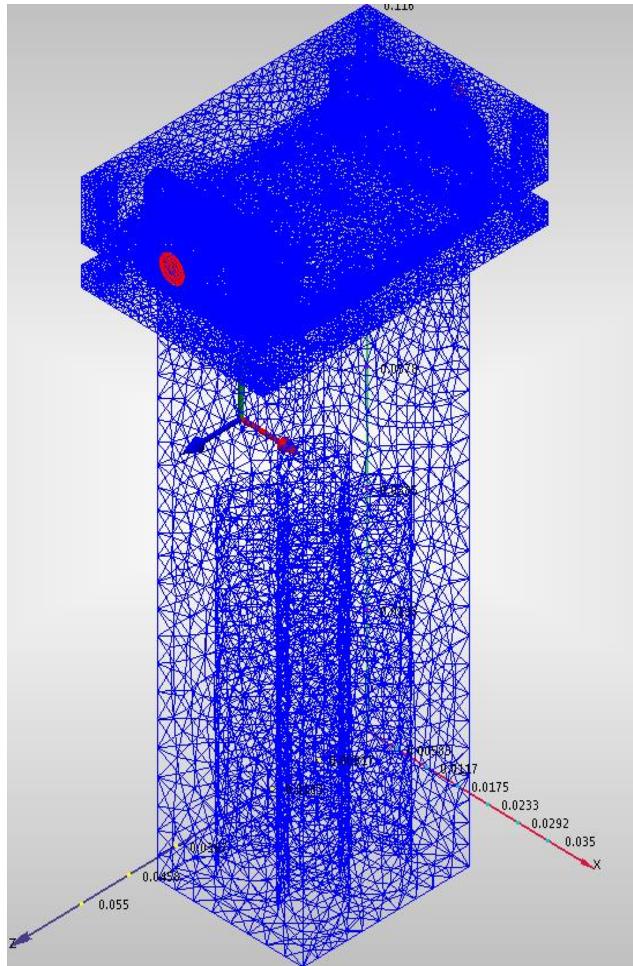

Figure 5.4: View of the grid on the test module.

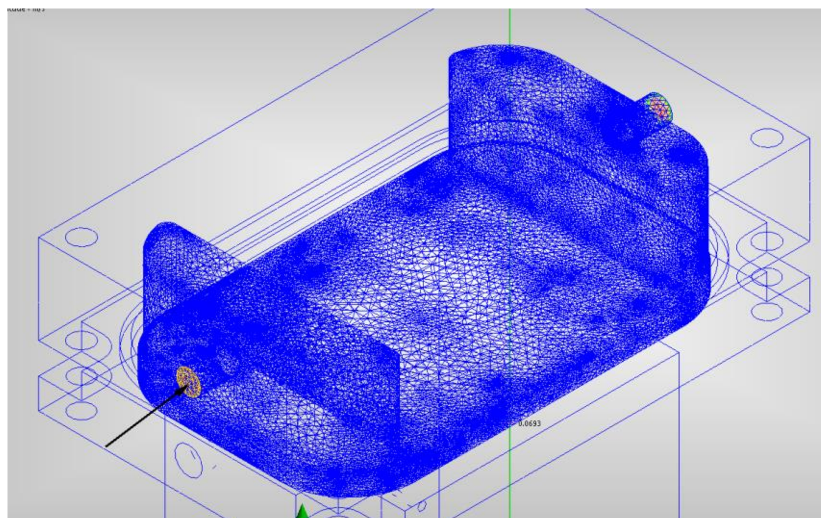

Figure 5.5: View of the mesh of the fluid domain.

5.4 SIMULATION PROCESS

The accuracy of the simulation process depends on several factors; numerical model, mesh quality and size. In addition, accuracy is also related to the accuracy of the input data, approximations, mesh transition, and mesh optimization. Simulation is set active for both flow and heat transfer. Turbulent model (Standard k-epsilon) is selected with static temperature equation and mix convection settings active.

5.5 POST PROCESSING AND RESULTS

The CFD results of temperature and pressure field are presented below for each mass flow rate. The data for temperature and pressure is given graphically. The measurements inside the flow channel are recorded as 2.5 mm inside the channel on both sides to avoid entrance and exit affects, Figure 5.3. In the following part, are discussed temperature and pressure profiles for each mass flow rate 0.01 kg/s to 0.04 kg/s.

5.5.1 Analysis for mass flow rate 0.01 kg/s

5.5.1.1 Heat transfer

The heat distribution through the test module for a mass flow rate of 0.01 kg/s is shown in Figure 5.6. The bottom part of the heater block experiences the highest temperature increase due to the heat input from cartridge heaters, Figure 5.7.

The temperature profile of the flow is presented in Figure 5.8. Fluid temperature rises in the flow direction. From the temperature profile, it is observed that side walls affect the temperature profile. The fluid temperature increases in the flow direction and is presented in Figure 5.9.

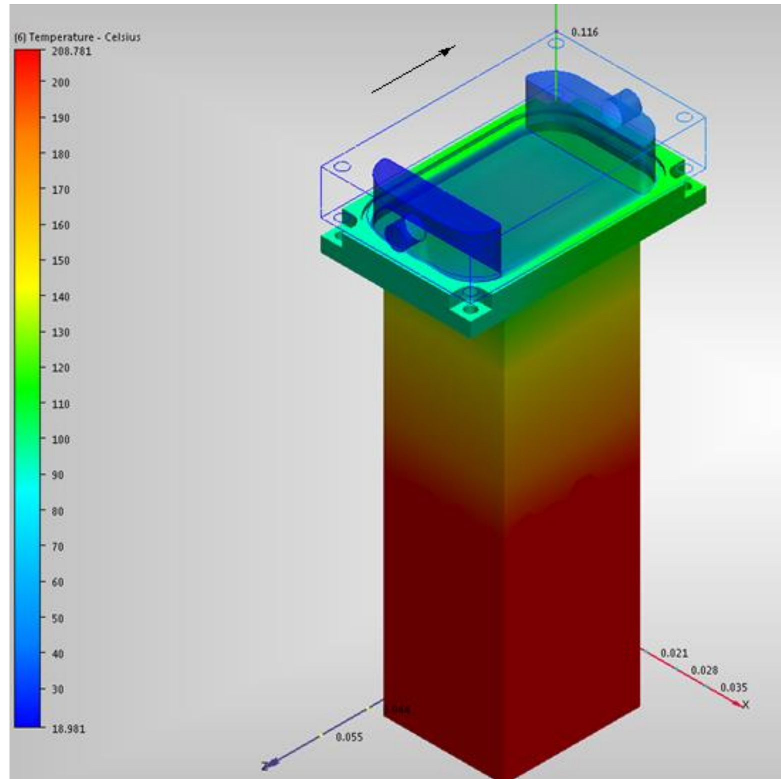

Figure 5.6: H. at distribution through the test module for m=0.01 kg/s.

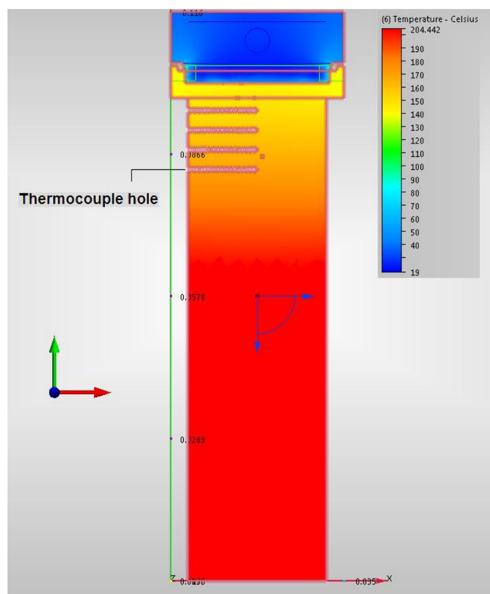

Figure 5.7: Temperature profile in the centre plane perpendicular to the flow, for m=0.01 kg/s.

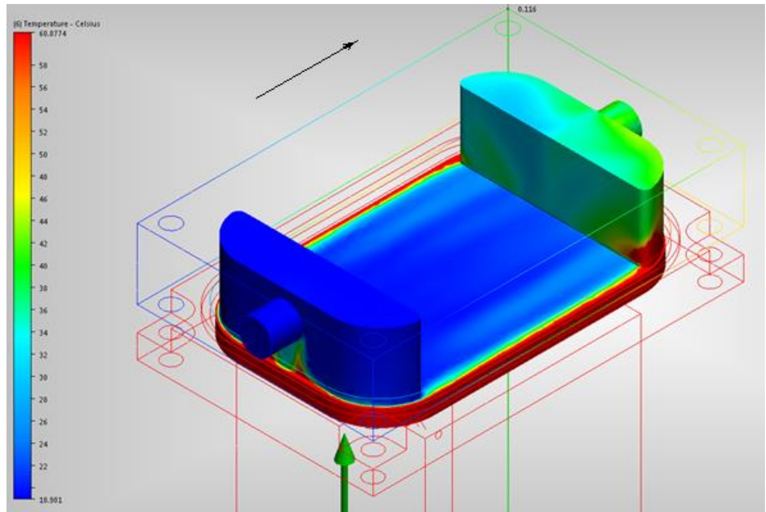

Figure 5.8: Temperature profile of the flow for m=0.01 kg/s.

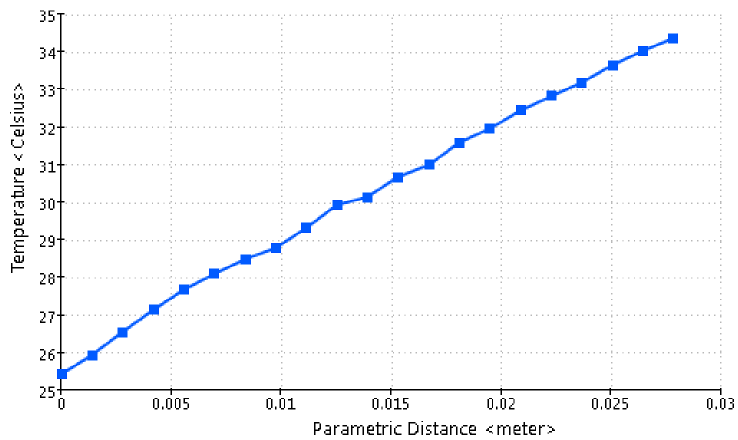

Figure 5.9: The fluid temperature increase in the channel for m=0.01 kg/s.

5.5.1.2 Pressure drop

Figure 5.10 shows the velocity profile of the flow, coloured by temperature. The inlet chamber equalizes the flow distribution into the smooth channel; however, there is a velocity variation at the inlet section of the channel (due to the effect of the entrance region), which is eliminated with progression of the flow.

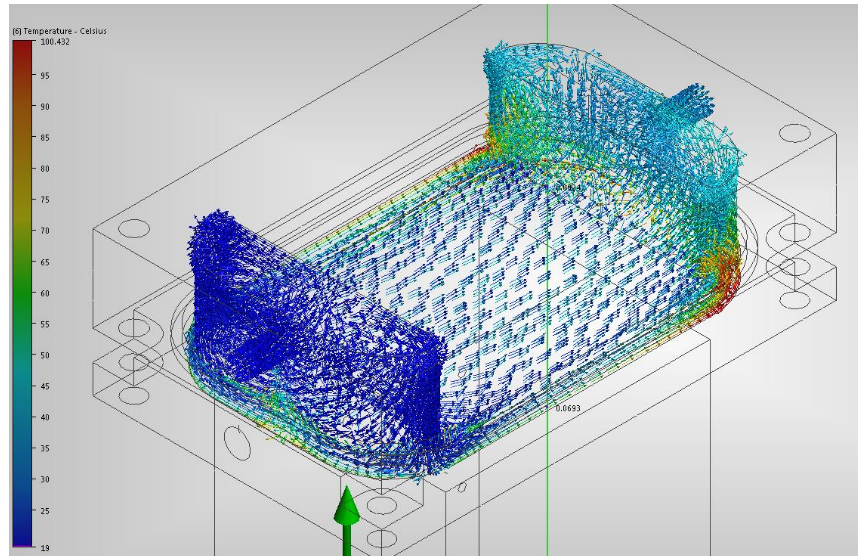

Figure 5.10: Velocity vectors coloured by temperature for m= 0.01 kg/s.

Figure 5.11 shows the velocity vectors in the centre plane that cuts across from the inlet to the outlet. Velocity is the function of the flow area and changes correspondingly. Velocity in the channel decreases slowly in the flow direction, due to energy loss to overcome friction.

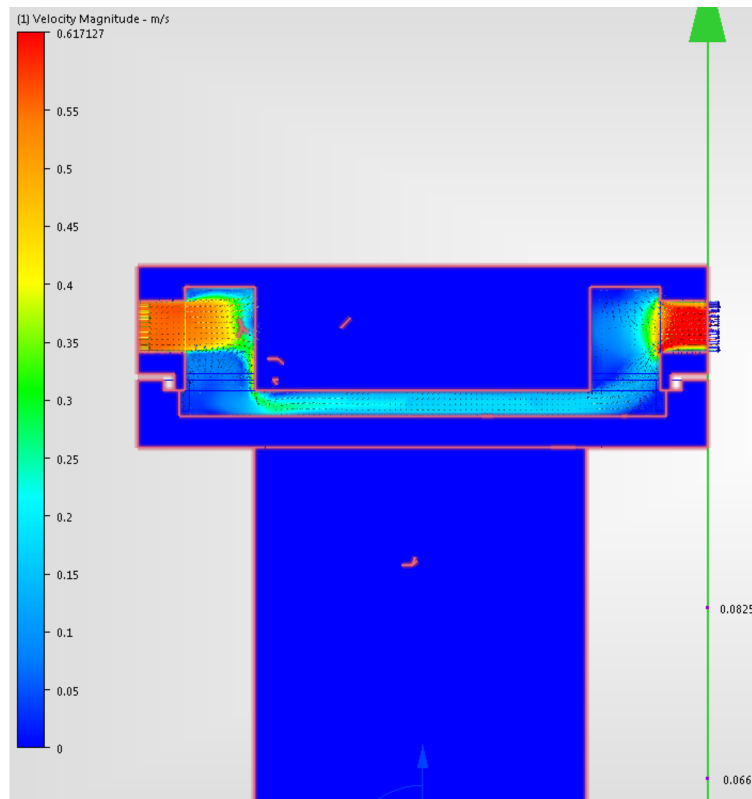

Figure 5.11: Centre plane velocity profile, m=0.01 kg/s.

Figure 5.12 presents the pressure profile through the test sample. At the inlet, premixing chamber pressure is high due to the conversion of kinetic energy (velocity) into potential energy (pressure). Pressure drop in the channel increases in the direction of the flow.

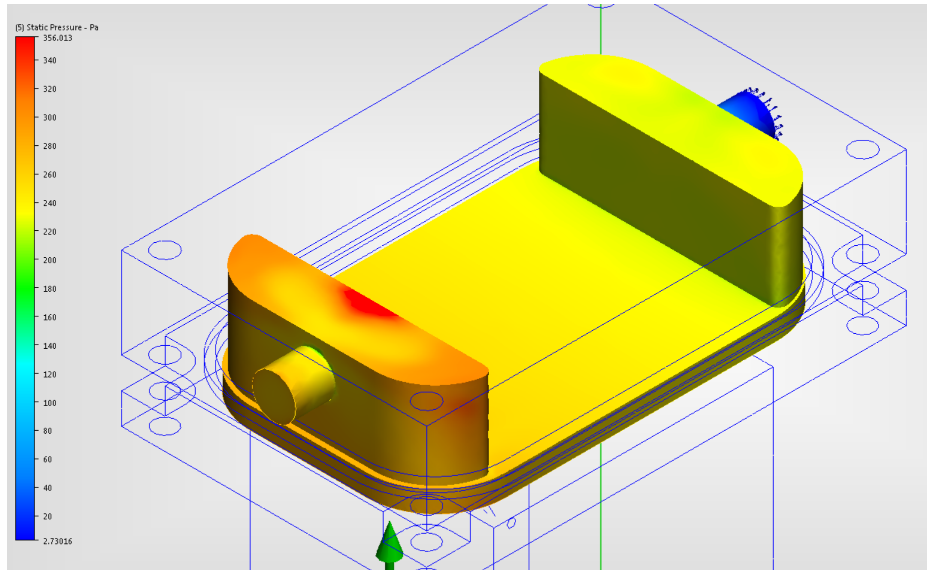

Figure 5.12: Pressure distribution of the flow for m=0.01kg/s.

Pressure drop in the channel is presented graphically in Figure 5.13. The pressure loss at the inlet section is affected by the entrance region. Because of the no-slip condition, the fluid layer in contact with the surface stops completely, affecting the nearby layer. Therefore, the pressure increases to overcome the friction. Pressure drops decrease gradually after the entrance region, Figure 5.13.

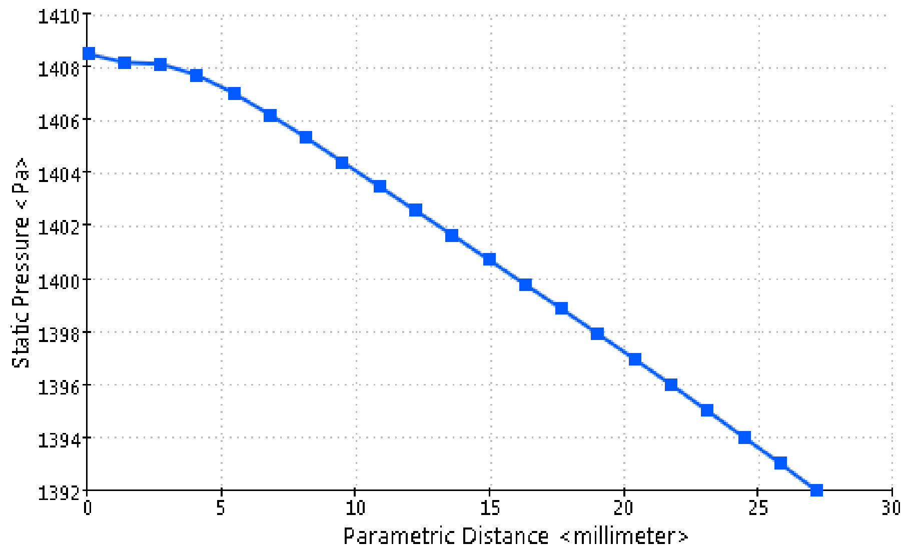

Figure 5.13: Pressure drop through the smooth channel, m=0.01 kg/s.

5.5.2 Analysis for mass flow rate 0.02 kg/s

5.5.2.1 Heat transfer

The fluid temperature rise in the channel is presented in Figure 5.14. According to the graph, temperature increases linearly in the direction of the flow. This indicates an equalized flow velocity profile through the channel.

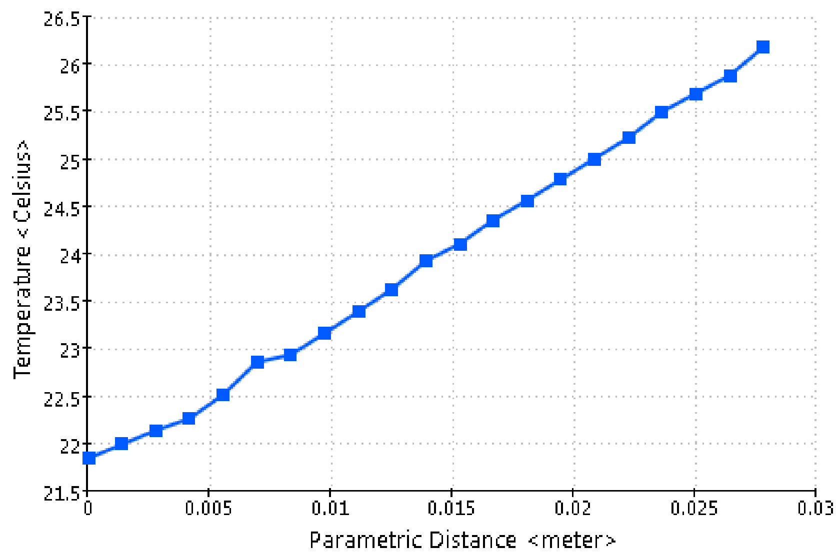

Figure 5.14: Fluid temperature rise in the channel for 0.02 kg/s fluid flow.

Figure 5.15 presents the surface temperature. It is observed that the temperature at inlet is lower. This is the effect of cold fluid entering the sample; however the temperature increases gradually in the flow direction.

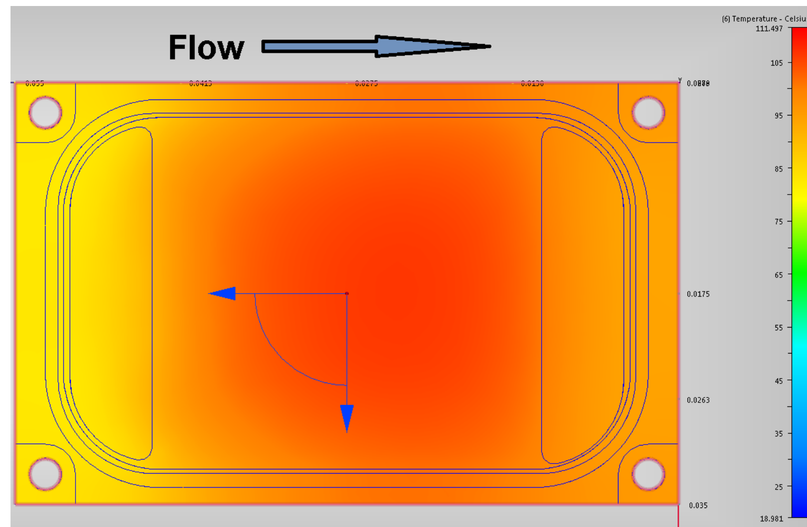

Figure 5.15: Heated surface temperature for mass flow rate 0.02 kg/s.

5.5.2.2 Pressure drop

The pressure in the channel, decreases in the flow direction, results for the pressure loss are shown in Figure 5.16.

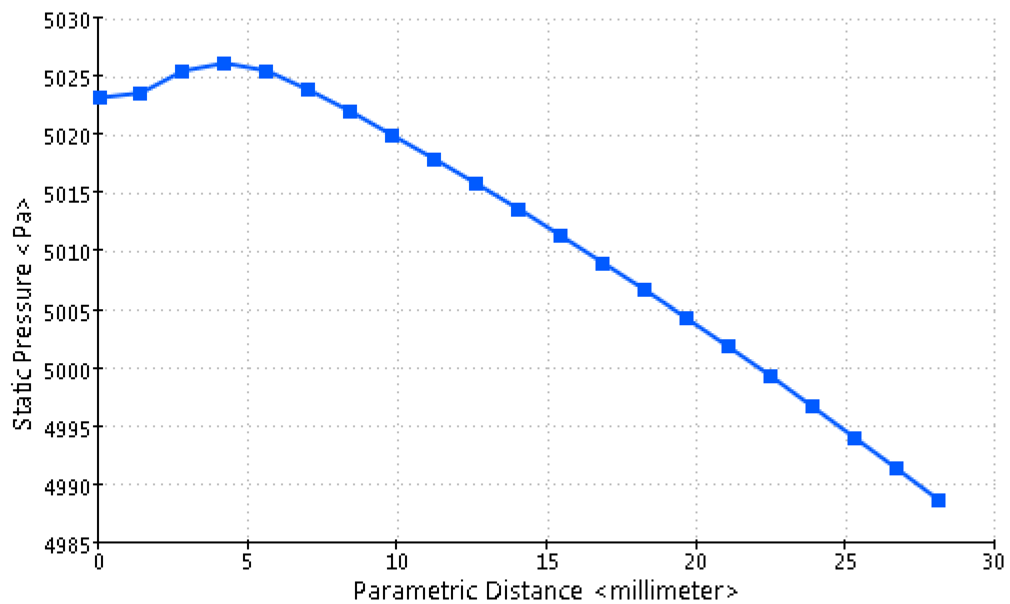

Figure 5.16: Pressure drop in the channel, for mass flow rate 0.02 kg/s.

5.5.3 Analysis for mass flow rate 0.03 kg/s

5.5.3.1 Heat transfer

Temperature distribution through the test module is shown in Figure 5.17. The temperature of the test module decreases with an increase of the mass flow. The temperature profile of the fluid part is presented in Figure 5.18. The flow is well distributed; however, it is obvious that the effect of the side wall heat input has on fluid flow, therefore, this must be taken into account during the evaluation of the heat transfer area. According to Figure 5.19, fluid temperature increases in the direction of the flow linearly. The entrance effects are negligible.

The heated surface temperature is presented in Figure 5.20. The surface temperature increases in the flow direction. The fluid flow at the inlet section provides cooling and maintains the surface temperature lower in this part.

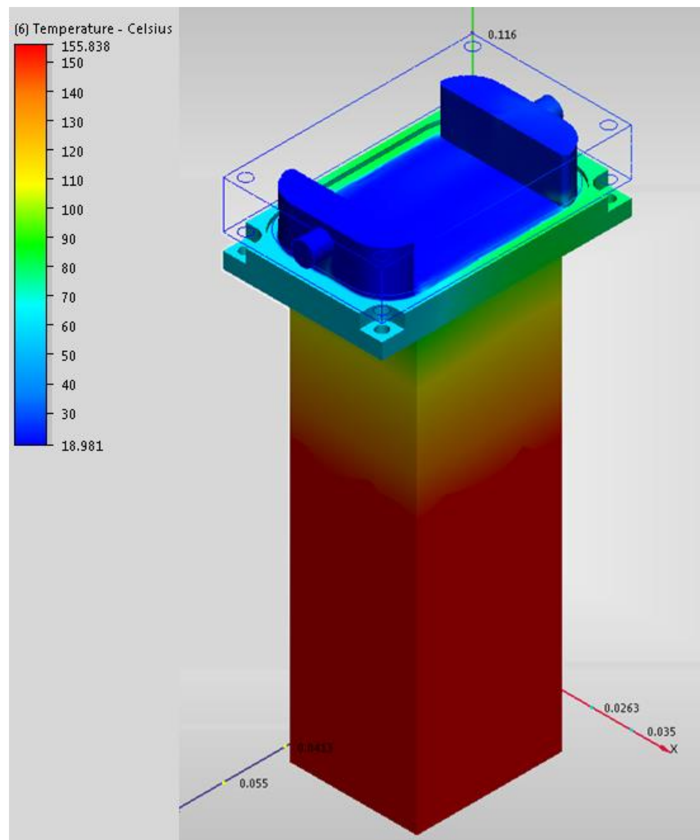

Figure 5.17: Heat distribution through the test module for mass flow rate 0.03 kg/s.

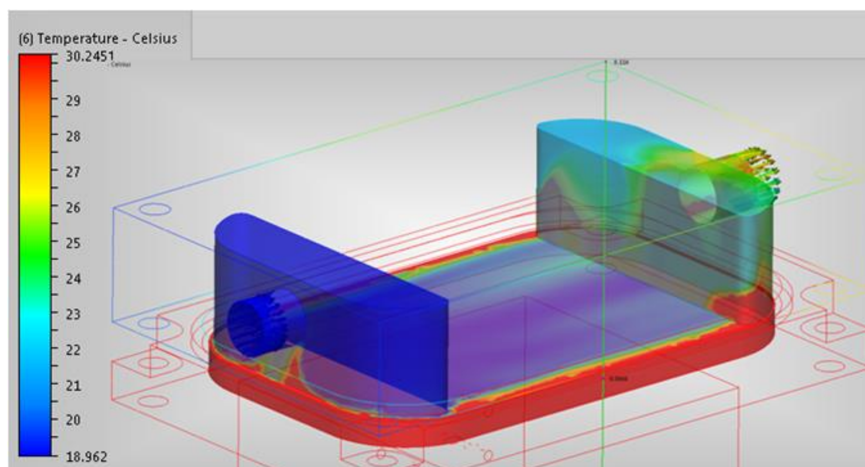

Figure 5.18: Temperature profile through the fluid for mass flow rate 0.03 kg/s.

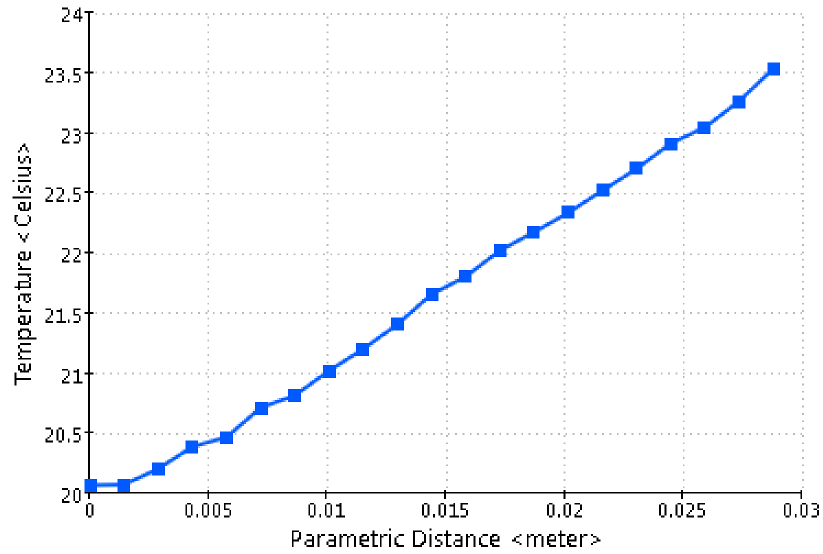

Figure 5.19: Fluid temperature from inlet to outlet, mass flow rate 0.03 kg/s.

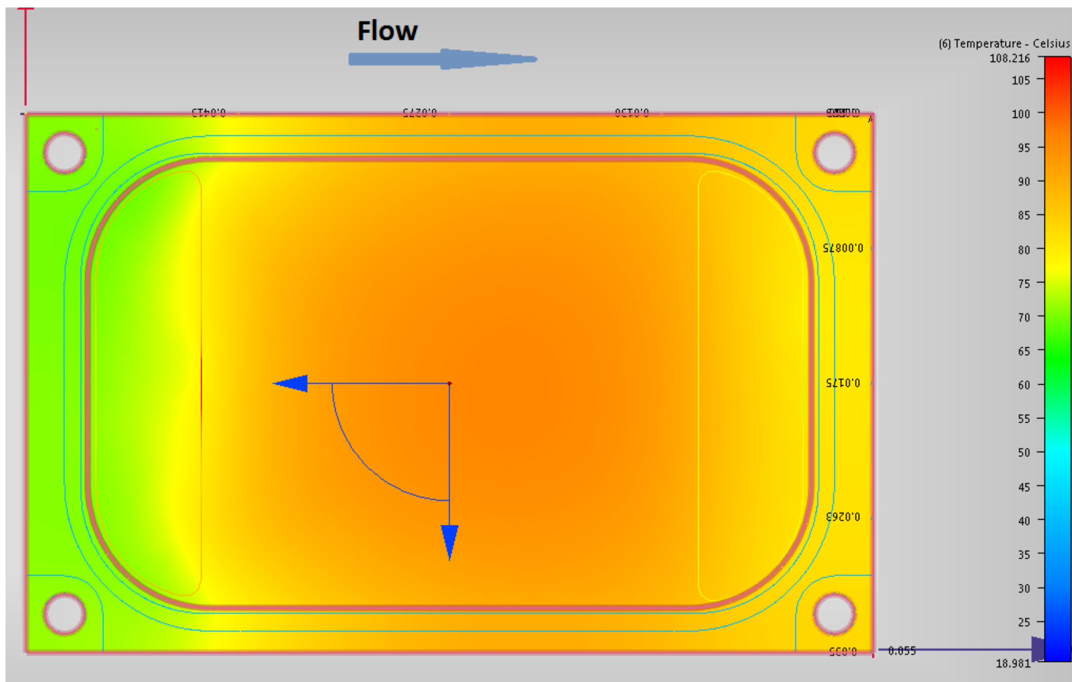

Figure 5.20: Temperature distribution over the smooth surface for 0.03 kg/s mass flow rates.

5.5.3.2 Pressure drop

Similar to the previous analysis, the pressure drop for mass flow rate 3 kg/s decreases in the flow direction. The entrance effect is visible.

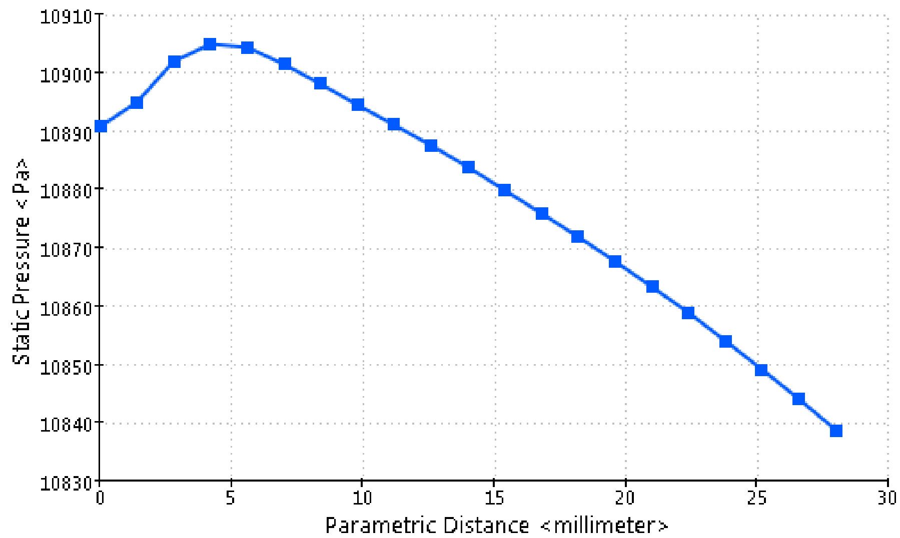

Figure 5.21: Pressure drop in the channel mass flow rate 0.03 kg/s.

5.5.4 Analysis for mass flow rate 0.04 kg/s

5.5.4.1 Heat transfer

The temperature distribution in the fluid flow is presented in Figure 5.22. Due to the high mass flow rate, fluid temperature does not change significantly. According to Figure 5.23, fluid temperature is affected slightly by the fluid flow. The flow regime for the given mass flow rate is in the transition regime, therefore, the evidence can be observed in the flow temperature profile. Entrance effects are also present. The heated surface temperature is given in Figure 5.24.

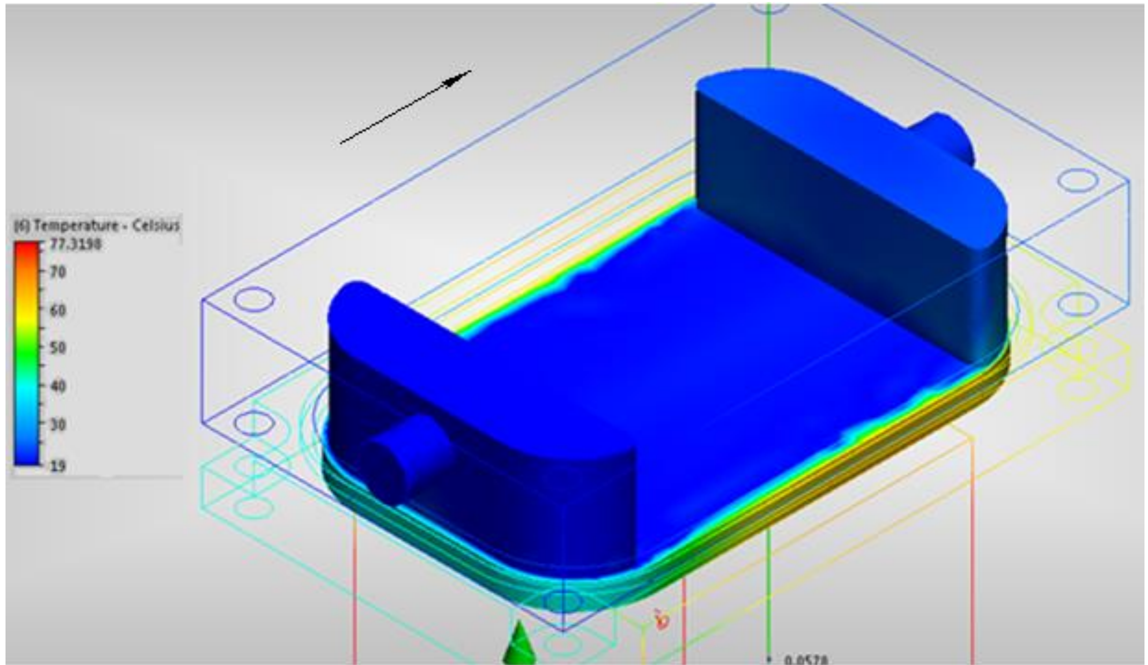

Figure 5.22: Temperature profile of the fluid flow for mass flow rate 0.04 kg/s

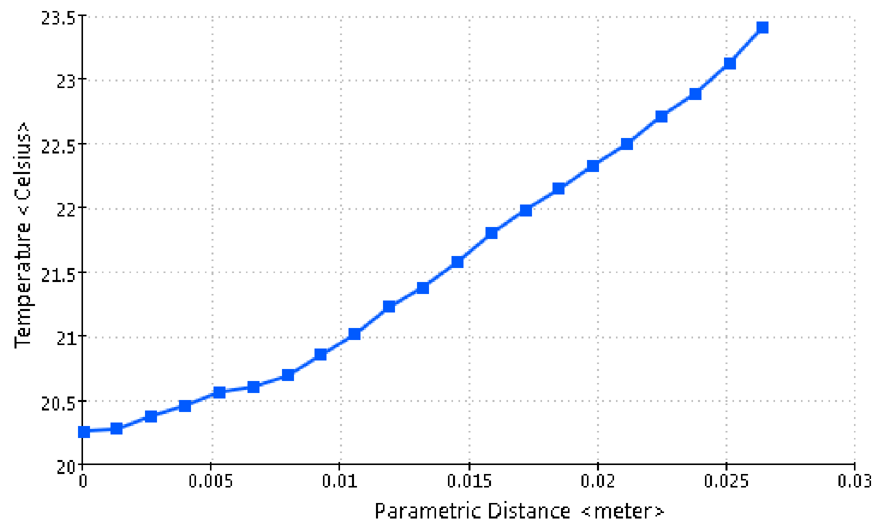

Figure 5.23: Fluid temperature from inlet to outlet, mass flow rate 0.04 kg/s.

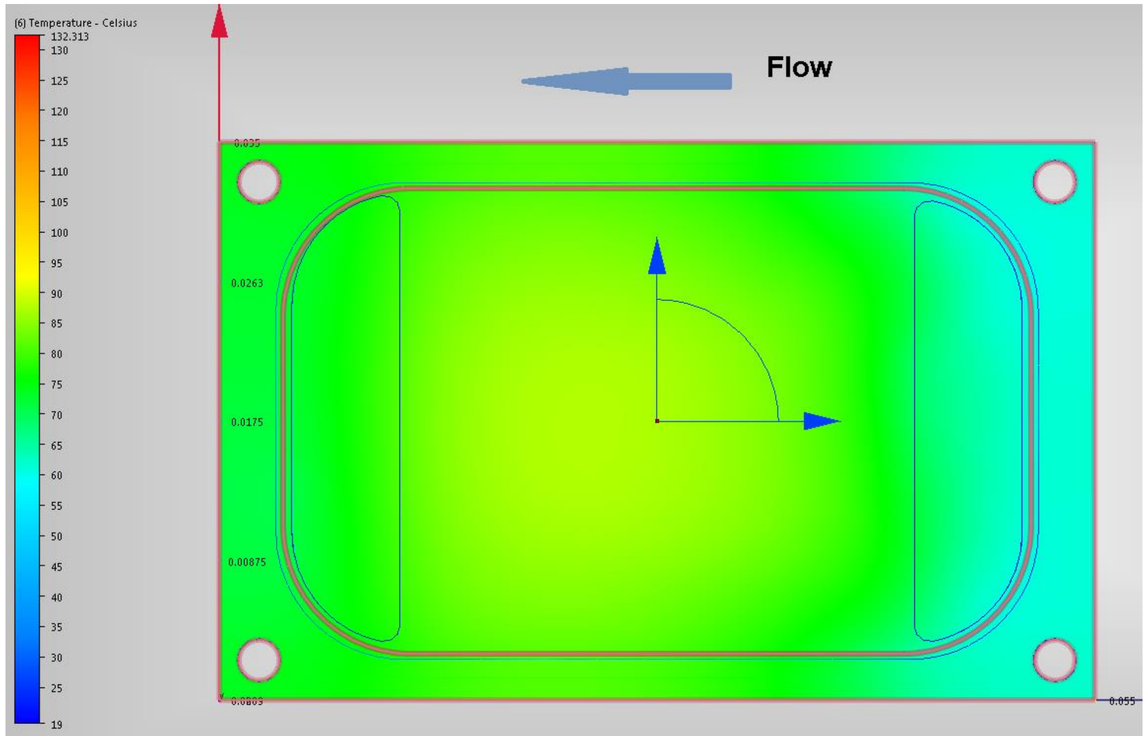

Figure 5.24: Surface temperature for mass flow rate 0.04 kg/s.

5.5.4.2 Pressure drop

Pressure decreases in the flow direction and the entrance effects are visible, Figure 5.25.

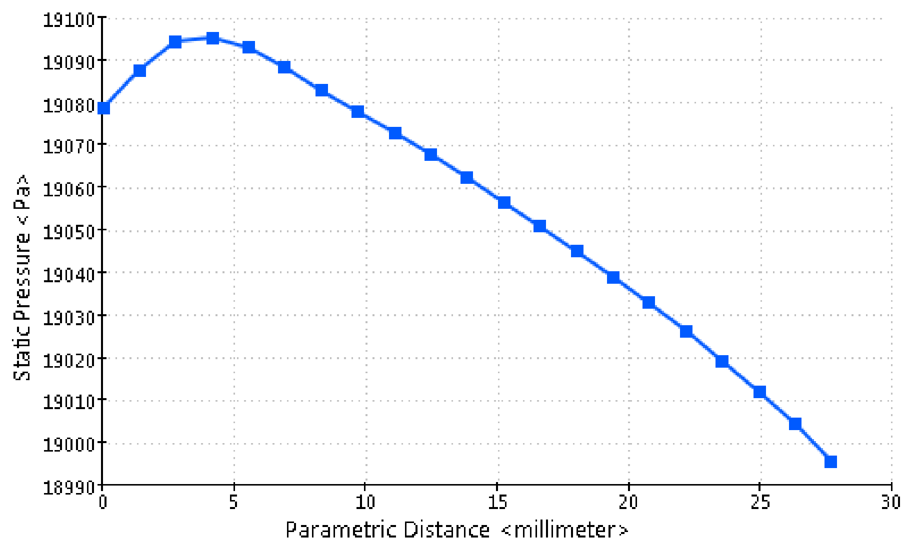

Figure 5.25: Pressure drop in the channel mass flow rate 0.04 kg/s.

5.6 RESULTS

This CFD study, examines the temperature and pressure drop of single phase flow over the smooth sample. The CFD data will be used to assess the experimental setup and the experimental procedure. The CFD analysis was performed for mass

5.6.1 Heat transfer

The Nusselt number increase with the mass flow rate. The evaluation of the heat transfer performance of developing flows at the entrance length is a complex problem due to the entrance effects. According to Figure 5.26 Nusselt number increases with Reynold number.

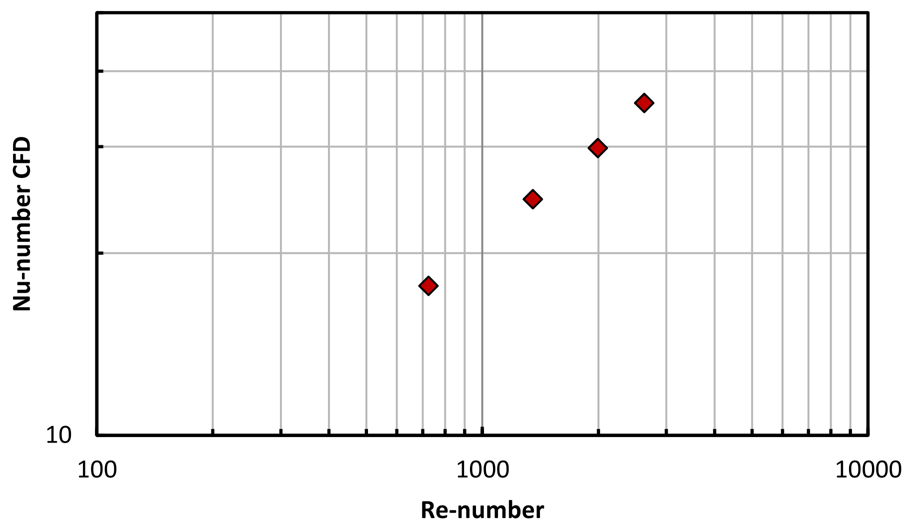

Figure 5.26: The Nusselt number versus Reynolds number for mass flow rates 0.01 kg/s to 0.04 kg/s and heat input 600 W.

5.6.2 Pressure drop

The pressure drop results from the CFD analysis is presented in Figure 5.27. According to Figure 5.27, pressure drop increases with an increase in

Reynolds number. In all cases, pressure at the entrance is higher due to the no-slip conditions, however after this zone shows a linear decrease.

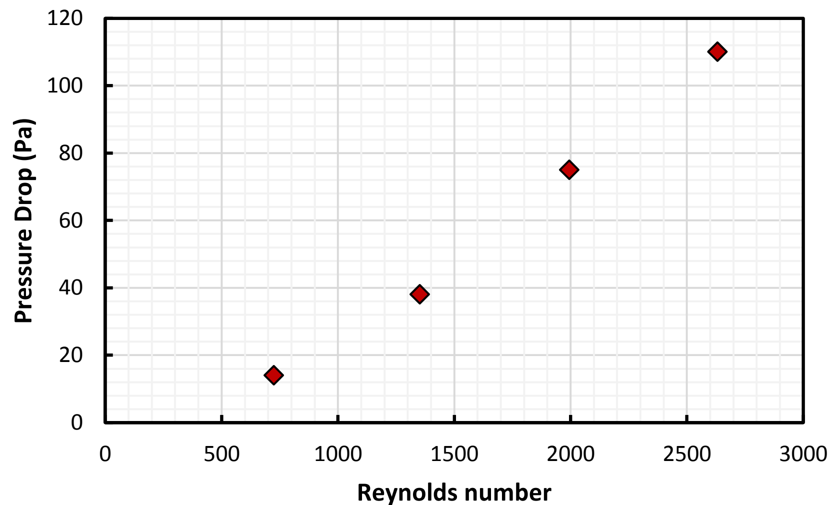

Figure 5.27: The pressure drop versus Reynolds number for mass flow rates 0.01 kg/s to 0.04 kg/s and heat input 600 W.

5.7 SUMMARY

A simplified smooth sample integrated in the test module under specific boundary conditions was analysed using Autodesk CFD 2013. The mass flow rates varied from 0.01 kg/s to 0.04 kg/s and the heat input remained constant 600 W. The automatic mesh generator was set active to ensure required distribution and a smooth mesh transition. Analysis was set active for heat transfer and fluid flow. The CFD analysis was based on the 'Standard k-epsilon' model. The CFD assessment provided temperature and fluid flow characteristics. The simulation results show heat transfer and flow characteristics, which are presented in terms of the pressure drop and Nusselt number.

Heat transfer evaluation under fluid flow condition is important for selection of an efficient liquid cold plate. The CFD, heat transfer evaluation provides significant information in the design and performance evaluation. The analysis is performed for the laminar regime and results show that the heat transfer rate increased with Reynolds number for all mass flow rates. The temperature of the heated surface decreases with an increase of mass flow rate, when there is a constant heat input. The highest surface temperature was observed approximately at the 2/3 of the length in the flow direction. The fluid temperature was observed to increase gradually from the inlet to the outlet. The temperature difference between heated surface and the fluid decreased in the direction of the flow as a consequence the highest heat transfer coefficient is expected at the entrance region.

The pressure drop is a parameter of interest because is related to the pumping power and as a consequence to the efficiency of the liquid cold plate. CFD reveals the effects of the entrance region in the pressure drop. Pressure had a tendency to increase at the entrance due to the entrance effects; however, it decreases gradually in the flow direction after the entrance region. Pressure drop was observed to increase with the increase of Reynolds number for all four mass flow rates. Based on the velocity profile at the inlet, the effect of the pre-mixing chamber has proven to be effective in reducing the velocity variation, and equalized the flow at the entrance. The temperature increase and pressure drop show a linear gradient in the channel.

6 EXPERIMENTAL FACILITY

This chapter presents a detailed description of the experimental facility, the test modules, the measurement equipment and uncertainty analysis. The experimental test facility was designed and constructed to provide reliable data for the determination of water flow and heat transfer characteristics of a smooth sample and three electron beam treated samples with different protrusion pattern, size, and density. The chapter is organized as follows: Section 6.1 provides a description of the test facility while section 6.1.1 gives the details of the test module and test samples investigated in this study. Section 6.2 presents the data reduction, and is followed by the Section 6.3 that presents the experimental uncertainty analysis. Section 6.4 presents the validation of the experimental facility and compares the experimental data for the smooth sample with correlation of Stephan (1959) and the CFD analysis.

6.1 TEST RIG DESIGN

The current experimental facility was designed and constructed by Thermacore Europe to provide controlled fluid flow for different heat transfer experimental analysis. Previously, test rig was used for evaluation of heat transfer and pressure drop in micro-channel for a two-phase flow regime, see (McGlen, et al., 2004). However, the experimental facility was fully refurbished and upgraded for this study to comply with requirements of present experimental work. In the current experimental rig the upgrade includes new chiller water control unit, flow meter, precision valves, heat supply and a complete measurement system.

Figure 6.1 shows a schematic diagram of the flow loop used to supply deionized water to the test sample at the required conditions. The fluid is provided at a controlled temperature of 20 ^{o}C, and pumped around the loop by a recirculation chiller unit (LabTech, H150-1500). The flow of the water passing through the test sample is regulated by a bypass valve and set to the desired value by a precision control valve. A Coriolis mass flow meter (Endress+Hauser, Promass 40E) with accuracy 0.05% is used to measure the mass flow rate. A differential pressure transducer (Omega MM Series) with accuracy 0.05% is connected to measure the pressure drop of the water across the heat transfer section in the test sample. A micro filter is fitted upstream of the test sample to remove any solid particles suspended in the fluid. The water flow exiting the test sample is returned to the chiller unit. The test facility is shown in Figure 6.2, while a list of components and their range is given in Table 6.1.

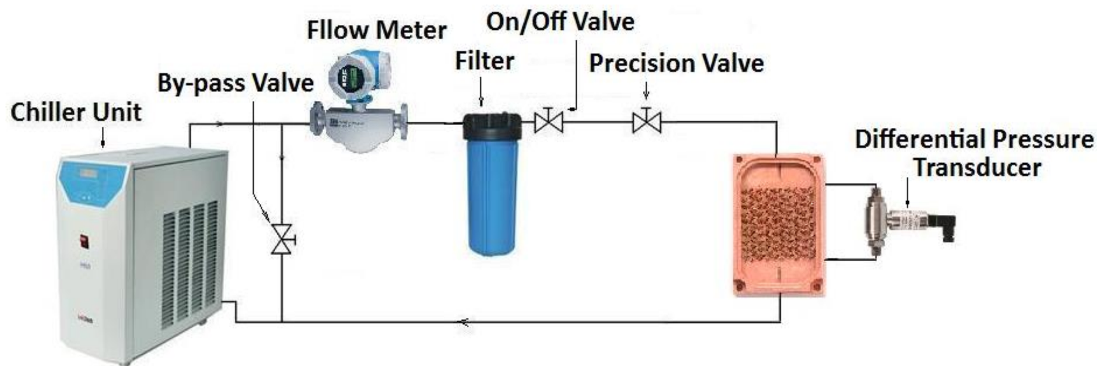

Figure 6.1: Schematic of the test flow loop.

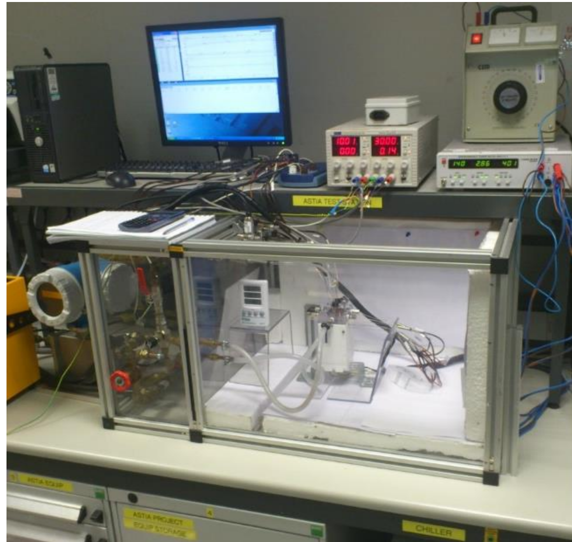

Figure 6.2: Picture of the test rig.

Table 6.1: List of the test loop elements.

Device type	Manufacturer and Model	Description	Accuracy
Liquid Pumping and Cooling	Lab-Tech H150-1500	0.10 ls^{-1}	
Flow-meter	Promag 40E	0.11 ls^{-1}	0.05%
Water Filter	Liff NP1	0.50 μm	
Variable Power Supply	EA-PS 9080-50	1.50 kW	1%
Pressure Transducer	Omega MM series	2.50 kPa	0.05%
Pressure Transducer	Omega MM series	17.00 kPa	0.05%

6.1.1 Test module

The test module assembly depicted in Figure 6.3 consists of three main components: the heater block, the test sample, and the transparent polycarbonate cover. The heater block is made of copper C101, and is 100 mm high with a rectangular cross-section (28 mm x 32 mm) matching the treated heat transfer surface in the test sample. Four cartridge heaters, each of 500 W power rating, 60 mm long and 10 mm diameter, are installed in the lower part of the block. The electrical power supplied to the cartridge heaters is set using a power supply and measured with a power meter. The distance between the end of the cartridge heaters and the base of the test sample is 40 mm, allowing one-dimensional heat conduction to become established in

the upper part of the block. Temperatures are measured at four positions along the vertical axis of the heater block. The top thermocouple is located 2.3 mm below the top surface of the block and the remainder are equally spaced 4 mm apart. In order to quantify the longitudinal temperature variation along the top surface of the heater block two additional thermocouples are located 3.5 mm from the upstream and downstream end faces. All heater block temperatures are measured with 0.75 mm diameter type-T sheathed thermocouples, which are secured into 1.0 mm diameter x 14 mm deep holes with thermally conductive compound.

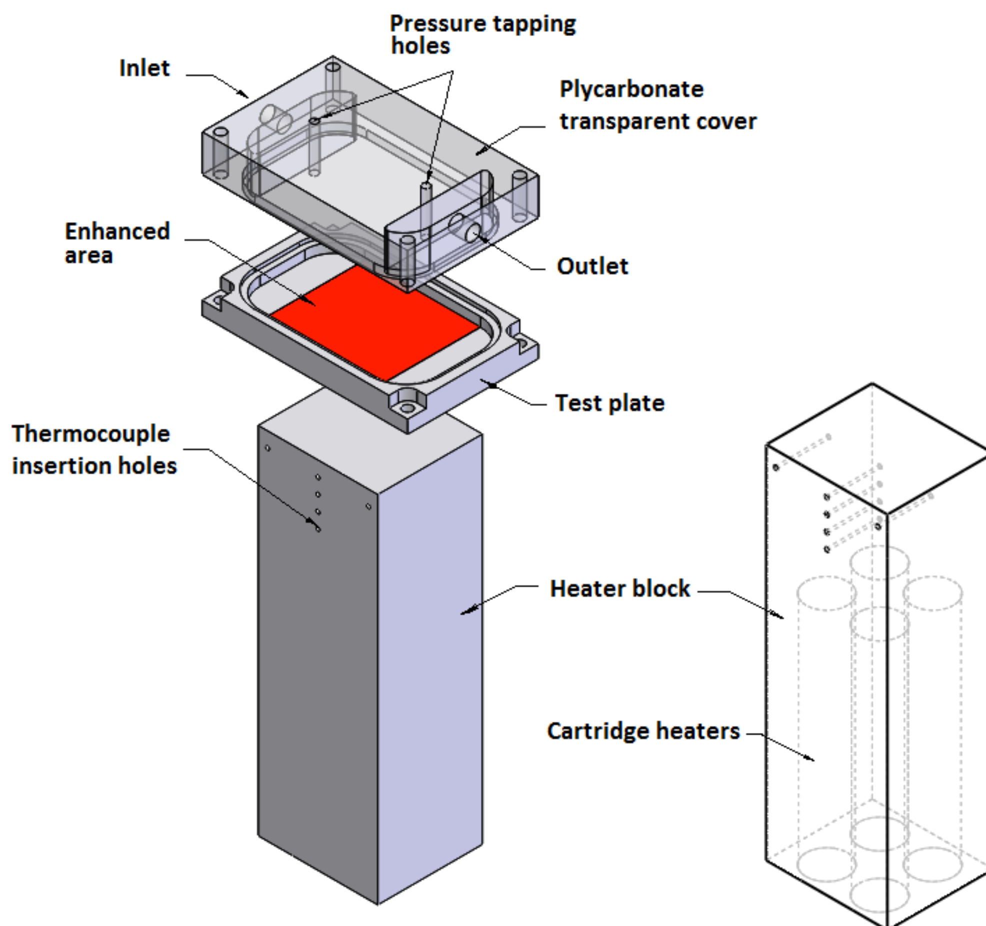

Figure 6.3: Schematic view of the test module.

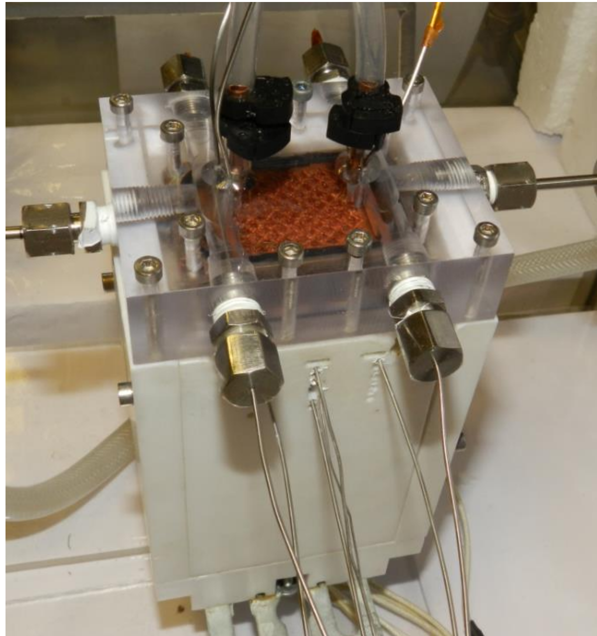

Figure 6.4: Picture of the Test Module.

The test samples were manufactured from 6.5 mm thick copper (C101) plate blanks 55 mm long x 35 mm wide. A flow space was machined in each test sample, reducing the base thickness to 3 mm. The electron beam treatment was then applied to a central area approximately 28 mm wide and 32 mm long in the flow direction as shown in Figure 6.5. The untreated sections at both ends of the flow space (7.5 mm long) provide smooth inlet and outlet surfaces, see Figure 6.5.

As discussed in Chapter 4, different surface protrusion patterns were applied to the three electron beam enhanced samples S1, S2 and S3, Figure 6.6. Magnified photographic images of the surfaces were utilized to estimate the transverse spacing (S_T) between protrusions and the longitudinal spacing (S_L) between protrusion rows. The height of protrusions (H_P) above the untreated substrate surface was checked at several points on each test sample using an electronic height gauge (TESA, micro-hite 350) with accuracy ±0.1 μm. It should be recalled that in addition to the formation of protrusions, the electron beam process creates associated cavities in the

substrate surface. Values of S_T, S_L and H_P for test samples S1, S2 and S3, determined as outlined are listed in Table 6.2.

The average protrusion densities for samples S1, S2, and S3 are 13, 11 and 25/cm^2 respectively. The test sample is vacuum brazed to the top of the heater block to ensure good thermal contact.

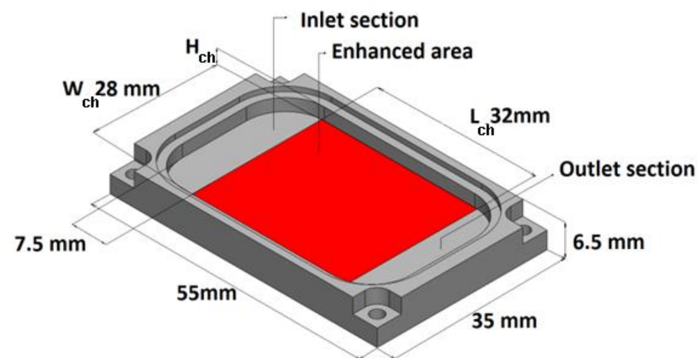

Figure 6.5: Interior view of test sample.

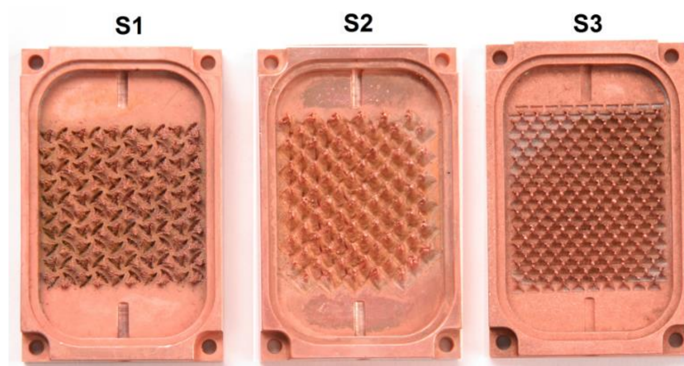

Figure 6.6: Three enhanced test samples.

Table 6.2: Protrusions and channel dimensions.

Sample	S_T	S_L	H_p	H_{ch}	A_c	D_h
	mm	mm	mm	mm	mm^2	mm
S1	5.6	2.8	2.5	2.80	82	3.00
S2	4.3	2.1	2.8	2.87	84	2.80
S3	2.6	1.5	1.6	1.68	49	1.59
Smooth	-	-	-	2.45	69	4.51

A transparent polycarbonate cover, 21 mm thick, is fitted to each test sample. The cover forms the upper surface of the flow channel over the test sample heat transfer surface and permits visual observation of the fluid flow. Transverse slots, 18 mm deep x 7.5 mm wide, are cut in the cover at each end to act as inlet and outlet plenums. The channel flow length (L) between the plenums is 32 mm. Holes are drilled through the cover to provide static pressure tapping points 2.7 mm downstream of the channel entry and 2.7 mm upstream of the channel exit. The plenums accommodate the flow connections and type-T thermocouples to measure the inlet and outlet water temperatures. Temperature was measured at two different locations across the flow at the inlet and as well at the outlet. By integrating these connections and measurement points in the cover, the thickness of the copper test sample is kept low, thus reducing heat losses from the sides. The low thermal conductivity of polycarbonate (k = 0.2 W/m K) ensures that the cover can be treated as adiabatic.

The height of the flow channel H_{ch} above the test sample heated surface is governed by the size of a step machined around the edge of the polycarbonate cover, locating it in the copper test sample. For the electron beam enhanced test samples, the step size was adjusted to maintain a clearance between the top of the protrusions and the cover. This clearance varied between about 0.1 mm and 0.3 mm as a result of the variation of the protrusion height between samples. Height of the channel also varied to accommodate the height of the protrusion for each sample and avoid the clearance. The flow cross-sectional area A_c is based on the channel geometry it does not take into account the enhancement and is evaluated as

the product of W_{ch} (channel width) and H_{ch} (channel height). Values of H_{ch} and A_c are listed in Table 6.2.

For the smooth surface test sample, the channel height and width are 2.45 mm and 28.0 mm respectively, corresponding to a free flow area of 68.6 mm^2, an aspect ratio of 11.4 (channel width/channel height) and a hydraulic diameter D_h of 4.51 mm.

A 10 mm thick PTFE enclosure is fitted around the test module assembly to provide thermal insulation. Figure 6.7 shows a schematic view of the integrated test module assembly.

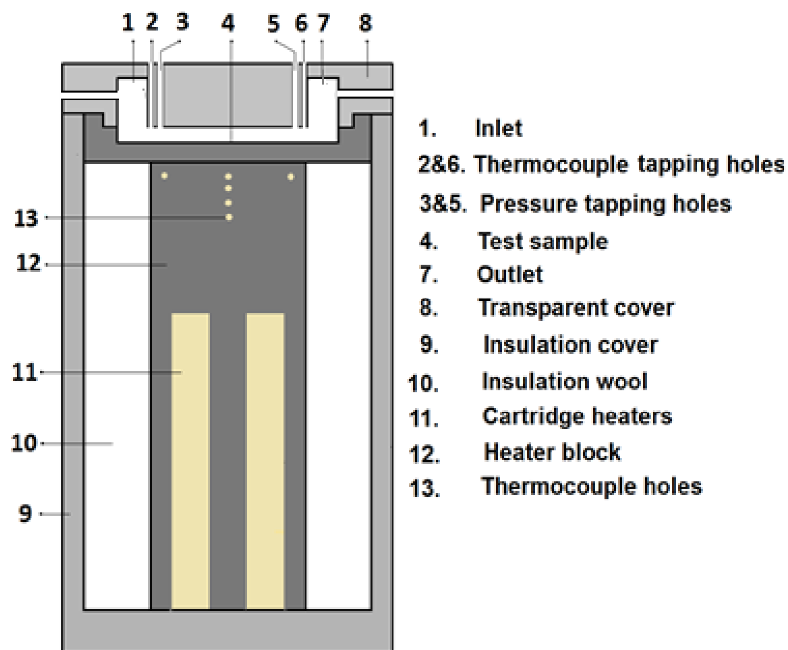

Figure 6.7: Schematic view of test module.

In order to reduce thermal losses, increase safety and create a compact test section, poly-tetra-fluoro-ethylene (PTFE) insulation material was used to insulate the test module from the ambient, Figure 6.8. Between the PTFE and the test sample the gap is filled with insulating wool 10 mm thick, see Figure 6.8. Insulation decreases losses, maintains test thermal stability and

increases safety. There are a considerable number of insulation materials; however, it is important that in the heat transfer process selection is based on thermal, mechanical and chemical properties. These factors have been examined and the isolation has a very low combustibility at very high-temperature levels, which are not in the scope of this experimental work. Mechanical properties such as breaking load, structural stability, and strength under compression, expansion and contraction were restrained to comply with the mechanical stability.

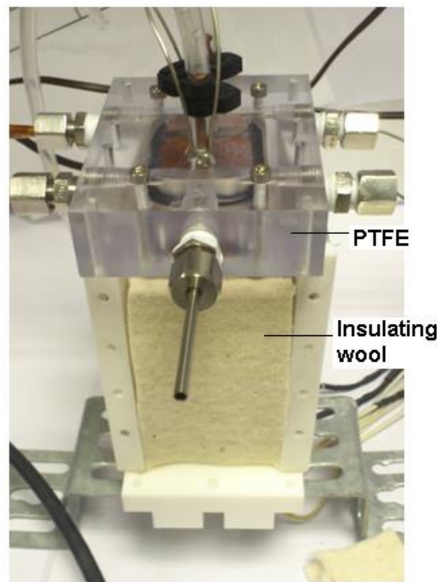

Figure 6.8: Picture of the test module insulation.

6.1.2 Measurement system

The measurement system is composed of a Pico Technology TC-08 data logger interfaced to a personal computer running Pico software that is used to measure, record and display the temperature sensor and pressure transducer outputs. Readings of each measured variable are acquired at one second interval. The water temperatures at the inlet and outlet of the test sample are measured with two thermocouples located in different locations across the inlet and outlet. Together with the heater block, temperatures are measured using T- type thermocouples with an average uncertainty of ±0.1

K. The differential pressure transducer with a range of 2.5 kPa and an accuracy of 0.05% of full-scale was used to measure the pressure drop between the channel tapping points shown in Figure 6.7. For higher pressure drops that arose for sample S3, the same model pressure transducer with a range 170 kPa and accuracy 0.05% was used. The Coriolis flow meter used to measure the mass flow rate of the water is calibrated from the manufacturer (provided with a calibration certificate) for flow rates up to 0.11 kg/h and has a specified accuracy of ±0.05% of reading.

T-type thermocouples with 0.75 mm diameter, which are pot sealed have been used for both fluid and wall temperature measurement. Error in the thermocouple reading is the change in measurement between the true value and measured value. The total error is described by (Coleman & Steel, 2009) as the sum of the bias and the precision error. Bias error is constant (consistent and repeatable) while precision error is irregular. However, if a considerable number of measurements are taken (theoretically infinite), it is possible to identify the precision error and also determine the bias error. Therefore, to minimize such effects it is important to calibrate the equipment. Calibration is a comparative process between a measured value, and an accurate measurement that is made in the same conditions. Calibration is an important process for an accurate measurement; the following part describes the practice in this study.

During the calibration process, the external influences listed below were carefully assessed and kept under observation.

I. Poor contact
II. Ambient temperature variation during the calibration.
III. Temperature variation in the cold junction inside the calibration pot.
IV. Voltage readings, auxiliary equipment (long extensions or selector switches).
V. Electro-magnetic field influences, i.e. (electric motors, powerful power supplies and furnaces).
VI. Mechanical and thermal stresses and deformations.

The calibration process improves the measurement accuracy and avoids misunderstanding of experimental results. The calibration process is made through an ‘Isotech apparatus’ model: ‘Isocal-6 Venus 2140’, this device meets the requirements of EU directive on electromagnetic compatibility EMC 89/336/EEC, see Figure 6.9. The device is an accurate temperature-controller consisting of, a calibration pot and two digital temperature identifiers. The first indicates the temperature setting in the pot and the second one monitors the temperature in the calibrating pot. There is a third external measurement from a thermocouple probe (that is inserted into the pot) with high accuracy and traceability to meet the requirements of (ISA 9000).

Based on the experimental scope thermocouples were calibrated at five points between 20 C^{o} to 100 ^{o}C. Calibration process began with 20 ^{o}C, 40 ^{o}C, 60 ^{o}C, 80 ^{o}C, and 100 ^{o}C.

6.1.2.1 Issues to be considered during calibration

The temperature calibration process can be affected by the ambient conditions. For example, in this case, the “Isotech Venus 2140” calibrating equipment was used. The first calibration was done in a group for all thermocouples, Figure 6.9. After the examination of the results a sinusoidal movement of temperature measurement was identified for all measurements, which was unexpected.

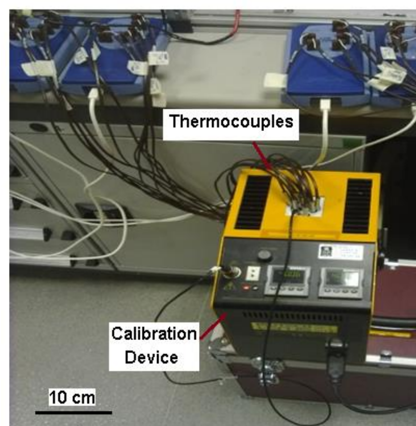

Figure 6.9: Thermocouple calibration process using (Isotech 2140) device.

By studying the calibration process step by step, no anomaly was identified. To eliminate external effects to the calibration process, ambient temperature was recorded in the laboratory during the day. Results revealed a sinusoidal movement of the ambient temperature, which conforms to the sinusoidal trend of the temperature in the calibration process. This simplified the explanation of this phenomenon caused by the air conditioning system.

The air conditioning system in general is composed of two main parts: an evaporator and a condenser. Evaporator is a single unit and is placed in the inside ambient of the laboratory to distribute the conditioned air. The disturbance of the air around the calibration destabilizes the energy balances (energy losses)[46] making it difficult for the calibrating machine temperature regulatory systems to respond quickly. Therefore, is important that such systems (air-conditioning, heating or other heat-generating equipment) that can create air movement or temperature change be eliminated from the surrounding area during the calibration process.

6.1.2.2 Calibration process

During the calibration process for each thermocouple, the temperature was measured every second for a period of 900 seconds. These data were compared with measurements made with the external probe thermocouple with a high accuracy. The temperature difference created by the reference taken with a high accuracy probe and the average temperature measured by each thermocouple gave the error of the measurement for each thermocouple. These measurements were recorded for ten thermocouples in the five set points mentioned above in the range 20 ^{o}C to 100 ^{o}C. Errors measured at a set temperature point for each thermocouple were averaged and included in a correction equation built for each thermocouple, i.e. (if the error was positive it was added to the value, when it was negative it was

[46] The calibration device depending on the ambient temperature inputs or removes heat in order to maintain constant temperature at the calibration pot. When this process is optimized the calibration pot reaches a constant temperature, however any change on the ambient temperature will disturb this balance and requires time to be stabilized.

subtracted from the value measured). In the second step a new calibration process was conducted with corrected thermocouple measurements. The thermocouple measurements taken over five set points were correlated to the calibration data using a linear function. Equations that correct reading of each thermocouple were recorded and inserted into the Pico-logger software to provide the accurate readings.

In order to have a constant mass flow and temperature control a liquid pumping and cooling system, (Lab-Tech H150-1500), was used Figure 6.1. The liquid circulating system was composed of two circulation loops, first is that of the working fluid flow and the second one is the refrigerant cooling loop (this loop via the heat exchanger maintain the desired temperature at the test loop), see Figure 6.10. The working fluid, which circulates through the test sample, is moved by a pump. To maintain the pressure stability and fluid capacity, in the series with the pump is a liquid collection tank. The other loop is that of the thermal control system which is composed, of a compressor, evaporator, and the condenser, both loops exchange heat via the heat-exchanger. The system is integrated into a single unit and automatically controlled by an electronic circuit.

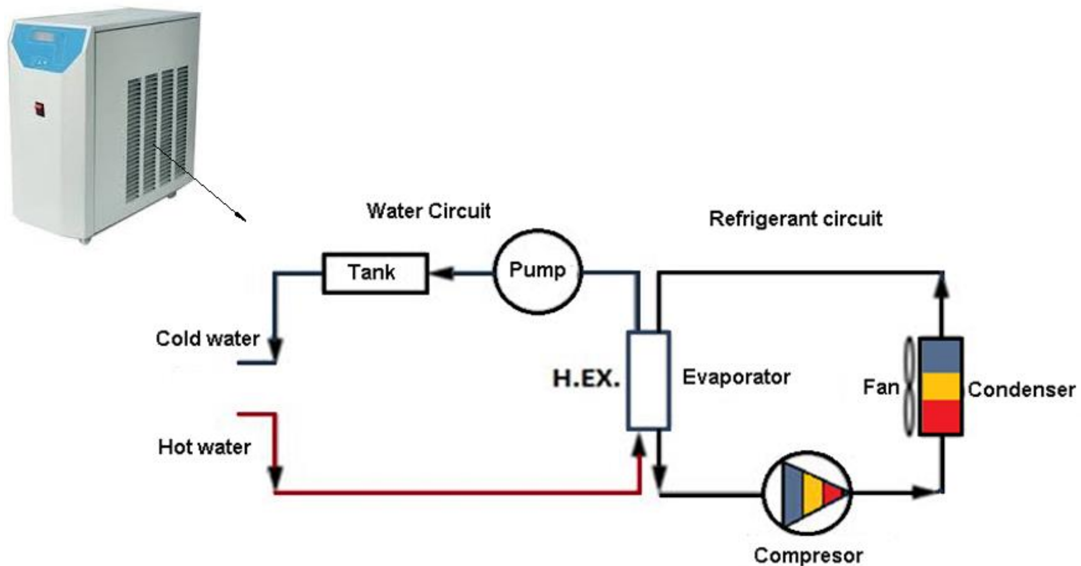

Figure 6.10: Schematics of liquid circulation and cooling system.

The working fluid used is deionized water. The water has been treated by manufacturer through a mineral removal process. The process removes the mineral ions, such as sodium, calcium, iron, copper, chloride, and bromide.

The energy used by the fluid to overcome friction in a duct appears as a pressure loss. Measurement of the pressure loss in the test section is made by; two differential pressure transducers (Omega MM series) with 2.5 kPa and 170 kPa that are used in turns to respond to the pressure drop in each sample. This device is of high performance and offers accuracy, stability and withstands high pressures. Accuracy for standard operating conditions is ±0.05%. The pressure transducers used were accompanied by calibration certificates provided by the manufacturer in accordance with standards of the National Institute of Standards and Technology (NIST); records can be found in (NIST traceable number: C-1954, C-2466). All testing performed complies with MIL-STD 45662-A, ISO 10012-1 and ANSI/NCSL Z540-1-1994 requirements.

The highly accurate Coriolis (Pro-mass 40E) flow meter, calibrated to an accuracy of ±0. 05% has been used to measure the water flow.

The Coriolis mass flow meter uses the oscillation method perpendicular to the flow direction to generate Coriolis forces[47] that correspond accurately to the mass flow rate. The oscillation is registered at the inlet and outlet ports of the oscillation tube, and processed to compute related mass flow rate. The system also measures density and temperature continuously to compensate for any thermal influences.

At the exit of the flow meter Figure 6.1, is placed a micro filter (Liff NP1) that is composed of housing and filter cartage (5 μm) to prevent any fouling or depositing on the surface of microstructures.

In order to maintain the flow constant to the test section two valves were deployed. The first is a bypass valve that regulates the main flow and is placed in parallel with the liquid feeding system, Figure 6.1. The second is a

[47] Force that a mass moving in a rotating system experiences perpendicularly to the direction of the flow.

precision valve at the inlet of test sample that regulates the flow at a desired value. In the flow loop after the precision valve, before the test module is a safety on/off valve that isolates the module in case of emergency.

The heater block was electrically heated using cartridge heaters that were fed by an (Electro-Automatic, EA-PS 9080-50) power supply. The power supply is measured with a (Hameg, HM8115-2) power meter with an accuracy of ±0.8%.

During the experimental work all variables were recorded using (Pichotech USB-08) data loggers. All data recorded from loggers was passed to a personal computer (PC) using “Pico-logger” software package that facilitates the data management in a single software unit. The software package includes an equation edition, which helped in converting (mV) signals in the required units.

6.1.3 Test procedure

In order to maintain safe operating conditions and record the data in a controlled environment a test procedure was developed.

The experimental start-up procedure follows these steps. The first step was to observe full operation of the measurement and data logging equipment. The second step was to regulate the flow by fully opening the precision valve and regulating the flow close to the required value by the bypass valve. The precision valve was used as a secondary regulator to set the flow at a desired value. The next step was to set the electricity value (current and Voltage) at the supply at a desired value. An automatic power meter verifies the value before it is switched to the cartridge heaters.

The experimental shut-down procedure follows these steps. The first step was to turn off the power at cartridge heaters and remove the connections. Second step was to record temperature through the heater block for a length of time to allow the water passing through to remove the heat and cool down the test module. After the temperature of the block, has reached that of the water at the inlet the fluid circulation unit was turned off. The last step was to

turn off data recording equipment and isolate the system from the electricity supply.

6.1.4 Operating condition

The experimental testing of the three electron beam enhanced surfaces and the smooth surface were conducted in nine steps for a range of mass flow rates of deionised water from 0.005 kg/s to 0.044 kg/s. The water inlet temperature was maintained close to 19°C for all tests. Pressure drop and heat transfer data were recorded at six values of power input that ranged from 100 W to 600 W.

Pressure and temperature were monitored for 120 minutes to ensure that steady conditions (constant temperature, flow rate, and heat input) are established before experimental data were collected. Measurements were recorded at a one second interval for a minimum period of 15 min after readings remained constant for at least 15 min. The recorded values for each measured variable were then averaged and the mean values were stored.

6.2 DATA REDUCTION

Analysis of the EB enhanced surfaces is complex due to the irregularity of the treatment. Therefore, two methodologies are used to evaluate both heat transfer and flow characteristics.

The first method analyses the treatment of surface irregularity and treats the problem, in the same way, as an internal flow through a smooth surface. This methodology does not take into account the increase of the heat transfer area and therefore will show high heat transfer coefficients per unit base area. Then again, this method shows clearly the enhancement capability of the electron beam technique compared to a smooth untreated sample.

The second method analyses the treatment as a regular pin-fin surface. Corresponding geometrical parameters such as equivalent diameter is used to theoretically optimize the reconstruction of an equivalent regular pin-fin structure. This methodology provides the corresponding heat transfer coefficient (takes in account increase of heat transfer area) and is used for comparison with other pin-fin geometries.

6.2.1 First method

The recorded temperatures, flow rate, and pressure drop were utilized to compute the average convection heat transfer coefficient and friction factor, respectively. All fluid properties were calculated at the bulk mean temperature, i.e. average between inlet and outlet.

6.2.1.1 Friction factor

The Reynolds number is evaluated based on the maximum velocity through the enhanced structure:

$$\mathrm{Re}_{D_h} = \frac{\rho V_{\max} D_h}{\mu} \tag{6.1}$$

The maximum velocity V_{max} is determined as:

$$V_{\max} = \frac{\dot{m}}{\rho A_{\min}} \tag{6.2}$$

where m is the mass flow rate of the fluid, D_h is hydraulic diameter, ρ and μ are fluid density and dynamic viscosity, A_{min} is the minimal flow area that is obtained from: $A_{min}=A_c - A_p$. The cross-sectional area A_c of the duct is given above in Table 6.2, while A_p is the area of the protrusions perpendicular to the flow. Due to the electron beam process, protrusions have irregular surfaces, however, for the flow analysis purposes; the frontal area of the protrusion has been approximated to be quasi-pyramidal with a flat top,

Figure 6.11 . Based on this assumption the frontal area of a protrusion is of a trapezoidal shape and is evaluated as:

$$A_{p_{front}} = N_{p_front}\left(\frac{(B+b)H_p}{2}\right) \quad (6.3)$$

where, N_p is the number of protrusions in the cross-sectional area of the flow, B is the bottom base width of the protrusion (the bottom base of the trapeze), b is the base width at the top of the protrusion (or the top base of the trapeze) and H_p height of protrusion, Figure 6.11.

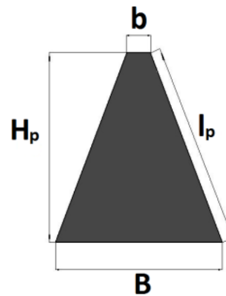

Figure 6.11: Frontal view perpendicular to the flow of the fin.

The Reynolds number and the friction factor for non-circular geometries are based on the hydraulic diameter. The hydraulic diameter is calculated as:

$$D_h = \frac{4A_{\min}}{P_{wett}} \quad (6.4)$$

where, P_{wett} is the wetted perimeter that corresponds to the minimal cross flow area and is evaluated as:

$$P_{wett} = P_{ch} + N_p(2l_p + b - B) \quad (6.5)$$

where, $P_{ch}=2(W_{ch} + H_{ch})$ is the perimeter of the duct and l_p is the length of the protrusion side (or rib of trapeze), see Figure 6.11. Based on the Reynolds number results, the flow is laminar and the hydrodynamic entry length is given by (Bejan & Kraus, 2003) as:

$$L_{h_laminar} \approx 0.05 \,\mathrm{Re}\, D_h \tag{6.6}$$

A parameter of interest in the analysis of fluid flow over electron beam enhanced structures is the pressure drop ΔP, since it is directly related to the pumping power and hence the overall efficiency. Hydro-dynamically the fluid flow over irregular enhanced structures is a complex problem, due to hydrodynamic and thermal boundary layers that develop on the surface of each protrusion creating no-slip conditions and flow separation. The problem is simpler for the smooth sample where the friction factor can be evaluated as follows.

According to Equation 6.6, the flow is hydro-dynamically developing and the entry length values ranged from 9.6 cm to 64 cm depending on Reynolds number. When considering a developing flow in the smooth sample the pressure drop is related to the apparent friction factor, (Shah, 1978), who proposed the following equation to predict (f_{app}Re)[48] in the hydrodynamic entry region of circular and non-circular ducts:

$$f_{app}\mathrm{Re} = 3.44(x^+)^{-0.5} + \frac{(f_{FD}\,\mathrm{Re}) + K(\infty)/(4x^+) - 3.44(x^+)^{-0.5}}{1 + C(x^+)^{-2}} \tag{6.7}$$

where f_{app} is the apparent Fanning friction factor (based on the pressure drop from L=0 to L) and is given as:

$$f_{app} = \frac{\Delta P}{0.5\rho V^2}\frac{D_h}{4L} = \frac{\Delta P}{0.5\rho V^2}\frac{1}{4x^+\,\mathrm{Re}_{D_h}} \tag{6.8}$$

where x^+ is the dimensional axial distance, determined as:

$$x^+ = \frac{L}{D_h\,\mathrm{Re}_{D_h}} \tag{6.9}$$

f_{FD} is the fully developed Fanning friction factor, K(∞) is the incremental pressure drop number that represents the change in momentum between developing and fully developed flow, while C is a constant coefficient. Fully

[48] Product of the apparent ‘Fanning’ friction factor and Reynolds number.

developed Fanning friction factor f_{FD}, K (∞) and C depend on the duct geometry, (Shah & London, 1978a). Equation 6.7 can be stated in terms of the pressure drop by replacing (f_{aap}) with equation 6.8 and multiplying both sides by $4x^+$ to obtain:

$$\frac{\Delta P}{0.5\rho V^2} = 13.76(x^+)^{0.5} + \frac{4x^+(f_{FD}\,\mathrm{Re}) + K(\infty) - 13.76(x^+)^{0.5}}{1 + C(x^+)^{-2}}. \tag{6.10}$$

For the smooth rectangular duct used in the experimental work, the duct aspect ratio $\alpha^* = H/W$ is 0.087. For fully developed flow in a rectangular duct, the product (f_{FD}Re) can be approximately determined using the following equation, (Shah & London, 1978a):

$$f_{FD}\,\mathrm{Re} = 24(1 - 1.3553\alpha^* + 1.9467\alpha^{*2} - 1.7012\alpha^{*3} + 0.9564\alpha^{*4} - 0.2537\alpha^{*5}) \tag{6.11}$$

From Equation 6.11 is obtained that f_{FD}Re = 21.49. The incremental pressure drop number K (∞) is also function of α^* and is found from tables in (Shah & London, 1978a). For the given duct, the aspect ratio the incremental pressure drop number K (∞) =0.76. The coefficient C, also depends on α^* and is presented in tables (Shah & London, 1978a) where it can be evaluated to be $C=5x10^{-5}$. The above values of f_{FD}Re, K (∞), and C are substituted into equations 6.7 and 6.10 to evaluate (f_{app}Re) and $\Delta P/0.5\rho V^2$ respectively. The Fanning friction factor for the smooth and treated samples S1, S2 and S3 are evaluated from experimental data as:

$$f = \frac{\Delta P D_h}{2L\rho V_{max}^2} \tag{6.12}$$

The required pumping power, to overcome the pressure loss, is determined as:

$$W_{pump} = \frac{m\Delta P}{\rho} \tag{6.13}$$

6.2.1.2 Heat transfer

The heat balance equation for the electrically heated surface can be expressed as:

$$Q_{elec} = IU = Q_{conv} + Q_{loss} \tag{6.14}$$

where Q indicates the heat transfer rate while subscripts elect., conv., and loss represent electric, convection and loss respectively. The heat loss from the system is composed of two components, radiation from the heated surface to the surroundings and second conduction through the insulation and convection to the atmosphere. In this case, the test section was well insulated and the heat losses have been determined as the difference between the electrical heat input at the cartridge heaters and Q_{conv}. This term is calculated in terms of the enthalpy rise of water, which is simply given as:

$$Q_{conv} = \dot{m} c_p (T_e - T_i) \tag{6.15}$$

In this study, the average convection heat transfer coefficient h_{av} is calculated based on $Q_{conv,}$ subscripts e and i, represent exit and inlet parameters respectively:

$$h_{av} = \frac{\dot{m} c_p (T_e - T_i)}{A_s \Delta T_{LMTD}} \tag{6.16}$$

The specific heat capacity of water c_p is evaluated at the bulk mean fluid temperature between the inlet and outlet. A similar approach in the calculation of the heat transfer coefficient was followed by other researchers (Halimic, et al., 2009) and (Weilin & Abel, 2009). ΔT_{LMTD} is the logarithmic mean temperature difference, and can be determined using the following equation:

$$\Delta T_{LMTD} = \frac{\Delta T_2 - \Delta T_1}{\ln(\Delta T_2 / \Delta T_1)} \tag{6.17}$$

ΔT_1 and ΔT_2 are the temperature differences between the surface T_{ref} and fluid at the inlet and outlet respectively both used to determine the ΔT_{LMTD}.

Since the enhancement is placed in a channel where the side walls are heated, the heat transfer area A_{ht} includes bottom (footprint of treated area of the channel) and the two side walls see Figure 6.5, and is evaluated as:

$$A_{ht} = (W_{ch} + 2H_{ch})L_{ch} \tag{6.18}$$

where, W_{ch} is the width, H_{ch} is the height and L_{ch} in the length of the channel. The temperature at the wetted surface T_{surf} is obtained at the inlet, centre, and outlet based on the measurements of wall temperature at those respective locations as:

$$T_{surf} = T_w - q\left[\left(\frac{l_{brazing}}{k_{brazing}}\right) + \left(\frac{l_{plate}}{k_{Cu}}\right)\right] \tag{6.19}$$

where, T_w is the temperature measured in the heater block, the top thermocouple is located 2.3 mm below the top surface of the heater block and reminder are equally spaced 4 mm apart. Hence, T_w is obtained by fitting an equation through the data measured by thermocouples in the heater block and extrapolating to the top of the heater block. In order to quantify the longitudinal temperature variation along the top surface of the heater block two additional thermocouples are located 3.5 mm from the upstream and downstream of faces. All heater block temperatures are measured with 0.75 mm diameter type-T sheathed thermocouples, which are secured into 1.0 mm diameter x 14 mm deep holes with thermally conductive compound. In Equation, (6.19, $l_{_brazing}$ is the thickness of the brazing and $l_{_plate}$ is the thickness of the cold plate. The brazing material thickness is 0.08 mm and the thermal conductivity is 371 W/m K, while the test sample thickness is 3 mm copper C101 with a conductivity of 391 W/m K. The heat flux q is obtained from the enthalpy rise as:

$$q = \frac{Q_{conv}}{A_{ht}} \tag{6.20}$$

The average Nusselt number is calculated based on the hydraulic diameter of the channel and is given as:

$$Nu_{D_h} = \frac{h_{av} D_h}{k} \tag{6.21}$$

where, k is the thermal conductivity of the fluid. The Nusselt number was compared with the Stephan (1959) correlation, (Bejan & Kraus, 2003) for a developing length in parallel plate channels developed in the range 0.1≤Pr≤1000 and given as:

$$Nu_{av} = 7.55 + \frac{0.024 x_*^{-1.14}}{1 + 0.0358 \Pr^{0.17} x_*^{-0.64}} \tag{6.22}$$

Where, x_* is dimensionless longitudinal coordinate in the thermal entrance region and the parallel plate channel is given as:

$$x_* = \frac{L/D_h}{\mathrm{Re}_{D_h} \Pr} \tag{6.23}$$

The thermal resistance R_{th} has been evaluated based on the heat transfer coefficient and the footprint of the enhanced surface:

$$R_{th} = \frac{1}{h_{av} A_{ht}} \tag{6.24}$$

6.2.2 Second method

The electron beam process focuses a large amount of energy in a very small area. During the process, the material is melted, displaced and solidified rapidly. Therefore it is impossible to accurately generate regular well-defined protrusions with smooth surrounding surface. In order to evaluate the performance of the enhanced structures and compare the data with other enhanced geometries the protrusions are approximated as regular fin structures with an equivalent diameter. The assumed regular pin-fin structure is characterized by the protrusion length Hf, an equivalent diameter of the protrusion de, as well as by transverse distance S_T, longitudinal distance S_L,

and diagonal S_D distances. The characteristics of the fluid flow over the enhanced area determine the local heat transfer coefficient (h) and temperature field over the base (end-wall) and the fin surface. In general due to the geometrical complexity, it is difficult to find the correct local heat transfer coefficient. Therefore, an average heat transfer coefficient h_{av} that combines both that of the fin and the base is used.

The definition of the Reynolds number in the present study is in line with that used in previous studies for circular or rectangular regular pin-fins:

$$Re_{d_e} = \frac{\rho U_{max} d_h}{\mu} \quad (6.25)$$

In the above Equation, U_{max} indicates the maximum water velocity occurring between fins; d_h is the corresponding hydraulic diameter of the protrusion. The protrusion shown in Figure 6.12 is a simplification. Therefore, the equivalent hydraulic diameter is an average between bottom and top hydraulic diameters that are described below:

$$d_{h_{base}} = \frac{4(W_{p_{base}} L_{p_{base}})}{2(W_{p_{base}} + L_{p_{base}})} \quad (6.26)$$

and the top corresponding equivalent diameter is:

$$d_{h_{top}} = \frac{4(W_{p_{top}} L_{p_{top}})}{2(W_{p_{top}} + L_{p_{top}})} \quad (6.17)$$

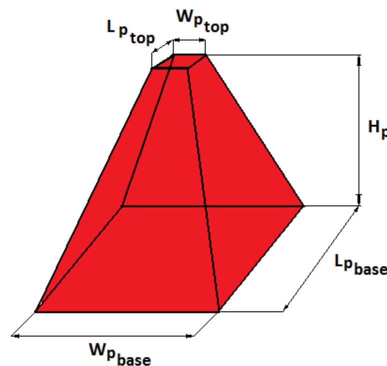

Figure 6.12: Protrusion dimensions.

While, the corresponding hydraulic diameter of protrusion is given as:

$$d_e = 0.5\left(d_{h_{base}} + d_{h_{top}}\right) \quad (6.28)$$

The geometrical data for each sample has been shown in

Table 6.3, and parameters associated with the notation that is described in Figure 6.12.

Table 6.3: Geometrical parameters of protrusions.

	Geometrical data of protrusion for each sample				
	Base Width	Base Length	Top Width	Top Length	Protrusion Height
	$W_{p\ base}$ mm	$L_{p\ base}$ mm	$W_{p\ top}$ mm	$L_{p\ top}$ mm	H_p mm
Sample S1	1.35	1.65	0.8	0.65	2.5
Sample S2	2.44	2.1	1.6	1.12	2.8
Sample S3	0.18	1.5	0.9	0.9	1.6

The total number of fins is determined as:

$$N = N_L N_T \tag{6.29}$$

where N_L is the number of protrusions in the stream-wise direction, and N_T is the number of protrusions in the span-wise direction. The heat transfer area is the sum of the area of protrusions, and the exposed base area includes the side walls of the channel given as:

$$A_{ht} = A_{ht_{base}} + A_{ht_p} + 2(H_{ch} L_{ch}) \tag{6.30}$$

The heat transfer area of the base is given as:

$$A_{ht_{base}} = (W_{ch} L_{ch}) - \left(N\pi \left(\frac{d_e}{2} \right)^2 \right) \tag{6.31}$$

The heat transfer area of the protrusions represented by the equivalent diameter is given as:

$$A_{ht_p} = N\pi d_e \left(H_p + \frac{d_e}{4} \right) \tag{6.32}$$

The minimum cross-sectional flow area A_{min} is evaluated as:

$$A_{\min} = H_{ch} W_{ch} - N(d_e H_p) \tag{6.33}$$

The pressure drop through the pin fin structures is proportional to the number of rows (N_L), friction correction factor (X), and dynamic pressure ($\rho V^2/2$) (Incropera, et al., 2006) and is given as:

$$\Delta P = N_L f X \frac{\rho V^2}{2} \quad (6.34)$$

6.2.2.1 Heat transfer

The heat dissipation for the enhanced structure is related to the average temperature between the inlet and outlet T_m. The average heat transfer of the working fluid and the surface temperature is evaluated as:

$$T_m = \frac{T_i + T_e}{2} \quad (6.35)$$

$$T_{surf} = \frac{T_{surf_{inlet}} + T_{surf_{center}} + T_{surf_{exit}}}{3} \quad (6.26)$$

and:

$$h_{av} = \frac{Q_{conv}}{(A_{ht_{base}} + \eta_p A_{ht_p} + 2H_{ch}L_{ch})(T_{surf} - T_m)} \quad (6.37)$$

where η_p is the protrusion efficiency given as:

$$\eta_p = \frac{\tanh(m_p H_p)}{m H_p} \quad (6.38)$$

The Nusselt number is evaluated as:

$$Nu_{d_e} = \frac{h_{av} d_e}{k_f} \quad (6.39)$$

6.3 UNCERTAINTY ANALYSIS

According to the literature, the most common method, to analyse uncertainty in the temperature measurement, is the least-square fitting, (Taylor 1997). In general a linear relation between two variables x and y is given as:

$$y = C + Mx \tag{6.40}$$

Therefore, the relation between the temperature value and associated uncertainty is presented as:

$$T = C + M\theta \tag{6.41}$$

where, T is the measured temperature, θ is the exact reference temperature in the calibration pot, while C is the intercept and M is the gradient. Both can be evaluated as:

$$C = \frac{\Sigma\theta^2\Sigma T - \Sigma\theta\Sigma\theta T}{\Delta} \tag{6.42}$$

$$M = \frac{N\Sigma T\theta - \Sigma\theta\Sigma T}{\Delta} \tag{6.43}$$

$$\Delta = N\sum\theta^2 - \left(\sum\theta\right)^2 \tag{6.44}$$

The results of Equations (6. and (6. give the best estimates for *N = 10* measured points.

The uncertainty in measurements of θ for values (± 0.03 K was neglected as specified by the manufacture), therefore, the temperature measurement points would be distributed around the calibration line. The average deviation of the measured temperature T_i is given as:

$$\sigma_T = \sqrt{\frac{1}{N-2}\sum_{i=1}^{N}(T_i - C - M\theta_i)^2} \tag{6.45}$$

This is the uncertainty of the temperature measurement.

The uncertainty of the constant C and M are given as:

$$\sigma_C = \sigma_T \sqrt{\frac{\Sigma\theta^2}{N\Sigma\theta^2 - (\Sigma\theta)^2}} \tag{6.46}$$

$$\sigma_M = \sigma_T \sqrt{\frac{N}{N\Sigma\theta^2 - (\Sigma\theta)^2}} \tag{6.47}$$

When readings are taken from a thermocouple, $T_{meas,}$ will be converted into calibrated value ($\theta_{calib} = T$) in following form:

$$\mathrm{T} = \frac{1}{M} T_{meas} - \frac{C}{M} \tag{6.48}$$

and then the following equation can be utilized to find the uncertainty:

$$\delta\mathrm{T} = \sqrt{\left(\frac{\partial \mathrm{T}}{\partial T_{meas}} \sigma T_{meas}\right)^2 + \left(\frac{\partial \mathrm{T}}{\partial \mathrm{C}} \sigma_C\right)^2 + \left(\frac{\partial \mathrm{T}}{\partial \mathrm{M}} \sigma_M\right)^2} \tag{6.49}$$

The corresponding uncertainty for each thermocouple is presented in Figure 6.13. The uncertainty increased with temperature. According to Figure 6.13 the calibration process has decreased significantly the measurement error.

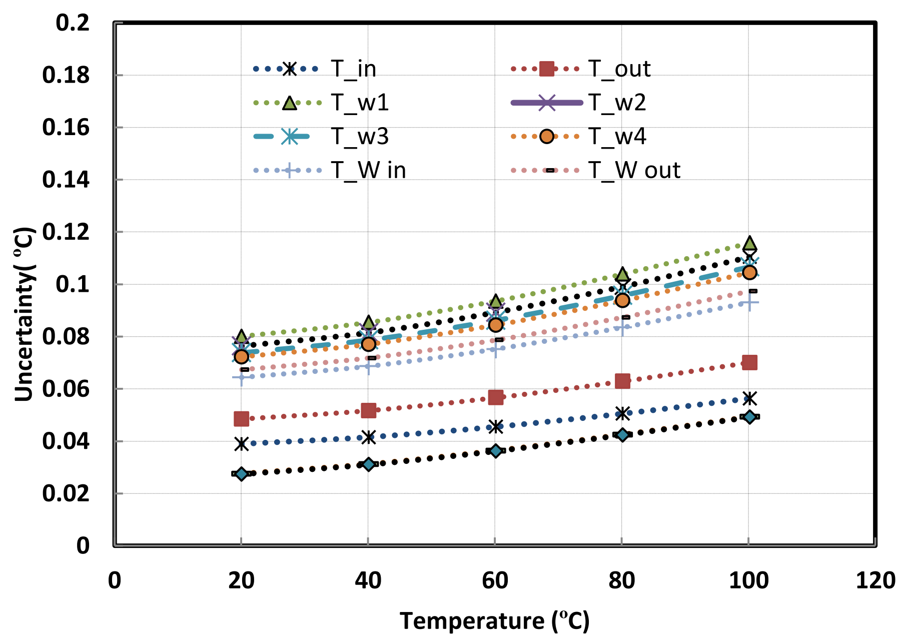

Figure 6.13: The uncertainty of the temperature measurements.

6.3.1 Geometrical parameters

Dimensions of the test sample such as channel width W_{ch}, height of the channel H_{ch}, and length of the channel L_{ch}, were computed by averaging several measurements. Due to the high accuracy of the measurement device (Tesa micro-hite 35) the measurement uncertainty is reduced drastically to 0.1 µm. The uncertainties in both areas i.e. that of the flow cross-section and the heat transfer area are evaluated as:

$$\frac{\partial A_c}{A_c} = \left[\left(\frac{\partial W_{ch}}{W_{ch}} \right)^2 + \left(\frac{\partial H_{ch}}{H_{ch}} \right)^2 \right]^{1/2} \tag{6.50}$$

$$\frac{\partial A_{ht}}{A_{ht}} = \left[\left(\frac{\partial W_{ch}}{W_{ch}} \right)^2 + \left(\frac{\partial H_{ch}}{H_{ch}} \right)^2 + \left(\frac{\partial L_{ch}}{L_{ch}} \right)^2 \right]^{1/2} \tag{6.51}$$

The hydraulic diameter uncertainty is composed of two uncertainties, that of the area and that of the perimeter. The uncertainty is evaluated as:

$$\frac{\partial D_h}{D_h} = \left[\left(\frac{\partial A_c}{A_c} \right)^2 + \left(\frac{\partial W_{ch}}{W_{ch} + H_{ch}} \right)^2 + \left(\frac{\partial H_{ch}}{W_{ch} + H_{ch}} \right)^2 \right]^{1/2} \tag{6.52}$$

The error associated with the Reynolds number integrates the errors of velocity, density, the hydraulic diameter and dynamic viscosity. The physical properties as density and viscosity will be assumed to be accurate; therefore the Reynolds number error will be given as:

$$\frac{\partial \mathrm{Re}_{\mathrm{Dh}}}{\mathrm{Re}_{\mathrm{Dh}}} = \left[\left(\frac{\partial \mathrm{D_h}}{D_h} \right)^2 + \left(\frac{\partial V}{V} \right)^2 \right]^{1/2} \tag{6.53}$$

The velocity uncertainty is a function of the mass flow rate, cross flow area, and density uncertainties. The density is assumed to be constant; therefore, the velocity uncertainty is evaluated as:

$$\frac{\partial V}{V} = \left[\left(\frac{\partial m}{m} \right)^2 + \left(\frac{\partial A_c}{A_c} \right)^2 \right]^{1/2} \quad (6.54)$$

6.3.2 Heat transfer

The heat transfer rate uncertainty is evaluated based on the uncertainty of the enthalpy rise. The specific heat has been assumed constant for a given bulk temperature. Therefore, the uncertainty depends on the uncertainty of the mass flow rate and the temperature differences between the outlet and the inlet.

$$\frac{\partial Q}{Q} = \left[\left(\frac{\partial \dot{m}}{\dot{m}} \right)^2 + \left(\frac{\partial \Delta T_{e_i}}{\Delta T_{e_i}} \right)^2 \right]^{1/2} \quad (6.55)$$

The uncertainty of the heat transfer rate is shown in the Figure 6.14 as a function of heat transfer rate.

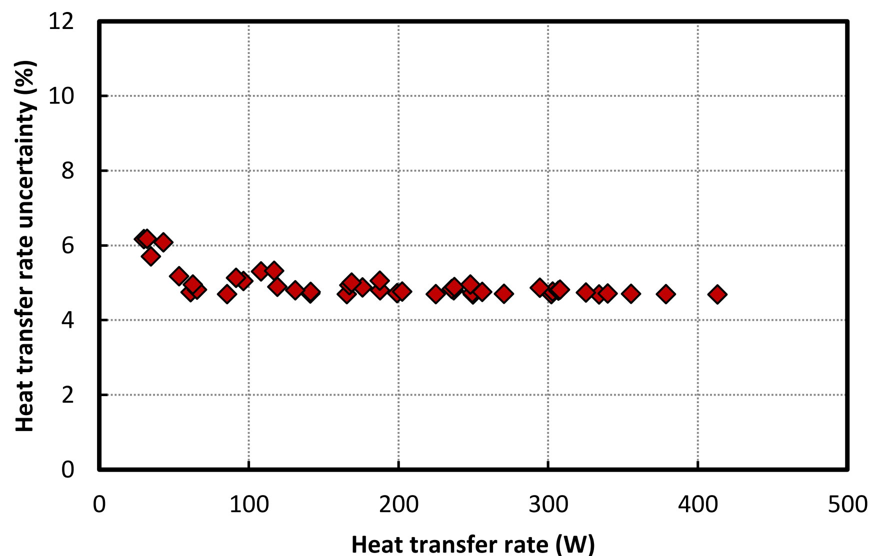

Figure 6.14: Uncertainty versus heat transfer coefficient.

The heat transfers coefficient uncertainty is a function of the combined uncertainties of the mass flow rate, heat transfer area, and the logarithmic mean temperature difference. The uncertainty of the logarithmic mean temperature difference is expressed as:

$$\frac{\partial \Delta T_{LMTD}}{\Delta T_{LMTD}} = \left[\left(\frac{\partial \Delta T_2}{\Delta T_2 - \Delta T_1} \right)^2 + \left(\frac{\partial \Delta T_1}{\Delta T_2 - \Delta T_1} \right)^2 + \left(\frac{\frac{\partial \Delta T_2}{\Delta T_1}}{\frac{\Delta T_2}{\Delta T_1} \ln\left(\frac{\Delta T_2}{\Delta T_1} \right)} \right)^2 \right]^{1/2} \tag{6.56}$$

The uncertainty of the heat transfer coefficient is given as the sum of the uncertainties of heat transfer rate, heat transfer area, and logarithmic mean temperature difference:

$$\frac{\partial h}{h} = \left[\left(\frac{\partial Q}{Q} \right)^2 + \left(\frac{\partial A_{ht}}{A_{ht}} \right)^2 + \left(\frac{\partial \Delta T_{LMTD}}{\Delta T_{LMTD}} \right)^2 \right]^{1/2} \tag{6.57}$$

The uncertainty of the heat transfer coefficient as function of the heat transfer coefficient is presented in Figure 6.15.

Figure 6.15: Uncertainty of heat transfer coefficient versus heat transfer rate.

The uncertainty of the Nusselt number is expressed as a function of the heat transfer coefficient and hydraulic diameter, while the conductivity of the fluid is assumed constant.

$$\frac{\partial Nu}{Nu} = \left[\left(\frac{\partial h}{h} \right)^2 + \left(\frac{\partial D_h}{D_h} \right)^2 \right]^{1/2} \tag{6.58}$$

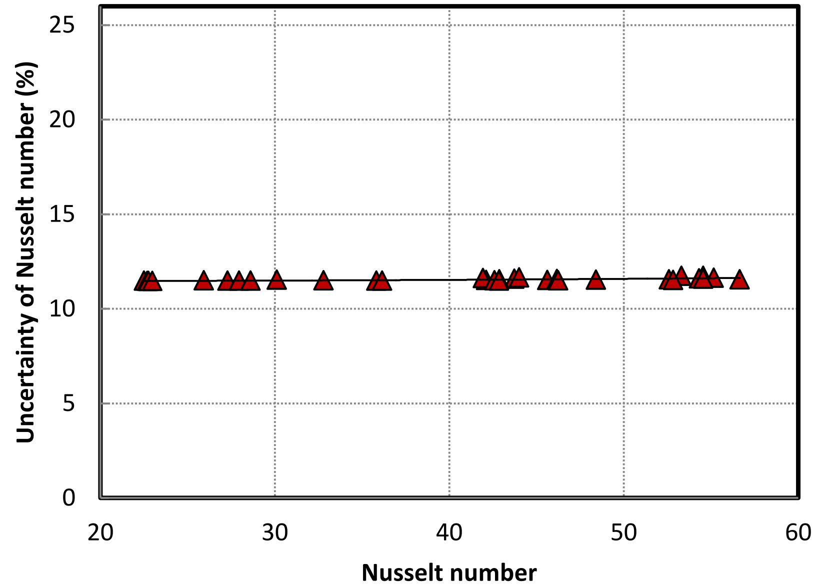

Figure 6.16: Uncertainty of the Nusselt number versus Nusselt number.

6.3.3 Friction factor

The friction factor uncertainty is a function of the pressure drop, hydraulic diameter, length, the velocity and fluid density. The uncertainty of density is assumed to be very small and can be neglected. The friction uncertainty can be expressed as:

$$\frac{\partial f}{f} = \left[\left(\frac{\partial \Delta P}{\Delta P} \right)^2 + \left(\frac{\partial D_h}{D_h} \right)^2 + \left(\frac{\partial L}{L} \right)^2 + \left(\frac{\partial V}{V} \right) \right]^{1/2} \qquad (6.59)$$

The uncertainty of the friction factor is evaluated to be approximately ±11%, Figure 6.17.

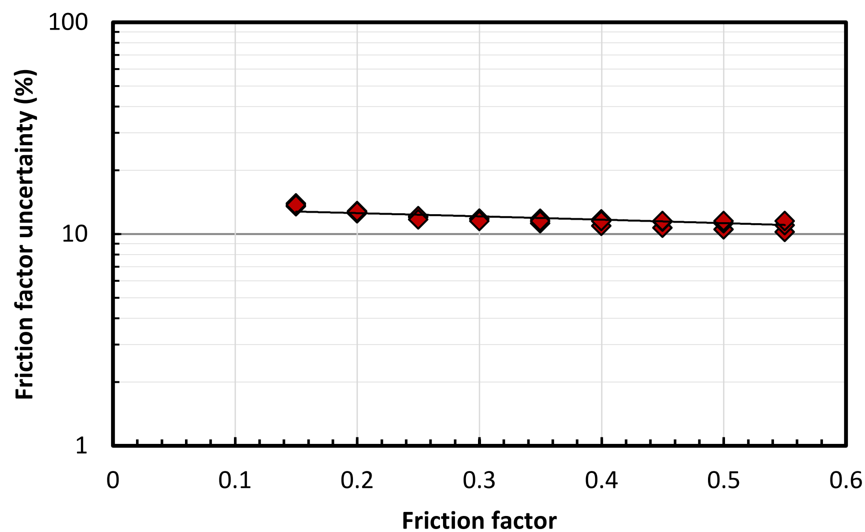

Figure 6.17: Uncertainty of the friction factor coefficient versus friction factor coefficient.

6.3.4 Summary

The application of general uncertainty analysis shows the correct values of the measurements that cannot be noticed in the data reduction correlations. The thermocouple uncertainty was reduced noticeably from a two scale calibration process. The friction factor uncertainty was related to pressure drop uncertainty, since the uncertainty in the geometric measurements was low.

6.4 VALIDATION OF THE TEST RIG

The heat transfer experimental data and the CFD data for the smooth test sample are validated with Stephens (1956) correlation for the flow between parallel plates. While, the pressure drop results for the experimental work

and the CFD study have been validated with the methodology of Shah and London (1974) for the friction factor, Equation 6.1. The experimental and CFD results are in good agreement with the predictions, the following present heat transfer and pressure drop results.

6.4.1 Experimental and CFD data for the heat transfer coefficient

The Nusselt number increase with the increase of mass flow rate. The evaluation of the heat transfer performance for developing flows is a complex problem due to the entrance effects. According to Figure 6.18, the CFD data are in good agreement with the experimental data and those predicted by (Stephan, 1956). The CFD, heat transfer and flow evaluation are an ideal case; while experimental work in laboratory condition is affected by a range of factors (ambient temperature fluctuation, temperature and flow measurements). Moreover, entrance effects are complex and can affect the temperature measurement (no-slip conditions create a large temperature gradient between heated surface and the flow); therefore the location of thermocouples can have an effect. The experimental results can be affected by the measurement point in solid and fluid (i.e. if the flow distribution is not very well equalized the thermocouple that is placed in a faster flow line will give a reading that is not representative of the cross section). However the error bars on the experimental data provide a better understanding of the phenomena. The discrepancy of the current experimental data from the CFD varies from 0% to the highest 10% for the Nusselt number, see Figure 5.26. Overall taking into account the error bars the CFD and experimental data are in agreement with each other. A discrepancy of 10% of engineering systems between the CFD and test results is widely acceptable since both experimental and numerical methods can produce errors.

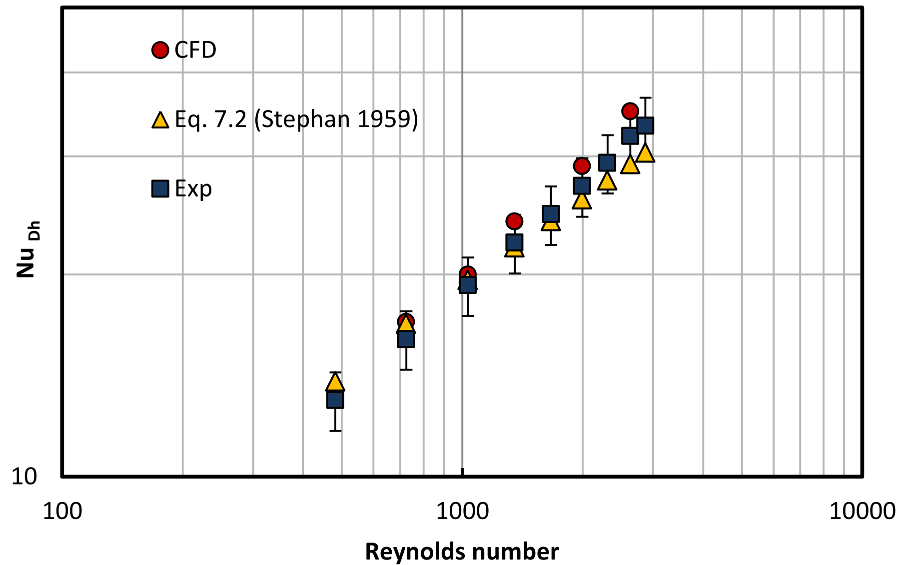

Figure 6.18: Nusselt number results for the CFD study, experimental work and Stephan (1959) Equation (7.2) versus Reynolds number.

6.4.2 Experimental and CFD data for the pressure drop

A comparison between experimental pressure drop and CFD data is presented in Figure 6.19 According to Figure 6.19 the experimental and CFD data are in accordance. Pressure drop decreased in the flow direction and increased with increase of the Reynolds number. The pressure drop at the entrance is increased to overcome the no-slip conditions at the entrance. Overall, both experimental and CFD analyses produced the same results.

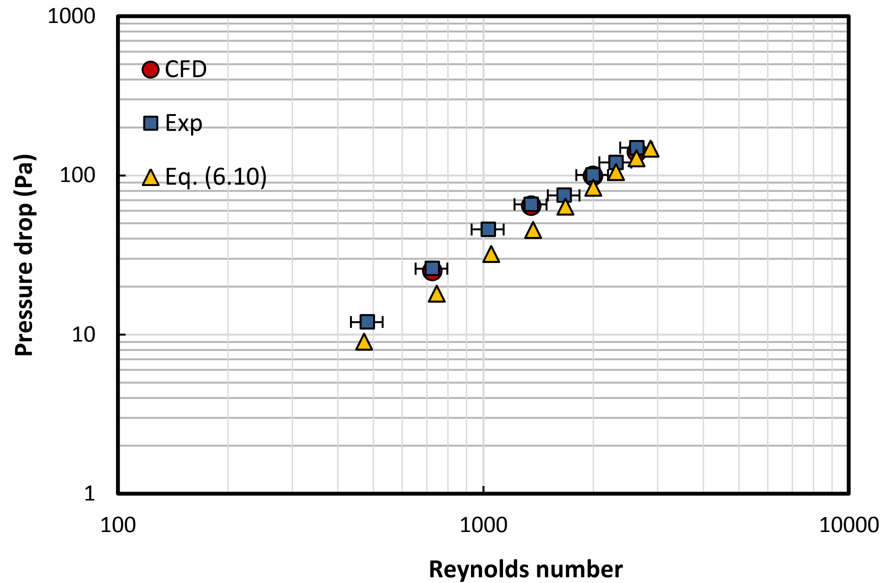

Figure 6.19: Comparison between experimental, CFD and prediction from Equation (6.10) of pressure drop for smooth sample.

6.4.3 Summary

The simplified smooth sample was analysed using Autodesk CFD 2013. The CFD analysis evaluated heat transfer and flow characteristics. The CFD results are in agreement with the experimental data. The main conclusions are drawn below.

CFD simulation provides significant information in relation to the performance. The experimental temperature variation on the solid part of the test module is predicted accurately by the CFD analysis. Heat transfer in the fluid flow is expressed in terms of Nusselt number; predictions by the CFD are in a good agreement with the experimental data and evaluations from Equation 7.2. All CFD results are inside the error band of the experimental data. The entrance effects and the developing flow regime increased the complexity in the flow behaviour, therefore cannot be predicted very accurately. This will require a very intensive mesh in this area (this requires large processing power and time) to extract the accurate temperature distribution. However, taking into account the error bars in the experimental

data, prediction of heat transfer from the CFD is in the acceptable values for a complex fluid flow in engineering systems.

The pressure drop is related to the pumping power and as a consequence to the efficiency of the liquid cold plate. CFD reveals the effects of the entrance region in all four analyses. Pressure had a tendency to increase at the entrance, however, after that it decreases gradually in the flow direction behind this region. The experimental and CFD results are in accordance. The effect of the premixing chamber proved effective since it reduced the velocity variability effects and equalized the flow at the entrance region.

7 EXPERIMENTAL RESULTS

This chapter presents the heat transfer and pressure drop experimental data of three electron beam enhanced samples and a smooth surface. Due to the complex nature of single phase flow over irregular (electron beam treated) surfaces, it is difficult to be investigated analytically. The experimental results are analysed by using two methods that can evaluate the efficiency improvement and compare results with current conventional enhancement techniques. The first method analyses the electron beam treatment as a surface irregularity, and does not take into account the surface area increase. The second method treats the enhancement as a regular pin-fin structure and takes into account the surface area increase and the effect on the flow. The following will present the experimental results that are processed using both methodologies.

Flow characteristics and heat transfer rate in the smooth (untreated) surface were examined as a base for the validation of the test facility and the assessment of the experimental methodology. Experimental data are compared to the available correlations and the CFD data. Therefore, it can be used as a baseline data in comparison with the enhanced surfaces. The smooth and three electron beam enhanced samples were tested using a similar experimental procedure and data processing methodology

7.1 ESTIMATION OF HEAT LOSS

The energy balance comparison was performed for three electron beam enhanced samples and a smooth sample, under a variety of mass flow rates that ranged from 0.005 l/s to 0.045 l/s, and increasing heat inputs that varied

from 100 W to 600 W. The energy balance evaluation is an important procedure because it provides an understanding of the thermal process in the experiment and quantifies the energy losses. In an ideal case, the electrical energy input into the test module would have been transferred completely into the water flow. However, in reality a part of the energy from the cartridge heaters[49] is conducted through the copper and transferred to the surroundings through insulation. These heat losses can be observed by comparing the electrical heat input to the heat output, enthalpy rise of water. The following presents the energy balances for each sample, where the difference is the energy loss. The measured data is presented graphically to compare the electrical power entering via the cartridge heaters with the heat transferred into the water from each sample. Data shows the variance of the heat output to the heat input for increasing mass flow rates.

Sample S1

During the experiment the test module was well insulated to reduce energy losses and reach a steady state experimental condition. According to Figure 7.1 overall heat losses are less than 20%.

[49] Electrical resistor insulated and encapsulated with a metallic cover.

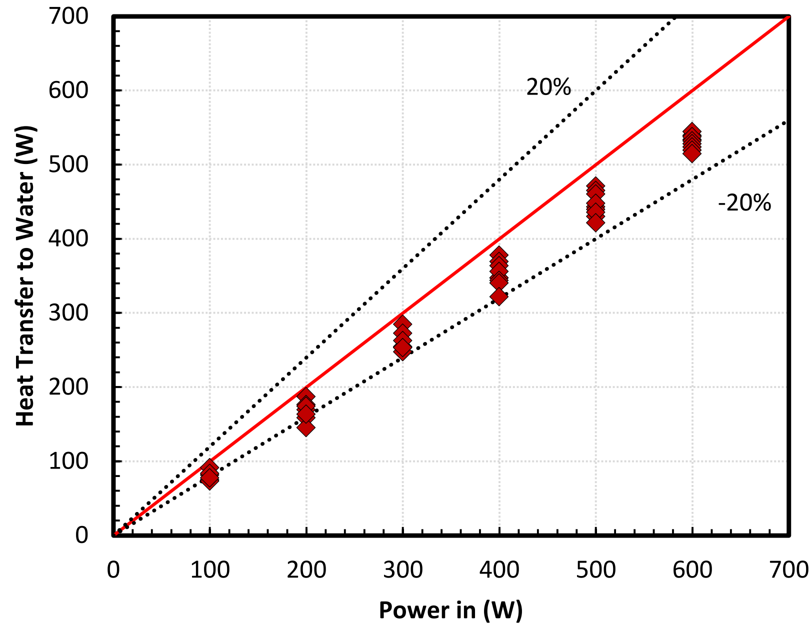

Figure 7.1: Heat transfer rate to water versus electrical power input, for sample S1.

Sample S2

The comparison between heat input and heat output for sample S2 is given in Figure 7.2. Heat losses are less than 20% and remain constant for all mass flow rates. In comparison with sample S1 heat losses remain at the same level. This shows a consistency in the experimental process.

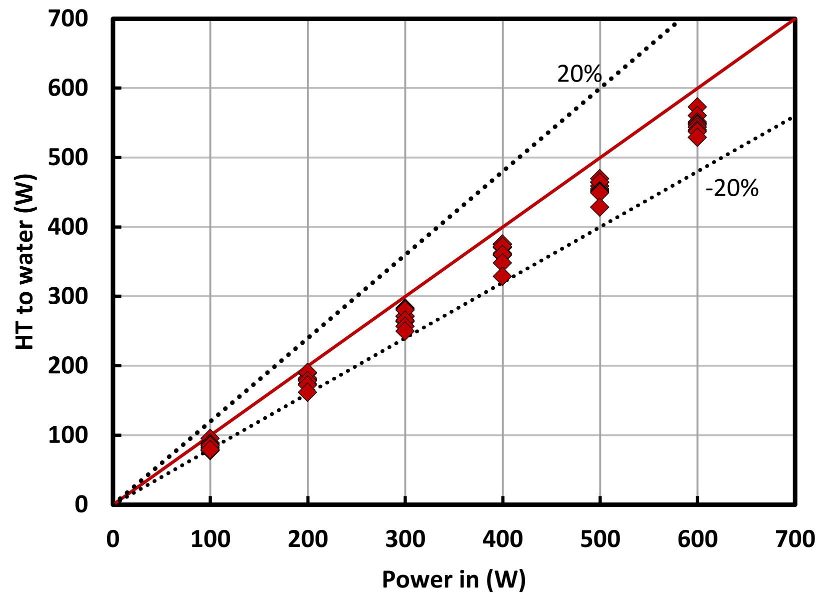

Figure 7.2: Heat transfer rate to water versus electrical power, for sample S2.

Sample S3

The energy balance for sample S3 is presented in Figure 7.3. The heat losses are constant and remain lower than 20%. This is in line with the results gained from samples S1 and S2.

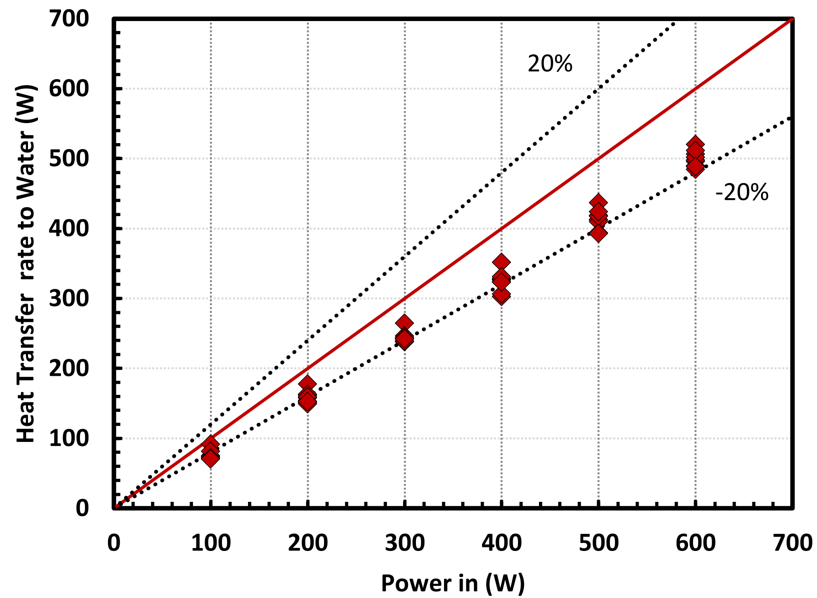

Figure 7.3: Heat transfer rate to fluid versus electrical power input, for sample S3.

Smooth sample

The heat losses for the smooth sample are shown in Figure 7.4. In this case heat losses are approximately 20%. The increase of heat losses compared to the enhanced samples is higher because it is affected by the temperature increase on the smooth test sample due to the low heat transfer coefficient in this case.

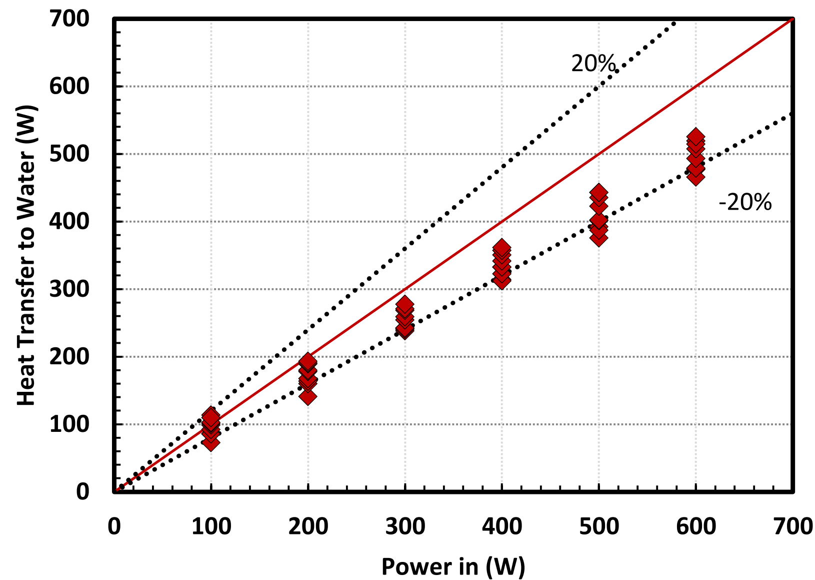

Figure 7.4: Heat transfer rate to fluid versus Electrical Power, for the smooth sample.

7.2 FIST METHOD

As described in the previous chapters the electron beam treatment generates protrusions that have irregular geometrical surface characteristics and cannot be treated as a regular structure. Therefore, in the first method, the heat transfer and the pressure drop results have been processed by treating the enhancement as a surface irregularity and using a similar assessment methodology to that of the smooth surface. The experimental data for the enhanced structures are compared to those of the smooth surface to show the benefit of the enhancement.

7.2.1 Friction factor

The friction factor variation with an increase of Reynolds number for all four samples is plotted in Figure 7.5. The data indicates a significant scatter of the friction factor for low Reynolds number less than 600. As the Reynolds number increases the scatter is much less and the friction factor follows a

weak decreasing trend with an increase of Reynolds number. The theoretical smooth sample friction factor f_{app} for developing flow has been obtained using the methodology of Shah and London (1978) described above; see Equation (6.8), while for developed flow in a rectangular cross section Equation (6.11) is used. This is compared to the experimental results obtained using Equation (6.12) with the pressure and velocity measurements.

7.2.1.1 Comparison of the experimental friction factor with available correlations

According to Figure 7.5 the experimental results for the smooth sample are in good agreement with the predicted data. At a Reynolds number below 600, friction factor is affected by viscous forces as predicted by Equation 6.11. While for a Reynolds number above 600, the flow rate increases and overcomes the viscous effects which is predicted by Equation (6.8).

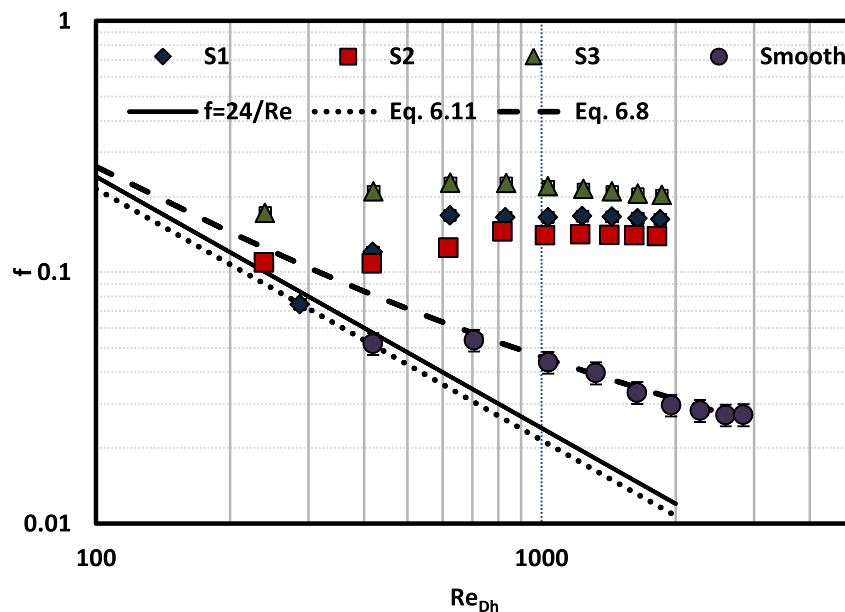

Figure 7.5: Friction factor versus Reynolds number for all four samples.

7.2.1.2 Friction factor correlations

Friction factor expressions based on the experimental data for the three enhanced samples are developed in the form of Blasius type correlations utilizing a power line fit function and are summarized in Table 7.1. The correlations predict the data for 600≤Re≤1900. The mean absolute percentage error (MAE) given in Table 7.1 for each correlation is defined as:

$$MAE = \frac{1}{M}\sum \frac{\left|f_{\exp} - f_{pred}\right|}{f_{\exp}} * 100\% \qquad (7.1)$$

where, M is the total number of data points.

Table 7.1: Friction factor data correlations, Reynolds number applicability and mean absolute error.

Test Sample	Correlation	Reynolds number	MAE %
S1	$f = 0.17 - 0.9*10^{-3}Re^{0.33}$	600-1900	2.18
S2	$f = 0.18 - 3.4*10^{-3}Re^{0.33}$	600-1800	2.8
S3	$f = 0.31 - 8.9*10^{-3}Re^{0.33}$	600-1800	1.2
Smooth	$f = 0.08-3.9*10^{-3}Re^{0.33}$	600-1800	4.1

7.2.1.3 Thermal performance as function of pumping power

Figure 7.6 presents the values of thermal resistance versus pumping power, as suggested by (Wang, et al., 2007) and (Peles, et al., 2005), in order to compare enhancement techniques. The thermal resistance decreases with increasing pumping power for all samples due to increase of fluid velocity and hence the convection heat transfer coefficient. As seen in the Figure 7.6 for a given pumping power the thermal resistance of all three samples is much lower than the resistance of the smooth plate verifying the effectiveness of the enhanced surfaces. The thermal resistance of samples S1 and S3 is similar for a range of pumping powers while the resistance of sample S2 is higher, particularly at higher pumping power.

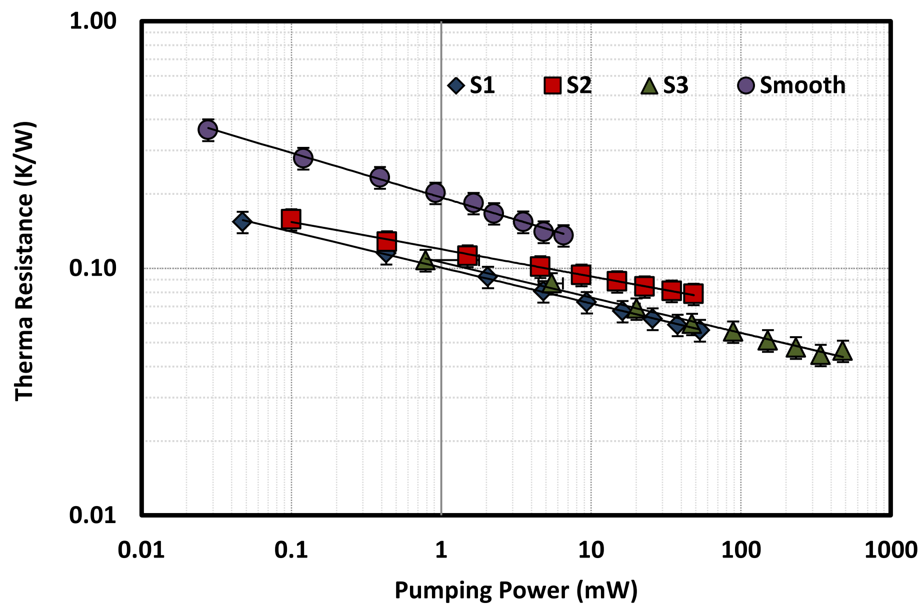

Figure 7.6: Thermal resistance = 1/hA (K/W) for each sample.

7.2.2 Heat transfer

The variation of heat flux with the surface temperature at a constant 0.045 kg/s mass flow rate (Re ≈1850) for all four samples are presented in Figure 7.7. The heat flux increases linearly with the surface temperature for constant flow rate due to the increase of temperature difference between the fluid and the surface. The effectiveness of the enhanced surfaces is prominent. For example a heat flux of, 300 kW/m^2 can be transferred with a wall surface temperature of 33 ^{o}C for sample S3, while that increases to 36 ^{o}C and 47 ^{o}C for samples S1 and S2 respectively. For a similar heat flux the corresponding surface temperature for the smooth test section is 59 ^{o}C. These observations suggest that all treatments and in particular sample S3 and S1 can be suitable for removing high heat fluxes and maintain the electronic equipment at a relatively low operating temperature. Electron beam enhanced surfaces can achieve high heat fluxes, i.e. heat fluxes, increase by 20 kW/m^2 for each degree increase in the surface temperature for sample S3. Therefore, enhanced surfaces can be used effectively in cooling systems for automotive, high-performance and cost-performance

category. The electron beam enhancement technology can be applied on heat exchange equipment to improve natural and forced convection. Results show that electron beam enhanced surfaces can improve thermal efficiency, reduce the size of a heat exchange device, and improve reliability, safety and efficiency.

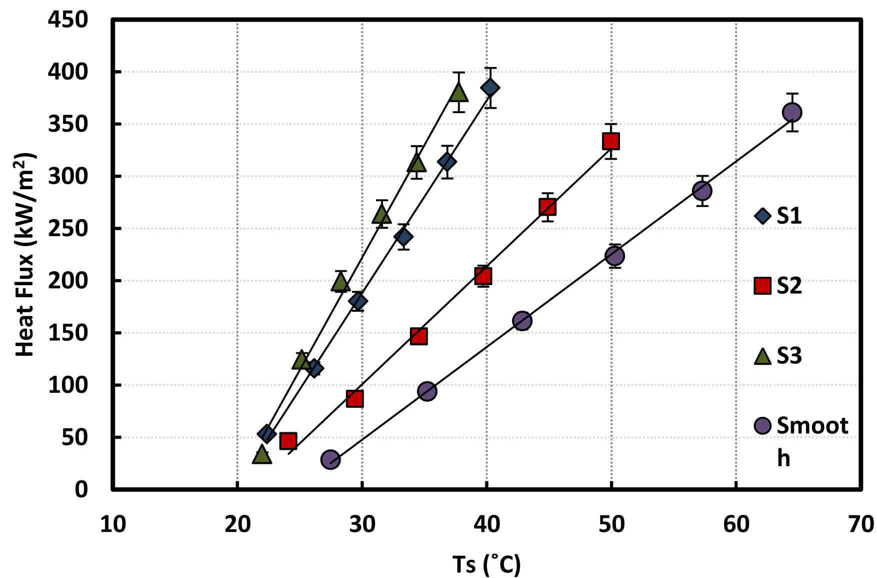

Figure 7.7: Heat flux versus surface temperature for constant mass flow rate of 0.045 kg/s, (Re ~ 1850) and inlet fluid temperature ≈19 ˚C.

Figure 7.8 presents the variation of the average Nusselt number with increasing Reynolds number. As observed in Figure 7.8, the Nusselt number increases with Reynolds number for all the test samples including the smooth test sample. The Nusselt number for sample S1 is approximately 3 times larger than that of the smooth test section, followed by sample S3 that depicts an increase in Nusselt number by approximately 2.5 times and sample S2 by approximately 2 times. The Nusselt number for the smooth sample was compared with that predicted from Stephan (1959), (Bejan & Kraus, 2003)for developing flow, given as:

$$Nu_{0-L} = 7.55 + \frac{0.024 x_*^{-1.14}}{1 + 0.0358 \Pr^{0.17} x_*^{-0.64}} \tag{7.2}$$

where, x_* is the dimensionless coordinate in the thermal entrance region given as follows:

$$x_* = \frac{x/D_h}{\mathrm{Re}_{D_h} \Pr} \tag{7.3}$$

The experimental data are in good agreement with Stephan's correlation.

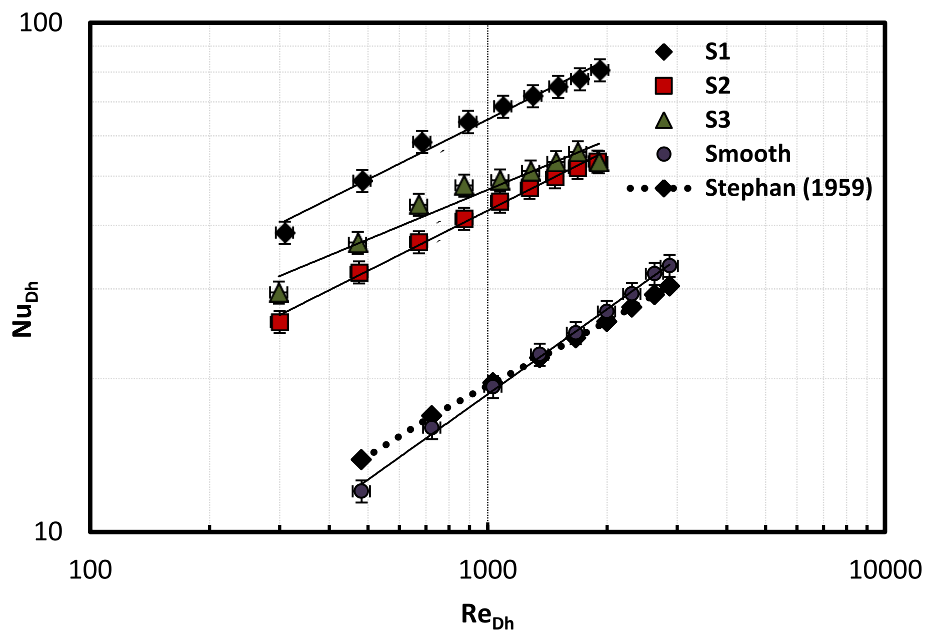

Figure 7.8: Nusselt number versus Reynolds number for all four samples.

7.2.2.1 Heat transfer correlations

The heat transfer data from the experimental work were correlated by a Dittus and Boelter type relationship of the form $Nu_{Dh}=CRe^{m}Pr^{n}$ utilizing the power line function, see Table 7.2. The mean absolute percentage error of an averaged Nusselt number is determined by employing an identical methodology to that of the friction factor Equation (7.1) and results are presented in Table 7.2.

Table 7.2: The heat transfer data correlations, Reynolds number applicability and mean absolute error.

Test Sample	Correlation	Reynolds number	MAE %
S1	$Nu_{Dh} = 3.52\ Re^{0.33} Pr^{1/3}$	290-1900	7.7
S2	$Nu_{Dh} = 2.38\ Re^{0.33}\ Pr^{1/3}$	230-1800	5.2
S3	$Nu_{Dh} = 2.63\ Re^{0.33}\ Pr^{1/3}$	230-1900	10

The comparison of the performance versus Reynolds number is presented in terms of the efficiency index, Figure 7.9: Efficiency index versus Reynolds number for three enhanced samples.. This is an important parameter in assessing the overall performance of an enhanced surface, (Han & Lee, 2005). This index can be defined as follows:

$$\eta = \frac{h/h_s}{f/f_s} \tag{7.4}$$

where, h is the heat transfer coefficient and f is the friction factor. Values with subscript *s* refer to the smooth or plain test section. High values indicate good surfaces, i.e. heat transfer rates are achieved without a significant penalty in pressure drop and hence pumping power. On the contrary, small values of the efficiency index, means that a high increase in pressure drop is required to achieve the enhancement level that may be needed. The efficiency index decreases rapidly with the Reynolds number for all the enhanced samples. Sample S1 and S3 have relatively better efficiency indexes compared to sample S2. This is due to the low heat transfer coefficient experienced in sample S2 in comparison with the other two.

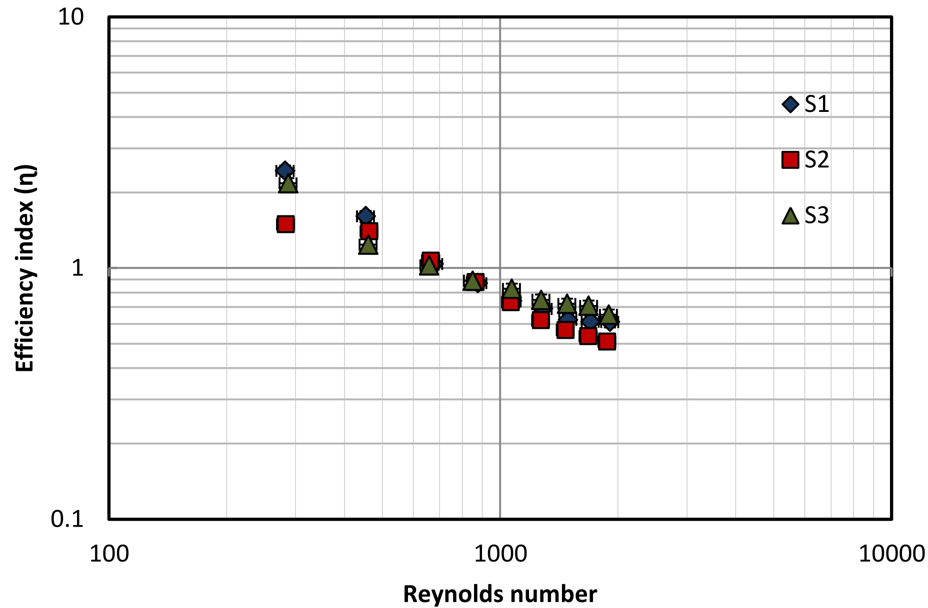

Figure 7.9: Efficiency index versus Reynolds number for three enhanced samples.

7.2.3 Summary

The primary aim of this study was to provide an experimental analysis of the heat transfer and the pressure drop for the laminar regime of deionized water flow in three electron beam enhanced surfaces, and compare these to a smooth surface tested under the same conditions. The results obtained have been presented and discussed in terms of friction factor and Nusselt number, and the following conclusions can be drawn:

Electron beam enhancement technology is a good way to improve heat removal capacity of liquid cooled plates. The three electron beam enhanced surfaces tested, have significantly higher Nusselt numbers compared to the smooth test section. However, the pressure drop is also higher and the best possible solution can only be reached if we consider the heat transfer performance, as well as the pressure drop together.

The friction factor in the smooth surface was in agreement with that predicted using established relationships such as that of Shah and London (1978). The pressure drop obtained with the EB enhanced structures was significantly higher than that of the smooth surface sample. The friction factor, as expected increases noticeably with the increase of the protrusion density, sample S3 which has the higher protrusion density and lowest hydraulic diameter gave the highest pressure drop. Sample S1 gave the highest Nusselt number followed by sample S3 and S2. The high heat transfer coefficients obtained confirm that the samples can meet the demand of high power heat removal. During the experimental work heat fluxes of 370 W/m^2 were removed from sample S3 with a surface temperature of 38 $^{\circ}C$. Additionally, for every 10 K increase in the surface temperature heat fluxes increased by, 200 kW/m^2.

The relationship between thermal resistance and pumping power was presented for practical evaluation. Enhanced samples S1 and S3 gave the lowest thermal resistance at a given pumping power. This is due to the high protrusion density and flow velocity. Therefore, if both the heat removal rates as well as pumping power are equally important these two samples should be chosen over the S2.

A comparison of the thermal and hydraulic performance was performed also by assessing the relationship between the efficiency index and the Reynolds number. Samples S1 and S3 achieved the highest efficiency index for a given Reynolds number. This is the result of their balanced hydraulic and thermal performance. Sample S2 performed better in pressure drop terms, but gave a low efficiency due to the low thermal performance. Therefore, if both the heat removal rate and the pumping power are equally important, S1 and S3 should be chosen over surface S2. Optimization of these structures is possible if we consider carefully the protrusion geometry and density and evaluate both the heat transfer and pressure drop performance.

7.3 SECOND METHOD

The accurate thermo-hydraulic evaluation of electron beam treated surfaces is challenging. The electron beam transfers a large amount of energy to melt and dislocates the material, this creates irregularities that are not easy to measure and characterise. However, attempts have been made to characterise the enhanced surface and to produce an equivalent regular model for the enhanced structure. The objective is to compare the experimental data with other available correlations and expand understanding of the performance.

The Electron beam enhanced structures are composed of protrusions of pyramidal shape that have irregularity on all sides of the surface. Furthermore, the base surface is also irregular due to the material excavation. Therefore, measurements have been taken to determine an equivalent diameter of each protrusion that can represent the geometry. Experimental data is compared to that of other researchers that have studied regular enhanced structures.

Heat transfer and pressure experiments were performed for mass flow rates ranging from 0.005 kg/s to 0.045 kg/s. The inlet temperature of the fluid was maintained close to 19 ^{o}C. Power input into the cartridge heaters ranged from 100 W to 600 W. The following part will present thermal and hydraulic results for each sample.

7.3.1 Flow characteristics

The pressure drop variation with an increase of Reynolds number for all four samples is plotted in Figure 7.10. The data shows that sample S2 has the lowest pressure drop for a given Reynolds number. Sample S1 shows lower pressure drop compared to sample S3, however, it also operates at a lower Reynolds number. Sample S3 has the highest pressure drop and it operates at relatively higher Reynolds number.

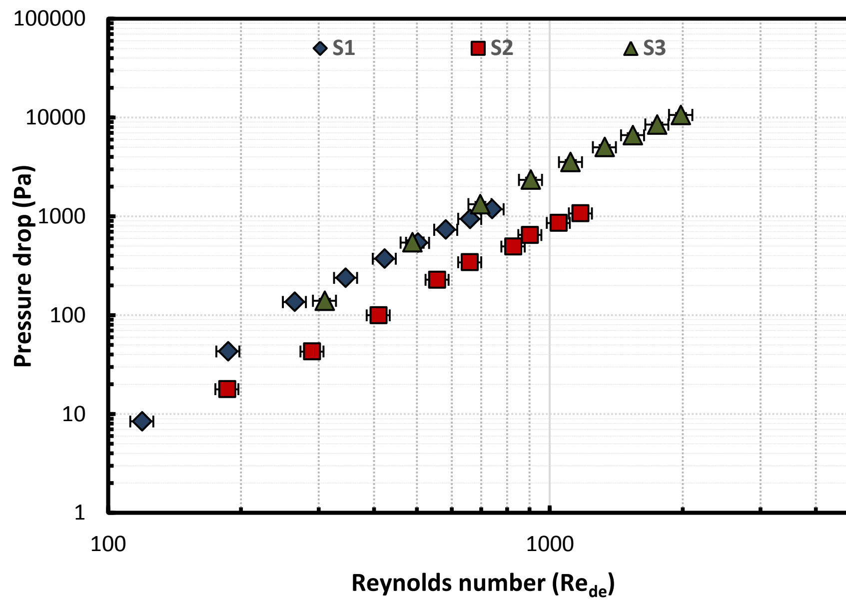

Figure 7.10: Pressure drop versus Reynolds number for three enhanced samples.

Fin friction factor for all three enhanced structures has been calculated using Equation (7.5) see (Incropera & DeWitt, 1996) and is given as:

$$f_{fin} = \frac{\Delta P}{N_L \chi \frac{\rho V^2}{2}} \tag{7.5}$$

where, f_{fin} is the friction factor of fin structure, N_L is the number of fin rows, X is a correction factor that is given in heat transfer literature, see (Incropera & DeWitt, 1996). The fin friction factor variation with an increase of Reynolds number for sample S1, S2 and S3 is presented in Figure 7.11, Figure 7.12 and Figure 7.13. The friction factor data shows a significant scatter for Reynolds number less than 250 for sample S1. A similar situation is observed for sample S2 and S3 for values of the Reynolds number up to 500. With the increase of Reynolds number, friction factor stabilises and follows a weak decreasing trend. Experimental data have been compared with those produced by Metzeger, et al. (1982) and Moores & Joshi (2003) for pin-fin structures see Table 3.3.

7.3.2 Comparison of the fin friction factor with other researchers

According to Figure 7.11 fin friction factors values of sample S1 for Reynolds number less than 250 are unstable, due to the inlet region and also the pressure drop is very small, and the limitation of the equipment. However, with the increase of Reynolds number, the friction factor stabilises and after that decreases slightly with an increase in Reynolds number. The experimental fin friction factor for Reynolds number larger than 250 becomes closer to the predicted values of Metzeger, et al. (1982). With the increase of Reynolds number predicted values are in good agreement with the experimental data.

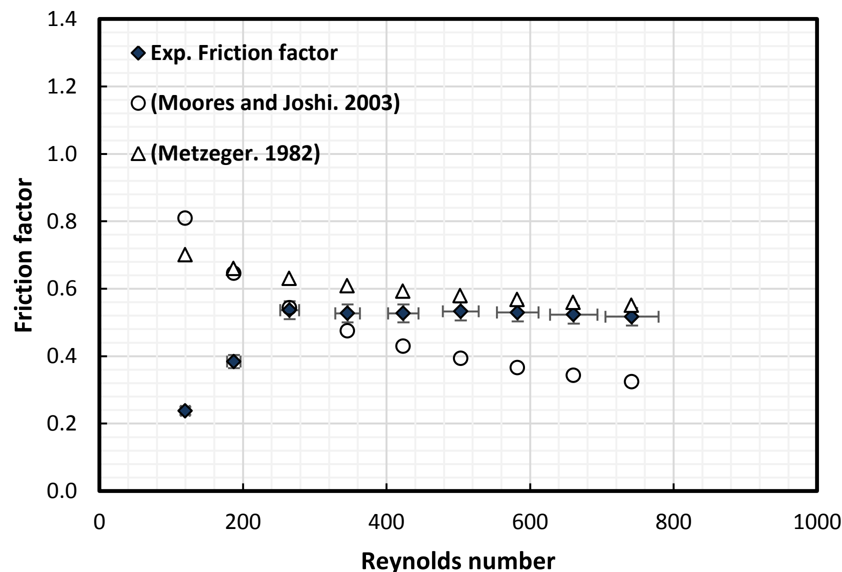

Figure 7.11: Friction factor versus Reynolds number for Sample S1.

Fin friction factor for sample S2 is presented in Figure 7.12. Fin friction factor for Reynolds lower than 500 is scattered due to the limitation of the equipment to measure a very low pressure drop. With an increase of Reynolds number, friction factor stabilises and can be predicted from the Moores & Joshi (2003) correlation, Figure 7.12

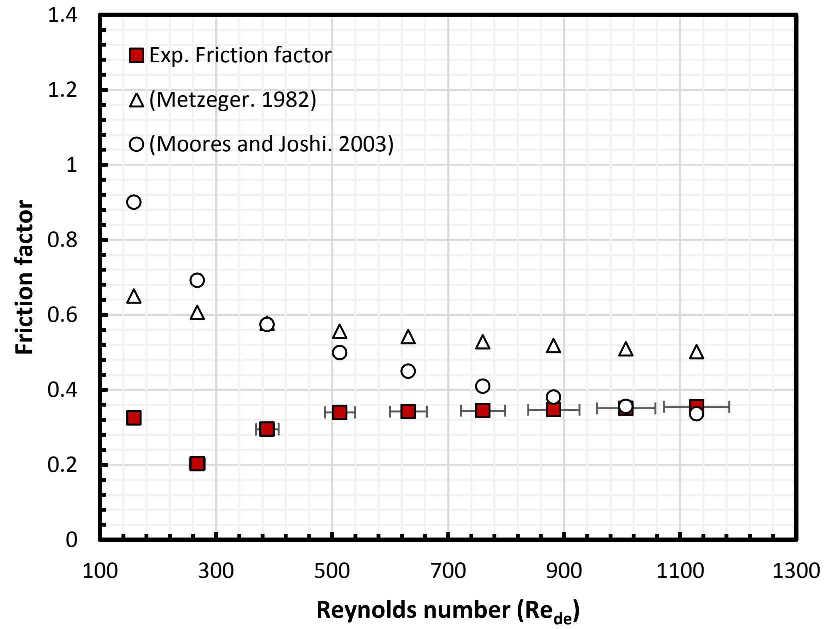

Figure 7.12: Friction factor versus Reynolds number for sample S2.

According to Figure 7.13 fin friction factor for the sample S3 at low Reynolds number <500 is unstable due to the equipment limitation, however stabilises with the increase of Reynolds number over 600. The experimental fin friction factor lies between those predicted from correlations of (Moores & Joshi, 2003) and (Metzeger, et al., 1982a)

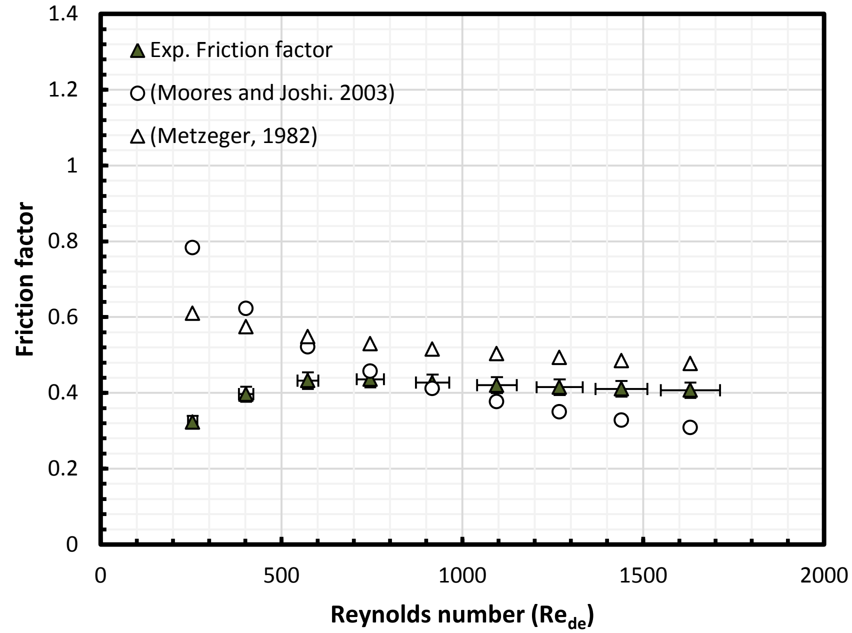

Figure 7.13: Friction factor versus Reynolds Number for sample S3

The experimental data for the fin friction factor in three enhanced samples was correlated utilizing a power line fit function and is presented in a Blasius type form correlation $f=mRe^n$ in Table 7.3. The mean percentage error (MAE) was calculated as previously explained in Equation 7.1 and is included in Table 7.3.

Table 7.3: Friction factor data correlations, Reynolds number applicability and mean absolute error.

Test Sample	Correlation	Reynolds number	MAE %
S1	$f=0.5969Re_{de}^{-0.02}$	350-740	11
S2	$f=0.2433Re_{de}^{0.0529}$	500-1100	8.9
S3	$f=0.7817\ Re_{de}^{-0.088}$	700-1600	15

Figure 7.14 presents the variation of the heat transfer coefficient with pressure drop. Sample S2 and S3 have similar values of the pressure drop; however the heat transfer coefficient of sample S1 is higher. Sample S3 has the highest pressure drop and also the highest heat transfer coefficient.

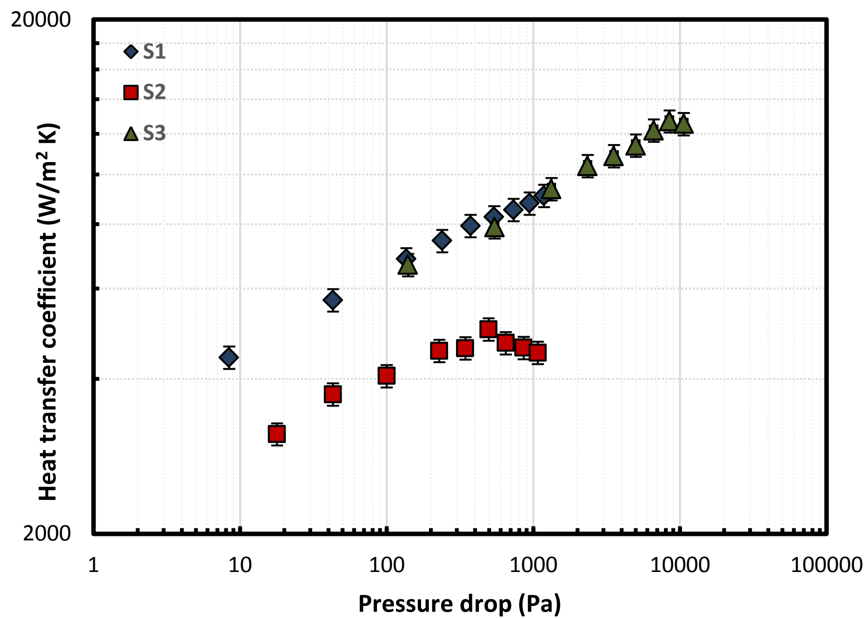

Figure 7.14: Heat transfer versus Pressure drop for three enhanced samples

7.3.3 Heat transfer characteristics

Figure 7.15 presents the variation of heat transfer coefficient with the Reynolds number for three electron beam enhanced samples. It is important to notice that in comparison with the first method of the evaluation the second method utilizes a Reynolds number that was calculated as a function of equivalent protrusion diameter d_e. According to Figure 7.15 the heat transfer rate increases with Reynolds number for all three samples. Sample S2 shows the lowest heat transfer rate. Heat transfer data reveal a transition effect that is observed for Reynolds above 800 for sample S2. The same phenomenon has been monitored by (Short, et al., 2002, a).

Sample S1 operates at Reynolds number 100 to 800 and it has a heat transfer rate 2 times larger than sample S2 that is comparable with sample S3 for Reynolds number ranging from 300 to 800. Sample S3 operates at higher Reynolds number compared to samples S1 and S2 and therefore obtains the highest heat transfer rate for a Reynolds number of 2000 when it is in the range of 12540 W/m^2K.

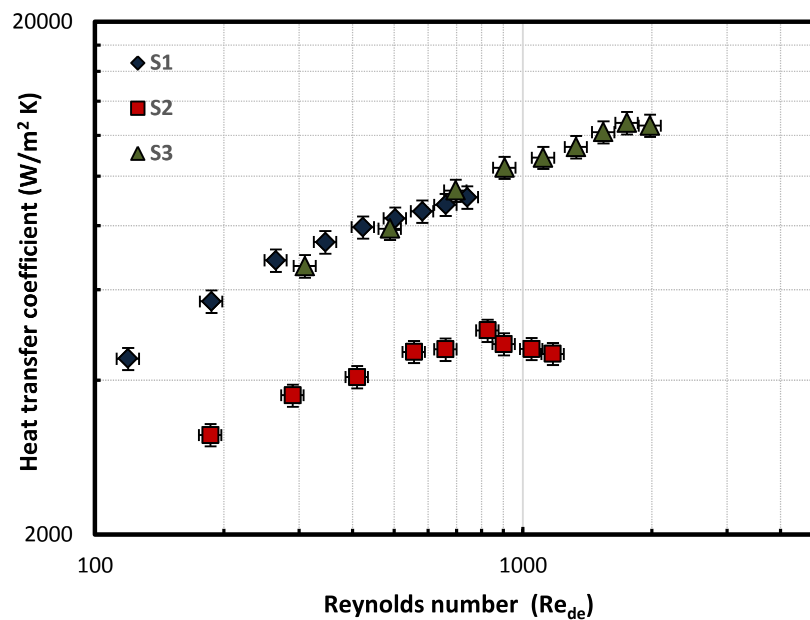

Figure 7.15: Heat transfer coefficient of equivalent pin-fin structure versus Reynolds number for three enhanced samples.

7.3.4 Comparison of experimental Nusselt number with other researchers

Experimental data for the single phase flow are compared in terms of the Nusselt number with other published literature in this area. There are a large number of correlations which can be found in the literature. Some of these correlations represent particular geometries and a set of conditions to fit their own experimental results. In the literature review, it is apparent that the majority of correlations are mainly produced for regular pin-fin structures. The methodology developed by Zukauskas (1987) for long tubes is deployed widely to assess the thermal and hydraulic experimental results on pin-fin geometries. Zukauskas's correlations have been developed for a range of Reynolds number, fin density, and pattern configurations (in-line and staggered), see (Incroprera & DeWitt, 1996). However, those correlations cannot be very accurate to assess thermo-hydraulic performance of pin-fin structures because it was developed for large tube banks.

In this section the experimental data have been compared to the research studies that evaluate pin-fin enhancement technology, i.e. (Liu, et al., 2011), (Short, et al., 2002) and (Short, et al., 2002, a) see Table3.2.

According to Figure 7.16 Nusselt number increases with Reynolds number for sample S1. Experimental data are in good agreement with Short et al (2002) correlation. Liu et al. (2011) correlation shows lower values of the Nusselt number for Reynolds 100 to 400, while for Reynolds higher than 400 predicts accurately the experimental data.

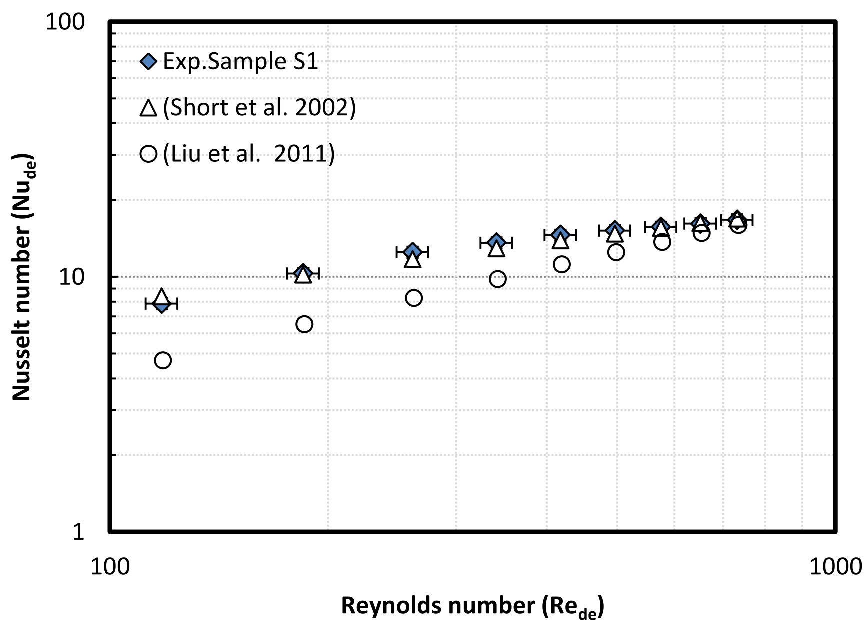

Figure 7.16: Nusselt number versus Reynolds number for sample S1.

Nusselt-number for the sample S2 increases with the increase of Reynolds number, see Figure 7.17. Values of the Nusselt number for Reynolds number less than 800 in the current study are higher compared to (Short et al. 2002) and (Liu et al. 2011) correlations. However, Nusselt number shows a transitional effect for Reynolds numbers over 900 and in this zone Liu et al (2011) correlation can predict the experimental data.

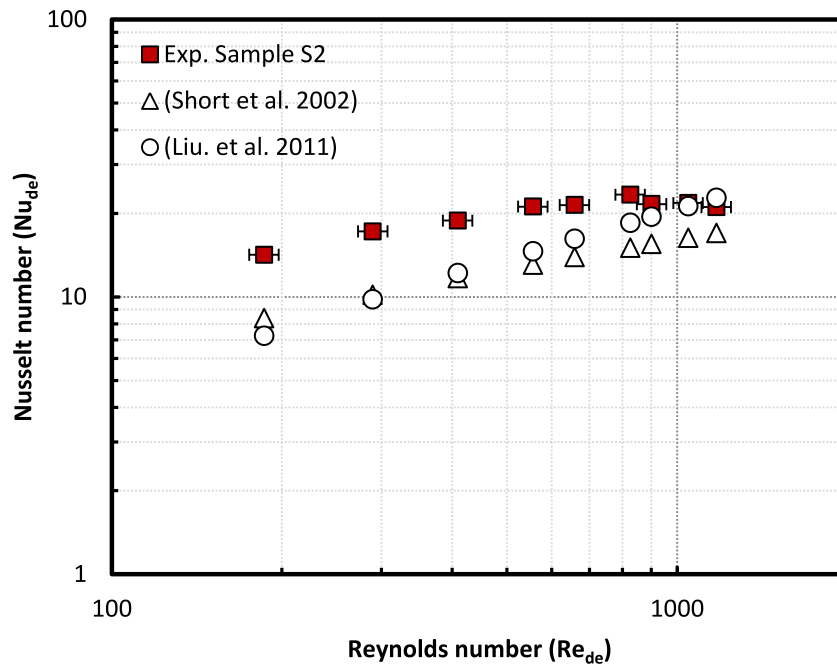

Figure 7.17: Nusselt number versus Reynolds number for sample S2.

Nusselt number for sample S3 and both correlations that of (Liu, et al., 2011) and (Short, et al., 2002) increases with Reynolds number. At low Reynolds number values, 100 to 800 heat transfer performance is higher than those predicted from (Short, et al., 2002) and (Liu, et al., 2011) correlations. With the increase in the Reynolds number over 900 the performance of sample S3 is predicted accurately from both correlations.

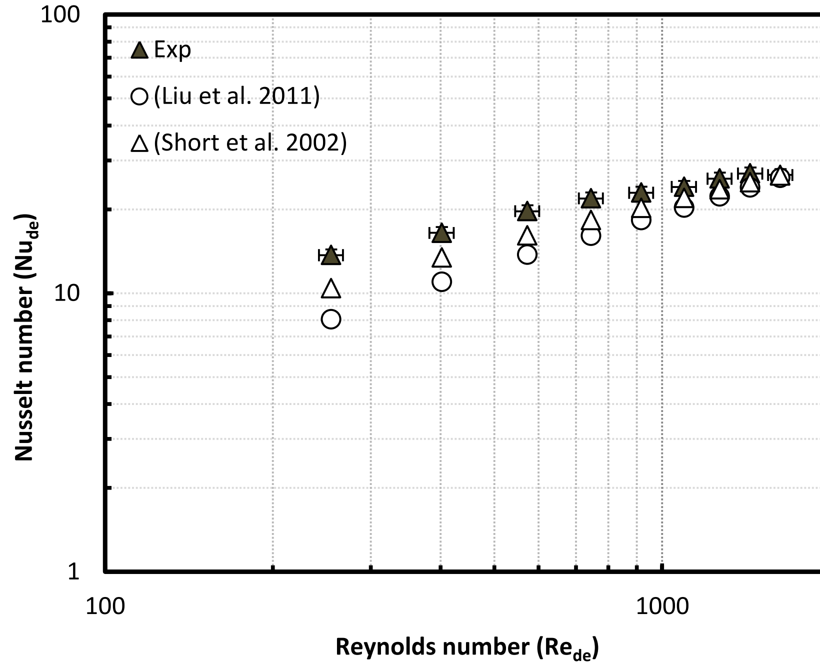

Figure 7.18: Nusselt number versus Reynolds number for sample S3.

The experimental data for the heat transfer has been correlated in terms of the Nusselt number for three enhanced samples utilizing a Dittus and Boelter type relationship $Nu=CRe^{m}Pr^{n}$. The mean absolute error has been evaluated in a similar form to that previously explained. The correlations produced from the experimental data and the Reynolds diapasons are presented in Table 7.4.

Table 7.4: Nusselt number data correlations, Reynolds number applicability and mean absolute error for the current experimental data

Test Sample	Correlation	Reynolds number	MAE %
S1	$Nu_{de}=0.8991Re_{de}^{0.3535}Pr^{1/3}$	120-740	6.5
S2	$Nu_{de}=2.0674\ Re_{de}^{0.2649}Pr^{1/3}$	200-820	3.8
S3	$Nu_{de}=1.3473\ Re_{de}^{0.321}Pr^{1/3}$	250-2600	19

7.4 SUMMARY

In this Chapter electron beam enhanced structures were characterized and the experimental data was processed in accordance with the methodology of Zukauskas (1987) for cross flow over tube banks that is widely used to assess regular pin fin structures, (Short, et al., 2002, a), (Peles, et al., 2005) etc. Results were compared with other correlations in the literature that examine regular enhancement pin-fin structures. In addition, experimental results have been correlated to produce relationships that can predict the performance and serve as a base for comparative assessments or as a design tool.

7.4.1 Pressure drop

The pressure drop on the electron beam enhanced structures is higher compared to the smooth samples. Sample S3 has the highest pressure drop, followed by sample S1 and S2. Pressure drop is a function of dynamic pressure ($\rho V^2/2$) that in itself is proportional to the fluid flow velocity. Therefore, an increase of the velocity is associated with a larger pressure drop. In cases when the cross flow section A_c is small ($V=m/\rho A_c$), i.e. sample S3 the flow velocity is higher and as a consequence it generates a large pressure drop. Consequently, channel size and the protrusion density affects the pressure drop drastically.

Due to a small number of test samples, in this study is not possible to optimize the fin geometry and the arrangement. The current electron beam treatments are different from one sample to the other. The experimental data reveals that the fin friction factor fluctuates at low Reynolds number from 100 to 600. The pressure fluctuation can be a result of the geometry at the inlet of enhanced area; here the flow contracts due to change in the cross flow area. Also the entrance region effects or so known “no-slip condition” can affect the flow due to a sudden change between the velocity close to the wall with that at the centre. Another issue is the equipment limitation to respond to very low values of the pressure drop. With the

increase of Reynolds number the pressure measurement stabilizes and experimental results show a similar trend with that produced by correlations of (Moores & Joshi, 2003) and (Metzeger, et al., 1982a).

Results for sample S1 are in good agreement with (Metzeger, et al., 1982a) correlation. Sample S2 shows similar behaviour for Reynolds numbers >900 and the experimental results are in agreement with those predicted by (Metzeger, et al., 1982a) correlation. Fin friction factor for sample S3 lies between (Moores & Joshi, 2003) and (Metzeger, et al., 1982a) predictions. Overall, experimental fin friction factor for three enhanced structures is comparable with the fin friction factor of regular heat transfer enhancement structures presented by above researchers. According to Figure 7.19 the friction factor is in the lower side or comparable to other pin-fin enhanced structures discussed in the literature.

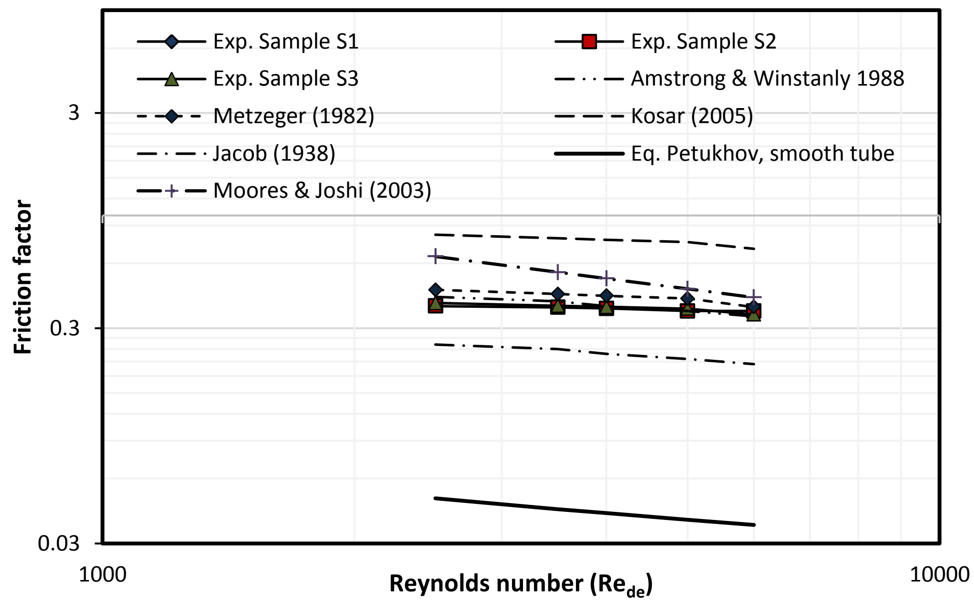

Figure 7.19: Friction factor for the test samples compared with those in literature versus Reynolds number.

7.4.2 Heat transfer

Heat transfer coefficient increases with the increase of the Reynolds number for all three samples S1, S2 and S3. Heat transfer is largely related to the heat transfer area enlargement, i.e. sample S3 has the highest fin density, approximately, 22 fins/cm^2 and as a result it has the highest heat transfer coefficient. Sample S1 has the second highest fin density approximately 11 fins/cm^2 and it has a slightly lower heat transfer coefficient compare to Sample S3. While sample S2 has a density of 77 fins/ cm^2 and it provides the lowest heat transfer coefficient among three samples. The effect of Reynolds number is also important, i.e. sample S3 operates at higher Reynolds number compared to sample S1 and S2, therefore, has a higher heat transfer coefficient.

Heat transfer results of sample S1, S2 and S3 are compared in terms of the Nusselt number with (Liu, et al., 2011) and (Short, et al., 2002). In all three cases the experimental Nusselt number is higher than the Nusselt number predicted by above correlations for Reynolds number 100 to 800. The increased performance is due to the surface irregularity of the electron beam enhanced structures that provide better conditions for heat transfer process by increasing the interaction between the fluid flow and the heated surface. Nusselt number for samples S1, S2 and S3 at Reynolds number over 900 is in line with predicted Nusselt numbers from above correlations. In addition, the experimental Nusselt number is comparted with those in the literature and shows relatively a very good performance, see Figure 7.20. The experimental results for each sample are correlated in terms of Nusselt number, see Table 7.4. Correlations can be used in the design process to predict thermal performance or to compare those to enhancement technologies.

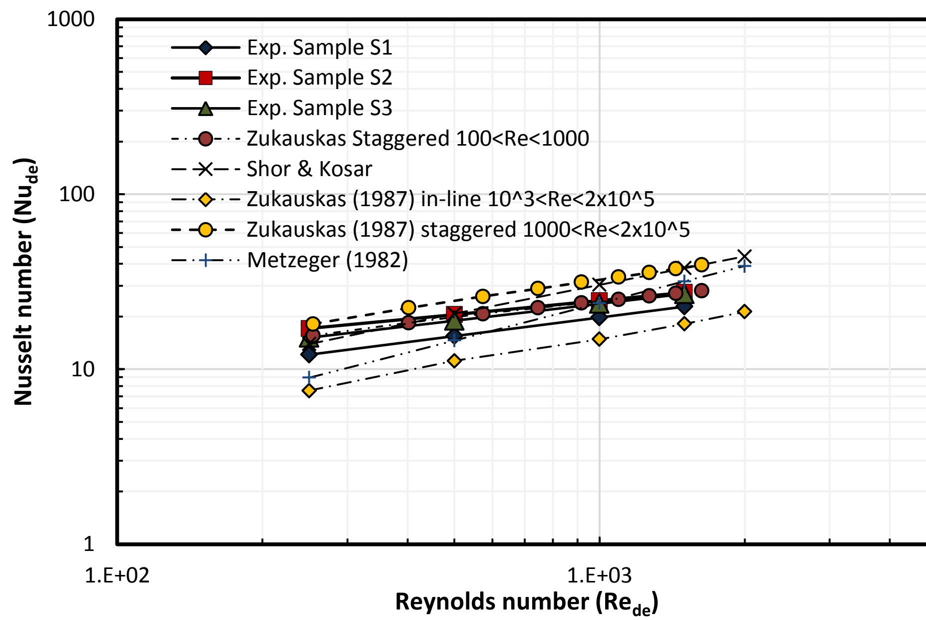

Figure 7.20: Comparison of the Nusselt number for the experimental work with those available in the literature versus Reynolds number.

8 CONCLUSION AND RECOMMENDATIONS

The application of the electron beam treatment for the improvement of the heat transfer in liquid cooling application is a new cutting edge technology. The aim is to improve of the liquid cooling capacity of liquid cooled plates for the electronics industry. This study is the first to assess thermal and hydraulic characteristics of the single phase flow in the electron beam enhanced surfaces. The main focus of this research was to evaluate the thermo-hydraulic performance of electron beam enhanced liquid cooled plates in the laminar regime of deionised water. Therefore, the main activities of the study are concentrated in the design and production of electron beam enhanced test samples, renovation of an experimental, design of the measurement system, data acquisition and the analysis of the experimental results. The work can be summarized with respect to the primary conclusions which correspond to the objectives set in the first chapter.

1. Review of the latest developments in the electronics industry to determine cooling requirements.

The assessment of the electronic industry is a continuous process, due to the emphasis that is created by the electronics product design and requirements for the thermal management systems. The main focus of the technical review is given on the component processing power and their cooling requirements. Currently, in the literature, is presented the historical path of the electronics component development, present and future trends, and the anticipated cooling needs and market implication. Therefore, the second chapter aims to address those issues and presents the following information:

- A historical review of the electronic sector development, which brings into light the challenges that the thermal management industry faces.

- Observation of the international roadmap for the semiconductor industry, transistor miniaturisation, the requirement for processor power, speed, and also the trend of transistor density in a range of products and the impact into the market growth.
- Analysis of the IT sector and the technology development. Assessment of requirements for cooling capacity. This part provides an insight into the challenges that the thermal management industry faces. Limitations of the current air cooling technology, the increasing scale of the miniaturisation and processing power, and requirements for larger and efficient cooling capacity. The importance of the liquid cooling technology, and technical issues, i.e. (fluid flow network, external cooling as radiator, fans, and a circulation pump). Such components are bulky and require space. Therefore, it is essential to reduce the size and the fluid flow rate. This is the reason why, the enhancement techniques are studied with interest to improve thermal efficiency that allows size reduction and material savings.
- Assessment of the current thermal management market and future trends show a growing trend for thermal management hardware from the electronics industry.

2. Review of the heat transfer enhancement literature.

Heat transfer enhancement is an objective in any thermal design since it reduces material, the space required, and increases the thermal performance. Research in this field is intense and has been carefully studied. The present review has been focused on pin-fin heat transfer enhancement and indicates that:

- The pin-fin arrangement effects on the heat transfer performance are noticeable. The staggered configuration has a better performance compared to the in-line configuration. The highest heat transfer rate is observed in the zone between the second and fifth row of fins.

- Reduction of stream-wise fin spacing improves the heat transfer a rate, a similar effect is observed with reduction of the span-wise fin spacing; however, in the second case the pressure drop increases considerably.
- The effect of the fin aspect ratio H/d on the heat transfer is insignificant for values H/d less than 2, nevertheless it increases considerably for values H/d larger than 4.
- The elliptically shaped fins provide the best thermo-hydraulic performance compared to other geometries.
- Clearance on top of the fin tip reduces both heat transfer and the pressure drop.

3. Electron beam technology

Application of the electron beam technology for surface treatment is a novel method of creating enhanced surfaces for heat transfer. In this study electron beam treatment was optimized for application in liquid cooled plates and production of three test samples. The electron beam technology has been explained step by step and concludes with a detailed description of the working principle of the electron beam treatment. The electron beam enhancement is e very rapid process with minimal human interaction. A summary of the benefits is given below:

Advantages of electron beam technology:

- Narrow Fusion Zone can be achieved due to a concentrated and focused beam of electrons on the work-piece.
- Vacuum environment prevents oxidisation and results to a high purity treatment zone.
- Variable heat input allows treatment of the heat sensitive materials.
- Higher depth of penetration, compared to other melting technology
- Accurate computer control of the treatment process parameters and repeatability.

- No material waste, fast, clean and economical with minimum distortion
- Generate treatments that are currently not possible to be achieved with conventional technologies

4. CFD analysis of the smooth sample.

The CFD analysis was used to validate the experimental methodology and assess the experimental data. The main conclusions are:

- Heat transfer results from the CFD analyses are in good agreement with the experimental results for the smooth sample and correlation of Stephen (1956) for parallel plates.
- Pressure drop results from the CFD analysis are in good agreement with the experimental results for the smooth sample and the methodology described by Shah and London, see Equation (7.1).

5. The main focus of this research has been the evaluation of the heat transfer and the pressure drop characteristics. The thermo-hydraulic performance of three electron beam enhanced and a smooth test sample has been studied through single phase flow in the laminar regime. In order to achieve this objective the work was concentrated in designing and producing the test rig, test samples, identifying the measurement devices, calibration, development of the experimental procedure, physical testing and analysis of the experimental results.
   The classic experiments of single phase flow are in accordance with the operating conditions of liquid cooled plates, and provide the required data for the evaluation of the performance. The experimental results for the smooth and enhanced structures indicate that:
   - Surface irregularity and the protrusion density improves heat transfer performance

- Heat transfer coefficient for sample S3, S1 and S2 is respectively 3, 2 and 1.5 times higher than that of the smooth sample.
- Fin density has a positive effect on the heat transfer improvement and a negative effect on the pressure drop.
- For a low Reynolds number ranging from 100 to 600, the experimental Nusselt is higher compared to a predicted Nusselt number.
- Improvement of the heat transfer coefficient is associated with a pressure drop increase. Sample S3 has ten times higher pressure drop compared to sample S1 and S2. While sample S1 and S2 have approximately nine times higher pressure drop than the smooth sample.
- Fin friction factor is comparable to other regular fin structures and for Reynolds numbers over 600 is in good agreement with predictions
- Sample S1 showed the highest heat transfer rate of a unit pressure drop.
- Electron beam enhanced structures are efficient in enhancing heat transfer, reduce space and material usage.
- Electron beam enhanced liquid cold plates provide adequate cooling in high heat fluxes environments and can maintain operating conditions.

The experimental data are processed and correlated to provide the bases for evaluation of electron beam enhancement technology. The information can be utilized by the designers for the design processes or comparative evaluation of the available techniques.

Overall results show that the electron beam treatment increases the heat transfer coefficient in the single phase flow regime and is very effective in providing cooling capacities required for the electronics industry. Sample S3 enhance the heat transfer performance approximately three times compared

to a smooth sample. The treatments are rapid and don’t produce material waste, therefore can reduce manufacturing costs and energy usage. The process is computer controlled with a very high accuracy and allows production of complex geometries, which are not achievable with current conventional technologies. The increase of the thermal performance reduces size, material usage and the overall required space inside the electronic module.

8.1 FUTURE WORK

This is the first experimental investigation of thermo-hydraulic performance of the electron beam enhanced surfaces. To extend investigations, further work will need to continue in the future.

1. Turbulent flow regime investigation.

The current experimental investigation provides the performance data for a part of the laminar regime, however, it would be of great interest that the turbulent flow regime is examined, since it may show further improvement of the heat transfer characteristics compared to the laminar flow regime. It is important to notice that the current experimental rig is incapable and therefore requires modifications. Firstly a larger water recirculating unit, that can provide adequate mass flow rates, is required. Secondly the test rig piping network needs to be upgraded and assessed to withstand high pressures that are developed during the turbulent flow regime.

2. Two phase flow boiling

A field of interest for heat transfer enhancement is that of the two-phase flow. The electron beam enhanced structures due to surface irregularity can serve as a nucleus for boiling initiation. As a result, there will be an interest to assess the flow characteristics and heat transfer performance in the flow-

boiling regime and to compare those results to the single-phase flow regime, and to other enhancement techniques used in the flow boiling regime.

3. CFD Analysis

An efficient way, to investigate the flow and heat transfer characteristics, is that of the CFD analysis. It is advised that in the future if processing power is available thermal performance and flow characteristics of enhanced structures can be analysed using CFD software. CFD analysis of electron beam treated surface allows a thorough investigation of different parameters and their effect in the performance and may help to understand the heat transfer enhancement mechanism.

4. Improvement of the treatment

In order to improve thermal and hydraulic performance, treatments are required to be optimized and this requires further testing. The methodology that can be followed is described in the following. The enhanced structure for optimization can be represented by two aspect ratios. The first aspect ratio diameter/height can be an image the protrusion while the second aspect ratio, height of the channel over height of the protrusion relates channel geometry with the protrusion geometry.

The first test can be performed by keeping constant both aspect ratios and the heat input while varying only the Reynolds number. From here the local Nusselt number can be plotted over the length of the channel and the average Nusselt number can be plotted against increasing Reynolds number. In addition, pressure drop can be plotted over the Reynolds number.

In the second test, the protrusion aspect ratio is varied. Reynolds number, second aspect ratio, and the heat input are kept constant. From here the local Nusselt number can be plotted over the length of the channel, and the average Nusselt number and also pressure drop can be plotted against the increasing Reynolds number.

In the third test a similar procedure to the second test can be followed, but in this case the aspect ratio that represents the channel is varied, while Reynolds number, heat input and aspect ratio one is kept constant. From here as previously explained in the second test, both the local and the average Nusselt number together with the pressure drop are plotted against the channel length and the Reynolds number respectively.

In the fourth test, Reynold number, protrusion aspect ratio and channel aspect ratio are kept constant while heat input is varied. From here the local Nusselt number is plotted over the length of the channel, the average Nusselt number and pressure drop are plotted against the increasing Reynolds number.

Presentation of the Nusselt number and pressure drop against the channel length and against the Reynolds number with different aspect ratios helps to determine the optimum protrusion geometry.

9 APPENDIX

9.1 EXPERIMENTAL DATA

Table 9.1: Experimental data for the Sample S1.

Sample S1														
Power in	Mass flow	T_{in}	$T_{in\ 1}$	$T_{in\ 2}$	T_{out}	$T_{out\ 1}$	$T_{out\ 2}$	$T_{w\ 1\ bottom}$	$T_{w\ 2}$	$T_{w\ 3}$	$T_{w\ 4}$	$T_{w\ inlet}$	$T_{w\ outlet}$	DP_{exp}
W	kg/s	°C	°C	°C	°C	°C	°C	°C	°C	°C	°C	°C	°C	Pa
600	0.0056	19.31	19.65	19.25	42.14	39.73	39.92	113.18	107.64	101.14	95.47	91.32	93.88	8
600	0.0100	19.20	19.52	19.11	32.15	29.52	30.85	94.77	89.21	82.63	76.86	73.19	74.69	43
600	0.0150	19.11	19.40	18.97	27.79	25.47	26.85	84.66	79.06	72.44	66.70	63.32	64.28	136
600	0.0200	19.00	19.30	18.85	25.41	23.48	24.61	78.85	73.18	66.57	60.86	57.59	58.32	239
600	0.0250	19.02	19.31	18.84	24.09	22.40	23.43	75.22	69.55	62.89	57.20	53.95	54.56	373
600	0.0300	19.04	19.33	18.85	23.25	21.73	22.65	72.53	66.83	60.20	54.52	51.31	51.83	541
600	0.0350	19.04	19.32	18.84	22.61	21.24	22.07	70.35	64.63	58.05	52.39	49.18	49.66	734
600	0.0400	19.03	19.31	18.83	22.13	20.88	21.66	68.75	63.04	56.44	50.81	47.57	48.00	943
600	0.0450	19.08	19.35	18.88	21.81	20.68	21.41	67.41	61.71	55.12	49.51	46.24	46.67	1182

Table 9.2: Experimental data for the Sample S2.

Sample S2														
Power in	**Mass flow**	**T_{in}**	**$T_{in\ 1}$**	**$T_{in\ 2}$**	**T_{out}**	**$T_{out\ 1}$**	**$T_{out\ 2}$**	**$T_{w\ 1\ bottom}$**	**$T_{w\ 2}$**	**$T_{w\ 3}$**	**$T_{w\ 4}$**	**$T_{w\ inlet}$**	**$T_{w\ outlet}$**	**DP_{exp}**
W	kg/s	°C	°C	°C	°C	°C	°C	°C	°C	°C	°C	°C	°C	Pa
600	0.0056	19.34	19.67	19.56	43.91	44.79	35.41	119.42	113.82	108.24	104.28	95.77	100.44	18
600	0.0101	18.87	19.09	18.99	32.16	31.42	28.23	100.46	94.95	89.45	85.34	77.48	81.14	43
600	0.0150	18.97	19.13	19.01	27.77	26.68	24.99	91.75	86.22	80.70	76.54	68.89	72.21	100
600	0.0200	18.90	19.05	18.92	25.46	24.30	23.35	86.39	80.87	75.36	71.21	63.61	66.70	228
600	0.0250	18.88	19.02	18.88	24.11	23.05	22.32	82.74	77.23	71.73	67.58	60.06	63.03	344
600	0.0301	18.87	19.00	18.84	23.19	22.20	21.61	80.05	74.55	69.06	64.89	57.39	60.36	496
600	0.0351	18.91	19.04	18.87	22.59	21.57	21.11	77.99	72.52	67.06	62.90	55.38	58.29	649
600	0.0401	18.98	19.11	18.93	22.18	21.20	20.78	76.53	71.06	65.60	61.44	53.85	56.76	860
600	0.0450	19.13	19.24	19.05	21.93	20.98	20.57	75.21	69.77	64.35	60.21	52.50	55.44	1073

Table 9.3: Experimental data for the Sample S3.

Sample S3													
Power in	**Mass flow**	**T_{in}**	**$T_{in\ 1}$**	**$T_{in\ 2}$**	**T_{out}**	**$T_{out\ 1}$**	**$T_{out\ 2}$**	**$T_{w\ 1\ bottom}$**	**$T_{w\ 2}$**	**$T_{w\ 3}$**	**$T_{w\ 4}$**	**$T_{w\ inlet}$**	**$T_{w\ outlet}$**	**DP_{exp}**
W	kg/s	°C	°C	°C	°C	°C	°C	°C	°C	°C	°C	°C	°C	Pa
600	0.0056	19.22	19.14	20.29	43.89	40.85	39.01	97.08	91.07	85.61	81.83	73.79	77.29	140
600	0.0100	18.87	18.49	18.86	32.00	29.46	30.02	81.88	75.73	70.16	66.41	59.49	61.27	544
600	0.0151	18.53	18.20	18.38	27.45	25.10	25.78	74.73	68.51	62.98	59.36	50.24	53.91	1330
600	0.0200	18.74	18.32	18.36	25.33	23.35	23.88	70.91	64.90	59.19	55.61	46.02	49.22	2347
600	0.0250	18.79	18.35	18.33	23.99	22.23	22.78	68.51	62.48	56.76	53.18	44.38	46.31	3547
600	0.0301	18.83	18.37	18.30	23.10	21.50	22.08	66.99	60.95	55.17	51.58	42.46	44.22	5013
600	0.0350	18.82	18.42	18.40	22.62	21.12	21.62	65.37	59.36	53.72	50.20	41.69	43.29	6638
600	0.0400	18.66	18.33	18.31	22.05	20.64	21.13	64.27	58.14	52.70	49.18	41.28	41.41	8494
600	0.0451	19.03	18.60	18.53	21.91	20.66	21.19	63.97	57.84	52.26	48.70	41.30	41.51	10621

Table 9.4: Experimental data for the Smooth sample.

Smooth sample												
Power in	Mass flow	T_{in}	$T_{in\ 1}$	T_{out}	$T_{out\ 1}$	$T_{w\ 1\ bottom}$	$T_{w\ 2}$	$T_{w\ 3}$	$T_{w\ 4}$	$T_{w\ inlet}$	$T_{w\ outlet}$	DP_{exp}
W	kg/s	°C	°C	°C	°C	°C	°C	°C	°C	°C	°C	Pa
600	0.0056	18.89	19.69	43.96	45.18	167.33	160.99	155.62	148.45	142.72	149.21	5
600	0.0109	18.56	19.15	32.47	29.28	147.55	140.93	135.37	128.21	123.43	131.33	12
600	0.0151	18.26	18.49	27.31	25.52	130.03	123.47	118.05	111.16	105.96	113.71	26
600	0.0208	18.29	18.57	25.26	23.99	120.12	113.50	108.02	101.37	96.55	103.87	46
600	0.0250	18.08	18.41	23.83	22.95	113.92	107.27	101.75	95.17	90.46	97.57	66
600	0.0300	18.20	18.61	23.13	22.55	108.98	102.36	96.68	90.35	85.85	92.71	75
600	0.0349	18.11	18.48	22.44	21.96	105.52	98.86	93.19	86.87	82.46	89.11	101
600	0.0400	18.15	18.53	21.90	21.75	101.77	95.19	89.53	83.26	78.74	85.27	121
600	0.0439	18.18	18.41	21.67	21.36	100.21	93.56	87.96	81.73	77.40	83.80	149

10 REFERENCES

Agostini, B., Thome, J. R., Fabri, M. & Michel, B., 2008. *Friction factor and heat transfer coefficient of R-134a liquid in microchannels.* s.l., IEEE Transactions on Components and Packaging Technologies, vol. 31.No. 3..

Ahmad, S. W., Lewis, J. S., McGlenn, R. J. & Krayiannis, T. G., 2014. Pool Boiling on Modified Surfaces Using R-123. *Heat Transfer Engineering,* Volume 35, p. 1491–1503.

Alsic, 2013. *CPS Technologies.* [Online]
Available at: http://www.alsic.com/hybrid-electric-vehicle-alsic-coolers.html
[Accessed 15 December 2013].

Ames, F. E., Dovorak, L. A. & Morrow, M. J., 2005. Turbulent augmentation of internal convection over pins in staggered pin fins arrays. *ASME J. Turbomach,* 127(1), pp. 183-190.

Amstrong, J. & Winstanly, D., 1988. A review of the staggered array pin fin heat transfer for turbine cooling applications. *J. Turbomach,* Volume 110, pp. 94-103.

Amulare, 2013. *Amulaire thermal technology.* [Online]
Available at: http://www.amulaire.com/products.php
[Accessed 24 January 2013].

Aris, M. S., McGlenn, R. J. & Sutcliffe, C. J., 2011. An Experimental Investigation into the Deployment of 3D, Finned Wing and Shape Memory Alloy Vortex Generators in a Forced Air Convection Heat Pipe Fin Stack. *Applied Thermal Engineering,* Volume 31, pp. 2230-2240.

Babus'Haq, R. F., Aktitund, K. & Probert, S. D., 1995. Thermal performance of a pin-fin assembly. *Int. J. Heat and Fluid Flow,* Volume 16, pp. 50-55.

Bakish, R., 1962 a. *Electron Beam Technology.* London: John Wiley & Sons.

Bakish, R., 1962 b. Evoluation of the Basic Science. In: R. Bakish, ed. *Introduction to Electron Beam Technology.* London: John Wiley & Sons, Inc, p. 2.

Bakish, R., 1962 c. *Introduction to Electron Beam Technology.* London: John Wiley & Sons, Inc.

Bejan, A. & Kraus, A. D., 2003 . *Heat Transfer Handbook.* New Jersey: John Wiley & Sons, Inc.

Bergles, A. & Webb, R., 1985. A guide to the literature on convective heat transfer augmentation in Advancesin Enhanced Heat Transfer II. HTD(43), pp. 81-90.

Bilen, K., Akyoul, U. & Yapici, S., 2001. Heat transfer and friction correlataions and thermal performance analysis for a finned surface. *Energy Conservation and Management,* Volume 42, pp. 1071-1083.

Blundell, S. J., 2012. *Magnetism.* Oxford: Oxford University Press.

Bueche, F., 1985. *Technical Physics.* 3 ed. NY: Harper & Row, Publishers, Inc..

Buxton, A. et al., 2009. *Electron Beam Surface Engineering for High Performance Heat Exchangers.* Chicago, IL, USA, TWI.

Cengel, Y. A., 2006. *Heat and Mass Transfer.* 3 ed. London: McGrawHill.

Cheng, L., Luan, T., Du, W. & Xu, M., 2009. Heat transfer enhancement by flow-induced vibration in heat exchangers. *International Journal of Heat and Mass Transfer,* 52(3-4), pp. 1053-1057.

Chomdee, S. & Kiatsiriroat, T., 2006. Enhancement of air cooling in staggered array of electronic modules by integrating delta winglet vortex generators. *International Communications in Heat and Mass Transfer,* Volume 33, pp. 618-626.

Chyu, M. K., 1990. Heat transfer and pressure drop for short pin-fins arrays with pin-endwall fillet. *J. Heat Transfer,* 112(4), pp. 926-932.

Chyu, M. K., Hsing, Y. C. & Natarajan, V., 1998. Convective heat transfer of cubic fin arrays in a narrow channel. *J. Heat Transfer,* Volume 120, pp. 362-367.

Chyu, M. K., Hsing, Y. C., Shih, T. I. P. & Natarajan, V., 1999. Heat Transfer Contribution of Pins and Endwall in Pin-Fin Arrays: Effect of thermal bounadry condition modeling. *ASME J. Turbomach,* 121(2), pp. 257-263.

Chyu, M. K., Siw, S. C. & Moon, H. K., 2009. Effects of Height to Diameter Ratio of Pin Element on Heat Transfer from Staggered Pin-Fin Arrays. *ASME Turbo Expo 2009. Paper No. GT2009-59814*, 8 June, pp. 705-713.

Coleman, H. W. & Steel, G., 2009. *Experimentation, Validation, and Uncertainty Analysis for Engineers.* 3 ed. NY: John Wiley & Sons, Inc.

Colinge, J. P; Colinge, C. A, 2002. *Physics of Semiconductor Devices.* Massachusttes: Kluwer Academic Publisher Group.

Dance, B. G. I. & Buxton, A. L., 2007. *An introduction to Surfi-Sculpt technology-New opportunities, new challenges.* Hallen, Germany, Procceedings on 7th International Conference on Beam Technology.

Darrigol, O., 2000. *Electrodynamics from Ampere to Einstein.* Oxford: Oxford University Press.

Dogrouz, M., Urdaneta, M. & Ortega, A., 2005. Experiments and modeling of the hydraulic resistance and heat transfer of in-line square pin fin heat sinks with top by-pass flow.. *International Journal of Heat and Mass Transfer,* Volume 48, p. 5058–5071.

Donahoo, E. E., Camci, C., Kulkarni, A. K. & Belegundu, A. D., 1999. Determination of optimal row spacing of staggered cross-pin array in a turbine blade cooling passage. *Enhanced Heat Transfer,* Volume 121, pp. 41-53.

Dong, J., Chen, J., Chen, Z. & Zhou, Y., 2007. Air-side thermal hydraulic performace of offset strip fin aluminium heat exchangers.. *Applaied Thermal Engineering,* Volume 27, pp. 306-313.

Electronics.Ca, 2012. *Electronics Industry Market Research and Knowladge Network.* [Online]
Available at: http://www.electronics.ca/thermal-management-technologies-marketies-report.html
[Accessed 5 January 2013].

Electronics.Ca, 2014. *Electroniks Industry Market Research and Knowladge Network.* [Online]
Available at: http://www.electronics.ca/thermal-management-technologies-marketies-report.html
[Accessed 23 May 2014].

Electronics.Ca, A., 2012. *Electronics.* [Online]
Available at: http://www.electronics.ca/
[Accessed 5 January 2013].

EPA, 2013. *Report on Server and Data Center Energy Efficiency.* [Online]
Available at:
http://www.energystar.gov/index.cfm?c=prod_development.server_efficiency_study
[Accessed 30 January 2013].

Frontier, 2011. *Contribution of the digital communications sector to economic growth and productivity in the UK.* [Online]
Available at:
https://www.gov.uk/government/uploads/system/uploads/attachment_data/file/77465/FE-Economic-Analysis-Paper_digitalcomms_economicgrowth.pdf
[Accessed 15 Novemeber 2013].

G.P. Celata et al, 2006. Frictional pressure drop in single-phase flow in narrow channels. *International Journal of mass and heat transfer,* pp. 717-724.

Galsworthy, J. C. & Bird, J., 1998. *The electron beam welding of marine components.* Toulon, s.n., pp. 821-828.

Geisler, K. J. L., Straznicky, I. & Bar-Cohen, A., 2004. *Immersion Cooling model for military COTS applications.* Las Vegas, Proceedings-Ninth Intersociety Conference on THermal and Thermodchemical Phenimena in Electronics Systems, pp. 67-74, 2004.

Gerken, J., 2007. *Welding Handbook, Welding processes.* 9 ed. Miami: American Welding Society.

Halimic, E., Mullen, D. & Agnew, B., 2009. *Effect of micro-channelsize, heat flux and mass flux on flow boiling heat transfer.* s.l., 11th UK Heat Transfer Conference.

Han, D. H. & Lee, K. J., 2005. Single-phase heat transfer and flow characteristics of micro-fin tubes. *Appliued Thermal Engineering,* Volume 25, pp. 1657-1669.

Hasan, M. I., 2014. Investigation of flow and heat transfer characteristics in micro pin fin heat sinks with nanofluid. *Applied Thermal Engineering,* 63(2), pp. 598-607.

Hoeflinger, B. E., 2012. *Chip 2020: A guide to the Fututre of Nanoelectronics.* s.l.:Springer.

Hwang, T. H. & Yao, S. C., 1986. Crossflow heat transfer in tube bundles at low Reynolds numbers. *ASME J. Heat Transfer,* 108(3), pp. 697-700.

IEA, 2013. *International Enenrgy Agency.* [Online]
Available at:
http://www.iea.org/media/workshops/2013/network_sept/hl1rozite.pdf
[Accessed 23 March 2013].

IEA, 2014. *International Energy Agency.* [Online]
Available at:
http://www.eia.gov/cfapps/ipdbproject/iedindex3.cfm?tid=2&pid=2&aid=12&cid=r3,&syid=2007&eyid=2011&unit=BKWH
[Accessed 24 January 2014].

Incropera, F. P., 1999. *Liquid cooling of electronic devices by single phase convection.* NY: John Wiley & Sons.

Incropera, F. P. & DeWitt, D. P., 1996. *Introduction to Heat Transfer.* 3 ed. NY: John Wiley & Soons, Inc..

Incropera, F. P., Dewitt, D. P., Bergman, T. L. & Lavine, A. S., 2006. *Fundamentals of Heat and Mass Transfer.* 6th ed. NY: John Wiley & Sons.

Incroprera, F. P., 1999. *Liquid Cooling of Electronic Devices by Single-phase Convection.* NY: John Wiley & Sons, Inc.

Incroprera, F. P. & DeWitt, D. P., 1996. *Introduction to heat transfer.* 3 ed. Canada: John Wiley & Sons, Inc..

Intel, 2013. *Intel.* [Online]
Available at: http://ark.intel.com/products/47932/Intel-Core-i7-980X-Processor-Extreme-Edition-12M-Cache-3_33-GHz-6_40-GTs-Intel-QPI
[Accessed 2 Decemebr 2013].

Intel, 2013. *Intel.* [Online]
Available at: http://ark.intel.com/products/52585/Intel-Core-i7-990X-Processor-Extreme-Edition-12M-Cache-3_46-GHz-6_40-GTs-Intel-QPI
[Accessed 29 November 2013].

Intel, 2013. *Intel Corporation.* [Online]
Available at: http://ark.intel.com/products/52585/Intel-Core-i7-990X-Processor-Extreme-Edition-12M-Cache-3_46-GHz-6_40-GTs-Intel-QPI
[Accessed 29 November 2013].

Intel, 2013. *www.intel.com.* [Online]
Available at: http://www.intel.com/content/www/us/en/processors/core/core-i7-900-ee-and-desktop-processor-series-datasheet-vol-1.html
[Accessed 2013 12 01].

Intel, 2014. *ARK home.* [Online]
Available at: http://ark.intel.com/compare/78931,78930
[Accessed 2 May 2014].

ITRS, 2013. *International Technology Roadmap for Semiconductor.* [Online] Available at: http://www.itrs.net/reports.html
[Accessed 23 November 2013].

Jakob, M., 1938. Heat transfer and flow resistance in cross flow of gases over tube banks. *ASME 60. 384.*

Jeng, T.-M., 2006. THermal performance of inline dimond-shaped pin fins in a rectangular duct. *Int. Comm. in Heat and Mass Transfer,* Volume 33, pp. 1139-1146.

Jeng, T.-M. & Tzeng, S.-C., 2007. Pressure drop and heat transfer of square pin-fin arrays in. *International Journal of Heat and Mass Transfer,* Volume 50, pp. 2364-2375.

Jeng, T.-M. & Tzeng, S.-C., 2007. Pressure drop and heat transfer of square pin-fins arrays in inline and staggered arrangements. *Int. J. of Heat and Mass Transfer,* Volume 50, pp. 2364-2375.

Kandikar, S. G. & Grande, W. J., 2004. Evaluation of single-phase flow in microchannels for high heat flux chip cooling-thermohydraulic performance enhancement and fabrication technology. *Heat Transfer Engineering,* 25(8), p. 5–16.

Kang, S., Miller, D. & Cennamo, J., 2007. *Closed loop liquid cooling for high performance computer systems.* s.l., Proceedings of the ASME Interpack Confernece, IPACK, pp. 509-515..

Karayiannis, T. G., 1998. EHD boiling heat transfer enhancement of R123 and R11 on tube bandle. *Applied Thermal Engineering,* 18(9-10), pp. 809-817.

Kast, W., 1974. *Druckverlust bei der Stromung quer zu Rohrbundeln- (Pressure drop in cross flow across tube bundles).* 2 ed. s.l.:s.n.

Kays, W. M. & Crawford, M. E., 1993. *Convective Heat and Mass Transfer.* 3rd ed. NY: McGraw-Hill.

Kim, J., 2007. Spray cooling heat transfer: The state of the art. *International Journal of Heat and Fluid Flow,* Volume 28, p. 753–767.

Konishi, C. A., Hwu, R., Qu, W. & Pfefferkorn, F. E., 2010. *Experimental study and numerical analysis of water single-phase pressure drop across a micro-pin-fin array.* Washington, Proceeding of IHTC14-23171.

Kosar, A., 2008. Two-phase pressure drop across a hydrofoil-based micro pin device using R-123. *Experimental Thermal and Fluid Science,* Volume 32, pp. 1213-1221.

Kosar, A. & Peles, Y., 2006. Thermal- Hydraulic Performance of MEMS-based Pin Fin Heat Sink. *Journal of Heat Transfer,* Volume 128, pp. 121-131.

Kosar, A. & Peles, Y., 2007. Boiling heat transfer in a hydrofoil-based micro pin fin heat sink. *International Journal of Heat and Mass Transfer,* Volume 50, p. 1018–1034.

Kosar, A., Schneider, B. & Y, P., 2005. Hydrodynamic characteristics of crossflow over MEMS-based pillars. *J. Fluid. Eng,* Volume 127, pp. 419-430.

Lawson, S. A., Thrift, A. A., Thole, K. A. & Kohli, A., 2011. Heat transfer from multiple row arrays of low aspect ratio pin fins. *International Journal of Heat and Mass Transfer,* Volume 54, pp. 4099-4109.

Lee, J. & Mudawar, I., 2009. *Low temperature two phase microchannel cooling for high heat flux thermal management of defence electronics..* s.l., IEEE Transactions on Components and Packaging Technologies, Vol. 32, No. 2..

Li, Q., Chen, Z., Flechterner, U. & Warnecke, H.-J., 1998. Heat transfer and pressure drop characteristics in rectangular channels with elliptic pin fins. *International Journal of Heat and Fluid Flow,* Volume 19, pp. 245-250.

Liu, M., Liu, D., Xu, S. & Chen, Y., 2011. Experimental study on liquid flow and heat transfer in micro square pin fin heat sink. *International Journal of Heat and Mass Transfer,* Volume 54, pp. 5602-5611.

Luviano-Ortiz, L., Hernandez-Guerrero, A., Rubio-Arana, C. & Romero-Mendez, R., 2008. Heat transfer enhancement in a horizontal channel by the addition of curved deflectors. *International Journal of Heat and Mass Transfer,* Volume 51, pp. 3972-3984.

Lyall, M. E., Thrift, A. A., Thole, K. A. & Kohli, A., 2011. Heat transfer from low aspect ratio pin fins. *Journal of Turbomashinery,* Volume 133, pp. 011001/1-10.

Maglik, R. & Bergles, A., 2004. Enhanced heat and mass transfer in the new millenium: a review of the 2001 literature. Issue 11.

Manglik, R. M. & Bergles, A. E., 1995. Heat Transfer and Pressure Drop Correlations for the Rectangular Offset Strip Fin Compact Heat Exchanger. *Experimental Thermal and Fluid Science ,* Volume 10, pp. 171-180.

McGlen, R. J., Jachuck, R. & Lin, S., 2004. Integrated thermal management techniques for high power electronic devices. *Applied Thermal Engineering,* Volume 24, pp. 1143-1156.

Mei, D. et al., 2014. Effect of tip clerance on the heat transfer and pressure drop performance in the micro-reactor with micro-pin-fin arrays at low Reynolds number. *Int. Journal of Heat and MAss Transfer,* Volume 70, pp. 709-718.

Metzeger, D. E., Barry, J. & Bronson, J. P., 1982. Developing heat transfer in rectangular ducts with staggered arrays of short pin fins. *ASME J. Heat Transfer,* Volume 104, pp. 700-706.

Metzeger, D. E., Fan, Z. X. & Shepard, W. B., 1982. *Pressure loss and heat transfer through multiple row of short pin fins.* Proceedings of the Seventh International Conference, Munich, West Germany, September, Washington, DC, Hemisphere Publishing Corp..

Metzeger, D. E. & Haley, S. W., 1982. Heat Transfer Experiments and Flow Visualisation for Arrays of Short Pin fins. *ASME PAper 82-GT-138.*

Moore, G. E., 1965. Cramming more components onto integrated circuits. *Electronics,* Volume 38.

Moore, G. E., 1975. *Progress in Digital INtegrated Electronics, Digest of the 1975 International Electron Devices Meeting.* New York, s.n., pp. 11-13.

Moores, K. A. & Joshi, Y. K., 2003. Effect of tip clerance on the thermal and hydraulic performance of ashrouded pin fin array. *ASME Journal of Heat Transfer,* Volume 125, pp. 999-1006.

Moores, K. A., Kim, J. & Joshi, Y., 2009. Heat transfer and fluid flow in shrouded pin fin arrays with and without tip clerance. *International Journal of Heat and Mass Transfer,* 52(25), pp. 5978 - 5989.

Mudawar, I., 2001. Assessment of high heat flux thermal management schemes. *Transactions on Components and Packaging Technologies,* 24(2), pp. 122-140.

Natarjan, G. & Bezama, R. J., 2007. Microjet cooler with distributed returns. *Heat Transfer Engineering,* Volume 28, pp. 779-787.

Nesis, E. I., Shatalov, A. F. & Karmataski, N. P., 1994. Dependency of heat transfer coefficient on the vibration amplitude and frequency of a vertical thin heater. *Journal of engineering physics and thermodynamics ,* pp. 696-698.

Nightinggale, K. R., Sanderson, A., Punshon, C. & Werme, L. O., 1998. *Advances in EB technology for the fabrication and sealing of large scale copper canisters for high level nuclear waste burial.* Toulon, s.n., pp. 323-330.

Nnanna, A. G. A., Rutherford, W., Elomar, W. & Snakowski, B., 2009. Assessment of thermoelectric module with nanofluid heat exchanger. *Applied Thermal Engineering,* Volume 29, pp. 491-500.

Owhaib, W. & Palm, B., 2004. Experimental investigation of single-phase convective heat transfer in circular microchannels. *Experimental thermal and fluid since,* 28(2-3), pp. 105-110.

Peles, Y. et al., 2005. Forced convective heat transfer accross a pin fin micro heat sink.. *International Journal of Heat and Mass Transfer,* Volume 48, pp. 3615-3627.

Peles, Y. et al., 2005. Forced convective heat transfer across a pin fin micro heat sink. *International Journal of Heat and Mass Transfer,* 48(17), pp. 3651-3627.

Phillips, R. J., 1988. *Forced-Convection, Liquid Cooled, Microchannel Heat Sinks. Technical Report 787,* s.l.: Lincoln Laboratory, Massachusetts Institute of Technology.

Pop, E., Sinha, S. & and Goodson, K., 2006. *Heat Generation and Transport in Nanometer-Scale Transistors.* Stanford, Proceedings of the IEEE.

Qu, W. & Siu-Ho, 2008. Liquid single phase flow inan array of micro-pin-fins-part I: heat transfer characteristics. *J. Heat Transfer,* 130(12), pp. 124501-124505.

Qu, W. & Siu-Ho, A., 2009. Experimental study of saturated flow boiling heat transfer in an array. *International Journal of Heat and Mass Transfer,* Volume 52, p. 1853–1863.

Rao, Y., Wan, C., Xu, Y. & Zang, S., 2011. Spatially-resolved heat transfer characteristics in channel with pin fin and pin fin-dimple arrays. *International Journal of Thermal Sciences,* Volume 50, pp. 2277-2289.

Reay, D. A., 1991. Heat transfer enhancement- A review of techniques and their possible impact on energy efficiency in the UK.. *Heat Recovery Systems & CHP,* 11(1), pp. 1-40.

Researchandmarkets, 2014. *Research and Markets.* [Online]
Available at:
http://www.researchandmarkets.com/research/brxtqc/global_thermal
[Accessed 30 May 2014].

Ricci, R. & Montelpare, S., 2006. An experimental IR thermographic method for the evalaution of the heat transfer coefficient of liquid cooled short pin fins

arranged in line. *Experimental Thermal and Fluid Science,* Volume 30, pp. 381-391.

Rosa, P., Karayiannis, T. G. & Collins, M. W., 2009. Single-Phase heat transfer in microchannels. The importance of scaling effcets. *Applied Thermal Engineering,* 29(17), pp. 3447 - 3468.

Russell, J. D., 1981. High Power Electron-beam Welding. *Aircraft Engineering and Aerospace Technology,* 53(11), pp. 21-24.

Salamon, D., Lammertink, R. & Wessling, M., 2010. Surface texturing inside ceramic macro/micro channels. *Journal of the European Ceramic Society,* Volume 30, pp. 1345-1350.

Sanderson, A. & Ribton, C. N., 1998. *The development of RF excited guns and intelligent power supplies for EBW at upto 150kW and 300kV.* Paris, s.n., pp. 611-621.

Schultz, H., 1993. *Electron Beam Welding.* UK: Woodhead Publishing Ltd.

Schulze, K. R. & Powers, D. E., 1998. *Nonvacuum electron beam welding: Convenient and highly productive.* Toulon, s.n., pp. 829-836.

ScienceDirect, 2014. *ScienceDirect.* [Online]
Available at:
http://www.sciencedirect.com/science?_ob=ArticleListURL&_method=list&_ArticleListID=-484741479&_sort=r&_st=13&view=c&_acct=C000228598&_version=1&_urlVersion=0&_userid=10&md5=42cb610be19f7b63273f2e3b688d07ed&searchtype=a
[Accessed 4 January 2014].

Scirus, 2013. *Scirus for since and information only.* [Online]
Available at:
http://www.scirus.com/srsapp/search?q=heat+transfer+enhancement&t=all&sort=0&g=s
[Accessed 10 January 2013].

SEMI, 2013. *Semiconductor Market Research and Market Reports.* [Online] Available at: http://www.semi.org/marketinfo
[Accessed 20 January 14].

Shah, R. K., 1978. A correlation for laminar hydrodynamic entry length solutions for circular and noncircular ducts. *J. Fluid Eng.,* Volume 100, pp. 177-179.

Shah, R. K. & London, A., 1978. *Laminar Flow Forced Convection in Ducts, Supplement 1 to Advances in Heat Transfer.* NY: Academic press.

Shah, R. K. & London, A. L., 1978. *Laminar Flow Forced Convection in Ducts.* NY: Academic Press.

Shimura, F., 1989. *Semiconductor Silicon Crystal Technology.* London: Academic Press Limited.

Short, B. E., Raad, P. E. & and Price, D. C., 2002. Performance of pin fin cast aluminium coldwalls, Part 2.Colburn j-factor correlations. *J. Thermophys. Heat Transfer,* 16(3), pp. 397-403.

Short, B. E., Raad, P. E. & Precey, D. C., 2002, a. Performance of pin fin cast aluminum coldwalls, Part 1: Friction factor correlations. *Journal of thermophysics and heat transfer,* 16(3), pp. 389-396.

Short, B. E., Raad, P. E. & Price, D. C., 2002. Performance of pin fin cast aluminium coldwalls, Part I: friction factor correlations. *Thermo-Physics,* 16(3), pp. 389-396.

SIA, 2014. *Semiconductor Marke.* [Online]
Available at:
http://www.semiconductors.org/news/2014/02/03/global_sales_report_2013/semiconductor_industry_posts_record_sales_in_2013/
[Accessed 20 February 2014].

Siddique, M., Khaled, A., Abdulhafiz, N. & Boukhary, A., 2010. Recent Advances in Heat Transfer Enhancements: A review Report. *International Journal of Chemical Engineering,* Volume Article ID 106461, pp. 1-28.

Siddique, M., Khaled, A., Abdulhafiz, N. & Boukhary, A., 2010. Recent advantages in heat transfer enhancements: A review report. *International Journal of Chemical Engineering,* Volume ID 106461, p. 28.

Siu-Ho, A. M., Qu, W. & Pfefferkon, F., 2006. *Pressure drop and heat transfer in a single-phase micro-pin-fin heat sink.* Chicago, ASME Int. Mech. Eng. Congress and Exposition .

Soodphakdee, B. M. & Copeland, D. W., 2001. A comparison of fin geometries for heat sinks in laminar forced convection: part1-round elliptical and plate fins in stagered and inline configuration. *Int. J. Microcircuits Electron. Packag,* 24(1).

Sparrow, E. M. & Liu, C. H., 1979. Heat-Transfer, Pressure-Drop and Performance Relationship for in-line, Staggered, and Continuous Plate Heat Exchanger. *Int. J. Heat and Mass Transfer,* Volume 32, pp. 1613-1625.

Sparrow, E. M., Niethammer, J. E. & Chaboki, A., 1982. Heat transfer and pressure drop characteristics of array of rectangular modules encountered in electronic equipment. *Journal Heat and Mass Transfer,* pp. 961-973.

Steinke, M. E. & Kandlikar, S. G., 2004. Review of single-phase heat transfer enhancement techniques for application in microchannels, minichannels and microdevices. *Heat and Technology,* 22(2), pp. 3-12.

Stone, K. M., 1996. *Review of Literature on Heat Transfer Enhancement in Compact Heat Exchngers,* Urbana: Prepared as part of ACRC Project 65. Air Conditioning and Refrigeration Centre University of Illinois. ref 217/ 33.3115.

Tahat, M. A., Babus'Haq, R. F. & Probert, S. D., 1994. Forced steady-state convection from pin-fin arrays. *Appl. Energy,* Volume 48, pp. 335-351.

Thermacore, 2012. *The Market of THermal Management Technologies,* Lancaster: Thermacore Europe.

Thome, J. R., 1990. *Enhanced Boiling Heat Transfer.* NY: Hemisphere.

Tuckerman, D. B. & Pease, R. F. W., 1981. High performance heat sink for VLSI. *IEEE Electronic Device Letters,* Volume 2, pp. 126-129.

Tullius, J. F., Tullius, T. K. & Bayazitoglu, Y., 2012. Optimization of short micro pin fins in minichannels. *Int. Journal of Heat and Mass Transfer,* Volume 55, pp. 3921-3932.

TWI, 2002. *Electron beam technique for material processing,* Cambridge: TWI.

TWI, 2013. *Laser Processing.* [Online]
Available at: http://www.twi-global.com/technologies/welding-surface-engineering-and-material-processing/lasers/
[Accessed 20 November 2013].

TWI, 2013. *Laser Surface Engineering.* [Online]
Available at: http://www.twi.co.uk/technologies/welding-surface-engineering-and-material-processing/lasers/laser-surface-engineering/
[Accessed 3 November 2013].

VanFossen, G. J., 1981. *Heat Transfer Coefficients for stagred array of shorts pin fins.* Houston, American Society of Mechanical Engineering.

Wang, Q. et al., 2007. Experimental study of heat transfer enhancement in narrow rectangular channels with longitudinal vortex generators. *Nuclear Engineering and Design,* 237(7), pp. 686-693.

Webb, R., 1993. *Principle of Enhanced Heat Transfer.* NY: Wiley.

Webb, R. & Eckert, E., 1972. Application of rough surfaces to heat exchaner design. *Heat and Mass Transfer,* pp. 1642-1658.

Webb, R. L. & Kim, N. H., 2005. *Principles of Enhanced Heat Transfer.* London: Taylor & Francis.

Wei, J., 2008. Challenges in cooling Design of CPU packages for high-performance servers. *Heat Transfer Engineering ,* 29(2), pp. 178-187.

Weilin, Q. & Abel, S.-H., 2009. Exprimental study of saturated flow boiling heat transfer in an array of staggered micro-pin-fins. *International Journal of Heat and Mass Transfer,* Volume 52, pp. 1853-1863.

Weilin, Q. & Mudawar, I., 2003. Flow boiling heat transfer in two-phase micro-channel heat sinks—I. Experimental investigation and assessment of correlation methods. *International Journal of Heat and Mass Transfer,* Volume 46, p. 2755–2771.

Whitaker, S., 1972. Forced convection heat transfer correlations for flow in pipe, past flat plates, single cylinders, and flow in packed-beds and tube bundles. *AIChE,* 182(2), pp. 361-371.

Wolverine, 2013. *Microcool.* [Online]
Available at: http://www.microcooling.com/technology/micro-deformation-manufacturing/micro-deformation-technology

Wong, M., Owena, I., Sutcliffe, C. J. & Puri, A., 2009. Convective heat transfer and pressure losses across novel heat sinks fabricated by Selective Laser Melting. *International Journal of Heat and Mass Transfer ,* Volume 52, p. 281–288.

Wong, M., Owen, I. & Sutcliffi, C. J., 2009. Pressure Loss and Heat Transfer Through Heat Sinks Produced by Selective Laser Melting. *Heat Transfer Engineering,* 30(13), p. 1068–1076.

WSTS, 2014. *WSTS Semiconductor Market Forecast Spring 2014.* [Online]
Available at: https://www.wsts.org/PRESS/Recent-News-Release
[Accessed 3 March 2014].

Xie, X. L., Liu, Z. J., He, Y. L. & Tao, W., 2009. Numerical study of laminar heat transfer and pressure drop characteristics in water cooled minichannel heat sink.. *Applied THermal Engineering,* Volume 29, pp. 64-74.

Yakut, K., Nihal Alemdaroglu, N., Kotcioglu, I. & Celik, C., 2006. Experimental investigation of thermal resistance of a heat sink with hexagonal fins.. *Applaied Thermal Enginering,* Volume 26, pp. 2262-2271.

Yang, B., Wang, P. & Ba-Cohen, A., 2007. Mini-contact enhanced thermoelectric cooling of hot spots in high power devices. *IEEE Transactions on Componentsand Packing Technologies,* Volume 30, pp. 432-438.

Young, P. L. & Kandlikar, S. G., 2008 . *Surface Roughnes Effects on Heat Transfer in Microscale Single Phase Flow: a Critical Review..* Darmstadt, Germany, ASME 2008 6th International Conference on Nanochannels, Microchannels, and Minichannels (ICNMM2008), pp. 189-201.

Yuan, M., Wei, J., Xue, Y. & Fang, J., 2009. Subcooled flow boiling heat transfer of FC-72 from silicon chips fabricated with micro-pin-fins. *International Journal of Thermal Sciences,* Volume 48, pp. 1416-1422.

Zhang, H. Y., Mui, Y. C. & Tarin, M., 2010. Analysis of thermoelectric cooler performance for high power electronic packages. *Applied Thermal Engineering,* Volume 30, pp. 561-568.

Zhang, H. Y., Pinjala, D., Wong, T. N. & Joshi, Y. K., 2005. *Development of liquid cooling techniques for flip chip ball grid array packages with high heat flux dissipations.* s.l., IEEE Transactions on Components and PAcking Technologies, vol. 28, no. 1..

Zhao, T. S. & Bi, Q., 2001. Co-current air water two-phase flow patterns in vartical triangular microchannels. *International Journal of Multiphase Flow ,* Volume 27, pp. 765-782.

Zhigang, L., Ning, G. & Chengwu, Z., 2013. Influence of tip clerance on heat transfer efficiency in micro-cylindres-group heat sink. *Experimental Thermal and Fluid Science,* Volume 46, pp. 64-73.

Zimbeck, W. et al., 2008. *Loop heat pipe technology for cooling computer servers.* s.l., 11th IEEE Intersociety Conference on Thermal and Thermomechanical Thenomena in Electronic Systems, I-THerm, art. no. 4544248, pp. 19-25.

Zimparov, V., 2002. Energy conservation through heat transfer enhancement techniques. *International Jornal of Energy Research,* Volume 26, pp. 675-696.

Zitzewitz, P. W., 2011. *The Handy Physics Answer Book.* 2 ed. USA: Visible Ink Press.

Zou, Z. J., North, M. T. & Wert, K. L., 2000. *High heat flux heat pipe mechanism for cooling of electronics.* s.l., Inter Society Conference on THermal Phenomena, IEEE 2000..

Zukauskas, A., 1972. *"Heat transfer from tubes in cross flow" in J. P. Hartnet and T. F. Irvine, Jr.,Eds.,.* New York: Academic Press.

Zukauskas, A., 1987. Heat transfer from tubes in cross flow. In: S. Kakac, R. K. Shah & W. Aung, eds. *Handbook of single phase convective heat transfer.* NY: Wiley.

Zukauskas, A. A., 1972. Heat transfer from tubes in crossflow. *Advances in Heat Transfer,* Volume 8, pp. 93-160.